



# Structure-properties relations in thienoacenes organic semiconductors

Federico Modesti

## ► To cite this version:

Federico Modesti. Structure-properties relations in thienoacenes organic semiconductors. Material chemistry. Université de Strasbourg, 2023. English. NNT : 2023STRAF033 . tel-04295865

**HAL Id: tel-04295865**

**<https://theses.hal.science/tel-04295865>**

Submitted on 20 Nov 2023

**HAL** is a multi-disciplinary open access archive for the deposit and dissemination of scientific research documents, whether they are published or not. The documents may come from teaching and research institutions in France or abroad, or from public or private research centers.

L'archive ouverte pluridisciplinaire **HAL**, est destinée au dépôt et à la diffusion de documents scientifiques de niveau recherche, publiés ou non, émanant des établissements d'enseignement et de recherche français ou étrangers, des laboratoires publics ou privés.

**ÉCOLE DOCTORALE DES SCIENCES CHIMIQUES**  
**UMR 7006 – Institut de Science et d'Ingénierie Supramoléculaires**

**THÈSE** présentée par :  
**Federico MODESTI**

soutenue le : **22 Septembre 2023**

pour obtenir le grade de : **Docteur de l'université de Strasbourg**

Discipline/ Spécialité : Chimie des Matériaux

**Relations structures-propriétés de semi-conducteurs  
organiques thiénoacènes**

**Structure-properties relations in thienoacenes organic  
semiconductors**

**THÈSE dirigée par :**

**M. EBBESEN Thomas**

Professor, Université de Strasbourg

**M. ERK Peter**

Directeur de recherches, BASF SE

**RAPPORTEURS :**

**Mme. AGHASSI-HAGMANN  
Jasmin**

Professor, Karlsruher Institut für Technologie

**M. WEITZ Thomas**

Professor, Georg-August-Universität Göttingen

---

**AUTRES MEMBRES DU JURY :**

**M. CIESIELSKI Artur**

Directeur de recherches, Université de Strasbourg



*“Every newly established fact and every new point of view, however insignificant, is sooner or later to be of use. In a year or in several decades they are bound to be of use to someone else.”*

Aleksandr Kitaigorodsky



# Acknowledgments

I would like to express my deepest gratitude to Dr. Peter Erk for his invaluable support and guidance during the past three years. I feel truly grateful to him for giving me the freedom to realize my ideas and for nurturing my scientific thinking. I sincerely appreciate all that I have learned from him, both professionally and personally. My deepest thanks go to Prof. Thomas Ebbesen for taking on the responsibility of being my PhD director, for the scientific discussions we had, and for welcoming me to his lab in Strasbourg.

I extend my heartfelt thanks to my colleagues Thomas Musiol, Thorsten Schwotzer, Sandra Gaube, and Sebastian Rath for generously investing their time in teaching me new lab techniques, for the insightful discussions, and for sharing their invaluable experimental knowledge with me. I would like to acknowledge Prof. Paolo Samori and Prof. Norbert Koch for hosting me and welcoming me during my secondments at the Supramolecular Science and Engineering Institute and Humboldt University of Berlin. I extend my gratitude to Dr. Guillaume Schweicher for his invaluable support and fruitful exchange of ideas. I am deeply grateful to Dr. Nicholas Turetta and Christos Gastios for their ability to teach me state-of-the-art measurements with conductive AFM and UPS, and more than that, for their company and the time we spent together. I would also like to express my thanks to Dr. Kripa Joseph for her dedication and patience in teaching me the secrets of optical cavities and vibrational strong coupling. I would like to thank all the principal investigators involved in the UHMob project for the fruitful discussions during the periodic meetings. I extend a special thank you to all my colleagues from the UHMob project: Martina, Rahul, Nemo, Marco, Mindaugas, Ann Maria, Lucia, Alessandro, Lamiaa, Priya, and Ines. They have not only been outstanding colleagues, but also friends and companions on this journey. I thank all of them for their great attitude towards science and for their willingness to collaborate both in and outside of the lab.

I would also like to extend my personal thanks to some individuals who have been with me throughout these years. I thank Frieda for her warm welcome and for sharing our lovely apartment in Mannheim. I would like to thank Cecilia for being a great friend and for being there for me whenever I needed her. I express my deepest thanks to Luigi and Cecilia for sharing this German adventure with me and for their unwavering support when I experienced experimental setbacks. I would like to express my gratitude to Giulia for her immense support and for bringing out the best in me during the most

challenging moments. I am grateful to her for consistently instilling in me a sense of curiosity and the appreciation for the beauty of discovery. Finally, I would like to express my deepest gratitude to my family, Mamma, Papà, and Francesca, even though they were far away, I always felt their strong support.

To all the other people I have met during these last three years, if I have not thanked you personally, know that each one of you has contributed to making this journey special.

# Contents

Preface .....	1
Chapter 1 Introduction .....	3
1.1 Introduction to organic semiconductors .....	3
1.2 Organic semiconductor materials .....	6
1.2.1 Organic polymers .....	6
1.2.2 Small molecules .....	6
1.3 Charge transport .....	10
1.3.1 Charge carrier mobility .....	11
1.3.2 Static and dynamic disorder .....	12
1.3.3 Transfer integrals and reorganization energy .....	13
1.3.4 Hopping model .....	13
1.3.5 Band model .....	14
1.3.6 Transient localization model .....	15
1.4 Organic field-effect transistors .....	17
1.4.1 Operating principles .....	18
1.4.2 Contact resistance .....	24
1.4.3 The organic semiconductor-contact interface .....	30
1.5 Coupling with the vacuum field .....	33
1.5.1 Theoretical description .....	33
1.5.2 Molecular and material properties under light-matter strong coupling .....	37
Chapter 2 Charge transport and charge injection properties of new thienoacene derivatives in thin-film transistors .....	40
2.1 Introduction .....	40
2.2 Crystal structures .....	45
2.3 Thin-film transistors fabrication .....	48
2.4 Thin-film characterization .....	51
2.4.1 Topography .....	51
2.4.2 Crystallinity .....	56
2.4.3 Ionization energy .....	58

2.5 Electrical performances .....	61
2.5.1 Thin film transistors based on DN4T and isoDN4T.....	61
2.5.2 Thin film transistors based on C <sub>8</sub> -DN4T and C <sub>10</sub> -DN4T.....	67
2.5.3 Thin film transistors based on <i>tert</i> -butyl thienoacene derivatives.....	70
2.5.4 Contact resistance evaluation .....	75
2.6 Discussion.....	77
2.6.1 Transfer integrals and reorganization energies .....	77
2.6.2 DN4T and isoDN4T vs DNTT, isoDNTT and L-DBTTA.....	79
2.6.3 C <sub>8</sub> -DN4T and C <sub>10</sub> -DN4T vs C <sub>8</sub> -DNTT and DN4T .....	83
2.6.4 Tert-butyl substituted thienoacenes .....	85
2.7 Summary .....	90
Chapter 3 Elucidating the influence of the molecular structure of thienoacenes organic semiconductors on contact resistance.....	92
3.1 Introduction.....	92
3.2 Crystal structures .....	94
3.3 Thin-film transistor fabrication .....	96
3.4 Thin-films characterization.....	97
3.4.1 Topography.....	97
3.4.2 Crystallinity .....	100
3.5 Thin-film transistors characteristics .....	103
3.5.1 TFTs with 25-nm-thick OSC layer.....	103
3.5.2 TFTs with 80-nm-thick OSC layer.....	112
3.6 Out-of-plane charge transport.....	120
3.6.1 Evaluation of the out-of-plane mobility .....	121
3.7 Charge injection area.....	125
3.8 Study of the OSC/contact interface using ultraviolet photoelectron spectroscopy .....	128
3.8.1 Hole injection barrier and ionization energy .....	129
3.8.2 Interfacial dipole .....	132
3.9 Discussion.....	136
3.9.1 Contact resistance in TC thin-film transistors.....	136
3.9.2 Contact resistance in BC thin-film transistors.....	140
3.10 Summary .....	142

Chapter 4 Exploring the effect of vibrational strong coupling on perylene crystallization in a Fabry-Perot cavity .....	145
4.1 Introduction.....	145
4.2 Perylene crystallization .....	147
4.2.1 Crystal structures .....	147
4.2.2 Crystallization experiments .....	148
4.3 Crystallization in Fabry-Perot cavity .....	152
4.3.1 Fabry-Perot cavity fabrication .....	152
4.3.2 Results and discussion.....	152
4.4 Summary .....	158
Chapter 5 Materials and methods .....	160
5.1 OSC materials.....	160
5.1.1 Synthesis of C <sub>8</sub> -DN4T and C <sub>10</sub> -DN4T .....	160
5.1.2 Synthesis of tBu-DNTT .....	161
5.1.3 Synthesis of tBu-DBTTT .....	163
5.2 Thin-film transistors fabrication and electrical measurements .....	164
5.3 Ultraviolet photoelectron spectroscopy measurements.....	164
5.4 Atomic force microscopy .....	165
5.4.1 Topography imaging .....	165
5.4.2 Conductive atomic force microscopy .....	165
5.5 Thin-films X-Ray Diffraction.....	166
5.6 Photoelectron Yield Spectroscopy .....	166
5.7 Optical Microscopy.....	166
5.8 Powder X-Ray diffraction .....	166
5.9 Fabry-Perot cavity fabrication .....	166
5.10 Fourier transformed infrared spectroscopy .....	167
5.11 Quantum calculations.....	167
5.11.1 Transfer integrals .....	167
5.11.2 Reorganization energies .....	167
5.11.3 Mobility Anisotropy .....	168
Appendix .....	170
Chapter 6 Conclusions.....	188

Résumé .....	192
References .....	201
List of Publications .....	216

# List of Figures

Figure 1.1: Charge delocalization in $\pi$ -molecular orbitals of benzene. ....	4
Figure 1.2: Typical crystalline packing motifs of molecular OSCs. ....	9
Figure 1.3: Organic semiconductor and electrode energy band diagrams. ..	11
Figure 1.4: Illustration of charge transport model mechanisms. ....	16
Figure 1.5: Schematic illustration of the four different OFET structures. ..	17
Figure 1.6: Idealized representation of operating principle and energy band diagram of a p-type OFET. ....	19
Figure 1.7: Charge carrier concentration profile of OFETs. ....	21
Figure 1.8: Transfer and output characteristics of a p-type OFET. ....	21
Figure 1.9: Contact resistance in OFET. ....	25
Figure 1.10: Contact resistance in OFETs with staggered and coplanar geometries. ....	27
Figure 1.11: Current crowding in staggered OFET. ....	28
Figure 1.12: Contact resistance extraction by using the transmission line method. ....	30
Figure 1.13: Organic semiconductor-contact interface. ....	32
Figure 1.14: Schematic illustration of two coupled harmonic oscillators. ....	34
Figure 1.15: Schematic energy diagrams of light-matter interaction. ....	36
Figure 2.1: Charge transport properties of tBu-BTBT. ....	43
Figure 2.2: Crystalline packing. ....	45
Figure 2.3: Contact angle of water droplets on bare $\text{Al}_2\text{O}_3$ and on TDPA/ $\text{Al}_2\text{O}_3$ . ....	49
Figure 2.4: Illustration of devices geometry. ....	50
Figure 2.5: AFM topography images of thin films deposited on TDPA/ $\text{Al}_2\text{O}_3$ at different substrate temperatures. ....	52
Figure 2.6: AFM topography images of $\text{C}_8$ -DN4T and $\text{C}_{10}$ -DN4T thin films deposited on TDPA/ $\text{Al}_2\text{O}_3$ . ....	54
Figure 2.7: AFM topography images of DN4T and isoDN4T thin films deposited on PFBT/Au. ....	55
Figure 2.8: XRD patterns of thin films. ....	57
Figure 2.9: PYS measurements performed on thin films of thienoacene derivatives. ....	59
Figure 2.10: Mobility vs substrate temperature for DN4T and isoDN4T. ...	62
Figure 2.11: Threshold voltage and on/off current ratio vs substrate temperature for DN4T and isoDN4T. ....	63
Figure 2.12: Transfer and output characteristics of DN4T and isoDN4T top-contact devices. ....	64
Figure 2.13: Mobility and on/off current ratio vs substrate temperature for BC and TC TFTs based on DN4T and isoDN4T. ....	65
Figure 2.14: Threshold voltage vs substrate temperature for BC and TC TFTs based on DN4T and isoDN4T. ....	66

Figure 2.15: Transfer and output characteristics of DN4T and isoDN4T bottom-contact devices.....	67
Figure 2.16: Mobility vs substrate temperature for C <sub>8</sub> -DN4T and C <sub>10</sub> -DN4T. ....	69
Figure 2.17: Transfer and output characteristics of C <sub>8</sub> -DN4T and C <sub>10</sub> -DN4T bottom-contact devices.....	70
Figure 2.18: Representative transfer and output characteristics of BC TFT based on tBu-BTBT.....	71
Figure 2.19: Charge carrier mobility as a function of the substrate temperature for TC TFTs based on tert-butyl thienoacene derivatives.....	73
Figure 2.20: Transfer (left) and output (right) characteristics of the best performing BC TFTs based on tert-butyl-substituted thienoacene derivatives. ....	74
Figure 2.21: Transmission line method applied to TFTs. ....	75
Figure 2.22: Molecular arrangement with respect to <i>a</i> , <i>b</i> and <i>c</i> directions..	79
Figure 2.23: Short contacts between adjacent molecules in the crystalline arrangement and calculated HOMO of DN4T and isoDN4T.....	82
Figure 2.24: Thin-film growth mode. ....	84
Figure 2.25: Mobility anisotropy plots. ....	88
Figure 3.1: Crystalline packing of the parent and alkylated compounds. ...	95
Figure 3.2: AFM topography images of thin films.....	98
Figure 3.3: XRD patterns of OSCs deposited onto TDPA/Al <sub>2</sub> O <sub>3</sub> and PFBT/Au substrates. ....	101
Figure 3.4: Transfer characteristics of TC TFTs with 25-nm-thick OSC layer. ....	104
Figure 3.5: Transfer characteristics of BC TFTs with 25-nm-thick OSC layer. ....	105
Figure 3.6: Transmission line method applied to TC and BC TFTs with 25-nm-thick OSC layer. ....	107
Figure 3.7: Width-normalized contact as a function of the gate-overdrive voltage of TC TFTs with 25-nm-thick OSC layer. ....	108
Figure 3.8: Width-normalized contact as a function of the gate-overdrive voltage of BC TFTs with 25-nm-thick OSC layer.....	109
Figure 3.9: Width-normalized contact resistance of TC and BC TFTs.....	110
Figure 3.10: Schematic illustration of the in-plane and out-of-plane directions of charge transport in a staggered device. ....	111
Figure 3.11: Transfer characteristics of TC TFTs with 80-nm-thick OSC layer. ....	113
Figure 3.12: Transfer characteristics of BC TFTs with 80-nm-thick OSC layer. ....	114
Figure 3.13: Transmission line method applied to TC and BC TFTs with 80-nm-thick OSC layer. ....	116
Figure 3.14: Width-normalized contact resistance of TC TFTs with 80-nm-thick OSC layer.....	117

Figure 3.15: Width-normalized contact resistance of BC TFTs with 80-nm-thick OSC layer. ....	118
Figure 3.16: Width-normalized contact as a function of the gate-overdrive voltage TFTs with 80-nm-thick OSC layer. ....	119
Figure 3.17: Sample geometry for SCLC measurements. ....	121
Figure 3.18: J-V characteristics measured using C-AFM on thin films plotted in logarithmic scale. ....	122
Figure 3.19: Charge carrier injection in TC and BC TFTs. ....	125
Figure 3.20: Transfer length extraction and contact resistivity in TC TFTs. ....	127
Figure 3.21: UPS spectra showing the valance region of thin film deposited onto Au and PFBT/Au substrates. ....	130
Figure 3.22: Secondary electrons cut-offs used to determine work functions. ....	133
Figure 3.23: Schematic energy-level diagram of the bands alignment at Au and PFBT/Au substrates. ....	135
Figure 3.24: Contact resistance vs intrinsic mobility. ....	138
Figure 4.1: Polymorphic forms of perylene. ....	146
Figure 4.2: XRD patterns and optical micrographs of $\alpha$ - and $\beta$ -form of perylene. ....	149
Figure 4.3: Recrystallization and slurry experiments. ....	150
Figure 4.4: Fabry-Perot cavity. ....	152
Figure 4.5: Fourier transformed infrared spectra of perylene and benzonitrile. ....	153
Figure 4.6: Recrystallization experiments conducted in the microfluidic cell. ....	155
Figure 4.7: Shift of the optical cavity modes due to temperature change. .	157

# List of Tables

Table 2.1: Crystallographic data of the investigated compounds. ....	47
Table 2.2: Averaged grain size extracted from AFM images. ....	53
Table 2.3: Values extracted from XRD and AFM measurements. ....	58
Table 2.4: Width-normalized contact resistance extracted from TC and BC TFTs. ....	76
Table 2.5: Reorganization energy ( $\lambda$ ), transfer integrals ( $J_T$ ) and charge carrier mobility ( $\mu$ ) of the investigated compounds. ....	78
Table 2.6: Crystalline packing, ionization energy (IE), and mobility ( $\mu$ ) of DN4T, isoDN4T, DNNT, isoDNNT and L-DBTTA. ....	80
Table 2.7: Ionization energy, threshold voltage and charge carrier mobility of C <sub>8</sub> -DN4T, C <sub>10</sub> -DN4T and C <sub>8</sub> -DNNT. ....	83
Table 2.8: Ionization energy (IE), threshold voltage ( $V_{th}$ ) and mobility ( $\mu$ ) of tert-butyl substituted thienoacenes. ....	86
Table 3.1: Crystallographic data of DNNT, DBTTT, C <sub>8</sub> -DNNT and C <sub>12</sub> -DBTTT. ....	94
Table 3.2: Fabrication parameters used for TC and BC TFTs. ....	96
Table 3.3: Averaged grain size extracted from AFM images of thin films deposited onto TDPA/Al <sub>2</sub> O <sub>3</sub> and PFBT/Au. ....	100
Table 3.4: Comparisons of the d-spacing, terrace height steps and unit cell long axis. ....	102
Table 3.5: Electrical performance of TC TFTs with 25-nm-thick OSC layer. ....	105
Table 3.6: Electrical performance of BC TFTs with 25-nm-thick OSC layer. ....	106
Table 3.7: Electrical performance of TC TFTs with 80-nm-thick OSC layer. ....	113
Table 3.8: Electrical performance of BC TFTs with 80-nm-thick OSC layer. ....	115
Table 3.9: Out-of-plane mobility ( $\mu_{out}$ ) obtained from J-V characteristics. ....	124
Table 3.10: Extracted transfer lengths ( $L_T$ ) and charge injection areas ( $A_{inj}$ ) for TC TFTs with 25-nm-thick OSC layer. ....	126
Table 3.11: Extracted values from UPS measurements. ....	134
Table 3.12: Electrical performances and injection barriers of TC TFTs. ...	136
Table 3.13: Contact resistance, charge carrier mobility and hole injection barrier of BC TFTs. ....	141

# List of Abbreviations

AFM	Atomic Force Microscopy
BGBC	Bottom-Gate Bottom-Contact
BGTC	Bottom-Gate Top-Contact
C-AFM	Conductive Atomic Force Microscopy
DOS	Density of States
EA	Electron Affinity
FET	Field-Effect Transistor
FP	Fabry-Perot
FT-IR	Fourier Transformed Infrared
HOMO	Highest Occupied Molecular Orbital
IE	Ionization energy
LUMO	Lowest Unoccupied Molecular Orbital
MO	Molecular Orbital
OFET	Organic Field-Effect Transistors
OLED	Organic Light-Emitting Diode
OPV	Organic Photovoltaics
PFBT	Pentafluorobenzenethiol
PYS	Photoelectron Yield Spectroscopy
PXRD	Powder X-Ray Diffraction
R <sub>c</sub> W	Width-normalized contact resistance
SAM	Self-Assembly Monolayer
SCFET	Single Crystal Field-Effect Transistor
SCXRD	Single Crystal X-Ray Diffraction
SCLC	Space Charge Limited Current
SECO	Secondary Electron Cut-Off
TC	Top Contact
TDPA	Tetradecyl phosphonic acid
THF	Tetrahydrofuran

TFT	Thin-Film Transistor
TLM	Transmission Line Method
TGBC	Top-Gate Bottom-Contact
TGTC	Top-Gate Top-Contact
UHV	Ultra-High Vacuum
UPS	Ultraviolet Photoelectron Spectroscopy
VSC	Vibrational Strong Coupling
XRD	X-Ray Diffraction


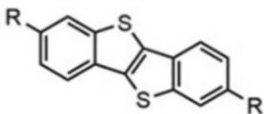
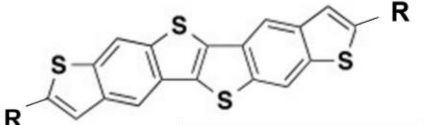
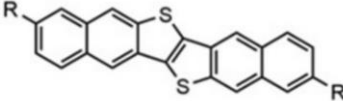
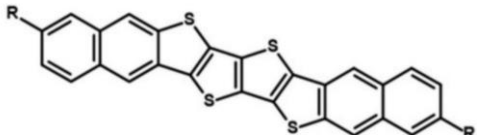
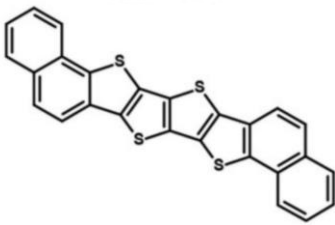
# List of Symbols

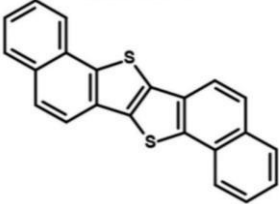
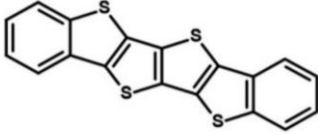
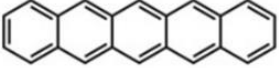
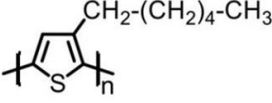
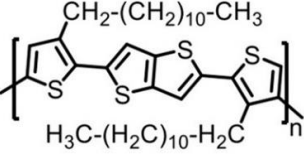
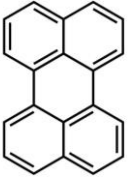
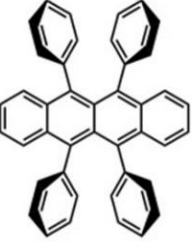
$\Delta$	Interfacial dipole
$\Delta V_D$	Voltage drop at the drain contact
$\Delta V_S$	Voltage drop at the source contact
$E_B$	Binding energy
$E_F$	Fermi energy
$E$	Electric field
$E_K$	Kinetic energy
$E_{SECO}$	Secondary electron cut-off energy
$g_m$	Transconductance
$\hbar$	Reduced Planck constant
$h\nu$	Monochromatic light energy
$\hbar\Omega_R$	Rabi-splitting
$I_d$	Drain current
$J$	Current density
$J_{ch}$	Channel current density
$J_{int}$	Interfacial current density
$J_T$	Transfer integrals
$K_{ET}$	Rate of charge transfer
$K_b$	Boltzmann constant
$L_{OV}$	Gate-to-contact overlap length
$L$	Channel length
$L_T$	Transfer length
$L_v$	Localization length
$m^*$	Effective mass of charge carrier
$\mu$	Charge carrier mobility
$\mu_0$	Intrinsic charge carrier mobility
$\mu_{in}$	In-plane charge carrier mobility
$\mu_{out}$	Out-of-plane charge carrier mobility

$n$	Charge carrier density
$N_{it}$	Interfacial trap density
$N_{bulk}$	Bulk trap density
$p$	Charge carrier density of the channel
$q$	Elementary charge
$R_{bulk}$	Bulk resistance
$R_C$	Contact resistance
$R_{CW}$	Width-normalized contact resistance
$R_D$	Drain contact resistance
$R_S$	Source contact resistance
$R_{ch}$	Channel resistance
$R_{int}$	Interfacial resistance
$R_{sh}$	Sheet resistance
$\sigma_{ch}$	Channel conductivity
$SS$	Subthreshold swing
$T$	Temperature
$T_s$	Substrate temperature
$v$	Drift velocity of charge carriers
$V_d$	Drain voltage
$V_{FB}$	Flat-band voltage
$V_g - V_{th}$	Gate-overdrive voltage
$V_{th}$	Threshold voltage
$V_{ch}$	Voltage drop across the channel
$W$	Channel width
$W_D$	Width of the depleted region
$W_F$	Work function
$WF_C$	Contact work function
$\lambda$	Reorganization energy
$\lambda_{in}$	Inner reorganization energy
$\lambda_{out}$	Outer reorganization energy
$\Phi_B$	Schottky barrier

$\Phi_{\text{B,n}}$	Electron injection barrier
$\Phi_{\text{B,p}}$	Hole injection barrier
$\varepsilon$	Relative dielectric constant
$\varepsilon_0$	Vacuum permittivity
$\eta_{\text{ch}}$	Channel efficiency

# Chemical Structures

Compound	Chemical Structure
Benzene	
BTBT derivatives	 <p> <math>R = H, BTBT</math>  <math>R = C_8H_{17}, C_8-BTBT</math>  <math>R = tBu, tBu-BTBT</math> </p>
DBTTT derivatives	 <p> <math>R = H, DBTTT</math>  <math>R = tBu, tBu-DBTTT</math>  <math>R = C_{12}H_{25}, C_{12}-DBTTT</math> </p>
DNTT derivatives	 <p> <math>R = H, DNTT</math>  <math>R = C_8H_{17}, C_8-DNTT</math>  <math>R = C_{10}H_{21}, C_{10}-DNTT</math>  <math>R = \text{phenyl}, diPh-DNTT</math>  <math>R = tBu, tBu-DNTT</math> </p>
DN4T derivatives	 <p> <math>R = H, DN4T</math>  <math>R = C_8H_{17}, C_8-DN4T</math>  <math>R = C_{10}H_{21}, C_{10}-DN4T</math> </p>
isoDN4T	

isoDNTT	
L-DBTTA	
Pentacene	
P3HT	
PBTTT	
Perylene	
Rubrene	





# Preface

The field of organic semiconductors (OSCs) has undergone extensive research and development over the past few decades, driven by the technological applications in printed electronics. OSC molecules in the solid-state are held together by weak intermolecular interactions, which influence their charge transport properties. Thin-film transistors (TFTs) based on OSCs are highly promising for electronic applications due to their flexibility, low processing-temperature fabrication, solution-processing for cost-effective large area applications, and tailor-made molecular design. However, the electrical performance of OSC-based TFTs is hampered by static and dynamic disorder. Rational design of OSCs is required to ensure a well-defined crystal packing along with suitable molecular properties to maximize their potential electronic application.

This thesis aims to investigate the structure-properties relations of small-molecule organic semiconductors, outlining guidelines for molecular design of high-performance organic TFTs. The first part of this work investigates the electrical performance of new classes of thienoacenes OSCs with different molecular cores and substitutions in TFTs. Structure-properties relations are established, unveiling the critical role of the thin film morphology, crystalline packing, and charge injection. In the second part, this work investigates the impact of molecular structures of thienoacenes on the contact resistance in TFTs. The study highlights the minor impact of molecular core substituents in both coplanar and staggered device geometry, while underlying the significance of maximizing in-plane charge carrier mobility to minimize contact resistance. In the third part, this thesis explores the effect of light-matter coupling on perylene crystal growth and polymorphism, revealing the limitations of performing recrystallization experiments in an optical cavity and providing guidance for future experimental setups.



# Chapter 1

## Introduction

### 1.1 Introduction to organic semiconductors

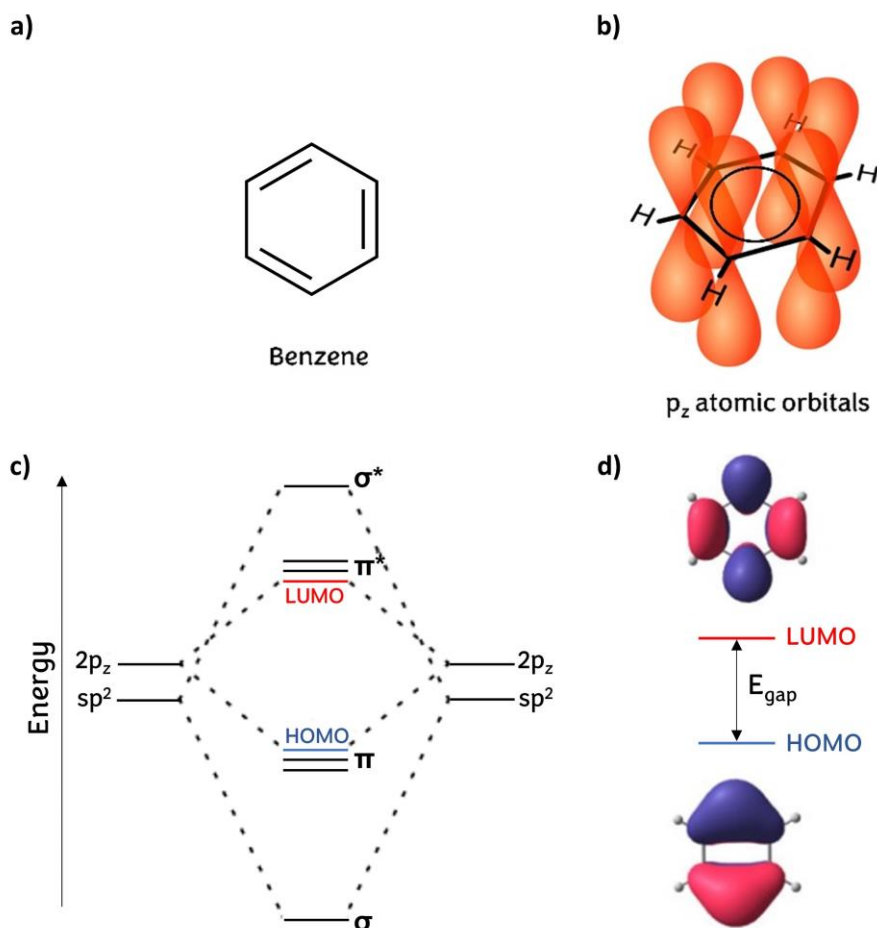
The research field of organic electronics has sparked interest among the scientific community starting from the mid of 1970s, when the first organic field-effect transistor (OFET),<sup>[1]</sup> organic light emitting diode (OLED)<sup>[2]</sup> and organic photovoltaic (OPV) cell <sup>[3]</sup> have been reported. Since then, this research field has been extensively studied and developed. One of the main advantages of using organic materials for optoelectronic applications, is the tunability of chemical and physical properties of organic semiconductors (OSCs) through molecular,<sup>[4,5]</sup> supramolecular<sup>[6]</sup> and crystal design.<sup>[7]</sup> In addition, OSCs are characterized by flexibility (depending on the utilised substrate),<sup>[8]</sup> low processing-temperature fabrication<sup>[9]</sup> and solution-processing for cost-effective large area applications<sup>[9]</sup>. All these features enable the synthesis of organic materials that can be designed for a tailor-made need. On the other hand, the main drawbacks of OSCs are the lower stability under ambient conditions and the lower electrical performances if compared to the inorganic counterpart.

The concept of utilizing conjugated organic molecules for electronic devices can be traced back to the 1940s.<sup>[10]</sup> However, significant attention towards practical applications only emerged after the discovery and advancement of conductive polyacetylene,<sup>[11]</sup> thanks to the pioneering studied of Heeger, MacDiarmid and Shirakawa, who have been awarded with the Nobel Prize in chemistry in 2000.

The physical origin of electrical conductivity in OSCs relies in charge carrier delocalization through conjugated  $\pi$ -system. The formation of this system can be explained considering the electronic configuration of carbon atoms constituting the backbone of OSCs. In OSCs, carbon atoms are connected via alternated single and doubled bonds with  $sp^2$  hybridised atomic orbitals. Considering the molecular orbital theory, adjacent carbon atoms exhibit overlapping  $sp^2$  hybridized atomic orbitals, resulting in the formation of bonding and antibonding  $\sigma$  and  $\sigma^*$  molecular orbitals (MOs). In contrast, the remaining atomic  $p_z$  orbitals overlap to a lesser extent, leading to the creation of bonding  $\pi$  and antibonding  $\pi^*$  MOs.

Benzene is one of the simplest aromatic compounds and consists of six carbon atoms. The combination of the  $2p_z$  orbitals leads to energetic splitting into

three bonding  $\pi$  MOs and three antibonding  $\pi^*$  MOs (**Figure 1.1**). The  $\pi$  molecular orbital with the highest energy is defined as the highest occupied molecular orbital (HOMO), while the  $\pi^*$  molecular orbital with lowest energy is defined as the lowest unoccupied molecular orbitals (LUMO). HOMO and LUMO are identified as frontier orbitals and at first approximation can be viewed as the valance and conduction band, respectively.



**Figure 1.1: Charge delocalization in  $\pi$ -molecular orbitals of benzene.**

(a) Molecular structure of benzene, (b) representation of the  $p_z$  atomic orbitals, (c) diagram illustrating the energy-level splitting that occurs during bonding in a benzene molecule, along with the formation of HOMO and LUMO energy levels. (d) Shape of the HOMO and LUMO of benzene.<sup>[12]</sup>

The electrons within these  $\pi$  bonds, namely  $\pi$ -electrons, are delocalized among all six  $2p_z$  orbitals. As a result, the  $\pi$  electrons can be envisioned as an electron cloud that is distributed across the planes both above and below the atomic plane. In the solid state, OSC molecules are held together by Van der Waals forces and coulombic interactions and the overlap of  $\pi$ -molecular

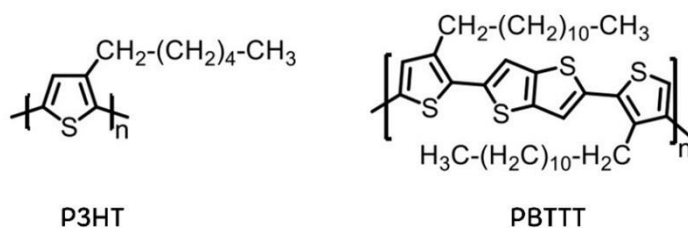
orbitals within neighbouring molecules provides charge conduction pathways. When charge carriers are introduced in the OSC by electrical injection or photoinduction, the energy of the HOMO and LUMO as well as their extension and overlap within neighbouring molecules determine the efficiency of charge carrier transport. Intermolecular charge transport across the OSC is enabled by the combined effects of charge delocalization, achieved through the  $\pi$  conjugated system, and the overlap of MOs within adjacent molecules.

The energy separation between the HOMO and the LUMO corresponds to the band gap ( $E_{\text{gap}}$ ) observed in inorganic semiconductors. In benzene, the band gap is approximately 5.9 eV,<sup>[12]</sup> causing it to possess insulating properties. In acenes, a group of compounds characterized by an increasing number of annealed benzene rings, the number of overlapping  $2p_z$  orbitals increases, changing the energetic splitting between bonding and antibonding molecular orbitals. This leads to a reduction in the HOMO-LUMO energy difference. For instance, pentacene, one of the most exploited OSCs, consists of five fused benzene rings and exhibits an energy gap of approximately 2.2 eV.<sup>[13]</sup>

## 1.2 Organic semiconductor materials

### 1.2.1 Organic polymers

OSCs can be divided in two classes: polymers and small molecules. Organic semiconductor polymers exhibit poorer film crystallinity and higher molecular disorder<sup>[14]</sup> compared to small molecule OSCs. OSC polymers are mostly semi-crystalline, characterized by alternating crystalline and amorphous domains. Charge transport is efficient through the crystalline regions but is hampered throughout the disordered regions. Thus, the latter is considered the bottleneck of electrical performances in devices based on OSC polymers, due to the high energetic barrier that charges must overcome to pass from one ordered domain to the other.<sup>[15]</sup> Charge carrier mobility is defined as the drift velocity of the charge carrier per unit of the electric field, and it is the reference figure of merit for electrical performances of OSCs. Charge carrier mobility can be enhanced by ensuring that polymer chains are of sufficient length to assist charge transport within crystalline regions, acting as a tie-chain.<sup>[16,17]</sup> **P3HT** is one of the most exploited OSC polymer, showing charge carrier mobility of about  $0.1 \text{ cm}^2\text{V}^{-1}\text{s}^{-1}$ .<sup>[18]</sup> **P3HT** has an additional hexyl side group if compared to polythiophene. The structural modification has shown to enhance the electrical properties of the **P3HT** thanks to the head-to-tail interaction of the hexyl side chains, leading to the formation of semicrystalline lamellar structures.<sup>[19]</sup> This solid-state ordering enabled by the structural modification, highlights how structure-properties relations play a major role in the development and design of OSCs. OFETs devices based on **PBTBT** has revealed charge carrier mobility up to  $1 \text{ cm}^2\text{V}^{-1}\text{s}^{-1}$ .<sup>[20]</sup> The semicrystalline structure is induced by sidechains interdigitation.



Scheme 1.1

### 1.2.2 Small molecules

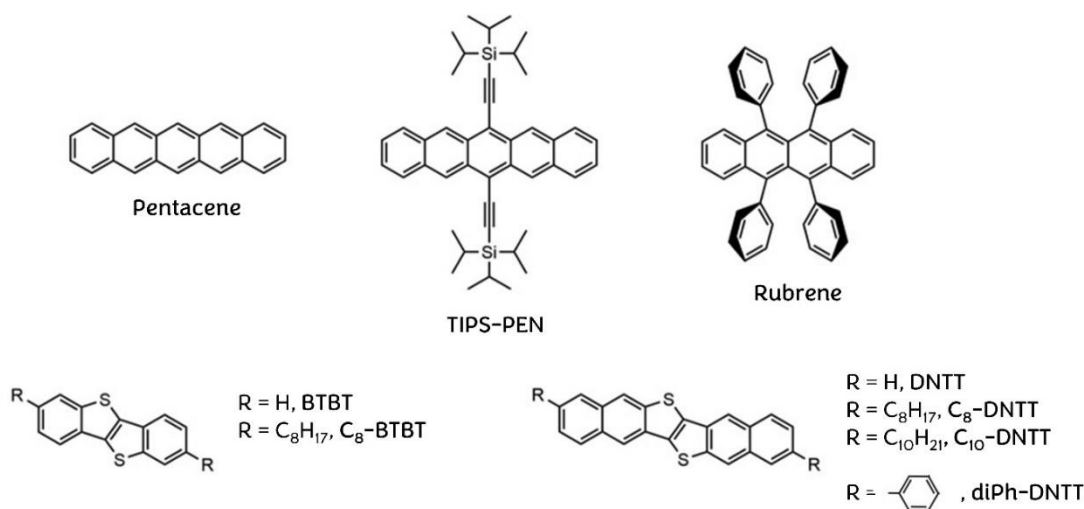
Compared to OSC polymers, small molecules are characterized by a higher degree of crystallinity resulting in more reproducible and reliable charge carrier mobility values in the range of 1 and  $10 \text{ cm}^2\text{V}^{-1}\text{s}^{-1}$  for state-of-art

molecular semiconductors.<sup>[21]</sup> As drawback, small-molecule OSCs have typically lower solubility in organic solvent compared to OSC polymers, preventing the deposition through solution-processing techniques. Nevertheless, solubility can be increased by the functionalization of the molecular cores with side groups (generally with long alkyl chains). Typical small molecule OSCs are shown in **Scheme 1.2**.

Pentacene has been extensively employed as benchmark for device physics studies. Due to the low solubility of pentacene, field-effect transistors are typically fabricated by vacuum deposition, giving charge carrier mobility of about  $0.5 \text{ cm}^2\text{V}^{-1}\text{s}^{-1}$ .<sup>[22,23]</sup> **TIPS-PEN** has been obtained through the functionalization with triisopropyl groups to the 6 and 13 positions of pentacene, enabling the fabrication of transistors through solution processing. While pentacene crystallizes with a herringbone packing, **TIPS-PEN** packs with a “bricklayer” crystalline motif.<sup>[24]</sup> This enhances the  $\pi$ - $\pi$  overlapping of neighbouring molecules, leading to mobility up to  $1.5 \text{ cm}^2\text{V}^{-1}\text{s}^{-1}$  (see the next section regarding the packing motif of OSC small molecules).<sup>[25]</sup> Among acenes, rubrene has shown the highest charge carrier mobility yet reported at room temperature, in the range of  $20 \text{ cm}^2\text{V}^{-1}\text{s}^{-1}$  in single crystal field effect transistor (SCFET).<sup>[26]</sup>

The introduction of thiophene rings into the acene structures results in ladder-type molecular structures, namely thienoacenes.<sup>[27]</sup> In this class of molecules, charge carrier mobility is boosted by an effective contribution of the sulphur atoms to the  $\pi$ - $\pi$  overlapping of adjacent molecules.<sup>[28]</sup> **BTBT** and **DNTT** and their derivatives are undoubtedly the most exploited OSCs among thienoacenes. The main challenges for the use of **BTBT** are the high ionization energy of about 5.8 eV which hinders charge injection from metal electrodes and, in addition, the poor film homogeneity when vacuum deposited.<sup>[28]</sup> The introduction of alkyl chains to the position 2 and 7 of **BTBT** enables solution-processing and facilitate charge carrier injection from electrodes due to the decrease of ionization energy to values of about 5.0 eV.<sup>[29]</sup> Specifically **C8-BTBT** unveils charge carrier mobility of about  $5 \text{ cm}^2\text{V}^{-1}\text{s}^{-1}$ .<sup>[30]</sup> Higher values of mobility have been claimed for **C8-BTBT**, but most likely these values were overestimated since extracted from devices with strongly gated contacts.<sup>[31–33]</sup> **DNTT** has two additional benzene rings annealed to the **BTBT** core. The extended conjugation results in lower ionization energy (compared to **BTBT**) of 5.4 eV, which facilitates charge carrier injection in OFETs.<sup>[34]</sup> Moreover, the pronounced electronic density on the sulphur atoms increases the  $\pi$ -orbital overlap between neighbouring molecules giving rise to high charge carrier mobility up to  $3 \text{ cm}^2\text{V}^{-1}\text{s}^{-1}$ .<sup>[27]</sup> **DNTT** is one of the most exploited OSCs and it has been used for several applications, i.e., sensors for healthcare applications,<sup>[35–37]</sup> flexible low voltage complementary circuits<sup>[38]</sup>

and neuromorphic devices.<sup>[39,40]</sup> **DNTT** derivatives functionalized in 2 and 7 positions such as **C<sub>8</sub>-DNTT**, **C<sub>10</sub>-DNTT** and **diPh-DNTT** exhibit even higher charge carrier mobility compared to the parent molecule, with values exceeding 10 cm<sup>2</sup>V<sup>-1</sup>s<sup>-1</sup> for alkylated DNTTs in solution-processed OFETs<sup>[41,42]</sup> and values of about 5 cm<sup>2</sup>V<sup>-1</sup>s<sup>-1</sup> for **diPh-DNTT** in vacuum-deposited thin-film transistors.<sup>[43,44]</sup> **C<sub>10</sub>-DNTT** has revealed record-breaking electrical performances in terms of lowest contact resistance (10 Ωcm) and highest on/off current ratio of (10<sup>10</sup>) in OFETs.<sup>[45,46]</sup>



**Scheme 1.2**

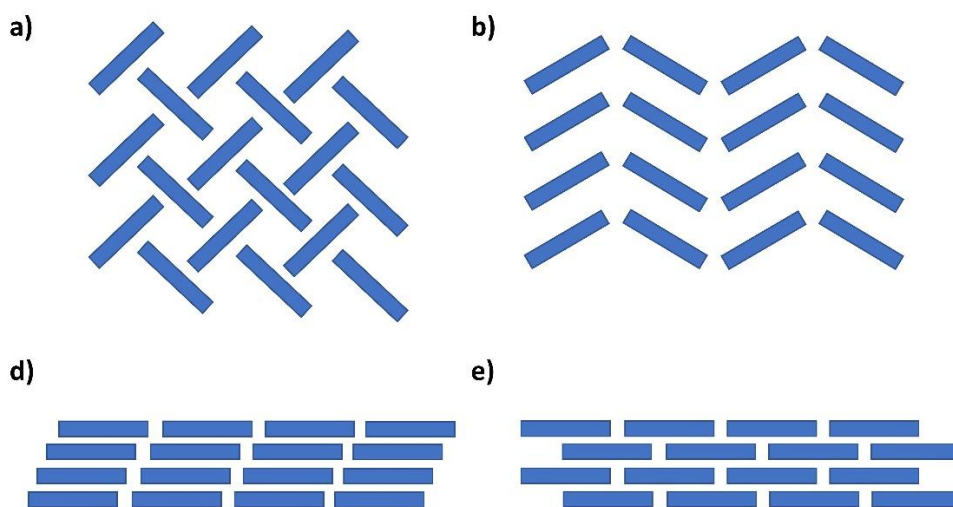
### 1.2.2.1 Molecular packing

The understanding of structure-properties relations is essential for the design of new high performance OSCs, considering that the molecular structure as well as the crystalline packing strongly influences charge transport properties of OSCs. Molecular packing features are mainly driven by intermolecular interactions.<sup>[47]</sup> Typically, the molecular packing motif should exhibit a large number and long-range intermolecular interactions to ensure optimal charge transport properties.<sup>[48]</sup>

The structural ordering of OSC molecular crystals can be described by the packing motif. This defines the pattern of orientation of the OSC molecular cores with respect to each other, reflecting the intermolecular interactions. The extensive research on the packing motif of molecular OSCs has led to the identification of four major packing motifs,<sup>[49]</sup> depicted in **Figure 1.2**.

The herringbone packing motif is characterized by C-H $\cdots\pi$  interactions, without  $\pi$ - $\pi$  overlap within adjacent molecules which pack with an edge-to-

face orientation. The slipped herringbone packing resembles the typical herringbone packing motif, but it is governed by both  $\text{C-H}\cdots\pi$  interactions and  $\pi$ - $\pi$  overlap, resulting in face-to-face orientation of adjacent molecules. The  $\pi$ - $\pi$  overlap is predominant both in slipped stack packing and brick-wall packing motifs. The former is characterized by columnar face-to-face molecular arrangement with columns tilted relative to one other. In the latter molecules are oriented face-to-face with respect to each other, forming alternated parallel columns.



**Figure 1.2: Typical crystalline packing motifs of molecular OSCs.**

(a) herringbone packing, (b) slipped herringbone packing, (c) slipped-stack packing and (d) brick-wall packing.

From a theoretical point of view, the brick-wall packing motif is the most optimal to ensure high charge carrier mobility, since it maximizes the  $\pi$ - $\pi$  overlap within neighbouring molecules.<sup>[50]</sup> Nevertheless, this crystalline arrangement is not a prerequisite to obtain high performance OSCs. For instance, rubrene (which exhibits one of the highest charge carrier mobility among OSCs) crystallizes with a slipped herringbone packing motif. In addition, many OSCs with excellent electrical performances such as **DNTT** and its alkylated derivatives, are characterized by a herringbone packing motif. Most generally, dense molecular packing and an effective overlap of the  $\pi$ -molecular orbitals are crucial for achieving efficient charge transport in molecular crystals.<sup>[51]</sup>

### 1.3 Charge transport

The charge transport mechanism taking place in OSCs has been debated for many years, due to the complexity to establish a comprehensive theoretical model for a wide variety of organic materials.<sup>[52]</sup> The intermolecular charge transport in OSCs can be influenced by both intrinsic and extrinsic factors. In the solid state OSC molecules are held together by Van der Waals forces. Hence, the overlap and the strength of interaction of electronic orbitals results to be susceptible to molecular orientation, temperature, static and dynamic disorder (see next sections), but also to the process and the materials used for the device fabrication. Yet, some fundamental principles are well established.

In crystalline OSCs, the interaction between the HOMO and the LUMO levels results in the formation of conduction and valence bands as in the case of inorganic semiconductors. It is worth noting that these transport bands are narrower in OSCs (on the order of 100 meV), if compared to the inorganic counterparts (on the order of few eV). In addition, in case of amorphous or disordered OSCs, static and dynamic disorder leads to a distribution of discrete occupied and unoccupied states rather than a continuous transport band (**Figure 1.3**). Charge carrier mobility depends on the width of the transport bands, which in turns reflects the strength of intermolecular interaction. The ionization energy (IE) and the electron affinity (EA) are defined as the energy difference between the vacuum energy level and the energy of HOMO and LUMO levels respectively:

$$IE = E_{vacuum} - E_{HOMO} \quad (1.1)$$

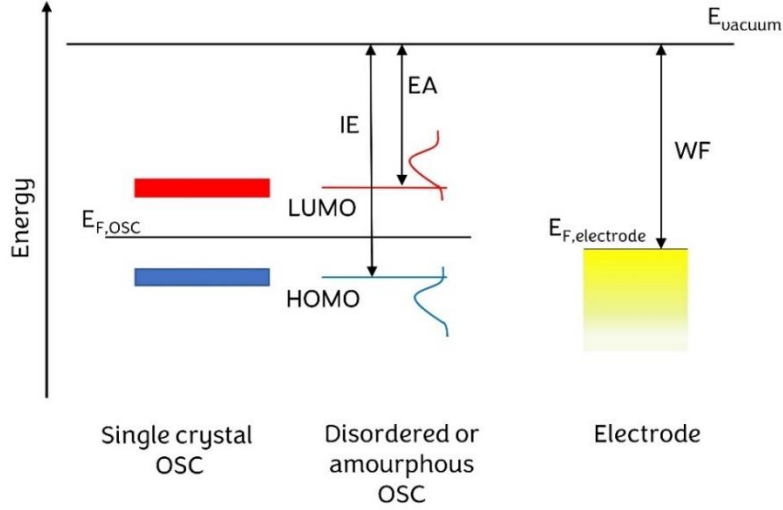
$$EA = E_{vacuum} - E_{LUMO} \quad (1.2)$$

As the inorganic counterpart, OSCs can be grouped depending on the transported charge carrier. This is mainly determined by the electronic structure of the OSC, which defines the HOMO and LUMO levels, and by the work function (WF) of the material used for the electrical contacts in devices. The work function is defined as the energy required to extract one electron from the Fermi level ( $E_F$ ) to the vacuum level (**Figure 1.3**):

$$WF = E_{vacuum} - E_F \quad (1.3)$$

Consequently, an OSC is defined as p-type (n-type) when the electrodes work function matches the ionization energy (electron affinity) of the OSC, leading to holes (electrons) transport. In some cases, OSCs can transport both electrons and holes and are defined as ambipolar.

Excess of charge carriers has to be accumulated in the conduction or valence bands to induce charge transport. This is accomplished by injecting charges from a metal electrode, in the case of OFETs and OLEDs, or by photoexcitation, in the case of OPVs.



**Figure 1.3: Organic semiconductor and electrode energy band diagrams.** Schematic illustration of (a) single crystal OSC where narrow conduction (in red) and valance (in blue) bands are formed, (b) disordered or amorphous OSC where distribution of states are formed and (c) metal electrode.

### 1.3.1 Charge carrier mobility

Charge carrier mobility ( $\mu$ ) relates the drift velocity ( $v$ ) of free carriers (electrons or holes) to the driving force of an applied electrical field ( $E$ ):

$$v = \mu E \quad (1.4)$$

Therefore, the current density ( $J$ ) generated by the charge transport is describes as follow:

$$J = q n v = q n \mu E \quad (1.5)$$

where  $q$  is the elementary charge and  $n$  is the charge carrier density. Charge carrier mobility is considered one of the most important parameters when comparing OSCs electrical performances.

For instance, in OFETs mobility determines the maximum current trough the device (at a given applied voltage), the maximum achievable switching speed and hence the maximum transient frequency.<sup>[53,54]</sup> Charge carrier mobility

can be extracted from OFETs, as explained in **Paragraph 1.4.** To date, the highest reliable and reproducible mobility in OSCs has been achieved for rubrene at room temperature, giving values of about  $20 \text{ cm}^2\text{V}^{-1}\text{s}^{-1}$ . Higher charge carrier mobilities have been claimed, but these values either have been extracted from non-ideal devices or have not yet been reproduced by other research groups. A literature survey has raised the problem of overestimated reported mobility, showing that more than the half of the articles reviewed in the survey either do not report the data from which mobility was extracted or the reported data set has some sort of nonideality.<sup>[55]</sup> Thus, state-of-art OSCs typically exhibit reliable and reproducible charge carrier mobilities between 1 and  $10 \text{ cm}^2\text{V}^{-1}\text{s}^{-1}$ , with few exceptions exceeding  $10 \text{ cm}^2\text{V}^{-1}\text{s}^{-1}$ .<sup>[52]</sup>

### 1.3.2 Static and dynamic disorder

The achievement of high charge carrier mobility in OSCs is hampered by static and dynamic disorder. Static disorder arises from impurities, defects, electrostatic effects (i.e., local dipoles) and in some cases from the presence of polymorphs.<sup>[56]</sup> In polycrystalline OSC thin films, static disorder is accentuated by grain boundaries which limit the charge transport between different crystalline domains.<sup>[57]</sup> The direct consequence of static disorder is the formation of trapping states, that are electronic defects where charge is trapped and spatially localized. Consequently, any defect and inhomogeneity in the crystal structure impacts the molecular orbitals overlap and locally induce changes of the electronic structure.

Dynamic disorder arises from the thermal motion of molecules in the crystalline arrangement. Considering the van der Waals intermolecular interactions, the phonon modes (vibrational motions of the lattice) tend to exhibit large vibration amplitudes, on the order of  $0.1 \text{ \AA}$ .<sup>[58,59]</sup> The phonon modes can interact with the charge motion, leading to the so-called electron-phonon coupling. This causes fluctuations of the molecular orbitals overlap and site energies across the molecular lattice.

In summary, impurities and defects results in static disorder, whereas thermal vibration of the molecules in the crystalline lattice results in dynamic disorder. Both give rise to trap states, which severely hinder charge transport in OSCs. While static disorder can be contained through the optimization of OSCs processing and device fabrication, there are currently no effective methods to prevent electron-phonon coupling. Nonetheless, large amplitude vibrations can be suppressed in OSCs with a stiff molecular structure.<sup>[60]</sup>

### 1.3.3 Transfer integrals and reorganization energy

At microscopic scale, charge transport is generally described by the transfer integrals ( $J_T$ ) and the reorganization energy ( $\lambda$ ). Considering two adjacent molecules,  $J_T$  expresses the overlap of the HOMO (or LUMO) wavefunctions. Specifically,  $J_T$  represents the strength of the interaction between the wavefunctions associated to the electronic configurations when charge is localized on the first molecule and when is localized on the second molecule.

The reorganization energy is composed by the inner ( $\lambda_{in}$ ) and the outer ( $\lambda_{out}$ ) parts.<sup>[21]</sup> The former is associated to the sum of the energies required for the geometric relaxation from the neutral state geometry to the charged state geometry and vice versa. In other words,  $\lambda_{in}$  reflects the energy needed for the conformational change upon charge transfer.  $\lambda_{out}$  accounts for the modification of the surrounding media due to polarization. Generally,  $\lambda_{out}$  is neglected because it is considerably lower compared to  $\lambda_{in}$ , reducing  $\lambda$  mainly to the sole contribution of  $\lambda_{in}$ .<sup>[61]</sup>

$J_T$  can be estimated within a fragment orbital approach only when the crystal structure of the investigated compounds is determined (electronic couplings are computed among pairs of close neighbours). On the contrary  $\lambda_{in}$  can be calculated theoretically prior to the synthesis of the OSC molecule, since it depends just on the molecular structure.<sup>[62]</sup>

When  $J_T \ll \lambda$ , the charge wavefunction tends to be localized on a single molecule and charge transport occurs because of incoherent hopping events within the molecules (hopping model mechanism). In contrast, when  $J_T \gg \lambda$ , charge is delocalized over several molecules and charge transport occurs through diffusion (band model mechanism).<sup>[52]</sup> OSC materials typically exhibit transfer integrals and reorganization energies in the range of 10-100 meV and 50-500 meV respectively,<sup>[52,63,64]</sup> hence  $J_T \approx \lambda$ . In this intermediate regime neither the hopping model nor the band model are solely appropriate to explain the charge transport mechanism. In the recent years, the transient localization model has been developed to describe charge transport of OSCs.<sup>[65]</sup> In this model charges show both localized and extended characters.

### 1.3.4 Hopping model

In the hopping model of transport charges are localized at singles sites and charge transport occurs through incoherent hopping events (**Figure 1.4**). To a first approximation, the rate of charge transfer ( $K_{ET}$ ) can be expressed by

using the semiclassical Marcus theory,<sup>[66]</sup> firstly developed to describe the electron transfer rate in donor-acceptor complex:

$$K_{ET} = \frac{2\pi}{\hbar} J_T^2 \frac{1}{\sqrt{4\pi K_b T}} \exp\left(\frac{-\lambda}{4K_b T}\right) \quad (1.6)$$

where  $\hbar$  is the reduced Planck constant,  $K_b$  is the Boltzmann constant, and  $T$  is the temperature. Assuming that charge transport occurs through hopping between individual sites placed on a 1D periodic array, charge carrier mobility can be defined as follow:

$$\mu = \frac{\Delta x}{E \Delta t} = K_{ET} \frac{\Delta x}{E} \quad (1.7)$$

where  $\Delta x$  and  $\Delta t$  are the intermolecular distance and the time interval of charge transfer, respectively. Considering **equations 1.6** and **1.7** and assuming that  $J_T$  and  $\lambda$  do not change with temperature,  $\mu$  follows an Arrhenius-type temperature dependence, indicating a thermally activated process.<sup>[52]</sup> In addition, from **equations 1.6** and **1.7**, it is clear that  $J_T$  has to be maximized and  $\lambda$  has to be minimized to enhance charge carrier mobility.

Generally, the hopping model is considered an appropriate description for charge transfer occurring in materials with low mobility ( $\mu \ll 1 \text{ cm}^2\text{V}^{-1}\text{s}^{-1}$ ), as in the case of disordered and amorphous OSC films.

### 1.3.5 Band model

In band like transport, the large overlap and strong interaction of molecular orbitals of neighbouring molecules results in the formation of narrow transport bands. Hence, charges are delocalized over the molecular units, leading to diffusive charge transport (**Figure 1.4**). This occurs when the energy of interaction between the molecular orbitals is stronger than dynamic and static disorder. However, the delocalized charge wavefunction may be scattered due to static and dynamic disorder.

In the Drude model, charge carrier mobility can be expressed as follow:

$$\mu = \frac{q\tau}{m^*} \quad (1.8)$$

where  $\tau$  is the mean scattering time and  $m^*$  is the effective mass of charge carrier. Band transport occurs when the mean free path of charge carrier is considerably larger than the lattice constant. Thus, the reorganization energy does not affect the charge carrier mobility, since the residence time of charge at a single molecular site is shorter than the time required for the geometrical relaxation upon charge transfer. Considering that  $m^*$  is inversely

proportional to  $J_T$ ,<sup>[65]</sup> larger transfer integrals increase charge carrier mobility. In contrast to the hopping regime, in the band model mobility decreases by increasing the temperature, due to the larger lattice vibrations which lead to higher number of scattering sites.

This model is considered appropriate to describe charge transport in high-quality single crystal OSCs with low density of charge traps ( $\mu \gg 10 \text{ cm}^2\text{V}^{-1}\text{s}^{-1}$ ).

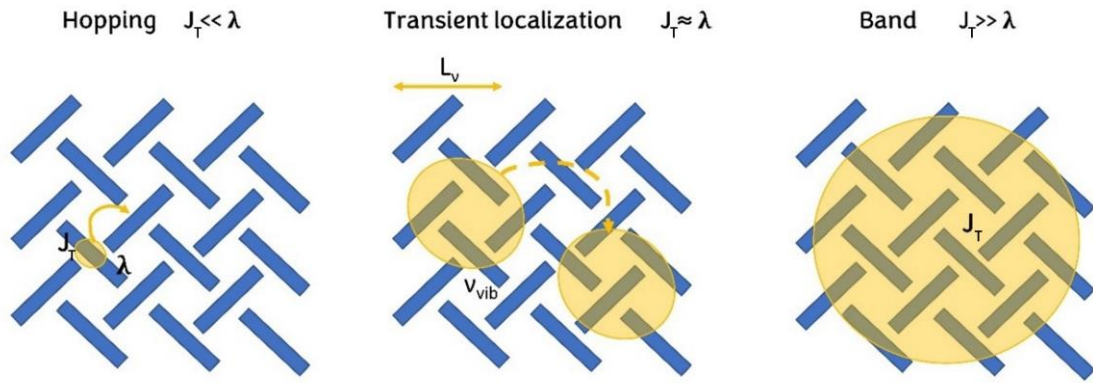
### 1.3.6 Transient localization model

Most of the state-of-art OSCs exhibit mobility in the range of  $1\text{-}10 \text{ cm}^2\text{V}^{-1}\text{s}^{-1}$ , with transfer integrals and reorganization energies on the same order of magnitude. In this regime neither hopping model nor band model are appropriate to describe charge transport mechanism. As already stated, the rather weak van der Waals forces which hold together OSC molecules in the crystal lattice, result in highly disordered energetic landscape through which charges are transported. This is caused by the large transfer integrals fluctuations arising from electron-phonon coupling, which limits charge carrier diffusion. The transient localization model describes charge transport as a combination of localized and extended characters of charges.<sup>[67]</sup> The model supposes that on timescale shorter than the timescale of intermolecular oscillations, charges are localized on molecular sites, while on longer timescale charge transport takes place through diffusion, governed by the molecular lattice fluctuations.<sup>[65]</sup> In this model, the charge carrier mobility depends on the temperature-dependent localization length ( $L_v$ ) and on the timescale of intermolecular vibrations ( $v_{\text{vib}}$ ):

$$\mu = \frac{q}{2K_bT} \frac{L_v^2}{v_{\text{vib}}} \quad (1.9)$$

The localization length defines the length over which charges are localized and transport occurs through diffusion of localized charges across the crystalline lattice driven by intermolecular vibrations (**Figure 1.4**).

Considering **equation 1.9**, the strategies to improve mobilities rely in the decreasing of intermolecular vibration frequency and the increasing of the localization length. The latter can be achieved by increasing the molecular orbitals overlap (i.e., larger transfer integrals) and minimizing the coupling with the intermolecular motions. At last, it has been shown that isotropic transfer integrals in the different crystal directions results in higher resilience of the OSC to dynamic disorder due to the reduced localization phenomena. <sup>[60,67]</sup>



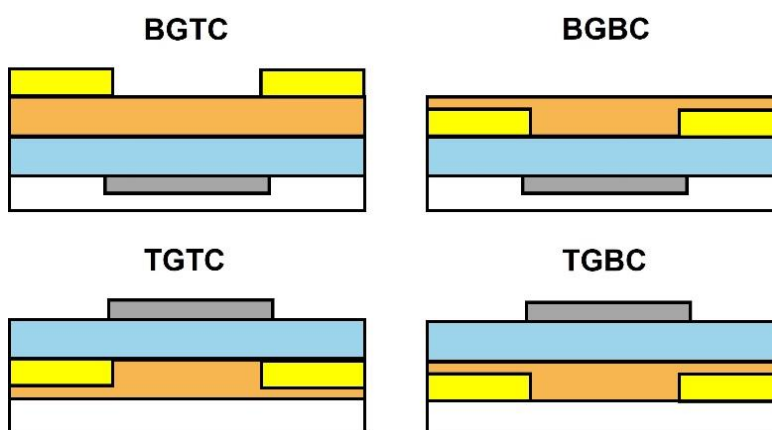
**Figure 1.4: Illustration of charge transport model mechanisms.**

The yellow areas exemplify the charge delocalization. The main parameters governing charge transport ( $J_T$ ,  $\lambda$ ,  $L_v$  and  $v_{vib}$ ) for each transport model are shown.

## 1.4 Organic field-effect transistors

Transistors are semiconductor-based devices largely used to amplify or switch an electrical signal. The word transistor comes from the words “transfer” and “resistor” since in this device the electrical current is transferred across a resistor, formed by two-terminal electrical components. Field-effect transistors (FET) are three-terminal components type of transistors which exploits an electric field to control the flow of current in the device. The first FET based on an organic semiconductor was developed in 1986 by Tsumura, showing a hole mobility of  $\approx 10^{-5} \text{ cm}^2\text{V}^{-1}\text{s}^{-1}$ .<sup>[1]</sup> Thereafter, the field of organic semiconductors for logic operations has experienced an enormous development, and nowadays the highest reproducible value of hole mobility reported is in the range of  $20 \text{ cm}^2\text{V}^{-1}\text{s}^{-1}$ .<sup>[26]</sup> This is the actual limit imposed by the dynamic disorder result of intermolecular interactions in organic semiconductor crystals, which entail significant thermal lattice fluctuations.

Albeit the organic material plays a dominant role on the final device performances; the dielectric layer, the contacts, the device geometry and the control of the materials properties at the interfaces are crucial to maximize the potential of this technology and obtain ideal and reliable devices. Since a thin-layer (ca. 20-30 nm) of OSC is generally deposited during the fabrication of OFET, these devices are also called thin-film transistors (TFTs). TFTs consist in the overlap of different layers, deposited via solution or vapor-processing, which can typically be assembled as depicted in **Figure 1.5**.



**Figure 1.5: Schematic illustration of the four different OFET structures.** Bottom-gate top-contact (BGTC), bottom-gate bottom-contact (BGBC), top-gate top-contact (TGTC) and top-gate bottom-contact (TGBC). The substrate is shown in white, the dielectric in light blue, the OSC in orange, the gate electrode in grey and the drain and source contacts in yellow.

In top gate devices (TG), the gate contact is placed on the top of the device structure, while for the bottom-gate (BG) counterpart, the gate contact is located on the bottom. Considering the position of the drain and source contacts, which can be deposited on the top (TC) or on the bottom (BC) of the organic thin-films, four structures are obtained by combining the gate, drain and source contacts positions: top-gate top-contact (TGTC), top-gate bottom-contact (TGBC), bottom-gate top contact (BGTC) and bottom-gate bottom-contacts (BGBC). BGTC and TGBC geometries are named staggered since the source and the drain contacts are on one side while the gate contact is on the opposite side of the OSC. In contrast, BGBC and TGTC geometries are named coplanar since the source, drain and gate contacts are placed on the same side of the OSC.

In this section the static operation of an organic TFT is exposed, considering a standard BGTC configuration and a hole (p-type) charge transport. However, the same considerations can be extended to devices with a different structure and to electron (n-type) charge transport, upon considering the change in polarity.

### 1.4.1 Operating principles

*In this section the charge transport in OFETs is explained according to the charge-sheet model, which treats the OSC/dielectric/gate electrode system as a parallel plate capacitor (i.e., all the mobile charge carriers are exclusively transported within the organic layer at the interface with the dielectric).*<sup>[68,69]</sup>

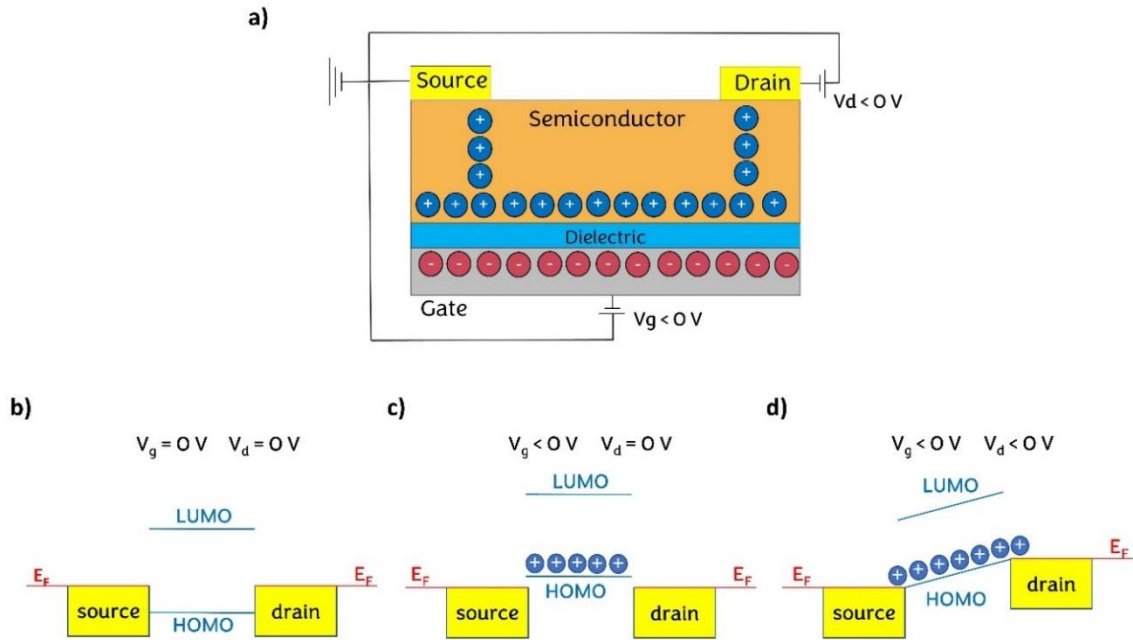
In OFETs, the OSC is coupled capacitively with a dielectric layer, as depicted in **Figure 1.6**. The application of a negative bias voltage between the source and the gate electrodes, namely the gate voltage ( $V_g$ ), results in the accumulation of holes at the OSC/dielectric interface, forming an accumulation channel. The gate voltage modulates the charge carrier density in the accumulation channel and hence its conductivity. By applying a bias voltage between the source and the drain contacts (drain voltage,  $V_d$ ), charges are injected into the OSCs and flow from the source to the drain electrodes across the accumulation channel. The measured current between the drain and the source contacts is defined as drain current ( $I_d$ ) and, according to the Drude model, can be expressed as follow:

$$I_d \propto \sigma_{ch} V_d = p q \mu V_d \quad (1.10)$$

where  $\sigma_{ch}$  is the channel conductivity and  $p$  is the charge carrier density in the channel.

For a better visualization of the role of the gate voltage modulation on the channel conductivity, we consider idealized and simplified energy level diagrams (**Figure 1.6**). No mobile charges are accumulated at the OSC/dielectric interfaces if no gate voltage is applied. Thus, the only mobile carriers in the channel are those that are thermally activated or induced by doping. In this case, upon the application of a drain voltage, the collected drain current is referred as off-state current.

When a negative  $V_g$  is applied, the HOMO (and LUMO) energy levels of the OSC bend upwards to match with the Fermi energy of the source contact, leading to the accumulation of holes at the OSC/dielectric interface. Upon the application of a negative  $V_d$ , holes are injected (electrons are ejected) from the source contact and travel across the accumulation channel to the drain contact.



**Figure 1.6: Idealized representation of operating principle and energy band diagram of a p-type OFET.**

(a) Schematic illustration of holes accumulation at the OSC/dielectric interface and transport when  $V_g < 0$  V and  $V_d < 0$  V. Idealized energy diagram for the case of (b)  $V_g = 0$  V and  $V_d = 0$  V, (c)  $V_g < 0$  V and  $V_d = 0$  V and (d)  $V_g < 0$  V and  $V_d < 0$  V.

It is important to underline that these energy level diagrams are useful to understand the operating mechanism of OFETs, but they are simplistic representations and do not account for several phenomena occurring at the

contact/OSC and dielectric/OSC interface, such as the presence of traps, charge transfers, interface dipole, band banding, Fermi level pinning, formation of a depleted region, etc. The charge carrier density at the OSC/dielectric interface is regulated by both the drain voltage and the gate voltage. Specifically, the charge carrier density per unit area ( $Q_{ind}$ ) at a given position  $x$  across the accumulation channel varies depending on the distance from the source contact edge and can be expressed as follow:

$$Q_{ind}(x) = C_i(V_g - V(x)) \quad (1.11)$$

where  $C_i$  is the dielectric capacitance per unit area, and  $V(x)$  is potential along the accumulation channel at a given position  $x$ . In real devices, generally mobile charge carriers are not induced into the OSC as soon as  $V_g < 0$ . The mismatch between the HOMO level of the OSC and the  $E_F$  of the electrodes leads to charge transfer between the two materials which in turns results in the formation of interfacial dipoles and band banding. Hence, the application of  $V_g \neq 0$  is necessary to achieve the flat-band condition ( $V_{FB}$ ).

Moreover, deep trap states arising from dynamic and static disorder must be filled, prior the formation of the accumulation channel. Thus, the gate voltage required to induce mobile charge carriers is defined as threshold voltage ( $V_{th}$ ) and **equation 1.11** transforms into:

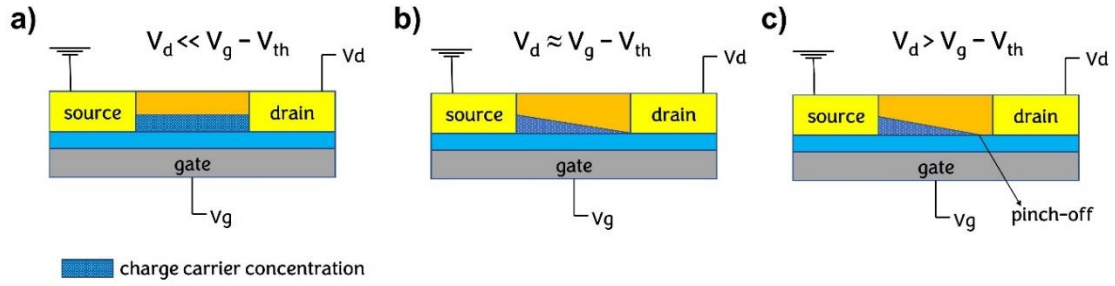
$$Q_{ind}(x) = C_i(V_g - V_{th} - V(x)) \quad (1.12)$$

Please note that the difference between  $V_g$  and  $V_{th}$  ( $V_g - V_{th}$ ) is referred as gate-overdrive voltage. For  $V_g > V_{th}$ , the current flowing from the source to the drain electrode is expressed as follow:

$$I_d = \frac{W}{L} \mu_0 \int_0^{V_d} Q_{ind}(x) dV(x) \quad (1.13)$$

where  $\mu_0$  is the intrinsic field-independent charge carrier mobility, while  $W$  and  $L$  are the channel width and the channel length respectively.

Assuming that  $V_{th}$  does not change with  $x$ , at a given  $V_g$  the charge carrier density across the accumulation channel is constant if  $V_d \ll V_g - V_{th}$  (linear regime). When  $V_d$  is nonzero and lower than  $V_g - V_{th}$ , the accumulation channel is characterized by a linear gradient of charge carrier concentration (**Figure 1.7**).

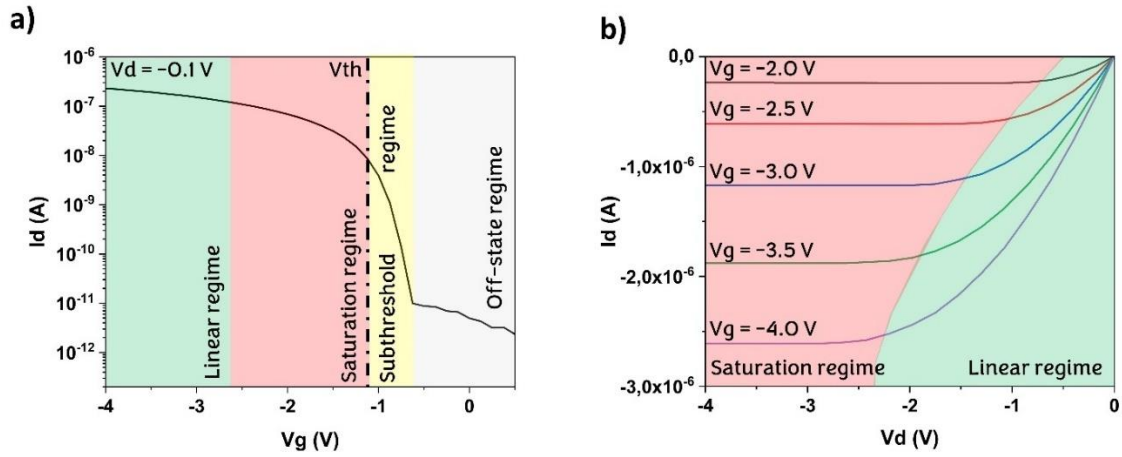


**Figure 1.7: Charge carrier concentration profile of OFETs.**

(a) linear regime, (b) starting point of saturation regime and (c) full saturation regime.

For  $V_d \approx V_g - V_{th}$  the accumulation channel becomes pinched, meaning that a region near to the drain contact completely depleted of mobile charges is formed (saturation regime). Increasing  $V_d$  to values larger than  $V_g - V_{th}$ , only leads to slightly move the pinch point backwards towards the source contact.

OFETs are typically characterized either by holding  $V_d$  constant and collecting  $I_d$  as a function of the varying  $V_g$ , namely transfer characteristics, or by holding  $V_g$  constant and collecting  $I_d$  as a function of the varying  $V_d$ , namely output characteristics (**Figure 1.8**).



**Figure 1.8: Transfer and output characteristics of a p-type OFET.**

(a) Transfer and (b) output characteristics. Depending on the values of  $V_g$  and  $V_d$ , the different regimes of operations are highlighted.

#### 1.4.1.1 Drain current in linear and saturation regimes

If the gradual channel approximation (GCA) is valid,\* the charge carrier concentration is uniform along the channel and the voltage drop across the channel is linear ( $V_d < V_g - V_{th}$ ), the integration of **equation 1.13** and its combination with **equation 1.12** leads to the following expression of drain current:

$$I_d = \frac{W}{L} \mu_0 C_i \left( V_g - V_{th} - \frac{V_d}{2} \right) V_d \quad (1.14)$$

This implies that in linear regime the drain current is linearly proportional to  $V_g$ .

The increasing of  $V_d$  to values approaching the gate overdrive voltage and beyond ( $V_d \geq V_g - V_{th}$ ) results in the saturation of the drain current since the gate voltage is no longer sufficient to meet the drain voltage demand. Substituting  $V_d = V_g - V_{th}$  into **equation 1.14**, yields to the equation describing the drain current in saturation regime:

$$I_d = \frac{W}{2L} \mu_0 C_i (V_g - V_{th})^2 \quad (1.15)$$

This implies that in saturation regime, the drain current is linearly proportional to the square of  $V_g$ .

#### 1.4.1.2 Subthreshold regime

Considering the transfer characteristic of an OEFT, the subthreshold regime occurs when  $V_{th} < V_g < V_{FB}$ . In this regime, the drain current increases exponentially with the increasing of the gate voltage. The subthreshold swing (SS) is defined as the inverse slope of the logarithmic  $I_d$  as a function of  $V_g$ :

$$SS = \left( \frac{\partial \log I_d}{\partial V_g} \right)^{-1} \quad (1.16)$$

The SS measures how fast the OEFT switch from the off-state to the on-state. This is directly connected to the density of trap states according to the following equation:

$$SS = \frac{KT \ln(10)}{q} \left( 1 + \frac{q^2 N_{it} + q \sqrt{\varepsilon N_{bulk}}}{C_i} \right) \quad (1.17)$$

---

\* The GCA assumes that the electric field perpendicular to the OSC/dielectric interface generated upon the application of  $V_g$  is much larger than the electric field parallel to the OSC/dielectric interface, generated upon the application of  $V_d$ .

where  $N_{it}$  is the interfacial trap density per unit area and unit energy at the OSC/dielectric interface,  $\varepsilon$  is the relative dielectric constant of the OSC and  $N_{bulk}$  is the bulk trap density per unit volume and unit energy. By neglecting the contribution of  $N_{bulk}$  (i.e., in the case of highly ordered OSC or in polycrystalline TFTs with a coplanar geometry), **equation 1.17** can be used to estimate the interfacial trap density at the OSC/dielectric interface in OFETs.

#### 1.4.1.3 Field-effect mobility

The derivatives of **equation 1.14** and **equation 1.15** refer to the transconductance ( $g_m$ ) in the linear and saturation regimes, respectively:

$$g_{m,lin} = \left. \frac{\partial I_d}{\partial V_g} \right|_{V_d} = \frac{W}{L} \mu_0 C_i V_d \quad (1.18)$$

$$g_{m,sat} = \left. \frac{\partial I_d}{\partial V_d} \right|_{V_g} = \frac{W}{L} \mu_0 C_i (V_g - V_{th}) \quad (1.19)$$

Thus, from the transfer characteristics, it is possible to extract the charge carrier mobility for the linear ( $\mu_{lin}$ ) and saturation ( $\mu_{sat}$ ) regimes:

$$\mu_{lin} = \frac{L}{W C_i V_d} \left. \frac{\partial I_d}{\partial V_g} \right|_{V_d} \quad (1.20)$$

$$\mu_{sat} = \frac{2L}{W C_i} \left( \left. \frac{\partial \sqrt{I_d}}{\partial V_g} \right|_{V_d} \right)^2 \quad (1.21)$$

It is worth noting that up to now the charge carrier mobility used for the description of the drain current in OFETs was assumed to be an intrinsic field-independent mobility of the OSC layer ( $\mu_0$ ). On the contrary, the extraction of the field-effect mobilities ( $\mu_{lin}$  and  $\mu_{sat}$ ) from transfer characteristics by using **equations 1.20** and **1.21**, introduces the dependence on the applied electric field and hence on the charge carrier concentration. The  $V_g$ -dependence of charge carrier mobility extracted from OFETs is complex and difficult to predict. Many factors play a role in determining the gate voltage dependence of mobility, such as the charge transport mechanism, the presence of defect and trap states, the dielectric surface roughness and the contact resistance.<sup>[70]</sup>

Most important, unreliable mobility values (and specifically overestimated values) are a major problem in the development of the organic transistors field. The overestimation of mobility extracted from OFETs arises mostly due to gated contacts, i.e., when contact resistance is larger than the channel

resistance, with the former exhibiting a strong dependence on the applied gate voltage.<sup>[55,70]</sup> It has been reported that charge carrier mobility extracted from OFETs can be overestimated by an order of magnitude when the contact resistance is strongly modulated by  $V_g$  and charge carrier injection controls the OFET characteristics.<sup>[31]</sup>

Therefore, the extraction of charge carrier mobility from OFETs characteristics should be performed on ideal devices (devices showing textbook like characteristics and ohmic contacts), to avoid over or underestimation. The respect of the following conditions, should result in the extraction of reliable mobilities: 1) the output and transfer characteristic should not exhibit sign of severe hysteresis and trapping, 2) the contribution of the contact resistance to the total device resistance should be negligible compared to the channel resistance contribution, 3) threshold voltage should be as near to 0 V as possible, to confirm the low concentration of traps, 4) the extracted mobility should not show a strong dependence on  $V_g$  and should be constant over the whole range of applied gate bias, 5) the extracted mobilities in linear and saturation regime should be equivalent.<sup>[52]</sup>

#### 1.4.1.4 On/off current ratio and hysteresis

Other important parameters to account in OFETs are the on/off current ratio and the hysteresis. The on/off current ratio is defined as the ratio between the drain current in the on-state (maximum  $V_g$ ) at the drain current in the off-state ( $V_g = 0$  V). The maximization of the on/off current ratio is critical for digital logic operation since it controls the difference between the logic levels. The hysteresis arises from the difference in drain current between the forward and backward sweep. Hysteresis should be minimized in OFETs for logic circuits since severe hysteresis affects the reproducibility and reliability of OFET characteristics.

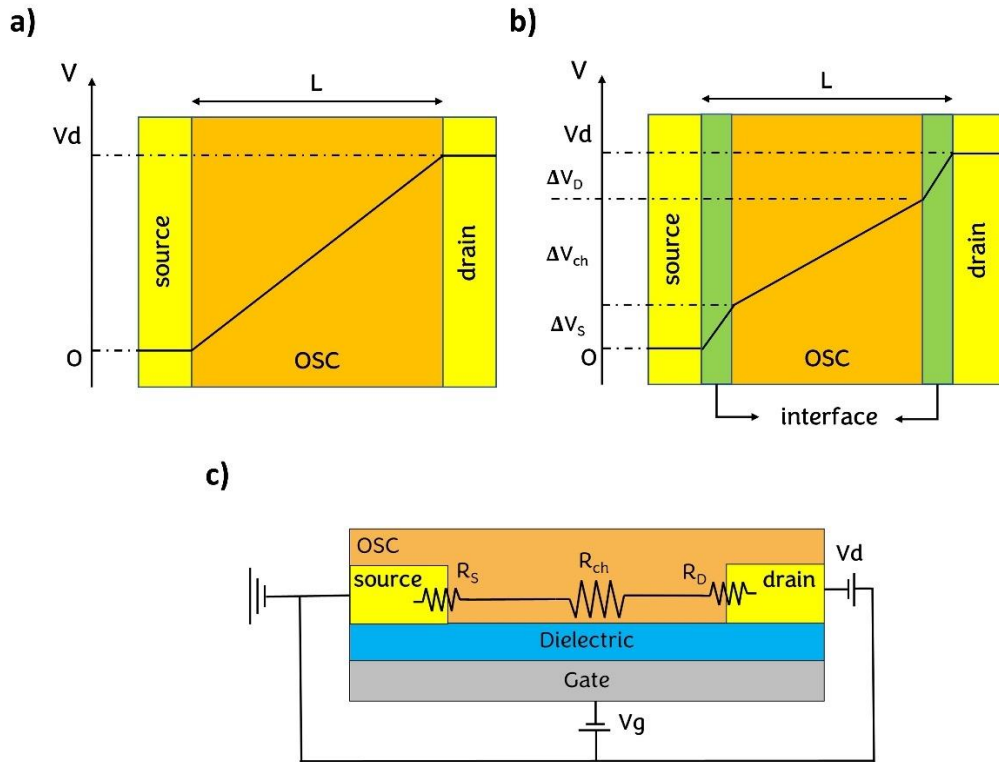
### 1.4.2 Contact resistance

Contact resistance ( $R_C$ ) originates from the voltage required to transfer the charges across the source contact/OSC interface and across the OSC/drain contact interface. Thus, the applied drain voltage can be expressed as:

$$\begin{aligned} V_d &= \Delta V_s + \Delta V_{ch} + \Delta V_d = I_d (R_S + R_{ch} + R_D) \\ &= I_d (R_C + R_{ch}) \end{aligned} \quad (1.22)$$

where  $\Delta V_s$ ,  $\Delta V_D$  and  $\Delta V_{ch}$  represent the voltage drop at the source contact, at the drain contact and across the OSC channel respectively, while  $R_S$ ,  $R_D$  and

$R_{ch}$  are the resistances associated to the source contact/interface, to the drain contact/OSC interface and to the OSC channel, respectively (**Figure 1.9**). In **equation 1.22** and hereinafter, the contacts are considered Ohmic, i.e., the voltage drop at the contacts is negligible compared to the voltage drop associated to the channel. This is not always the case, depending on the OSC material, the electrodes material and device geometry. For instance, a small  $R_{ch}$  obtained either by increasing the OSC mobility or by scaling down the channel length, may lead to devices dominated by the contact resistance.<sup>[71]</sup> In this case, the GCA is not valid anymore and the use of **equations 1.13** and **1.14** may lead to mischaracterization of device properties, including over or underestimation of charge carrier mobility.<sup>[72]</sup>



**Figure 1.9: Contact resistance in OFET.**

(a) Voltage drop profile of an ideal OEFT (with  $R_c = 0$ ), (b) voltage drop profile of a real OFET with voltage drops at the source and drain contacts ( $R_c \neq 0$ ) and (c) schematic illustration of the resistance associated to the source contact ( $R_s$ ), to the channel ( $R_{ch}$ ) and to the drain contact ( $R_D$ ).

The contact resistance is affected by several factors, such as the OSC material, the electrodes material, the OSC/contact interface, and device related parameters. Depending on the interfaces and on the device being

investigated, the parameters influencing the contact resistance may be interdependent, making complex the disentangling of the different contributions to the final device performance.

#### 1.4.2.1 Influence of the device geometry

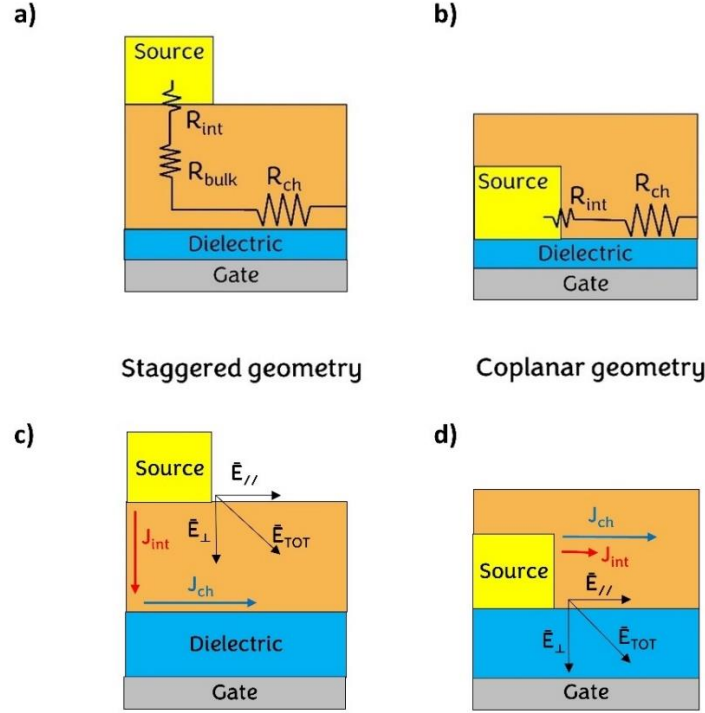
The adopted OFET geometry affects contact resistance depending on the position of the drain and source contact with respect to the accumulation channel. In staggered devices charges injected from the source contact must travel perpendicular to the OSC/dielectric interface to achieve the accumulation channel. Similarly, after being transported across the channel, charges must travel perpendicular to the OSC/dielectric interface to reach the drain contact. Consequently, the contact resistance is given by two components: the resistance associated to the charge injection across the contact/OSC interface ( $R_{\text{int}}$ ) and the one associated to the charge transport through the thickness of the OSC ( $R_{\text{bulk}}$ ).<sup>[72]</sup> This introduces a  $R_C$  dependence on the OSC thickness, i.e., thicker OSC layer results in larger  $R_{\text{bulk}}$ .<sup>[73–75]</sup> In contrast, in coplanar geometry charges are injected from the source contact into the OSC channel straightaway, removing the contribution of  $R_{\text{bulk}}$  (**Figure 1.10**).

Staggered devices typically exhibit larger injection area compared to the coplanar counterpart. This has been generally ascribed as the main reason of smaller contact resistance compared to the coplanar counterparts, for devices consisting of the same material and OSC thickness.<sup>[76–79]</sup>

In coplanar devices the injection area is limited by the height of the contact edge. In contrast, in staggered devices the larger injection area is provided by the extended overlap between the contacts and the channel region of gate-induced charge carriers underneath the contacts. In this case the charge carrier injection is regulated by the *current crowding* formalism.<sup>[80,81]</sup> This considers the area underneath the contacts as a network of resistors. The charge injection area in staggered devices is not simply given by the geometric overlap of the contact with the gate ( $L_{\text{ov}}$ ), whereas it is determined by the balance of contact resistance, which includes the contribution of  $R_{\text{int}}$  and  $R_{\text{bulk}}$ , and sheet resistance of the OSC in the channel region ( $R_{\text{sh}}$ )<sup>†</sup>. In fact, in staggered devices the channel region of gate-induced charge carriers extends under the source and drain contacts (**Figure 1.11**).

---

<sup>†</sup> Note that  $R_{\text{ch}} = R_{\text{sh}} \frac{W}{L}$



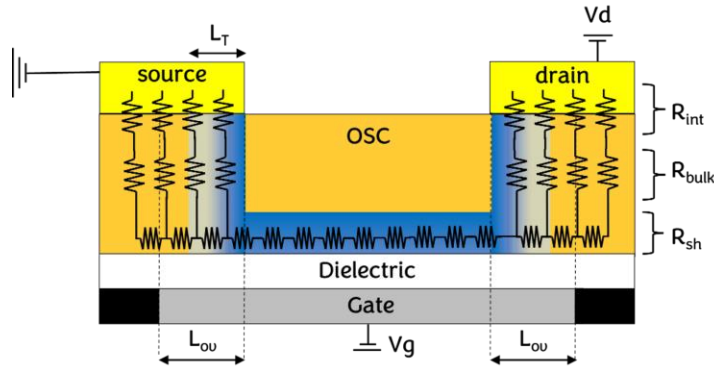
**Figure 1.10: Contact resistance in OFETs with staggered and coplanar geometries.**

(a) In device with staggered geometry  $R_C$  is given by the contribution of  $R_{int}$  and  $R_{bulk}$ , while (b) in device with coplanar geometry  $R_{bulk}$  contribution is neglected. (c)(d) Directions of electric fields components ( $\vec{E}_\perp, \vec{E}_\parallel$ ), charge injection current ( $J_{int}$ ) and channel current ( $J_{ch}$ ) in staggered and coplanar FETs. The schematic illustrations refer only to the source side of the OFETs.

Thus, charges injected at the far edge of the source contact must firstly pass through the OSC thickness to reach the channel region of gate-induced charge carriers under the contacts and afterward must travel parallel to the OSC/dielectric interface to reach the active channel (here referred as the accumulation channel between the source and drain contacts, neglecting the regions underneath the contacts).

The characteristic length over which the 63% of charges are injected across the contact/OSC interface is defined as transfer length ( $L_T$ ) and it is determined by the balance of  $R_{sh}$ ,  $R_{bulk}$  and  $R_{int}$ .

Thus, when the contribution of contact resistance to the total device resistance is negligible compared to the contribution of channel resistance (Ohmic contacts), charge injection/ejection occurs over a narrow area close to the edge of the source/drain contacts. Best performing OSCs have shown  $L_T$  in the range of 1.5 and 15  $\mu m$ .<sup>[82–85]</sup>



**Figure 1.11: Current crowding in staggered OFET.**

Schematic illustration of charge injection in a staggered OFET, according to the current crowding effect. Charge injection occurs over a narrow area close to the edge of the contacts, defined by the transfer length  $L_T$ . The blue region indicates the current density.

At last, the dielectric thickness is another geometric parameter which influences contact resistance. In field-effect transistors the application of the drain voltage and of the gate voltage results in two electric field components, that are perpendicular ( $\vec{E}_\perp$ ) and parallel ( $\vec{E}_\parallel$ ) to the OSC/dielectric interface, respectively. The sum of these two components gives the total effective applied electric field at the contact ( $\vec{E}_{TOT}$ ). The perpendicular component primarily contributes to charge carrier injection in staggered devices, while in coplanar devices  $\vec{E}_\perp$  has no impact on charge carrier injection, in first approximation. Conversely, the parallel component plays a key role in charge carrier injection in coplanar devices where the injected current ( $J_{int}$ ) flows in the same direction of the channel current ( $J_{ch}$ ), parallel to the OSC/dielectric interface (**Figure 1.10**). Thus, the contribution of  $\vec{E}_\parallel$  on charge carrier injection in coplanar devices would depend on the dielectric thickness. This has been firstly confirmed by drift diffusion simulations, which have shown that a reduced dielectric thickness facilitates charge injection in a BGBC organic thin-film transistors.<sup>[86,87]</sup> In fact, the larger  $\vec{E}_\parallel$  component due to the thinner dielectric layer, gave rise to higher charge carrier concentration in the accumulation channel and smaller potential drop at the source contact. These theoretical findings have been corroborated by the fabrication of TFTs with different dielectric thickness. The TFTs analysis showed that contact resistance in coplanar devices based on **diPh-DNTT** is lower than the one of the staggered counterpart if the dielectric layer is thinner than 30 nm and if the OSC morphology is similar across the contact-to-channel interface.<sup>[85]</sup>

#### 1.4.2.2 Measuring contact resistance: the gated transmission line method

The gated transmission line method (TLM), referred also as gated transfer line method, is one of the most employed methods to extract contact resistance from current-voltage characteristics of OFETs with varying channel length. This method was first developed for FETs based on inorganic semiconductors and further applied to OEFTs.<sup>[88]</sup> The major assumptions of TLM are: 1) the GCA is valid, 2) the voltage drop at the contacts is negligible compared to the voltage drop across the channel, 3) the charge carrier concentration is homogeneous along the channel and 4) channel resistance scales linearly with the channel length, while the contact resistance is not affected by the channel length variation.<sup>[72,89]</sup>

The total resistance ( $R$ ) of a FET is given by the sum of the contact resistance ( $R_C$ ) and the channel resistance ( $R_{ch}$ ), where  $R_C$  accounts for the contribution of both the source ( $R_S$ ) and drain ( $R_D$ ) contacts:

$$R = R_D + R_S + R_{ch} = R_C + R_{ch} \quad (1.23)$$

The channel resistance varies linearly with the channel length ( $L$ ) and can be expressed as follow:

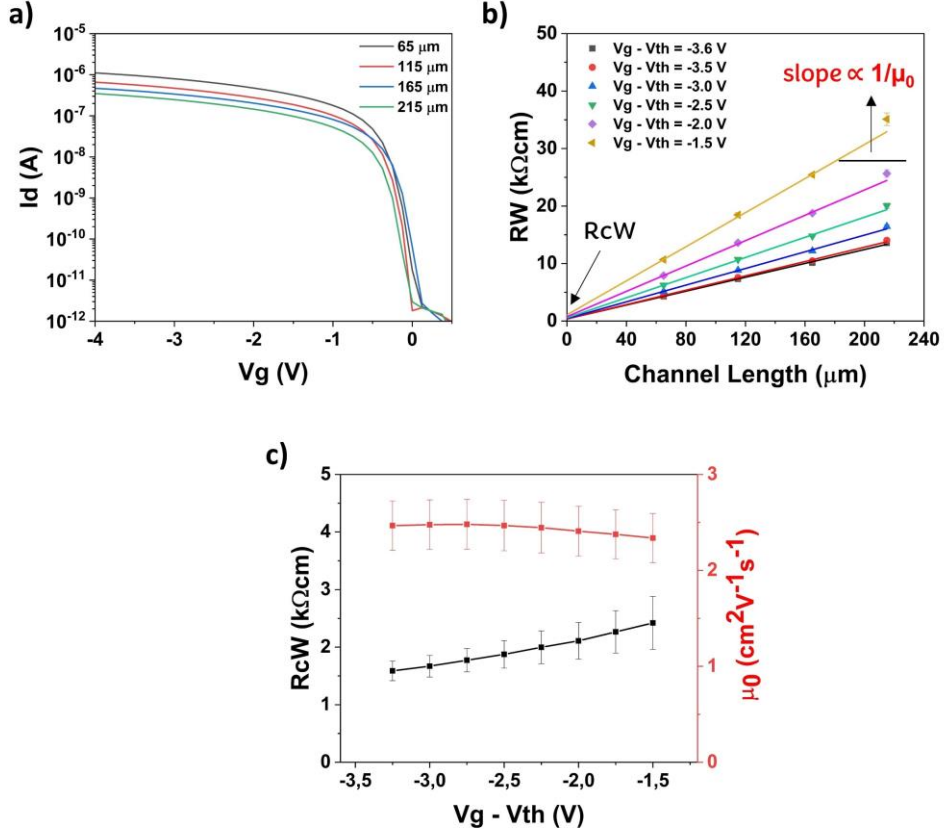
$$R_{ch} = R_{sh} \frac{W}{L} = \frac{L}{W\mu_0 C_i(V_g - V_{th})} \quad (1.24)$$

By combining **equations 1.23** and **1.24**, and normalizing by the channel width ( $W$ ), the width-normalized contact resistance ( $R_C W$ ) is obtained:

$$RW = R_C W + \frac{L}{W\mu_0 C_i(V_g - V_{th})} \quad (1.25)$$

Thus, by measuring the transfer characteristics in the linear regime of field-effect transistors with varying channel length, the with-normalized contact resistance ( $R_C W$ ) and the intrinsic channel mobility ( $\mu_0$ ) are obtained from the linear fit to the  $RW$  vs  $L$  data points. Specifically, the intercept of the linear fit with the Y-axis ( $L = 0$ ) gives  $R_C W$ , while  $\mu_0$  is obtained from the slope at each defined gate-overdrive voltage (**Figure 1.12**).

It is worth noting that by using the TLM it is not possible to separate the source and drain contributions since they are both encompasses in  $R_C W$ . Other methods can be used to access the contribution of  $R_S$  and  $R_D$  to the contact resistance, such as Kelvin probe force microscopy,<sup>[90]</sup> gated four probe method<sup>[91]</sup> and gated van der Pauw method.<sup>[92]</sup> The major drawbacks of these methods relies in the requirement of special measurement equipment, the long measurement and analysis time, and the special structure of the analysed devices.



**Figure 1.12: Contact resistance extraction by using the transmission line method.**

(a) Transfer characteristics of TFTs with varying channel length, (b) linear fits to the total resistance vs channel length data points at varying gate-overdrive voltage, (c) width-normalize contact resistance and intrinsic mobility extracted from (b) as a function of the gate-overdrive voltage.

### 1.4.3 The organic semiconductor-contact interface

The contact resistance associated to charge injection across the OSC/contact interface ( $R_{int}$ ) is mainly related to the potential energy barrier that forms at the interface also known as charge injection barrier. In the easiest approximation (Schottky-Mott limit), the charge injection barrier, namely Schottky barrier ( $\Phi_B$ ), is given by the energy difference between the work function of the contact ( $WF_c$ ) and the ionization energy of the OSC for hole injection in p-type OSC ( $\Phi_{B,p}$ ) and by the difference between the work function of the contact and the electron affinity of the OSC for electron injection in n-type OSC ( $\Phi_{B,n}$ ):<sup>[93]</sup>

$$\Phi_{B,p} = WF_c - IE \quad (1.26)$$

$$\Phi_{B,n} = WF_c - EA \quad (1.27)$$

In this model, the WF of the contact and the IE (or EA) of the OSC are those of isolated materials.

However, the Schottky-Mott rule can only provide an estimate of the charge injection barrier at the interface. In reality, charge injection barriers are influenced by a number of factors, such as electrochemical processes, interface morphology, electrostatic interactions and interfacial trap states. From thermodynamic considerations when two different materials are brought into contact the resultant system must reach thermodynamic equilibrium. This is typically achieved by charge carrier transfer across the interface until their electrochemical potentials (Fermi levels) establish a common Fermi level (Fermi level pinning).<sup>[94]</sup> The charge redistribution creates an electric field across the interface, commonly referred as the interface dipole ( $\Delta$ ). The presence of the electric field can basically shift the vacuum level and bend the electronic energy levels. In such a case the charge injection barriers will be given by **equations 1.28** and **1.29**.

$$\Phi_{B,p} = \text{WF}_c - \Delta - IE \quad (1.28)$$

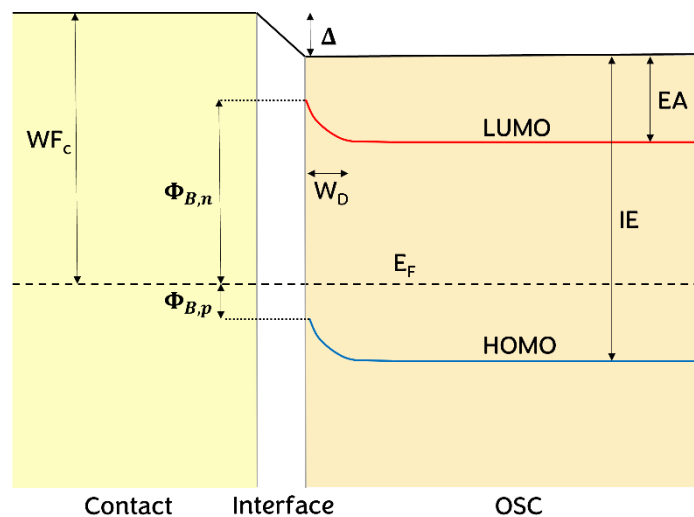
$$\Phi_{B,n} = \text{WF}_c - \Delta - EA \quad (1.29)$$

The origin of the interface dipole is attributed to different factors, such as charge transfer across the OSC/contact interface (resulting in anions or cations formation), potential chemical reactions at the interface, changes of OSC molecular orientation at the interface, intrinsic dipole moment of the OSC molecules and push-back effect.<sup>[43]</sup> The latter arises from the electron density of the OSC molecules in proximity to the interface which suppresses the electron cloud extending away from the contact surface.<sup>[95]</sup>

In the region close to the interface, due to the electric field between the OSC and the contact caused by charge transfer, the transport bands edges of the OSC are shifted, namely band bending (**Figure 1.13**). This leads to the formation of a region depleted of charge carriers at the interface, which extends towards the OSC bulk. The width of this depleted region ( $W_D$ ) depends on the interfacial trap density, which in turns is influenced by the OSC morphology across the interface.<sup>[96]</sup> All these complex phenomena occurring at the OSC/contact interface contributes to determining the mechanism of charge carrier injection in a device and ultimately affect contact resistance.<sup>[72]</sup>

In this context, ultraviolet photoelectron spectroscopy (UPS) is a powerful experimental technique used to study the electronic structure of solid surfaces, thin films, and interfaces. By irradiating the sample with ultraviolet photons, UPS can measure the energies of photoemitted electrons and provide

information about the electronic levels of the material. In the case of organic semiconductors, UPS is particularly useful for determining the energy of the HOMO, the injection barrier, work function, and interfacial dipole at organic semiconductor interfaces.



**Figure 1.13: Organic semiconductor-contact interface.**

Schematic energy levels diagram of the OSC/contact interface which accounts for the formation of an interfacial dipole ( $\Delta$ ), band bending and a region depleted of carriers in proximity of the interface ( $W_D$ ).

## 1.5 Coupling with the vacuum field

In the last decade, strong coupling between light and matter has been explored to modify the physical and chemical properties of molecular systems. Strong light matter interaction between a molecular transition and a resonant optical mode can lead to the formation of new hybridized light-matter states, called as polaritonic states. Such coupling is possible when the exchange of energy is faster than any relaxation process. This interaction has been successfully employed to alter molecular properties. The first part of this section is focused on the theoretical model that have been developed in the framework of light-matter strong coupling, while in the second part a brief overview of the effect of light-matter strong coupling on the chemical and physical properties of materials is presented.

### 1.5.1 Theoretical description

In order to have a better understanding of the basic light-matter interaction, it is advisable to start with the classical analogy of two coupled harmonic oscillators. When two harmonic oscillators are not coupled, they act as independent systems, preserving their parameters, i.e., the oscillation frequency. But, when the oscillators are coupled and their interaction is strong enough (the energy exchange is faster than any dissipation processes), they start to act as a singular system. Considering two independent oscillators with masses  $M_1$  and  $M_2$  and spring constants  $k_1$  and  $k_2$ , the system can be described through the Newton's second law (introducing  $k_3$  as the spring constant when the oscillators are coupled, see **Figure 1.14**):<sup>[97]</sup>

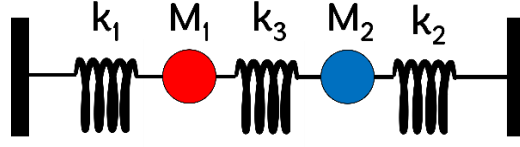
$$M_1 \frac{d^2 x_1}{dx} + k_1 x_1 + k_3 (x_1 - x_2) = 0 \quad (1.30)$$

$$M_2 \frac{d^2 x_2}{dx} + k_2 x_2 + k_3 (x_1 - x_2) = 0 \quad (1.31)$$

Solving the differential equations, we obtain:

$$\omega_{\pm} = \frac{1}{2} (\omega_1 + \omega_2 + \sqrt{4\Omega^2 + (\omega_1 - \omega_2)^2}) \quad (1.32)$$

where  $\omega_1$  and  $\omega_2$  are the frequencies of the two oscillators,  $\Omega$  is the frequency of splitting and  $\omega_{\pm}$  are the two new frequencies obtained due to the coupling. It is worth noting that in this description no damping or dissipation effects are accounted, which should be introduced with a frictional term. The system is defined as strongly coupled when the dissipation is smaller than the coupling strength.



**Figure 1.14: Schematic illustration of two coupled harmonic oscillators.**

The description of the coupled system using a classical theory, does not sufficiently explain the strong coupling phenomenon obtained by the interaction of molecular transitions with vacuum field fluctuations. Vacuum field fluctuations can be described as the ground state energy of the quantized electromagnetic field (EM). This was firstly described by Plank and Einstein in 1911 and 1913, respectively, using a quantum description.<sup>[97]</sup> Dirac established the fundamental principles of quantum electrodynamics (QED)<sup>[98]</sup> and elucidated the mechanism behind the interaction between an excited emitter and the vacuum fields, which facilitates energy transfer via spontaneous photon emission.<sup>[99]</sup> In the free space, the electromagnetic field has a continuous spectrum of modes that tend to interact weakly with the emitter. To augment this interaction, a cavity can be utilized to confine the emitter. For example, a cavity constructed using two parallel metallic mirrors can be employed for this purpose. In such a constrained arrangement, the EM field manifests a discrete spectrum of modes.<sup>[100]</sup>

The strong coupling regime in light-matter interaction can be described using QED. In the easiest approximation we consider an atom formed by a two-level system interacting with a single mode of quantized electromagnetic field, by using the Jaynes-Cummings model.<sup>[101]</sup> Other models have been developed, such as the Tavis-Cummings model which describes the interaction of a single mode of the electromagnetic field with  $N$  identical atoms.<sup>[102]</sup> In the following, by using the Jaynes-Cummings formalism, a simple model of light-matter coupling is presented. The complete description of model can be found in ref. <sup>[101,103]</sup>.

The Jaynes-Cummings Hamiltonian accounts for the atom ( $\widehat{H}_a$ ), the electromagnetic field mode ( $\widehat{H}_f$ ) and the atom-field interaction ( $\widehat{H}_i$ ):

$$\widehat{H}_{JC} = \widehat{H}_a + \widehat{H}_f + \widehat{H}_i \quad (1.33)$$

The atomic Hamiltonian is described as a two-dimensional state space with two energy eigenstates and eigenvalues, i.e., the ground state  $|g\rangle$  and the

excited state  $|e\rangle$ . Defining  $\hat{\sigma}$  and  $\hat{\sigma}^\dagger$  as the operators that describe the transition from the ground to the excited state and vice versa, and  $\hat{\sigma}_z$  as the Hermitian Pauli operator that describes the energies of the states,  $\widehat{H}_a$  can be expressed as follow:

$$\widehat{H}_a = \frac{1}{2} \hbar \omega_0 \hat{\sigma}_z \quad (1.34)$$

where  $\omega_0$  is the transition frequency of the atom.

Likewise, defining  $\hat{a}$  and  $\hat{a}^\dagger$  as the creation and annihilation operators of the electromagnetic field mode and  $\omega$  as the frequency of the field mode,  $\widehat{H}_f$  can be expressed as follow:

$$\widehat{H}_f = \hbar \omega (\hat{a}^\dagger \hat{a}) \quad (1.35)$$

At last, the atomic-field interaction Hamiltonian describes the interaction between the transition dipole moment ( $\hat{d}$ ) of the atom and the electric field ( $\hat{\varepsilon}$ ) operators, i.e.:  $\widehat{H}_i = -\hat{d} \cdot \hat{\varepsilon}$ . Within the rotating wave approximation (RWA),<sup>3</sup> the atomic-field interaction Hamiltonian is expressed as:

$$\widehat{H}_i = -i \hbar g (\hat{a}^\dagger \hat{\sigma} + \hat{\sigma}^\dagger \hat{a}) \quad (1.36)$$

where  $g$  accounts for the magnitude of light-matter coupling strength. Thus, the final expression of the Jaynes-Cummings Hamiltonian is given by:

$$\widehat{H}_{JC} = \frac{1}{2} \hbar \omega_0 \hat{\sigma}_z + \hbar \omega (\hat{a}^\dagger \hat{a}) - i \hbar g (\hat{a}^\dagger \hat{\sigma} + \hat{\sigma}^\dagger \hat{a}) \quad (1.37)$$

The diagonalization of the Jaynes-Cummings Hamiltonian yields to the description of these new two eigenstates, as a linear combination of light and matter states, namely polaritonic states or polaritons ( $P^+$  and  $P^-$ ):

$$\begin{aligned} |P^+\rangle &= \cos \theta |e, 0\rangle + i \sin \theta |g, 1\rangle \\ |P^-\rangle &= \sin \theta |e, 0\rangle - i \cos \theta |g, 1\rangle \end{aligned} \quad (1.38)$$

where  $\theta$  is defined as:

$$\tan 2\theta = - \frac{2g}{\omega - \omega_0} \quad (1.39)$$

When the transition frequency of the atom is resonant with the electromagnetic mode, the polaritons are hybrid state with half-matter and

---

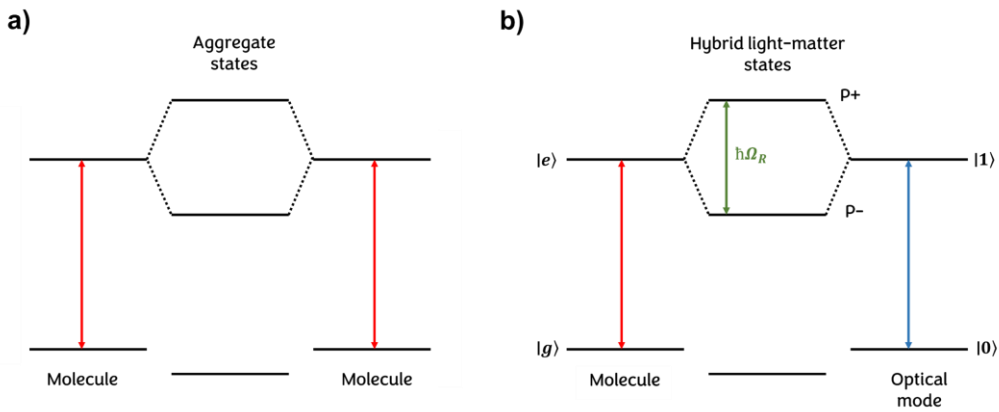
<sup>3</sup> The product between  $\hat{d}$  and  $\hat{\varepsilon}$  gives four terms. Two terms are related to the normal absorption (emission) of photon associated to a transition to the upper (lower) state, and two terms are related to anti-resonant processes. The latter terms are neglected within the RWA.

half-light character. The energy gap between  $P^+$  and  $P^-$  is called Rabi-splitting ( $\hbar\Omega_R$ ) and in absence of dissipation is described as:

$$\hbar\Omega_R = 2 \hbar g = 2 d \sqrt{\frac{\hbar\omega}{2\varepsilon_0 v_e}} \sqrt{n_{ph} + 1} \quad (1.40)$$

where  $d$  is the transition dipole,  $\hbar\omega$  is the resonant energy,  $\varepsilon_0$  the vacuum permittivity,  $v_e$  is the volume of the electromagnetic mode and  $n_{ph}$  the number of photons involved in the coupling. As can be seen in **equation 1.40**, in the absence of photons, there is still a residual coupling to the vacuum electromagnetic field, the quantum EM fluctuations of the optical resonator. In other words, strong coupling occurs even in the dark.

The light-matter strong coupling can be compared to a molecular analogy., i.e., the formation of J- and H-aggregates shown by  $\pi$ -conjugated organic molecules.<sup>[104]</sup> In higher concentrated dye solutions, the self-association of molecules is frequently encountered due to strong intermolecular attractive forces between molecules. According to exciton theory, the molecule is described as a dipole which can interact with another molecule/dipole, leading to the formation of two new eigenstates. The molecules may aggregate in a parallel way (plane-to-plane stacking) to form a sandwich type arrangement (H-aggregates) or in a head-to-tail arrangement to form J-aggregates. In the first case (H-aggregates) the transition dipole moments are (anti-)parallel, while in the second case (J-aggregates) the transition dipole moments are perpendicular. Therefore, due to the coupling between molecular transition dipole moments, two new states are obtained (**Figure 1.15**).



**Figure 1.15: Schematic energy diagrams of light-matter interaction.**

Schematic illustration of (a) the electronic coupling between transition dipole moments resulting in the formation of J- and H-aggregates and (b) the analogy with the interaction between a molecular transition and an optical mode resulting in the formation of two new hybrid light-matter states ( $P^+$  and  $P^-$ ).

In order to complete the analogy, we can imagine light-matter coupling as the previously described interaction, replacing a molecule transition dipole with a mode of the electromagnetic field.

### **1.5.2 Molecular and material properties under light-matter strong coupling**

From experimental point of view, light-matter strong coupling is typically achieved by confining the investigated compound in an optical or plasmonic cavity. The role of the cavity is to enhance the interaction between its optical modes (in case of an Fabry-Perot cavity) or its surface plasmon polaritons (in case of a plasmonic structures) and the transition dipoles of the molecules, though a confinement of the electromagnetic field.

The material properties can be altered by coupling either electronic transition, namely electronic strong coupling (ESC) and vibrational modes, namely vibrational strong coupling (VSC). Most important, chemical and physical properties of molecules can be modified by vibrational strong coupling and cooperative vibrational strong coupling.<sup>[105]</sup> The latter is required when the investigated compound is dissolved in a solvent and the direct coupling between the optical mode of the cavity and the molecular vibration is not possible (due to the low concentration of the solute). Thus, cooperative VSC consists in coupling the optical mode with a vibrational mode of the solvent that is resonant with a vibrational mode of the solute. The effect of ESC, VSC and cooperative VSC on material properties has started to be extensively investigated in last decade.

Hutchison et al. made the first observation of the impact of strong coupling in chemistry,<sup>[106]</sup> showing how ESC could change the energy landscape of reactants in case of spiropyran-merocyanine photoisomerization. Thereafter, the modification of work function,<sup>[107]</sup> the enhancement of energy transfer<sup>[108–111]</sup> and the boost of conductivity in OSC have been reported.<sup>[112,113]</sup>

VSC and cooperative VSC have shown to greatly modify the chemical reactivity and the outcome of various reactions, such as cyclization,<sup>[114]</sup> charge transfer,<sup>[115]</sup> solvolysis<sup>[105]</sup> and enzymatic<sup>[116,117]</sup> reactions. Recently, cooperative VSC has been revealed as an effective tool to influence the supramolecular assembly and ordering of materials. Specifically, the selective crystallization of a pseudo-polymorphic form of zeolitic imidazolate frameworks<sup>[118]</sup> and the modification of the morphology of supramolecular assemblies<sup>[119,120]</sup> have been reported. This opens to new possibilities in the field of crystallography and supramolecular chemistry, where the molecular ordering can be modified via matter-light interaction. Specifically, crystal

packing and polymorphism strongly affected charge carrier mobility in OSCs. The development of methods to induce selective crystallization, preventing the concomitant growth of polymorphic forms, may offer new opportunities to maximize charge carrier mobility in OSCs.

Very recently, a 6 order of magnitude boost in the conductivity of polystyrene was reported when a subset of vibrations of the polystyrene were coupled to a Fabry-Perot cavity.<sup>[121]</sup> This surprising result shows the promise of VSC for OSCs.

At last, it is worth noting that there are still many aspects of strong coupling that are unclear. Yet, in order to properly comprehend the mechanism in coupled systems and be able to forecast the result of strong coupling on a specific molecular property, more comprehensive theoretical explanations are required.



# Chapter 2

## Charge transport and charge injection properties of new thienoacene derivatives in thin-film transistors

### 2.1 Introduction

Due to their excellent hole mobility exceeding  $10\text{ cm}^2\text{V}^{-1}\text{s}^{-1}$ ,<sup>[27,52]</sup> chemical stability and reproducibility, thienoacenes have been extensively studied and serve as benchmarks in small-molecule organic TFTs device physics. **BTBT** was firstly reported by Takimya et al.,<sup>[28]</sup> who recognized its potential application in electronic devices due to an effective contribution of sulphur atoms to the intermolecular HOMO overlap which favours charge transport within adjacent molecules. **BTBT** has two main disadvantages: high ionization energy (IE) and poor film formation. Typically, IE of **BTBT** is ca. 5.8 eV, which severely limits charge carrier injection from electrodes into this OSC. The often-reported poor homogeneity of vacuum deposited thin-films prevents the preparation of functioning **BTBT** thin-film transistors.

The extension of the  $\pi$ -conjugated molecular core and the molecular shape have been demonstrated to affect electronic properties of OSCs. In the first place, the  $\pi$ -extension results in better delocalization of molecular orbitals, which in turns is reflected in reduced structural difference between the neutral and charged state (smaller reorganization energy).<sup>[122–124]</sup> Thanks to the  $\pi$ -extension, also the overlap of molecular orbitals within adjacent molecules can be enlarged, wherein the intermolecular distance and crystalline packing is preserved. This is expected to boost charge carrier mobility. The design of structurally modified **BTBT** derivatives has led to OSCs with high mobility and facile charge injection. Particularly, **DNTT**,<sup>[34,125–127]</sup> and **DBTTT**<sup>[128]</sup> have been synthesized by annealing thienyl and benzyl rings to the **BTBT** core, achieving mobilities  $> 3\text{ cm}^2\text{V}^{-1}\text{s}^{-1}$  along with low contact resistance.

In contrast **L-DBTTA**, despite the extended  $\pi$ -core consisting of a central motive comprising two annealed thienyl groups between two naphthyl moieties, has shown lower mobility, with values of  $0.15\text{ cm}^2\text{V}^{-1}\text{s}^{-1}$ .<sup>[129]</sup> The poorer electrical performance compared to **DNTT** and **DBTTT** has been attributed to the stacked crystalline motif,<sup>[130]</sup> which disfavours charge

transport due to severe anisotropy of electronic interactions within adjacent molecules in the crystalline arrangement.

Also, the molecular shape of thienoacenes plays a role in the design of new OSCs since it affects translational motions of molecules in crystal structures. Particularly, in case of OSCs that pack with an herringbone (HB) motif, motions along the longest molecular axis are suspected to weaken the HOMO wavefunctions overlap.<sup>[58,60]</sup> N-shape molecular semiconductors which deviate from a linear molecular shape, even slightly such as **DNTT**, can decrease such detrimental motions.<sup>[131,132]</sup>

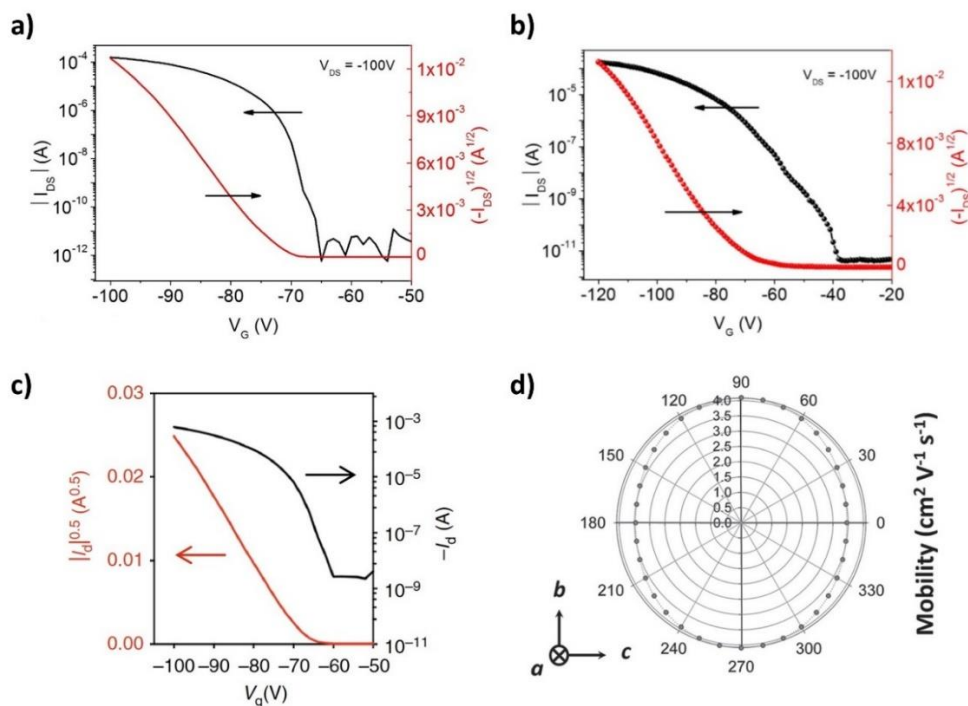
With this view, the charge transport properties of two new isomeric thienoacene-based semiconductors **DN4T** and **isoDN4T** (**Scheme 2.1**) are investigated in TFTs. From a structural point of view, **DN4T** and **isoDN4T** have two additional thienyl rings in the central motif compared to **DNTT** and **isoDNTT**. **DN4T** and **L-DBTTA** share the same central motif of four thienyl rings, annealed by terminal naphthene or benzene moieties, respectively. The aim is to see whether the extended  $\pi$ -system, comprising four fused thienyl rings between two naphthyl moieties, and the more accentuated N-shape compared to **DNTT** leads to high charge carrier mobility while preserving HB packing.

Moreover, TFTs of octyl- and decyl-substituted derivatives **C<sub>8</sub>-DN4T** and **C<sub>10</sub>-DN4T** are investigated, and their electrical performances are compared with the parent compound (**DN4T**) and the octyl-substituted derivative of **DNTT**, namely **C<sub>8</sub>-DNTT**. The functionalization of **DNTT** and **BTBT** with alkyl chains, besides enabling the device fabrication through solution processing, has shown to lead to more isotropic and balanced transfer integrals as well as to intermediate thermal disorder, boosting charge carrier mobility compared to the parent compound.<sup>[58,60]</sup> Thus, a similar effect is expected for alkylated DN4Ts.

A significant enhancement of charge carrier mobility in **BTBT** derivatives has been obtained by introducing *tert*-butyl groups on the 2,7-positions (**tBu-BTBT**). This enhancement is related to the increased dimensionality of charge transport, made possible by making slight modifications to the tilt angles and distances between molecules in the crystalline structure. These adjustments were achieved by introducing an appropriate bulky side group, which resulted in significantly larger and more evenly distributed isotropic transfer integrals.<sup>[133]</sup> Specifically, kinetic Monte Carlo simulations revealed an almost perfect isotropic charge transport in the herringbone layer planes. Charge carrier mobilities of 7.1 and 2.4 cm<sup>2</sup>V<sup>-1</sup>s<sup>-1</sup> have been reported for **tBu-BTBT** in single crystal (SCFET) and thin-film field-effect transistors, respectively.<sup>[133,134]</sup>



behaviour of ideal devices. Hence, relevant deviation from ideal textbook-like characteristics (i.e., non-ideal behaviour such as high threshold voltage, gate voltage dependent mobility, discrepancy in mobility values extracted from linear and saturation regime, relevant hysteresis and high contact resistance), as in the case of the reported OFETs based on **tBu-BTBT**, could lead to severe overestimation of the claimed mobility.



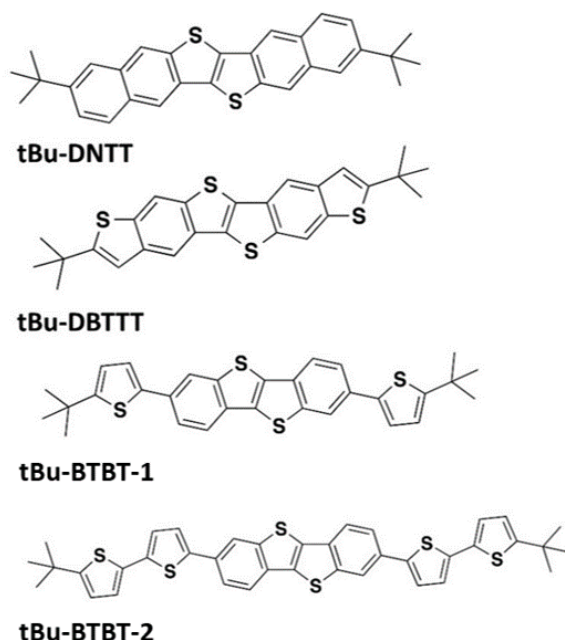
**Figure 2.1: Charge transport properties of **tBu-BTBT**.**

(a) Transfer characteristics of (a) SCFET exhibiting  $\mu$  of  $7.1 \text{ cm}^2 \text{V}^{-1} \text{s}^{-1}$  [133] (b) TFT fabricated through solution shearing technique exhibiting  $\mu$  of  $2.4 \text{ cm}^2 \text{V}^{-1} \text{s}^{-1}$  [133] (c) TFT fabricated through solution shearing technique exhibiting  $\mu$  of  $1.9 \text{ cm}^2 \text{V}^{-1} \text{s}^{-1}$ . [134] All the curves are collected in saturation regime ( $V_d = -100$  V) and exhibit  $V_{th}$  of  $\approx -70$  V (over an applied  $V_g$  of  $-100$  V for (a) and (c) and of  $-120$  V for (b)). (d) Calculated field-effect anisotropy as a function of the crystallographic orientation ( $bc$  plane corresponds to the herringbone layer plane). [133]

As mentioned above, the extension of the  $\pi$ -conjugated molecular core influence both the reorganization energy and the transfer integrals, due to the larger charge delocalization. In addition, given that the ionization energy is the energy required to remove one electron from the HOMO of molecules, the increased charge delocalization due to the  $\pi$ -extension, generally results in high-lying HOMO energy levels. [28,122,133,135] Even the manner of the  $\pi$ -extension play a key role in determining the electronic properties of OSCs. Annealed systems generally show smaller reorganization energies compared

to oligomeric systems. Specifically, due to the presence of single bonds connecting the aromatic rings, oligomeric systems have more molecular motions comprising rotation around the single bonds. In contrast, annealed molecular structure would result in lower molecular geometric variation upon charge transfer.<sup>[124]</sup>

With this view, the influence of the  $\pi$ -extension and of the manner of  $\pi$ -extension on the ionization energy and charge transport characteristics in new *tert*-butyl derivatives are investigated, by means of photoelectron yield spectroscopy and fabrication of thin-film transistors. Specifically, the targeted compounds are *tert*-butyl derivatives of **DNTT** and **DBTTT** (**tBu-DNTT** and **tBu-DBTTT**), along with *tert*-butyl-thienyl derivatives of BTBT (**tBu-BTBT-1** and **tBu-BTBT-2**), depicted in **Scheme 2.2**



**Scheme 2.2**

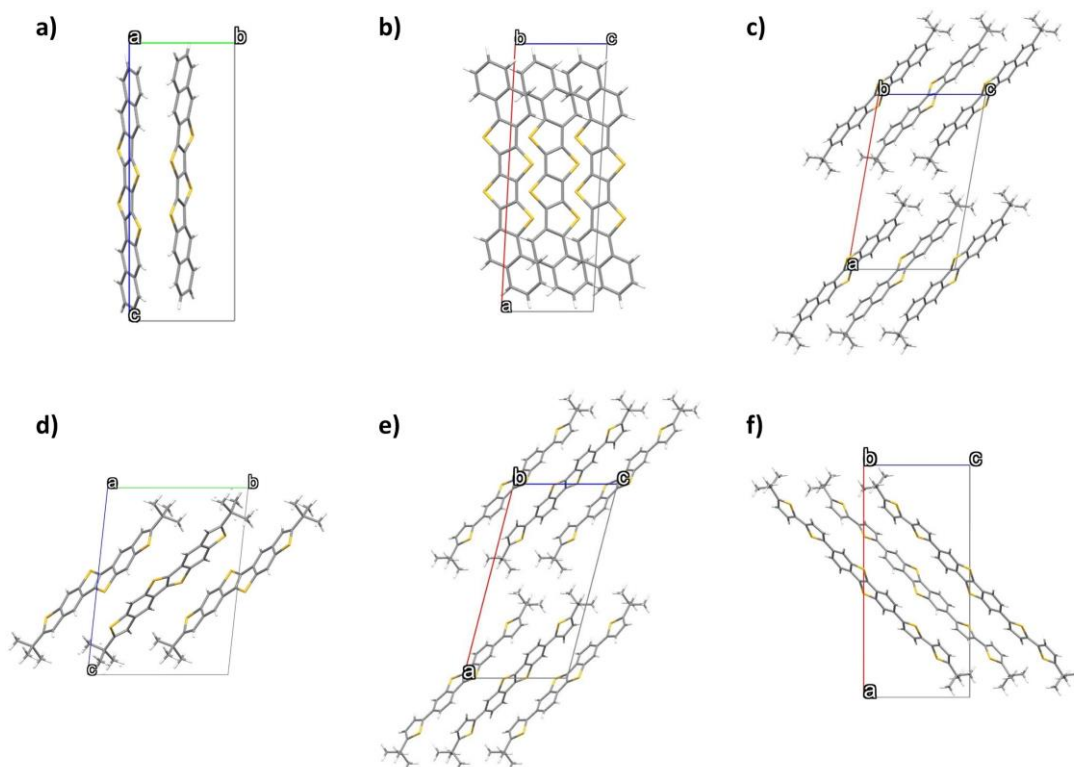
The extension of the  $\pi$ -system of the molecular core is obtained through an annealed approach (**tBu-DNTT** and **tBu-DBTTT**) and through an oligomer approach (**tBu-BTBT-1** and **tBu-BTBT-2**). The aim is to improve charge carrier injection in thin film transistors, with the view to obtain ideal and reliable behaviours, while preserving high charge carrier mobility. At last, the charge transport properties of the analysed compounds are related to quantum chemical calculations, enabling structure-properties relations derivation.

## 2.2 Crystal structures

*Crystal structures of the analysed compounds have been resolved and provided by Dr. Jiu Liu (Université libre de Bruxelles) and Dr. Alan Kennedy (University of Strathclyde).*

The crystal structures of **C<sub>8</sub>-DN4T** and **C<sub>10</sub>-DN4T** have not yet been solved. Hence, in this section the alkylated DN4Ts are not considered.

The compounds investigated in this chapter adopt a standard layer-by-layer herringbone (HB) packing motif (**Figure 2.2**), with a HB angle between two adjacent molecules ranging from 46.4° to 53.8°, in line with previously reported thienoacenes with a similar packing arrangement.<sup>[136,137]</sup> In herringbone arrangement, charge transport is facilitated by edge-to-face interactions. Among the most encountered packing motif in organic semiconductor crystals, herringbone packing has shown to give rise to high mobility, along with brick-wall packing, if compared to slipped  $\pi$ -stacking and slipped-stack packing motifs.<sup>[52]</sup>



**Figure 2.2: Crystalline packing.**

(a) DN4T, (b) isoDN4T, (c) tBu-DNTT, (d) tBu-DBTTT, (e) tBu-BTBT-1 and (f) tBu-BTBT-2.

**DN4T** belongs to monoclinic space group  $P 2_1$ , while **tBu-DBTTT** belongs to the triclinic  $P-1$ , both with one unique molecule in the asymmetric unit ( $Z' = 1$ ). All the other compounds belong to monoclinic space group  $P 2_1/c$ , with half molecule in the asymmetric unit ( $Z' = 0.5$ ), as reported in **Tables 2.1**.

If we consider the short contacts (which are defined as any intermolecular contact shorter than the sum of the van der Waals radii of the involved atoms), all the compounds exhibit C-H $\cdots\pi$ , S $\cdots$ C and S $\cdots$ S interactions, except **isoDN4T**. The latter exhibits only C-H $\cdots\pi$  interactions. This discrepancy in intermolecular interactions may play a role for the charge transport properties in **isoDN4T**. Sulphur atoms have relevant electron density compared to carbon and hydrogen atoms. Crystal arrangements which unveil S $\cdots$ C and S $\cdots$ S short contacts may show higher electron density of the HOMO that leads to a more efficient charge transfer within adjacent molecules. Considering a transient localization scenario, charges are delocalized over several molecules instead to be confined on one. Therefore, more efficient pathways for electron transfer enhance charge delocalization, which increases charge carrier mobility.

At last, it is worth mentioning that no polymorphic forms have been reported for the investigated compounds.

**Table 2.1: Crystallographic data of the investigated compounds.**

<b>Compound</b>	<b>DN4T</b>	<b>isoDN4T</b>	<b>tBu-DNTT</b>	<b>tBu-DBTTT</b>	<b>tBu-BTBT-1</b>	<b>tBu- BTBT-2</b>
<b>Formula</b>	C <sub>26</sub> H <sub>12</sub> S <sub>4</sub>	C <sub>26</sub> H <sub>12</sub> S <sub>4</sub>	C <sub>30</sub> H <sub>28</sub> S <sub>2</sub>	C <sub>26</sub> H <sub>24</sub> S <sub>4</sub>	C <sub>30</sub> H <sub>28</sub> S <sub>4</sub>	C <sub>38</sub> H <sub>32</sub> S <sub>6</sub>
<b>Temperature (K)</b>	172	100	123	255	100	123
<b>Crystal system</b>	Monoclinic	Monoclinic	Monoclinic	Triclinic	Monoclinic	Monoclinic
<b>Space group</b>	P 2 <sub>1</sub>	P 2 <sub>1</sub> /c	P2 <sub>1</sub> /c	P-1	P2 <sub>1</sub> /c	P2 <sub>1</sub> /c
<b>a (Å)</b>	6.15993(17)	19.1163(18)	17.5612(4)	6.2944(2)	20.3894(12)	24.1489(6)
<b>b (Å)</b>	7.5925(2)	7.6335(8)	6.1886(11)	11.9761(4)	5.9706(2)	5.87800(10)
<b>c (Å)</b>	20.0487(6)	6.5402(5)	10.5700(2)	16.0005(4)	10.5460(5)	11.0355(2)
<b>α (deg)</b>	90	90	90	94.024(2)	90	90
<b>β (deg)</b>	91.695(3)	92.970(8)	99.974(2)	100.072(3)	104.531(5)	90.017(2)
<b>γ (deg)</b>	90	90	90	100.828(3)	90	90
<b>Volume [Å<sup>3</sup>]</b>	937.25(5)	953.09(16)	1131.38	1159.78	1242.77	1566.46
<b>Z</b>	2	2	2	2	2	2
<b>Z'</b>	1	0.5	0.5	1	0.5	0.5

## 2.3 Thin-film transistors fabrication

TFTs were fabricated through thermal evaporation in high vacuum. Typically, OSCs were deposited at a base pressure of  $\approx 10^{-6}$ - $10^{-7}$  mbar onto substrates consisting of highly doped silicon wafer, which serves as global gate electrode, overgrown by atomic layer deposition with a 30 nm thick dielectric layer of  $\text{Al}_2\text{O}_3$ . The substrate was immersed in a 1.5 mM solution of n-tetradecylphosphonic acid (TDPA) in isopropanol prior to the deposition of the organic semiconductors, resulting in the formation of a self-assembled monolayer (SAM) on the dielectric surface. Phosphonic acids have been widely used for  $\text{Al}_2\text{O}_3$  dielectric functionalization due to their ability to form stable and highly-order SAM. The TDPA/ $\text{Al}_2\text{O}_3$  dielectric surface results to be highly hydrophobic if compared to the bare  $\text{Al}_2\text{O}_3$  surface (**Figure 2.3**) minimizing the unintentionally contamination of the dielectric surface with water molecules and preventing electrochemical reactions between the charge carrier in the accumulation layer and the moisture at the dielectric interface.<sup>[138]</sup>

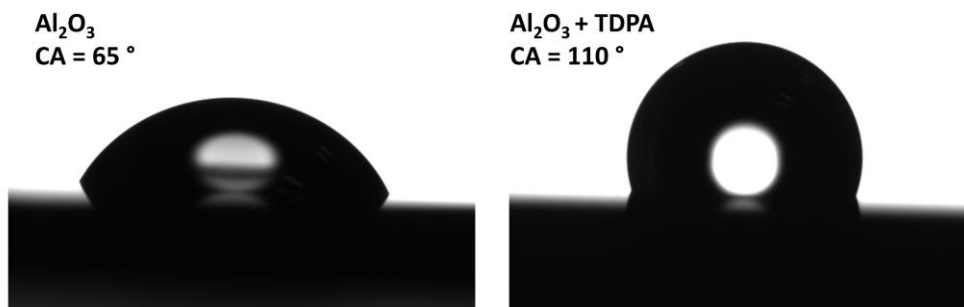
The gate-dielectric capacitance ( $C_{\text{diel}}$ ) was calculated as follow:

$$C_{\text{diel}} = \varepsilon_0 \left( \frac{t_{\text{ox}}}{\varepsilon_{\text{ox}}} + \frac{t_{\text{SAM}}}{\varepsilon_{\text{SAM}}} \right)^{-1} \quad (2.1)$$

where  $\varepsilon_0$  is the vacuum permittivity,  $t_{\text{ox}}$  is the  $\text{Al}_2\text{O}_3$  thickness,  $t_{\text{SAM}}$  is the TDPA-SAM thickness,  $\varepsilon_{\text{ox}}$  is the relative permittivity of  $\text{Al}_2\text{O}_3$  and  $\varepsilon_{\text{SAM}}$  is the relative permittivity of TDPA-SAM. The calculated unit-area capacitance is 185 nF  $\text{cm}^{-2}$ . OSCs were deposited at  $0.3 \text{ \AA s}^{-1}$  and with nominal thickness (monitored with a quartz crystal microbalance) of 25 nm. In case of alkylated DN4Ts, the deposition rate was set at  $0.1 \text{ \AA s}^{-1}$ , as previously reported for other alkylated thienoacenes.<sup>[60,92]</sup> Semiconductor thickness between 20 and 30 nm is usually employed in TFTs, since it ensures a sufficient coverage of the active channel. Using thicker semiconductor layer may result in larger contact resistance in TC devices, due to the poor vertical charge transport through the semiconductor thickness (in case of small-molecule OSCs). Moreover, thicker semiconductor layer exhibit larger trap-state density in small-molecule p-type OSC.<sup>[74,139]</sup>

Both, bottom-gate top-contact (BGTC, hereinafter shortened to TC) and bottom-gate bottom-contact (BGBC, hereinafter shortened to BC) configurations were fabricated by thermal evaporation of gold electrodes with a typical thickness of ca. 50 nm by using shadow masks at a base pressure of  $10^{-5}$ - $10^{-6}$  mbar. In case of BC devices, gold contacts were deposited before the OSCs and their surfaces were functionalized with pentafluorobenzenethiol (PFBT), by immersing the substrate in a 10 mM solution of PFBT in

isopropanol. The treatment results in the formation of a PFBT-SAM, which promotes a more uniform semiconductor morphology across the interface between the contacts and the active channel. Moreover, PFBT exhibits a large dipole moment created by the high density of fluorine atoms which points downward with respect to the gold surface. This large dipole increases the work function of gold contacts of  $\approx 0.4$  eV,<sup>[85]</sup> which can improve charge injection in p-type OSCs by reducing the height of the nominal charge-injection barrier. Also, BC devices with bare gold contacts were fabricated and compared to BC devices with PFBT treated gold contacts.



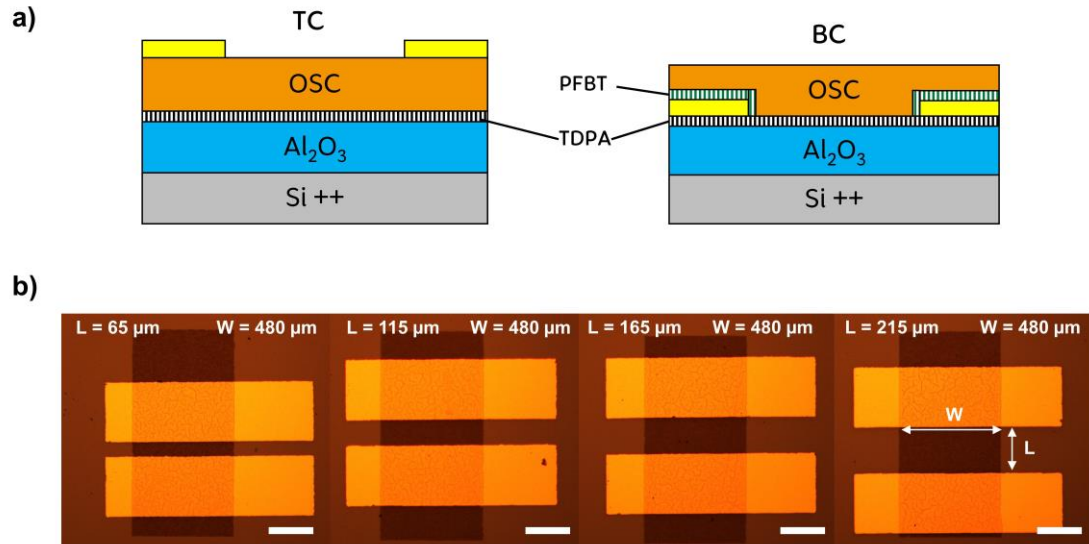
**Figure 2.3: Contact angle of water droplets on bare  $\text{Al}_2\text{O}_3$  and on TDPA/ $\text{Al}_2\text{O}_3$ .**

On the left:  $2\ \mu\text{m}$  water droplet onto bare  $\text{Al}_2\text{O}_3$  substrates, with contact angle of  $65^\circ$ . On the right:  $2\ \mu\text{m}$  water droplet onto TDPA/ $\text{Al}_2\text{O}_3$  substrates, with contact angle of  $110^\circ$ .

During the OSCs deposition, the substrates were kept at temperatures ranging from  $40^\circ\text{C}$  to  $140^\circ\text{C}$  with  $20^\circ\text{C}$  steps, for **DN4T** and **isoDN4T**, and from  $40^\circ\text{C}$  to  $130^\circ\text{C}$  with  $30^\circ\text{C}$  steps for the other compounds.<sup>5</sup> The substrate temperature during OSCs deposition ( $T_s$ ) is one of the most important parameters to control in order to achieve the best charge carrier mobility. By increasing the substrate temperature, the surface diffusion of the adsorbed molecules onto the substrate increases as well, allowing the deposited molecules to find the lowest energy sites and inducing a long-range structural ordering within the OSC film. The heating of the substrate beyond a certain temperature leads to a decrease of the sticking coefficient of the organic molecules which is reflected in lack of inter-grain connectivity and partial dewetting of the OSC.<sup>[140]</sup>

<sup>5</sup> We acknowledge Michael Eustachi for his contribution to the development of the controlled substrate temperature feature integrated into the OSC evaporator (UNIVEX 300).

A schematic representation of the TC and BC devices is presented in **Figure 2.4**. The fabricated TFTs have a channel length (L) of 65, 115, 165 and 215  $\mu\text{m}$  and a channel width (W) of 480  $\mu\text{m}$ . A more detailed procedure of TFTs fabrication is presented in **Chapter 5**.



**Figure 2.4: Illustration of devices geometry.**

(a) Schematic illustration of TC (on the left) and BC (on the right) TFTs, (b) optical micrographs of fabricated devices with channel length (L) of 65, 115, 165 and 215  $\mu\text{m}$  and channel width (W) of 480  $\mu\text{m}$ . Scale bar: 200  $\mu\text{m}$ .

## 2.4 Thin-film characterization

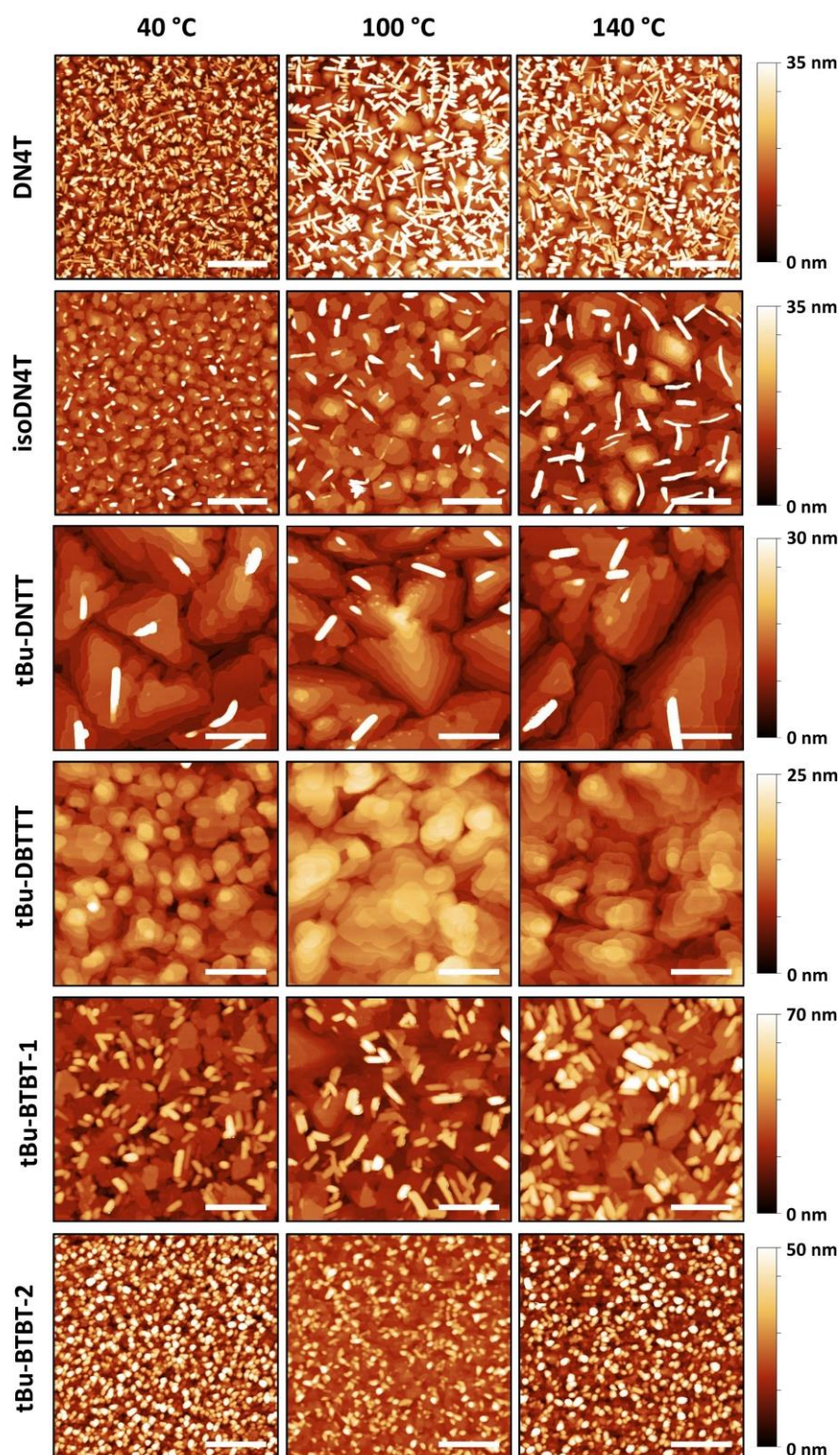
### 2.4.1 Topography

#### 2.4.1.1 Deposition onto TDPA/Al<sub>2</sub>O<sub>3</sub>

The morphology of the thin films was evaluated through atomic force microscopy (AFM) in tapping mode performed on the active channel of fabricated transistors with  $T_s$  of 40, 100 and 140 °C. All the compounds, except for the alkylated DN4Ts, exhibit a terrace structure topography characterized by the diffuse presence of grain boundaries which define the micro- (or nano) crystalline domains (**Figure 2.5**). In contrast, the alkylated DN4Ts are characterized by small crystallites exhibiting a slightly elongated shape (**Figure 2.6**). Hence, in this section the analysis of thin film topography of non-alkylated parent compounds is discussed at first, due to common terraced topography, followed by the analysis of alkylated DN4Ts.

By analysing the AFM images, the averaged grain size and height of the terrace steps of the parent compounds were extracted. The grain diameters are in the range of 200-1300 nm, depending both on the substrate temperature and on the compound. The average terraces height steps exhibit values between  $\approx 18$  Å to  $\approx 24$  Å.

For all the compounds the grain size increases from  $T_s$  of 40 °C to  $T_s$  of 100 °C and eventually decreases for  $T_s$  of 140 °C (**Table 2.2**). The largest grain sizes were identified for **tBu-DNTT**, with averaged diameter of  $\approx 1340$  nm, followed by for **tBu-DBTTT**, with values of  $\approx 800$  nm and **isoDN4T**, with values of  $\approx 460$  nm. In these compounds the grain size increases up to 2.5 times passing from  $T_s$  of 40 °C to  $T_s$  of 100 °C and eventually slightly decreases at  $T_s$  of 130 °C. At last, in case of **DN4T**, **tBu-BTBT-1** and **tBu-BTBT-2**, the grain size increases by increasing the substrate temperature, but showing a weaker variation with respect to different  $T_s$ , resulting in values of  $\approx 250$  nm,  $\approx 350$  nm and  $\approx 200$  nm for **DN4T**, **tBu-BTBT-1** and **tBu-BTBT-2** respectively. In polycrystalline TFTs, charge carrier mobility can be significantly limited by the charge transport from one grain to another. Increasing the grain size (and therefore reducing the number of grain boundaries that charges must overcome) results in enhancement of the electrical performances, especially in term of charge carrier mobility. Hence, higher charge carrier mobility is expected in TFTs where the OSCs were deposited at  $T_s$  of 100 °C, compared to those with  $T_s$  of 40 and 140 °C.



**Figure 2.5: AFM topography images of thin films deposited on TDPA/Al<sub>2</sub>O<sub>3</sub> at different substrate temperatures.**

Nominal thickness of the films: 25 nm. Lateral scale bar size: 500 nm.

In contrast to the grain size, the heights of the terraces' steps did not change significantly upon the variation of the substrate temperature. The extracted heights correspond to the longest axis of the unit cell of each respective compound (see **Table 2.2**), suggesting that in the thin films, molecules adopt a polycrystalline layer by layer structure with an upright orientation with respect to the dielectric layer.

**tBu-DBTTT** is characterized by a smoother and flatter topography compared to the other compounds, which results to be ideal for AFM analysis. In contrast, the thin films formed by the other compounds show a more disordered topography, with the presence of numerous single crystals aggregates that stand out from the terraces surface by tens of nm. Particularly, the massive presence of crystals aggregates in **tBu-BTBT-2** thin films hinders the clear observation of the underneath terraces layers and makes it difficult the grains size estimation. It is still unclear the role of these crystalline aggregates on the final device performances.<sup>[92]</sup>

**Table 2.2: Averaged grain size extracted from AFM images.**

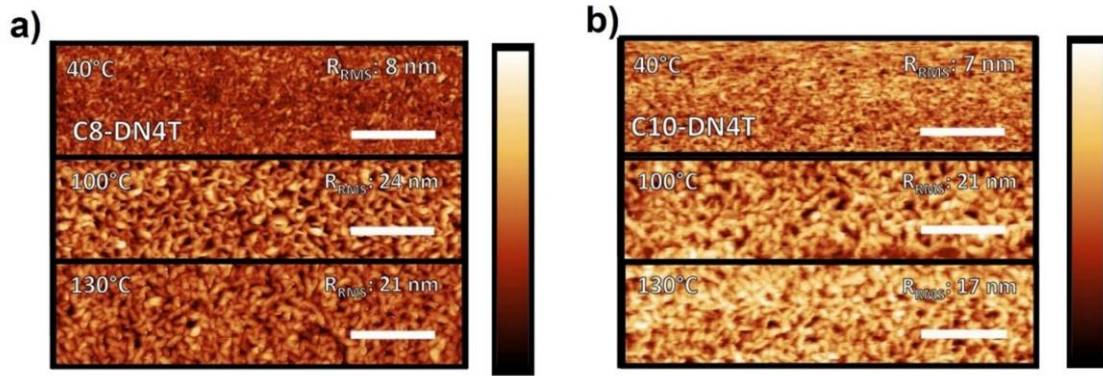
The values are expressed in nm.

Compound	40 °C	100 °C	130 °C
<b>DN4T</b>	145 ± 30	250 ± 60	200 ± 15
<b>isoDN4T</b>	190 ± 30	460 ± 75	320 ± 55
<b>tBu-DNTT</b>	958 ± 205	1339 ± 253	1022 ± 290
<b>tBu-DBTTT</b>	317 ± 110	799 ± 230	620 ± 180
<b>tBu-BTBT-1</b>	360 ± 70	380 ± 60	370 ± 80
<b>tBu-BTBT-2</b>	194 ± 33	242 ± 46	216 ± 48

In contrast with the non-alkylated compounds, thin films based on alkylated DN4Ts do not show a terraced topography but are characterized by small crystallites of elongated shape with an average size lower than 100 nm (**Figure 2.6**).

These thin films were found to be mechanically delicate compared to similar compounds, such as **C<sub>8</sub>-DNTT** or **C<sub>12</sub>-DBTTT** (see **Chapter 3**). A non-destructive AFM imaging is unexpectedly very critical even by reducing the tip-surface interaction force to the minimum value that allowed to resolve the surface profile. Alkylated DN4Ts thin films show a particularly high roughness (between 7 and 24 nm) with respect to their absolute thickness (30

nm). These roughness values suggest that the growth of OSC crystalline domains does not occur in a layer-by-layer mode. OSC grains are not well connected, especially for films grown at higher temperatures, where large dips (at the substrate level or a few layers above) and other features (as high as 80 nm) appear on the surface.



**Figure 2.6: AFM topography images of C<sub>8</sub>-DN4T and C<sub>10</sub>-DN4T thin films deposited on TDPA/Al<sub>2</sub>O<sub>3</sub>.**

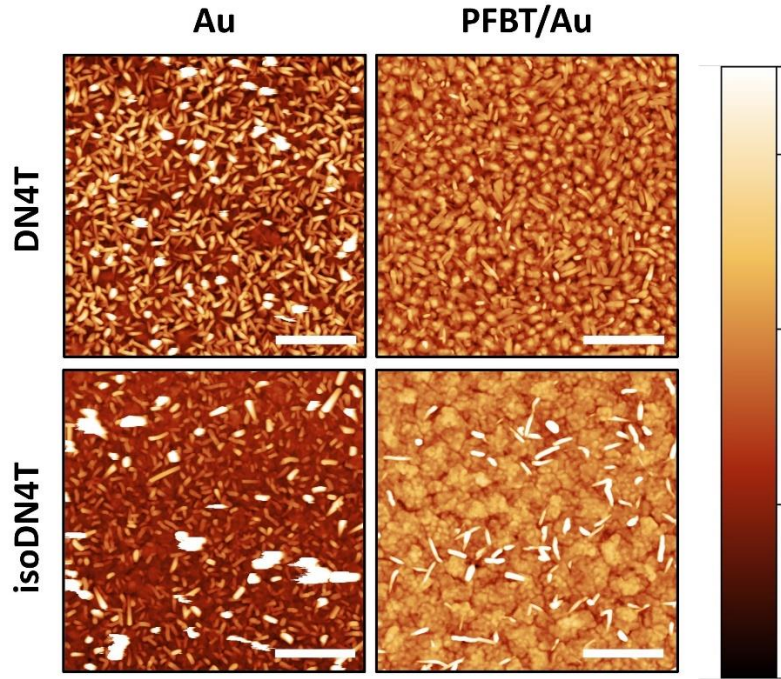
Nominal thickness of the films: 25 nm. Lateral scale bar size: 1  $\mu\text{m}$ . Root mean square roughness ( $R_{\text{RMS}}$ ) values are calculated on  $1 \times 1 \mu\text{m}^2$  areas. Z-scales (Z) are expressed in nm for each temperature as follows: (a) C<sub>8</sub>-DN4T: 40 °C (Z = 95), 100 °C (Z = 175), 130 °C (Z = 175). (b) C<sub>10</sub>-DN4T: 40 °C (Z = 60), 100 °C (Z = 150), 130 °C (Z = 110).

Despite the pitted thin-film morphology, the charge carrier percolation paths in the films are still sufficiently interconnected to give operating transistors. It is worth noting that the high roughness of the OSC thin films alongside with the large number of grain boundaries may limit the achievement of higher mobility values in polycrystalline TFTs.

#### 2.4.1.2 Deposition onto Au and PFBT/Au

In BC devices, OSCs are deposited onto drain and source gold contacts. An important requirement for efficient charge carrier injection is to have a similar morphology within the OSC deposited onto the contacts and the OSC deposited onto the dielectric.<sup>[141,142]</sup> DN4T and isoDN4T were used to exemplify the change of the thin film morphology when deposited onto gold contacts and PFBT-treated gold contacts. AFM measurements were performed on the contact region covered by the OSCs.

In case of **DN4T**, thin film deposited on Au exhibits a large presence of needle-shaped single crystals aggregates which hinders the observation of the underneath layers (**Figure 2.7**).



**Figure 2.7: AFM topography images of DN4T and isoDN4T thin films deposited on PFBT/Au.**

$T_s = 100\text{ }^{\circ}\text{C}$ . Nominal thickness of the films: 25 nm. Lateral scale bar size: 500 nm. Z-scales (Z) are expressed in nm for each sample as follows: (a) **DN4T** on Au ( $Z = 80$ ), **DN4T** on PFBT/Au ( $Z = 35$ ), **isoDN4T** on Au ( $Z = 80$ ), **isoDN4T** on PFBT/Au ( $Z = 40$ ).

On the contrary, **DN4T** thin film deposited onto PFBT/Au shows a more uniform morphology unveiling small grain crystallites with grain diameter of  $\approx 95\text{ nm}$ .

In case of **isoDN4T**, thin film deposited onto Au shows small grain crystallites (grain diameter of  $\approx 85\text{ nm}$ ) covered by numerous crystals aggregates (**Figure 2.4**). On the contrary, thin film deposited onto PFBT/Au resembles the morphology of thin film deposited onto TDPA/ $\text{Al}_2\text{O}_3$  but exhibiting smaller grain diameter ( $\approx 225\text{ nm}$ ).

In conclusion, the functionalization of gold contacts with PFBT showed to promote a similar semiconductor morphology across the interface between the metal gold contacts and the active channel (where the OSCs are deposited onto TDPA/ $\text{Al}_2\text{O}_3$ ), as previously reported.<sup>[85,141,142]</sup>

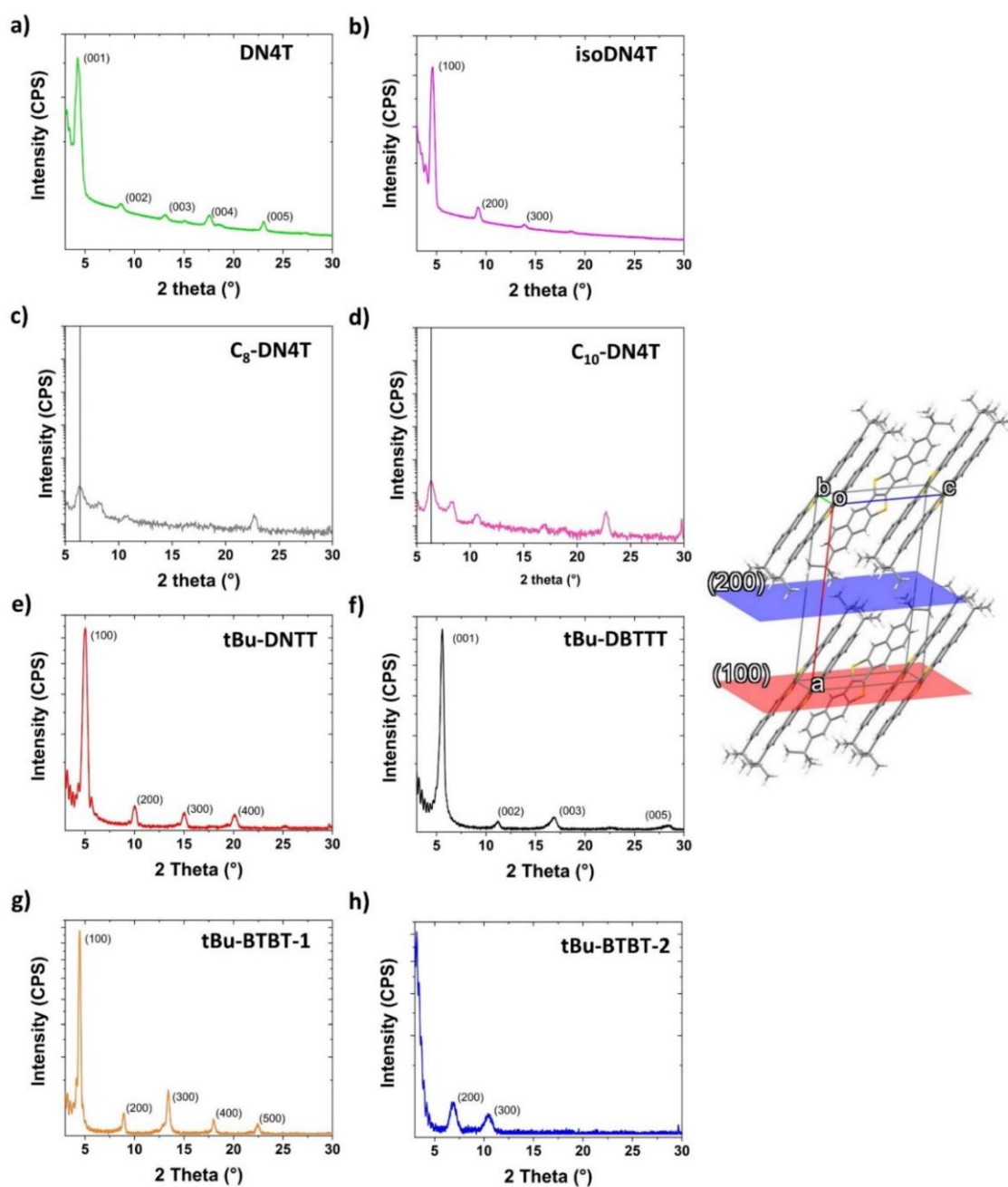
## 2.4.2 Crystallinity

To further investigate the film orientations, XRD patterns of the thin films were collected. Due to the larger spot size needed for the measurement, XRD was performed on thin films deposited through vacuum sublimation onto TDPA/Al<sub>2</sub>O<sub>3</sub> substrate hold at 100°C during the deposition (**Figure 2.8**), and not on the active channel as for AFM measurements. The deposition parameters were the same used for TFTs fabrication.

Bragg peaks along the out-of-plane direction were indexed except for the alkylated DN4Ts, since for the latter it was not possible to solve the crystal structures. The peaks were assigned to the family planes {001} and {100}, depending on the compound. These planes can be defined as herringbone layer planes and are those enclosed between the two shorter axis of the unit cell of each respective compound. In other words, the d-spacing associated to these planes corresponds to the longest axis of the unit cell (see **Figure 2.8**).

The averaged d-spacing for each compound was calculated by applying the Bragg law, showing values between 15.7 Å and 25.6 Å (see **Table 2.3**). These values correspond to the height of the terrace steps extracted by AFM and as well to the unit cells long axis of each respective compound. Consequently, all the thin films adopt a layer-by-layer structures with the molecules standing approximately upright on their long axis respect to the dielectric surface, with the herringbone layer plane parallel to the dielectric.

Considering the position of the Bragg peaks for both **C<sub>8</sub>-** and **C<sub>10</sub>-DN4T** and their analogy with other classes of alkylated thienoacenes like **C<sub>8</sub>-DNTT**, **C<sub>10</sub>-DNTT** and **C<sub>10</sub>-DNBDT**,<sup>[92]</sup> we can attribute the peaks at 2θ values of 7.02° and 6.36° (highlighted by vertical lines in **Figure 2.8**) to the crystal plane (003), assuming the c-axis of the unit cell as the longest axis. The d-spacing related to the peaks was calculated, giving values of 37.8 Å and 41.7 Å for **C<sub>8</sub>-DN4T** and **C<sub>10</sub>-DN4T** respectively. These values should correspond to the length of the alkylated DN4Ts and are in fact similar to the molecular lengths of the aforementioned alkylated thienoacenes. The difference between these lengths is related to the different length of the alkyl chains.



**Figure 2.8: XRD patterns of thin films.**

All the compounds were deposited onto TDPA/ $\text{Al}_2\text{O}_3$  at substrate temperature of  $100^\circ\text{C}$  with a nominal thickness of 25 nm. On the right: illustration of the (100) and (200) planes, belonging to the family plane  $\{100\}$  of **tBu-DNTT**.

**Table 2.3: Values extracted from XRD and AFM measurements.**

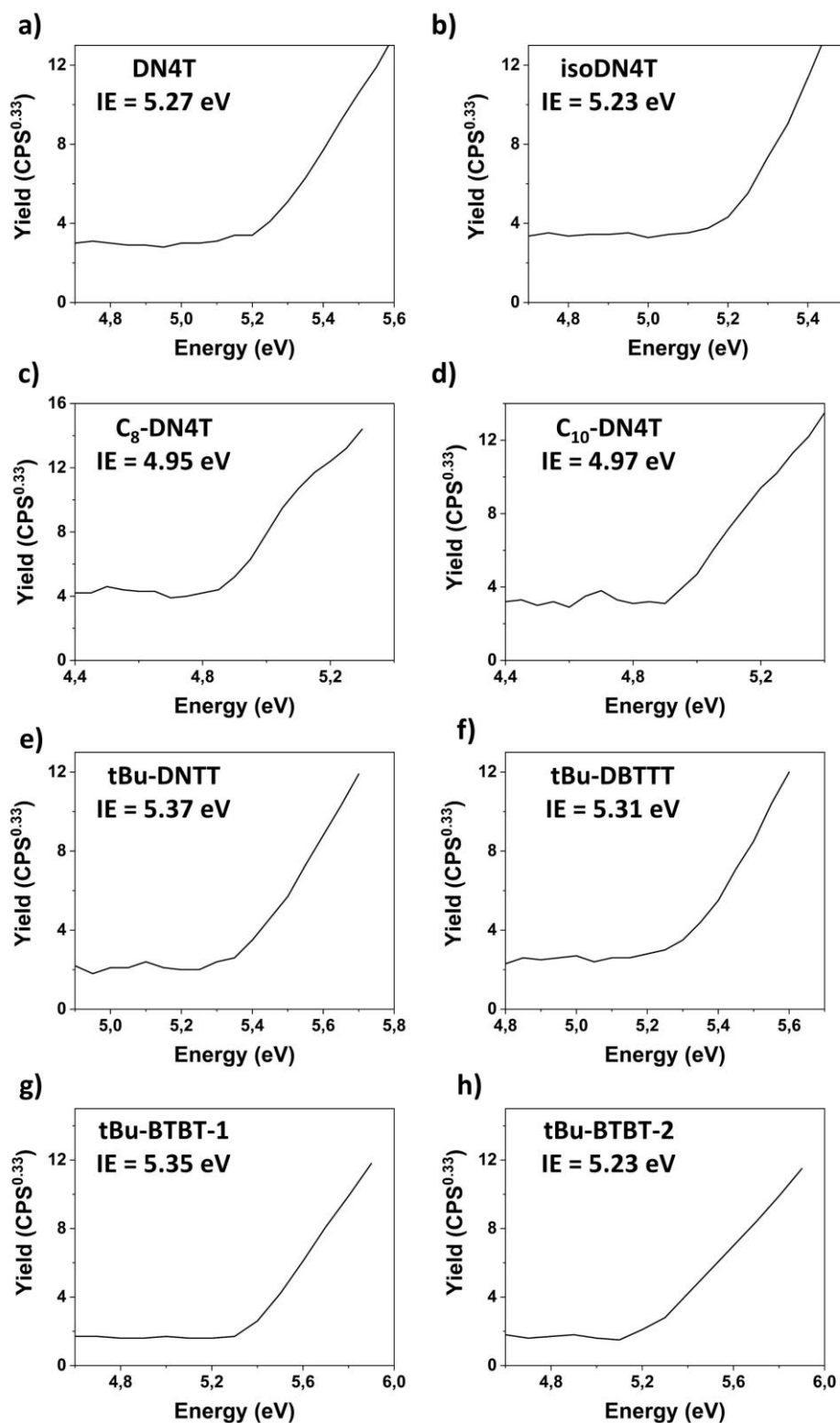
d-spacing calculated from XRD patterns (d XRD), terrace height steps obtained from AFM (d AFM) and cell long axis from SCXRD (L SCXRD). <sup>a</sup> average values obtained from all the Bragg peaks referred to the same family plane {001} or {100}; <sup>b</sup> average values

Compound	d XRD (Å) <sup>a</sup>	d AFM (Å) <sup>b</sup>	L SCXRD (Å)
<b>DN4T</b>	20.2 ± 0.5	20.0 ± 1.0	20.0
<b>isoDN4T</b>	19.2 ± 0.1	18.0 ± 1.0	19.1
<b>tBu-DNTT</b>	17.9 ± 0.5	17.5 ± 1.2	17.6
<b>tBu-DBTTT</b>	15.7 ± 0.1	15.0 ± 1.4	16.0
<b>tBu-BTBT-1</b>	19.8 ± 0.1	19.0 ± 0.9	20.4
<b>tBu-BTBT-2</b>	25.6 ± 0.2	23.6 ± 2.0	24.2

Taking into account the crystallinity of the films and their morphology, we suppose that alkylated compounds adopt a 3D growth (Volmer-Weber type)<sup>[140]</sup> when deposited onto TDPA/Al<sub>2</sub>O<sub>3</sub> substrates, instead of a typical 2D layer-by-layer growth. 3D growth in organic semiconductor thin films has shown to limit the electrical performance in term of charge carrier mobility due to the formation of voids into the film and the presence of many grain boundaries.<sup>[143,144]</sup>

### 2.4.3 Ionization energy

The ionization energy of the compounds was measured by photoelectron yield spectroscopy (PYS). The measurements were performed at ambient conditions on the same thin films used for XRD analysis. This technique enables the collection of the number of emitted photoelectrons per photon absorbed (quantum yield of photoelectron, Y) as a function of the incident photon energy (hν). Once the photon energy exceeds the ionization energy of the sample (threshold ionization energy, I<sub>th</sub>), photoemission occurs. In the case of organic materials, the threshold region of the spectrum follows  $Y \propto (h\nu - I_{th})^n$ , with  $n = 3$ .<sup>[145]</sup> Ionization energy is obtained by the onset of the yield curve (see **Figure 2.9**).



**Figure 2.9: PYS measurements performed on thin films of thienoacene derivatives.**

Thin films were obtained through vacuum deposition onto  $\text{Al}_2\text{O}_3$ /TDPA substrates at substrate temperature of 100°C.

At least 3 measurements for each film were recorded, giving standard deviation lower than 0.05 eV for all the samples. The compounds exhibit ionization energy between 4.94 eV and 5.37 eV.

Remarkably, alkylated DN4Ts show IE of  $\approx 4.9$  eV, that is about 0.3 eV lower compared to IE of **DN4T** and **isoDN4T**. The lowering of IE due to the introduction of alkylated substituents has been already reported for thienoacenes, as in the case of **BTBT** (5.8 eV)<sup>[146]</sup> and its decyl derivative **C<sub>8</sub>-BTBT** (5.0 eV),<sup>[147]</sup> as well as for **DNTT** (5.4 eV) and its octyl derivative, namely **C<sub>8</sub>-DNTT** (4.9 eV, **Figure A1.6** in the **Appendix**). The reason behind the lower IE in alkylated derivatives is discussed later, in **Paragraph 2.6.4**. Notably, the *tert*-butyl derivatives exhibit IE in the range of 5.23 and 5.37 eV, confirming the lowering of IE compared to **tBu-BTBT** due to the  $\pi$ -core extension. This is expected to ease charge carrier injection in TFTs, eventually leading to low threshold voltage and low contact resistance.

## 2.5 Electrical performances

TFTs were measured in dark at ambient air and at room temperature, by using a manual probe station and an Agilent 4156C Semiconductor Parameter Analyzer. The transfer characteristics were measured at a drain-source voltage ( $V_d$ ) of -0.1 V for the linear regime and -4 V for the saturation regime and applying a source-gate voltage ( $V_g$ ) from 1 to -4 V, sweeping  $V_g$  in steps of -0.225 V. The output characteristics were recorded at constant source-gate voltage ranging from -2 V to -4 V with -0.5 V steps and varying the source-drain voltage from 0.5 V to -4 V, with steps of -0.225 V.

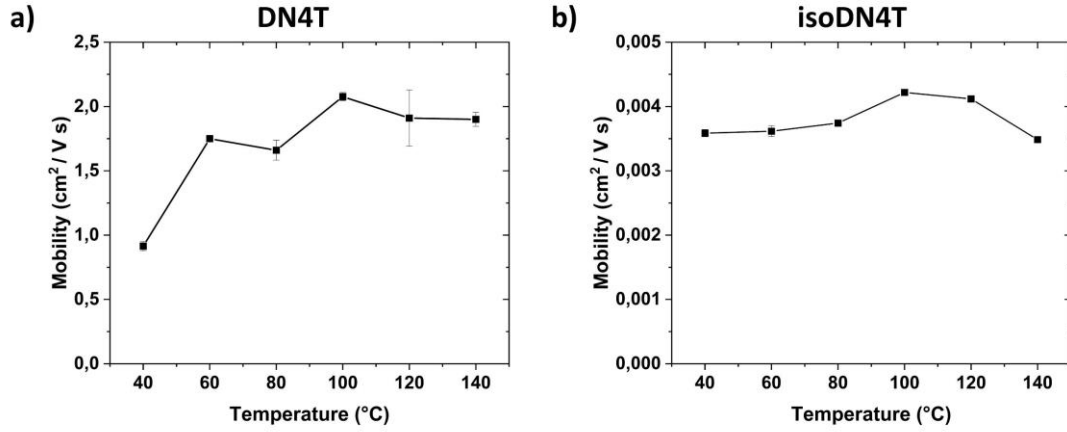
Charge carrier mobility ( $\mu$ ), threshold voltage ( $V_{th}$ ) and on/off current ratio ( $I_{ON/OFF}$ ) data reported in the main text of the thesis are always refereed to the linear regime of operation ( $V_d = -0.1$  V) and to TFTs with channel length of 215  $\mu\text{m}$  and channel width of 480  $\mu\text{m}$ , unless otherwise stated.

### 2.5.1 Thin film transistors based on DN4T and isoDN4T

#### 2.5.1.1 Impact of the substrate temperature

The key role of the substrate temperature in term of charge carrier mobility enhancement was confirmed by analysing the electrical characteristics of TC devices based on **DN4T** and **isoDN4**. For both the compounds, mobility increases by increasing the substrate temperature from 40 °C to 100 °C and eventually decreases for substrate temperature of 120 °C and 140 °C (**Figure 2.10**).

Particularly, for **DN4T** the mobility passes from 0.9  $\text{cm}^2\text{V}^{-1}\text{s}^{-1}$  at  $T_s$  of 40 °C to 2.1  $\text{cm}^2\text{V}^{-1}\text{s}^{-1}$  at  $T_s$  of 100 °C, incrementing more than 2 times. For substrate temperature of 120 and 140 °C, mobility slightly decreases to values of 1.9  $\text{cm}^2\text{V}^{-1}\text{s}^{-1}$ . TFTs based on **isoDN4T** shows a lower modulation of mobility upon the change of substrate temperature, passing from 0.0036 at  $T_s$  of 40 °C to 0.0042  $\text{cm}^2\text{V}^{-1}\text{s}^{-1}$  at  $T_s$  of 100 °C. Remarkably, the highest mobility values for both the compounds were found at substrate temperature of 100 °C, that corresponds to thin films which exhibit the longest grain diameter, as displayed in **Figure 2.5** and **Table 2.2**.



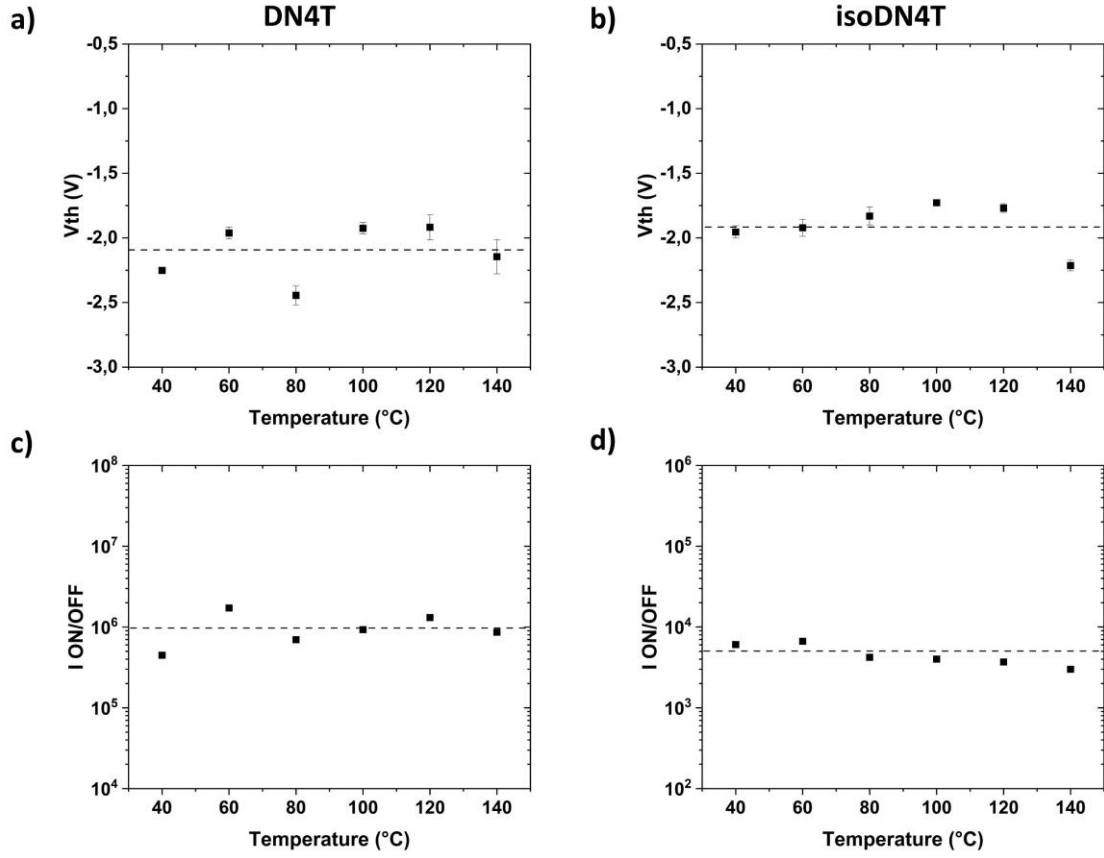
**Figure 2.10: Mobility vs substrate temperature for DN4T and isoDN4T.** Mobility as a function of the substrate temperature in (a) **DN4T** and (b) **isoDN4T** based TC TFTs. The values are referred to the linear regime and to devices with  $W/L = 480/215 \mu\text{m}$ .

Threshold voltage and on/off current ratio were not notably affected by the variation of the substrate temperature (**Figure 2.11**). TFTs based on **DN4T** shows  $V_{\text{th}}$  between -1.9 and -2.4 V along with  $I_{\text{ON/OFF}}$  of  $\approx 5 \times 10^5 / 2 \times 10^6$  and **isoDN4T** based devices shows  $V_{\text{th}}$  between -1.9 V and -2.2 V, along with  $I_{\text{ON/OFF}}$  of  $\approx 3 \times 10^3 / 6 \times 10^3$ .

In summary, the variation of substrate temperature showed to have a major role in the enhancement of charge carrier mobility, as predicted by topography images obtained through AFM. No significant trend was found for threshold voltage and on/off current ratio upon the variation of  $T_s$ .

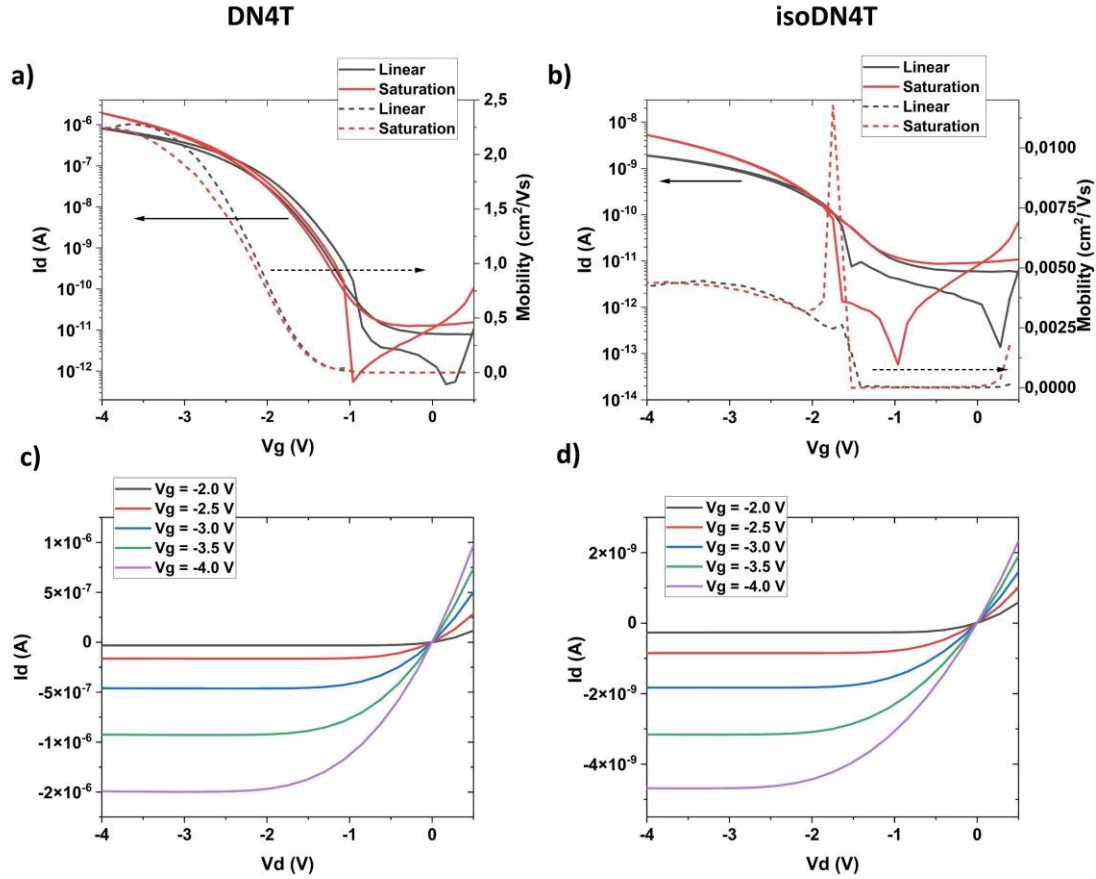
In **Figure 2.12** the transfer and output characteristics of **DN4T** and **isoDN4T** based TC at  $T_s$  of 100 °C are displayed. Remarkably, a negligible hysteresis between the forward and backward scan is observed for all the devices, suggesting a minor presence of traps.

Values of  $\mu$ ,  $V_{\text{th}}$  and  $I_{\text{ON/OFF}}$  in the saturation regime are consistent with those extracted in linear regime for different  $T_s$ , confirming the reliability of the fabricated devices. Moreover, devices built on common substrate shows very low variation of mobility values, underling the high reproducibility of the fabricated TFTs.



**Figure 2.11: Threshold voltage and on/off current ratio vs substrate temperature for DN4T and isoDN4T.**

Threshold voltage and on/off current ratio as a function of the substrate temperature in (a),(c) **DN4T** and (b),(d) **isoDN4T** based TC TFTs. The values are referred to the linear regime and to devices with  $W/L = 480/215 \mu\text{m}$ . The dot lines indicate the averaged values of  $V_{th}$  and  $I_{ON/OFF}$ .



**Figure 2.12: Transfer and output characteristics of DN4T and isoDN4T top-contact devices.**

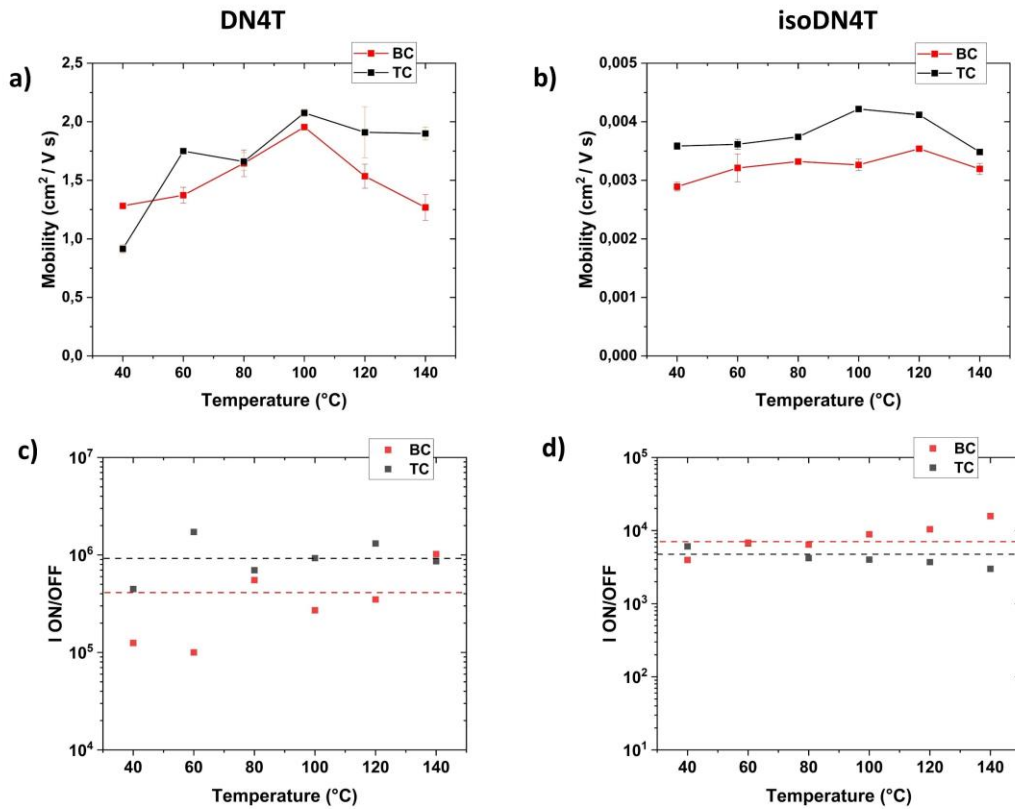
On the top: representative transfer (on the top) and output (on the bottom) characteristics of TC TFTs based on (a),(c) **DN4T** and (b),(d) **isoDN4T** at substrate temperature of 100 °C. In transfer characteristics, solid lines are referred to drain current and dot lines are referred to mobility. TFTs have  $W/L = 480/215 \mu\text{m}$ .

### 2.5.1.2 Impact of the device geometry

To investigate the impact of device geometry on the electrical performance of **DN4T** and **isoDN4T** based TFTs, BC devices were fabricated and compared with the TC counterparts. As already stated above, the functionalization of source and drain gold contacts with PFBT is a necessary step to obtain operating devices. Bottom-gate bottom-contact devices with bare gold contacts were fabricated at  $T_s$  of 100 °C for both the isomers. All the measured devices did not show drain current modulation. The morphology of thin films of OSCs deposited onto bare gold contacts differs significantly from those deposited onto TDPA/ $\text{Al}_2\text{O}_3$ , as shown in **Figure 2.7**. This dissimilarity in morphology across the contact-to-channel interface may be responsible for the

absence of field-effect response in bottom-gate bottom-contact TFTs fabricated with bare gold contacts.

In case of BC TFTs fabricated with PFBT-treated gold contacts, OSCs were deposited at different  $T_s$ , from 40 to 140 °C with 20 °V steps. Both for **DN4T** and **isoDN4T**, charge carrier mobilities extracted from transfer characteristics follow the same trend observed in TC devices, along with similar values (**Figure 2.13**).



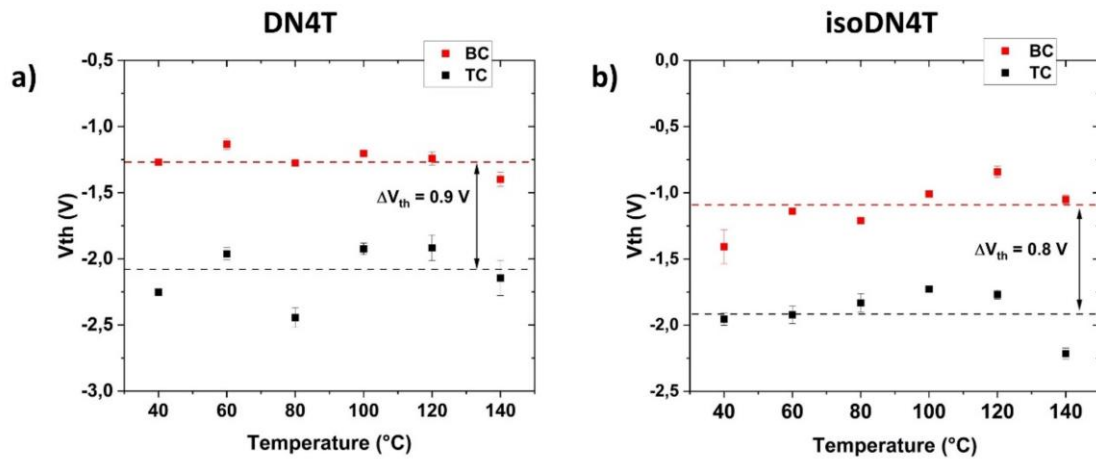
**Figure 2.13: Mobility and on/off current ratio vs substrate temperature for BC and TC TFTs based on DN4T and isoDN4T.**

On the top: Mobility as function of the substrate temperature for BC and TC TFT based on (a) **DN4T** and (b) **isoDN4T**. On the bottom: on/off current ratio as function of the substrate temperature for BC and TC TFT based on (a) **DN4T** and (b) **isoDN4T**. The dot lines indicate the average values.

For **DN4T** based BC devices, mobility goes from 1.3 cm²V⁻¹s⁻¹ at  $T_s$  of 40 °C to 2.0 cm²V⁻¹s⁻¹ at  $T_s$  of 100 °C and eventually decreases to 1.3 cm²V⁻¹s⁻¹ at  $T_s$  of 140 °C. Likewise, for **isoDN4T** based BC devices, mobility goes from 0.0029 cm²V⁻¹s⁻¹ at  $T_s$  of 40 °C to 0.0033 cm²V⁻¹s⁻¹ at  $T_s$  of 100 °C and afterward decreases to 0.0032 cm²V⁻¹s⁻¹ at  $T_s$  of 140 °C. On/off current ratio is not

significantly affected by the change of device geometry, giving comparable values with those of TC devices (**Figure 2.13**).

While  $\mu$  and  $I_{ON/OFF}$  did not change greatly between the TC and BC geometries, threshold voltage was found to be always lower in BC devices compared to TC counterparts for both the compounds (**Figure 2.14**). Particularly, for **DN4T** based TFTs,  $V_{th}$  was found to be up to 1.3 V (on average 1.2 V) lower in BC devices and for **isoDN4T** based TFTs,  $V_{th}$  was found to be up to 1.1 V (on average 0.8 V) lower in BC devices. This notable  $V_{th}$  decrease may be related to lower contact resistance observed in BC devices for both **DN4T** and **isoDN4T** based TFTs (see the **Paragraph 2.5.4**), which should result in a more facile charge carrier injection.

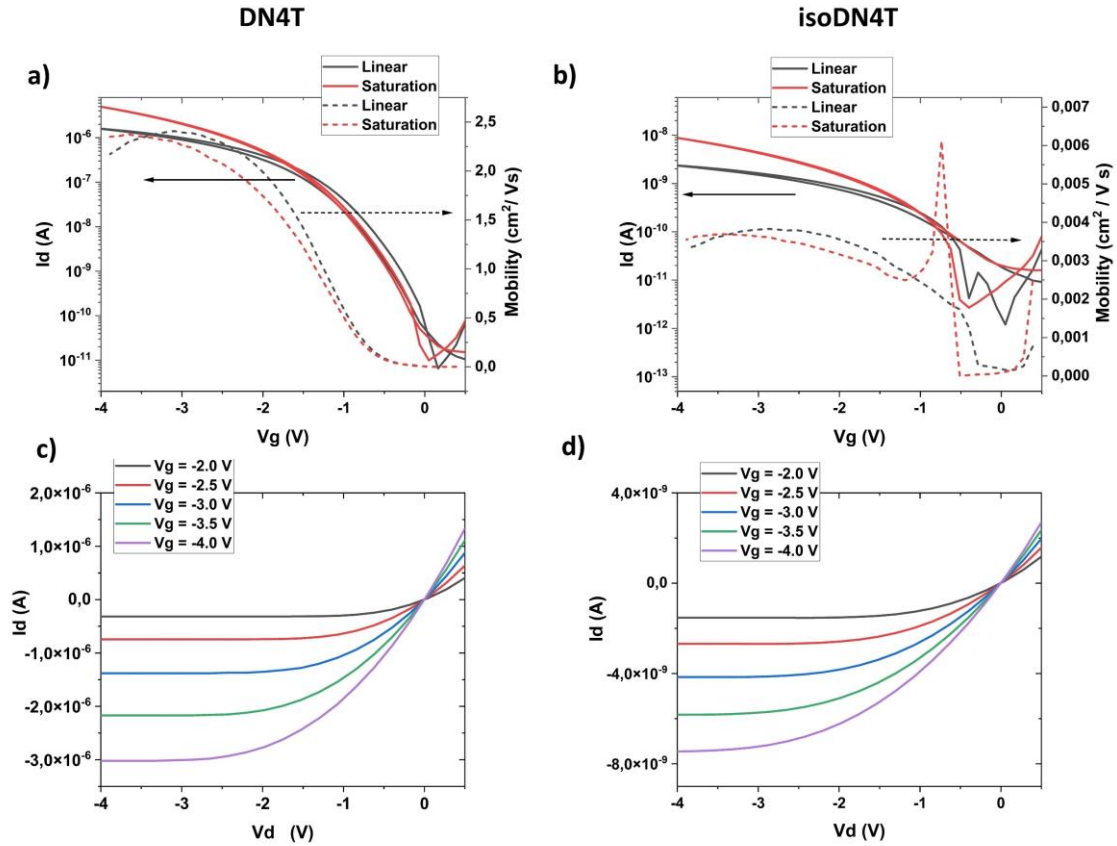


**Figure 2.14: Threshold voltage vs substrate temperature for BC and TC TFTs based on DN4T and isoDN4T.**

$V_{th}$  as function of the substrate temperature for BC and TC TFTs based on (a) **DN4T** and (b) **isoDN4T**. The dot lines indicate the average values.

In **Figure 2.15**, transfer and output characteristics of **DN4T** and **isoDN4T** based BC TFTs at  $T_s$  of 100 °C are displayed. The same considerations reported above for TC devices apply here. The high reproducibility and reliability of the devices is confirmed by negligible hysteresis, low  $V_{th}$ , similar mobility values extracted in linear and saturation regime and low standard deviation (SD) of mobility values obtained from devices fabricated on the same substrate (maximum value of SD in **DN4T** based TFTs is  $0.22 \text{ cm}^2\text{V}^{-1}\text{s}^{-1}$  with averaged mobility of  $1.9 \text{ cm}^2\text{V}^{-1}\text{s}^{-1}$ , while maximum value of SD in **isoDN4T** based TFTs is  $0.00024 \text{ cm}^2\text{V}^{-1}\text{s}^{-1}$  with averaged mobility of  $0.0032 \text{ cm}^2\text{V}^{-1}\text{s}^{-1}$ ).

All the values of  $\mu$ ,  $V_{th}$  and  $I_{ON/OFF}$  for linear and saturation regime are reported in the **Appendix (Table A1.1)**.



**Figure 2.15: Transfer and output characteristics of DN4T and isoDN4T bottom-contact devices.**

On the top: representative transfer (on the top) and output (on the bottom) characteristics of BC TFTs based on (a),(c) **DN4T** and (b),(d) **isoDN4T** at substrate temperature of 100 °C. In transfer characteristics, solid lines are referred to drain current and dot lines are referred to mobility. TFTs have  $W/L = 480/215 \mu m$ .

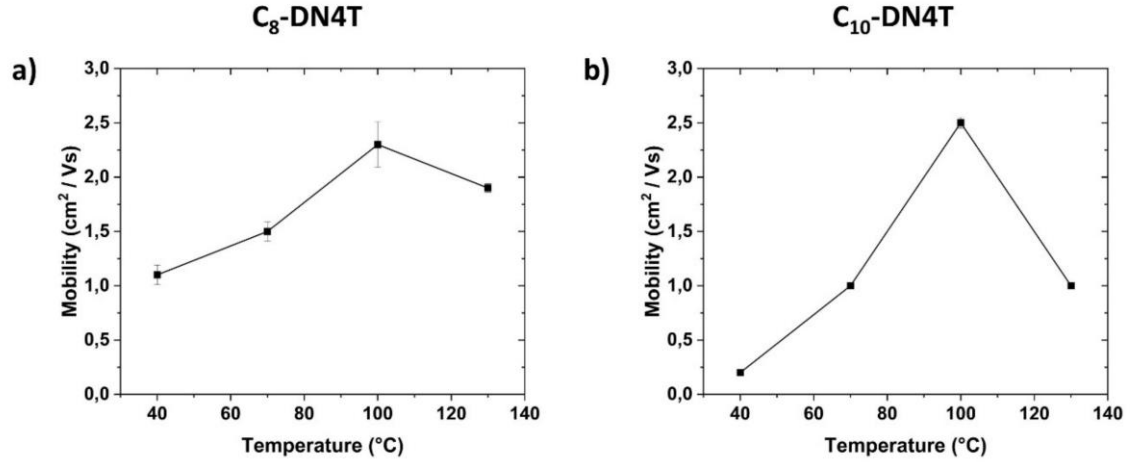
### 2.5.2 Thin film transistors based on **C<sub>8</sub>-DN4T** and **C<sub>10</sub>-DN4T**

To access charge transport properties of alkylated DN4T derivatives, polycrystalline BC and TC TFTs based on octyl- (**C<sub>8</sub>-DN4T**) and decyl-substituted (**C<sub>10</sub>-DN4T**) derivatives were fabricated. As previously shown for **DN4T** and **isoDN4T** based devices, BC TFTs show better performances in terms of lower threshold voltage along with similar mobility and on/off current ratio compared to the TC counterparts. Therefore, in the following section, only BC devices are reported in order to draw the attention to the electrical properties of **C<sub>8</sub>-** and **C<sub>10</sub>-DN4T** rather than to device geometry. All

the data extracted from TC devices are presented in the **Appendix (Figure A1.1 and Table A1.2)**. In this case, the substrates were held at temperature of 40, 70, 100 and 130 °C during the OSCs deposition. Considering the results obtained for **DN4T** and **isoDN4T** devices along with already reported TFTs based on other classes of thienoacenes obtained through vacuum deposition<sup>[131,148]</sup>, 30 °C steps can be sufficient to find the optimal range of substrate temperature which gives the best electrical performances.

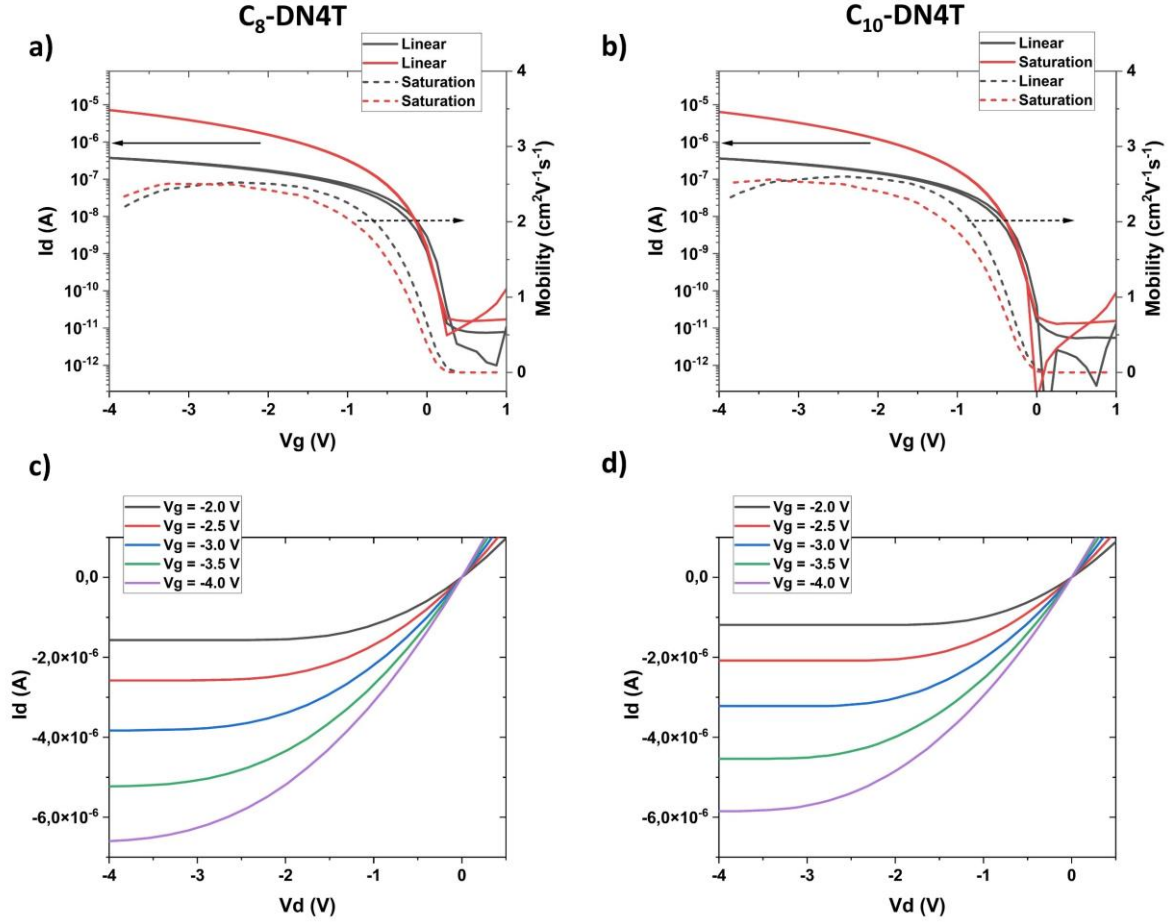
Comparing the substrate temperature dependent mobilities for **C<sub>8</sub>-DN4T** and **C<sub>10</sub>-DN4T** based devices, we observed a similar trend that was already exhibited by **DN4T** and **isoDN4T** devices. In case of **C<sub>8</sub>-DN4T** based TFTs, mobility increases more than 2 times upon increasing  $T_s$  from 40 to 100 °C with values of 1.1 and 2.3 cm<sup>2</sup>V<sup>-1</sup>s<sup>-1</sup> respectively, and eventually decreases to 1.9 cm<sup>2</sup>V<sup>-1</sup>s<sup>-1</sup> at  $T_s$  of 130 °C. In case of **C<sub>10</sub>-DN4T** based TFT, a stronger effect on  $\mu$  was noticed. Mobility increases more than 12 times upon increasing  $T_s$  from 40 to 100 °C with values of 0.2 and 2.5 cm<sup>2</sup>V<sup>-1</sup>s<sup>-1</sup> respectively, and eventually decreases to 1.0 cm<sup>2</sup>V<sup>-1</sup>s<sup>-1</sup> at  $T_s$  of 130 °C (**Figure 2.16**).

Considering the 3D crystalline growth of **C<sub>8</sub>-** and **C<sub>10</sub>-DN4T** thin films observed by AFM (**Figure 2.6**), we cannot derive relations between charge carrier mobility and thin-films morphology. The films do not show any significant difference which may be related to charge carrier mobility enhancement. The reason behind the increase of mobility upon substrate heating is linked to crystallinity and morphology of the first deposited layers onto the dielectric, which are not reflected in the crystal growth of the upper layers. Unfortunately, the diffuse presence of individual grains in the 100-nm height range severely limits the AFM imaging to the surface morphology of the grains with poor information about the underneath layers. Threshold voltage and on/off current ratio were not significantly affected by  $T_s$  (**Figure A1.2, in the Appendix**). **C<sub>8</sub>-DN4T** based devices shows  $V_{th}$  between -0.2 and -0.4 V, along with  $I_{ON/OFF}$  of  $\approx 8 \times 10^4 / 2 \times 10^5$ , while **C<sub>10</sub>-DN4T** based devices shows  $V_{th}$  between -0.3 and -0.6 V, along with  $I_{ON/OFF}$  of  $\approx 1 \times 10^4 / 4 \times 10^5$ .



**Figure 2.16: Mobility vs substrate temperature for C<sub>8</sub>-DN4T and C<sub>10</sub>-DN4T.** Mobility as a function of the substrate temperature in (a) C<sub>8</sub>-DN4T and (b) C<sub>10</sub>-DN4T based BC TFTs. The values are referred to the linear regime and to devices with W/L = 480/215  $\mu\text{m}$

Transfer and output curves (**Figure 2.17**) further confirm the ideal behaviour of the devices due to the absence of hysteresis and a constant mobility over the applied gate voltage range, (both in linear and saturation regime). The high reproducibility is corroborated by the low mobility values variation within TFTs fabricated on one substrate. The highest value of SD in C<sub>8</sub>-DN4T based TFTs is 0.21  $\text{cm}^2\text{V}^{-1}\text{s}^{-1}$  over an averaged mobility of 2.3  $\text{cm}^2\text{V}^{-1}\text{s}^{-1}$ , while the highest value of SD in C<sub>10</sub>-DN4T based TFTs is 0.05  $\text{cm}^2\text{V}^{-1}\text{s}^{-1}$  over an averaged mobility of 2.5  $\text{cm}^2\text{V}^{-1}\text{s}^{-1}$  for C<sub>10</sub>-DN4T, respectively. All the values of  $\mu$ ,  $V_{\text{th}}$  and  $I_{\text{ON/OFF}}$  both in linear and saturation regime at different  $T_s$  are reported in the **Appendix (Table A1.2)**.



**Figure 2.17: Transfer and output characteristics of  $C_8$ -DN4T and  $C_{10}$ -DN4T bottom-contact devices.**

On the top: representative transfer (on the top) and output (on the bottom) characteristics of BC TFTs based on (a),(c)  $C_8$ -DN4T and (b),(d)  $C_{10}$ -DN4T at substrate temperature of 100 °C. In transfer characteristics, solid lines are referred to drain current and dot lines are referred to mobility. TFTs have  $W/L = 480/215 \mu\text{m}$ .

## 2.5.3 Thin film transistors based on *tert*-butyl thienoacene derivatives

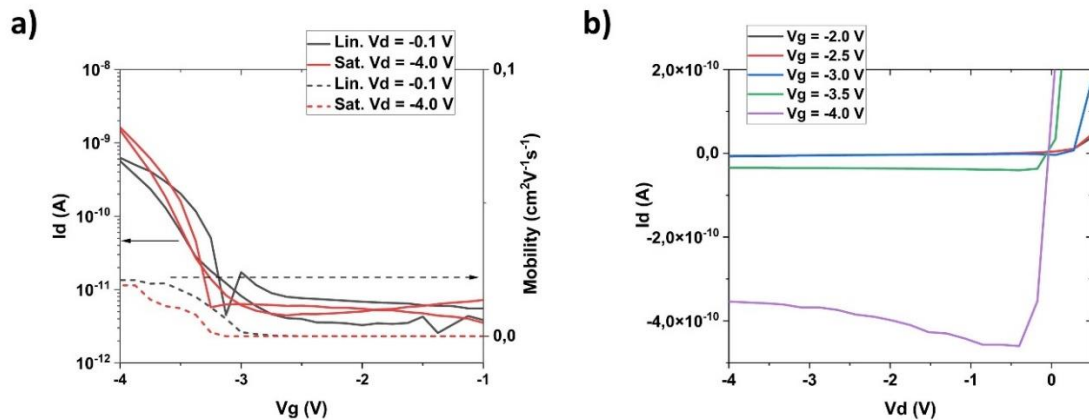
### 2.5.3.1 Thin-film transistors based on tBu-BTBT

The reported charge transport properties of **tBu-BTBT** were obtained from thin-film transistors fabricated through solution shearing processing or from single crystal devices.<sup>[133,134]</sup> The reported devices were fabricated with a TC geometry, with contacts made through the deposition of a thin layer of  $\text{MoO}_3$  (7-8 nm) and silver or gold (35-40 nm). The insertion of  $\text{MoO}_3$  layer between the OSC and the metal contacts is known to alleviate large injection barriers, by increasing the contact work function.<sup>[133,149]</sup> Nevertheless the reported device highlight a non-ideal behaviour. To have a fair comparison between

**tBu-BTBT** and the new *tert*-butyl-substituted thienoacene derivatives with extended  $\pi$ -core reported in this work, BC and TC TFTs based on **tBu-BTBT** were fabricated, by varying  $T_s$  from 40 °C to 130 °C with 30 °C steps.

In this case, 40-nm-thick OSC films were deposited, since the deposition of 25 nm of **tBu-BTBT** resulted in discontinuous films with dewetted areas along the TFTs active channel (see optical micrographs in the **Appendix, Figure A1.5**). This incomplete coverage resulted in no field effect response both in case of TC and BC devices at all substrate temperature. In contrast, 40-nm-thick OSC film results in a sufficient coverage of the active channel at all substrate temperature.

No field effect response was observed in TC devices at all substrate temperature as well as for BC devices with  $T_s$  of 70,100 and 130 °C. Drain current modulation upon the application of a gate bias was recorded for BC TFTs with  $T_s$  of 40 °C, allowing the collection of transfer and output characteristics (**Figure 2.18**).



**Figure 2.18: Representative transfer and output characteristics of BC TFT based on tBu-BTBT.**

(a) Transfer and (b) output characteristics. In transfer characteristics, solid lines and dashed lines are referred to drain current and mobility respectively. All TFTs have  $W/L = 480/215 \mu\text{m}$ .

At first sight, it is evident that **tBu-BTBT** exhibits poor performances highlighted by moderate hysteresis, high threshold voltage (-3.1 V) and low on/off current ratio ( $\approx 2 \times 10^2$ ). At last, the extracted mobility gives values up to  $0.027 \text{ cm}^2\text{V}^{-1}\text{s}^{-1}$  in linear regime. As already mentioned, the deep ionization energy of **tBu-BTBT** (5.7 eV) strongly affects the electrical performances in

TFTs, due to inefficient charge carrier injection which in turn is reflected in high  $V_{th}$ .

It is worth noting that TC devices were fabricated using the same process used for BC devices (except for the contacts fabrication). Therefore, the thin film across the active channel exhibits a similar morphology at given substrate temperature. Nonetheless, TC devices deposited at  $T_s$  of 40 °C did not show field-effect response, in spite of BC devices deposited at  $T_s$  of 40 °C. The reason behind this different device response may be linked to the film thickness and the ionization energy of **tBu-BTBT**. 40-nm-thick films may result in large contact resistance in TC devices, due to the poor charge transport properties of small-molecule OSCs along the film thickness. Moreover, in BC devices the gold electrodes are functionalized with a PFBT-SAM which increases the work function of gold contacts from 4.7 eV to 5.2 eV (see **Chapter 3**) reducing the height of the nominal charge-injection barrier.

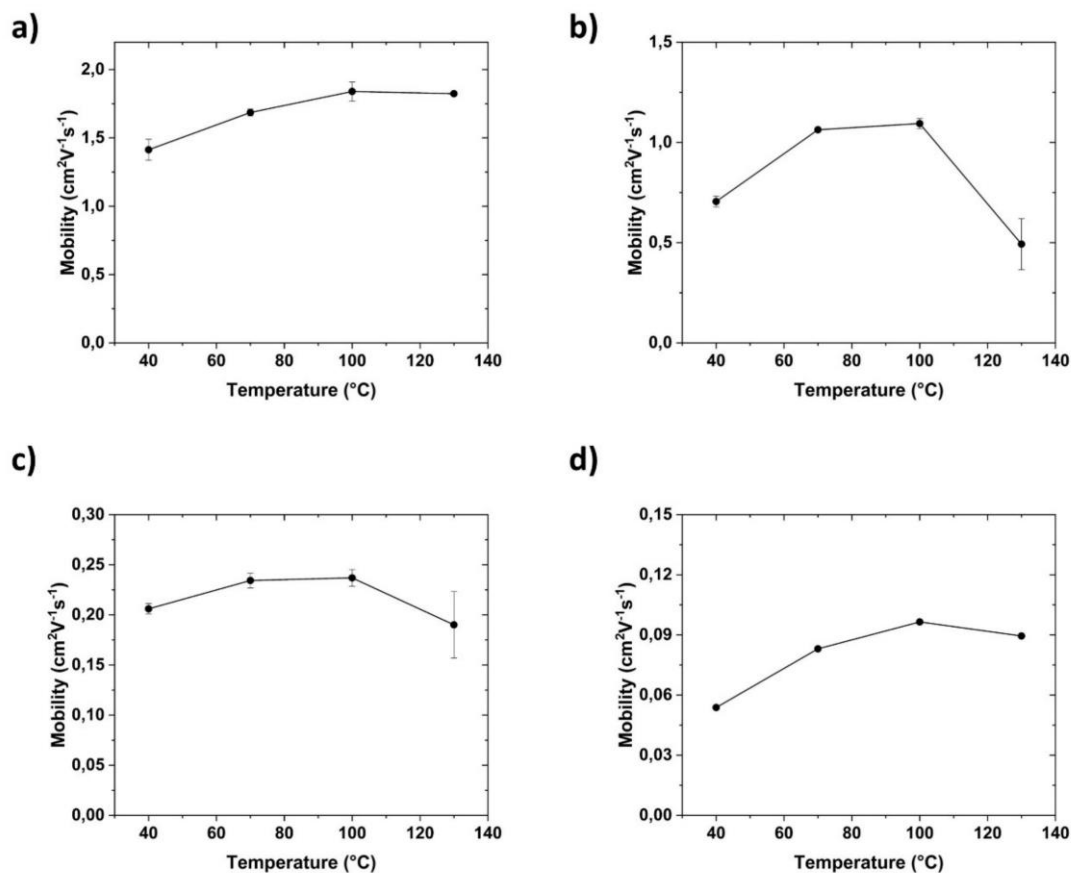
#### 2.5.3.2 Thin-film transistors based on *tert*-butyl thienoacene derivatives with extended $\pi$ -system

As in the case of TFTs based on alkylated DN4Ts, in this section only TFTs with a BC geometry are reported, while the electrical performances of TFTs with a TC geometry are shown in the **Appendix (Figure A1.3 and Tables A1.3, A1.4, A2.5 and A1.6)**. In addition, even in this case, the substrate temperature was varied between 40 °C and 130 °C, with 30 °C steps.

The substrate temperature dependent electrical performances in terms of charge carrier mobility, threshold voltage and on/off current ratio were evaluated. Here again as in the case of TFTs based on **DN4T**, **isoDN4T** and alkylated DN4Ts, the substrate temperature shows to have a major role in the enhancement of charge carrier mobility, while its effect of  $V_{th}$  and  $I_{ON/OFF}$  can be considered negligible (**Figure A1.4**, in the **Appendix**). For all the compounds, charge carrier mobility improved by increasing the substrate temperature from 40 °C to 100 °C and consequently decreased for  $T_s$  of 130 °C (see **Figure 2.19**).

Specifically, considering devices with  $T_s$  of 100 °C, **tBu-DNTT** exhibits the highest charge carrier mobility, with values exceeding  $1.9 \text{ cm}^2\text{V}^{-1}\text{s}^{-1}$ , followed by **tBu-DBTTT**, with  $\mu$  up to  $1.1 \text{ cm}^2\text{V}^{-1}\text{s}^{-1}$ , **tBu-BTBT-1**, with  $\mu$  up to  $0.25 \text{ cm}^2\text{V}^{-1}\text{s}^{-1}$  and **tBu-BTBT-2** with  $\mu$  up to  $0.10 \text{ cm}^2\text{V}^{-1}\text{s}^{-1}$ . Also in this case, the augmented charge transport mobility obtained through the optimization of the substrate temperature is reflected in the thin-films topography investigated by AFM, which highlights the presence of bigger grain size for samples with  $T_s$  of 100 °C. As shown for TFTs based on **DN4T**, **isoDN4T** and

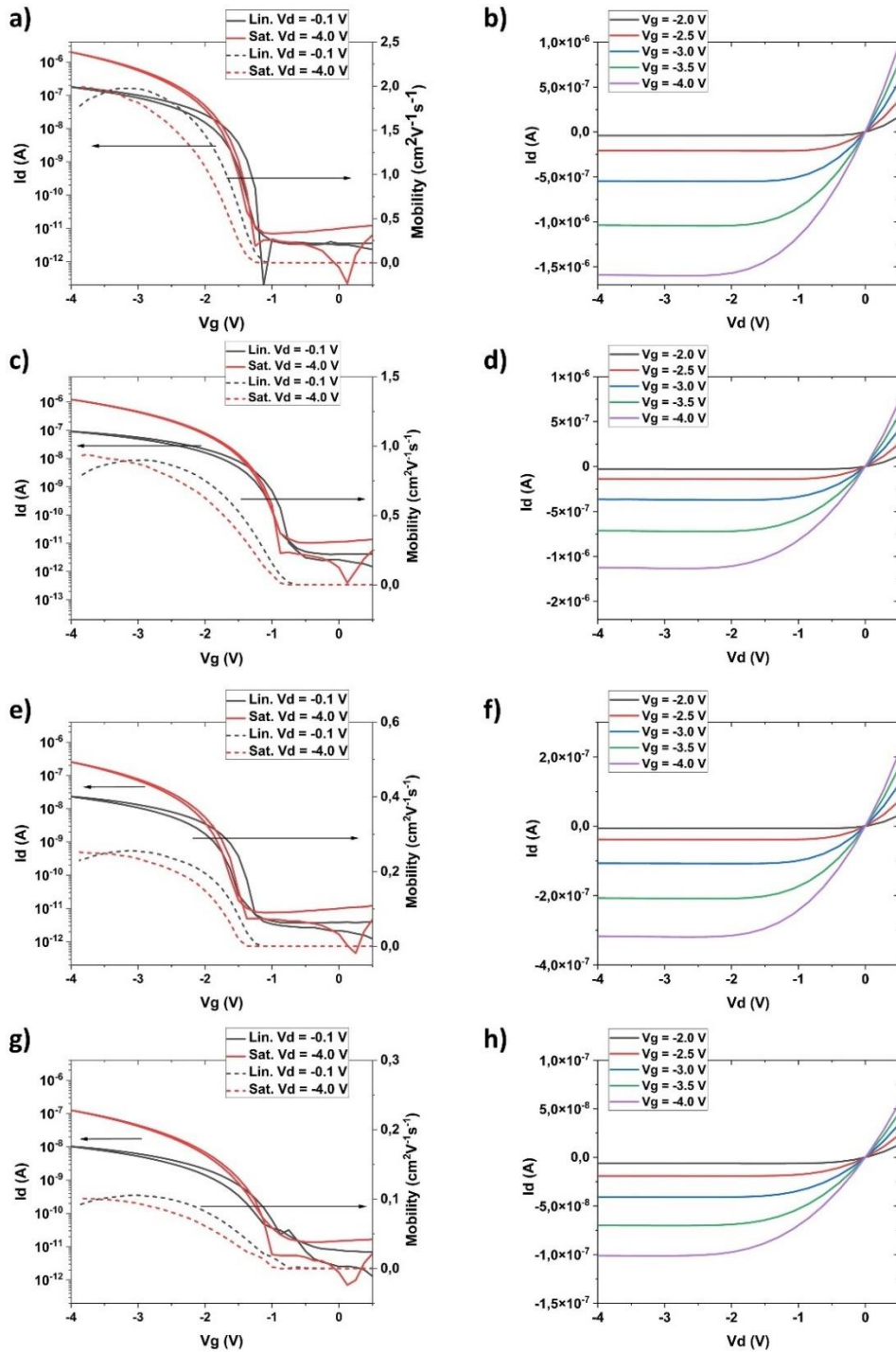
alkylated DN4Ts, also for *tert*-butyl thienoacene derivatives the highest mobilities were achieved at  $T_s$  of 100 °C, confirming this temperature as the most optimal for thienoacenes-based devices examined in this work.



**Figure 2.19: Charge carrier mobility as a function of the substrate temperature for TC TFTs based on *tert*-butyl thienoacene derivatives. (a) tBu-DNTT, (b) tBu-DBTTT, (c) tBu-BTBT-1 and (d) tBu-BTBT-2.**

All the compounds exhibit moderate  $V_{th}$ , with values of about -1.7 V for **tBu-DNTT**, between -1.3 and -1.4 V for **tBu-DBTTT**, between -1.7 and -1.9 for **tBu-BTBT-1** and between -1.4 and -1.7 V for **tBu-BTBT-2**. Similarly, all the TFTs exhibit  $I_{ON/OFF}$  between  $\approx 1 \times 10^4$  and  $\approx 7 \times 10^4$  (**Figure A2.4**). In **Figure 2.20**, representative transfer and output characteristics of the best performing devices based on the *tert*-butyl thienoacene derivatives are displayed. All the TFTs show negligible hysteresis, constant mobility over the applied  $V_g$  in transfer characteristics and linearity of the output curves for  $V_d$  close to 0 V, which suggest low contact resistance. The low device-to-device

variation is supported by the small values difference of extracted mobility and threshold voltage for TFTs fabricated with the same compound at given  $T_s$ .



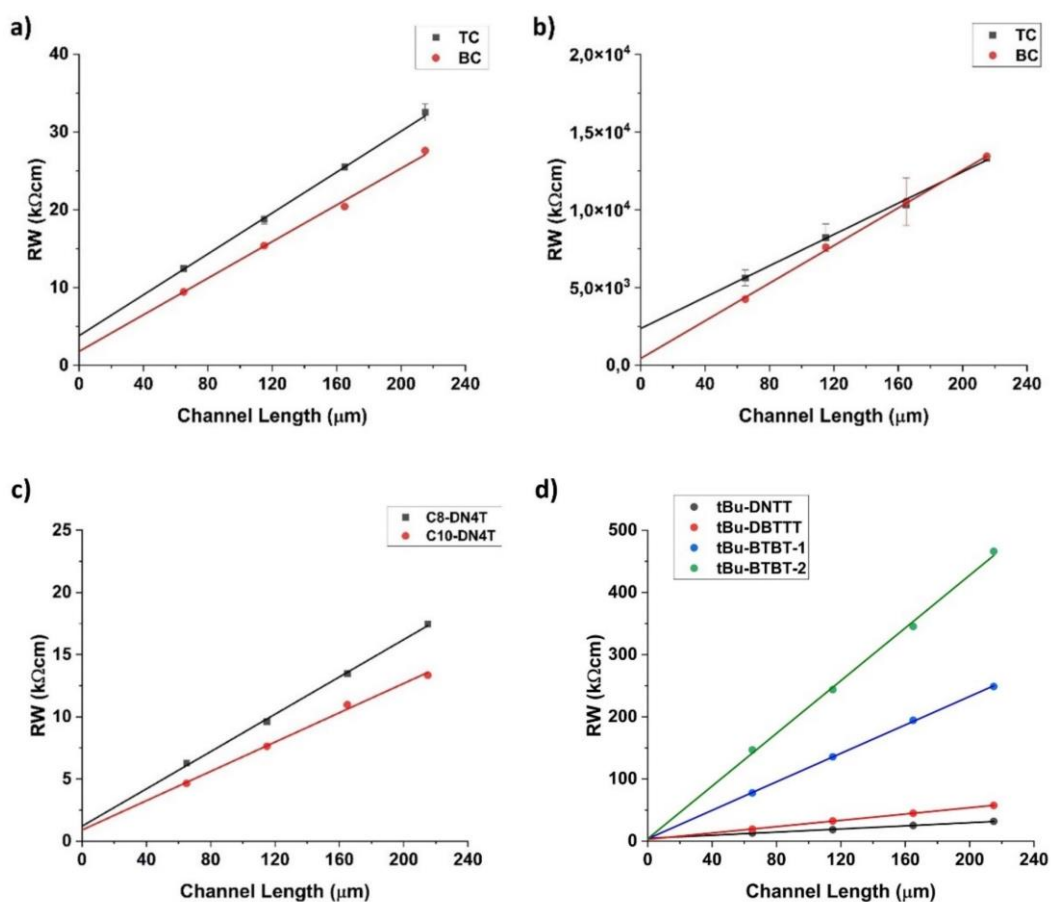
**Figure 2.20: Transfer (left) and output (right) characteristics of the best performing BC TFTs based on tert-butyl-substituted thienoacene derivatives.**

(a, b) **tBu-DNTT**, (c, d) **tBu-DBTTT**, (e, f) **tBu-BTBT-1** and (g, h) **tBu-BTBT-2**. In transfer characteristics, solid lines and dashed lines are referred to drain current and mobility respectively. All TFTs have  $W/L = 480/215 \mu\text{m}$ .

## 2.5.4 Contact resistance evaluation

The channel-width-normalized contact resistance ( $R_CW$ ) was calculated with the transmission line method (TLM) by using TFTs with channel length of 65, 115, 165 and 215  $\mu\text{m}$  (channel width of 480  $\mu\text{m}$ ) fabricated at  $T_s$  of 100  $^\circ\text{C}$  and for gate overdrive voltage of -2.0 V (**Figure 2.21**). Measurements were conducted in linear regime ( $V_d = -0.1$  V) to ensure a homogeneous charge carrier distribution in the channel.

TFTs with a BC geometry exhibit  $R_CW$  between 1.0 and 4.4  $\text{k}\Omega\text{cm}$ , except for **isoDN4T** that shows  $R_CW$  of 445  $\text{k}\Omega\text{cm}$  (see **Table 2.4**). Particularly, the lowest  $R_CW$  is shown by the alkylated DN4Ts, with values of 1.0  $\text{k}\Omega\text{cm}$  and 1.2  $\text{k}\Omega\text{cm}$  for **C<sub>10</sub>-DN4T** and **C<sub>8</sub>-DN4T** respectively.



**Figure 2.21: Transmission line method applied to TFTs.**

Linear fits to the width-normalized total resistance (RW) as a function of the channel length (L) for TC and BC devices of (a) **DN4T** and (b) **isoDN4T**, BC devices of (c) alkylated DN4Ts and (d) tert-butyl substituted thienoacenes. The fits are referred to gate-overdrive voltage of -2.0 V. TFTs with channel length of 65, 115, 165 and 215  $\mu\text{m}$  are fabricated on the same substrate hold at 100  $^\circ\text{C}$  during the OSCs deposition.

Notably the alkylated DN4Ts exhibit the highest charge carrier mobility, while **isoDN4T** exhibits the lowest charge carrier mobility along with the largest contact resistance among the investigated OSCs. Contact resistance in BC devices can be split in two components, the injection at the metal/OSC interface and the charge transport through the depleted region formed at the metal/OSC interface.<sup>[150–152]</sup> Considering that the injection barrier is similar for the **isoDN4T** and alkylated DN4Ts due to a comparable HOMO energy ( $\approx 5.2$  eV and  $\approx 5.0$  eV respectively),  $\mu$  plays a crucial role in determining the contact resistance. The resistance associated to the depleted region is proportional to  $1/\mu$ ,<sup>[86]</sup> resulting in more facile charge injection into to accumulation channel for high mobility OSCs.

It is worth noting that in case of **DN4T** and **isoDN4T**, TFTs exhibit  $R_cW$  variation depending on the device geometry. **DN4T** TFTs shows  $R_cW$  of 3.8 and 1.8  $k\Omega\text{cm}$  for TC and BC devices respectively, while **isoDN4T** TFTs shows  $R_cW$  of 2373 and 351  $k\Omega\text{cm}$  for TC and BC devices (**Figure 2.21**). These experimental results agree with already reported experimental observations and device simulations, which evidence that BC organic thin-film transistors can show lower contact resistance compared to TC organic TFTs, if conditions are met. It has been shown that BC TFTs fabricated with a small organic molecule have lower contact resistance than a TC TFTs if the dielectric is sufficiently thin ( $< 30$  nm) and if the energy barrier at contact-semiconductor interface is minimized (by treating the drain/source contacts with PFBT in case of BC devices).<sup>[85]</sup>

An extensive study of the role of mobility and molecular structure of thienoacenes organic semiconductors on the contact resistance in TFTs is presented in **Chapter 3**.

**Table 2.4: Width-normalized contact resistance extracted from TC and BC TFTs.**

$R_cW$  is obtained by TLM at gate-overdrive voltage of -2.0 V.

Compound	Geometry	$R_cW$ ( $k\Omega\text{cm}$ )
<b>DN4T</b>	BC	$1.8 \pm 0.4$
	TC	$3.8 \pm 0.3$
<b>isoDN4T</b>	BC	$351 \pm 103$
	TC	$2373 \pm 217$
<b>C<sub>8</sub>-DN4T</b>	BC	$1.2 \pm 0.1$
<b>C<sub>10</sub>-DN4T</b>	BC	$1.0 \pm 0.2$
<b>tBu-DNTT</b>	BC	$4.4 \pm 0.7$
<b>tBu-DBTTT</b>	BC	$2.9 \pm 0.3$
<b>tBu-BTBT-1</b>	BC	$3.8 \pm 0.2$
<b>tBu-BTBT-1</b>	BC	$3.8 \pm 0.4$

## 2.6 Discussion

The discussion of this chapter is divided in four parts: the first part is focused on the quantum chemical calculations of transfer integrals and reorganization energies of the investigated compounds, except for the alkylated DN4Ts due to the lack of their crystal structures. The second part concerns the electrical properties of **DN4T** and **isoDN4T** and their comparison with the already reported materials. The third part refers to the effect of the functionalization of the **DN4T** molecular core with alkyl chains (**C<sub>8</sub>-DN4T** and **C<sub>10</sub>-DN4T**). At last, the fourth part is focused on the effect of the  $\pi$ -system extension in *tert*-butyl derivatives.

### 2.6.1 Transfer integrals and reorganization energies

*Quantum chemical calculations of transfer integrals and reorganization energies were provided by Dr. Vincent Lamaur and Marco Bardini (both Université de Mons). Internal reorganization energies were evaluated at the Density Functional Theory (DFT) level using the B3LYP functional and a 6-31G\*\* basis set with the Gaussian16 package.<sup>[153]</sup> HOMO transfer integrals were computationally estimated in a fragment approach at the DFT level (B3LYP/DZ) with the Amsterdam Density Functional (ADF) package.<sup>[154,155]</sup>*

The reorganization energy ( $\lambda$ ) reflects the geometric changes of the molecules involved in the charge transport upon charge transfer.<sup>[156]</sup> The reorganization energies of the investigated compounds were found to be in the range of 143-309 meV (**Table 2.5**), in line with already reported thienoacenes.<sup>[52]</sup>

**DN4T**, **tBu-DNTT** and **tBu-DBTTT** unveil the lowest reorganization energy of 152, 143 and 145 meV, respectively, along with the highest mobility in TFTs (2.0, 1.9 and 1.0 cm<sup>2</sup>V<sup>-1</sup>s<sup>-1</sup>, respectively). These values are almost the half compared to *tert*-butyl-thienyl derivatives of BTBT, which exhibit  $\lambda$  of 308 meV for **tBu-BTBT-1** and 263 meV for **tBu-BTBT-2**. Larger reorganization energy should disfavour hole transport considering a pure hopping regime. This is the case of the *tert*-butyl-thienyl derivatives of BTBT, which exhibit charge carrier mobilities of 0.25 cm<sup>2</sup> V<sup>-1</sup> s<sup>-1</sup> and 0.10 cm<sup>2</sup> V<sup>-1</sup> s<sup>-1</sup> for **tBu-BTBT-1** and **tBu-BTBT-2**, respectively, that are 1 order of magnitude lower compared to **tBu-DNTT** and **tBu-DBTTT**. It is worth noting that in the case of *tert*-butyl-substituted derivatives, **tBu-DNTT** and **tBu-DBTTT** show lower reorganization energy compared to thienyl substituted BTBTs. This suggests that annealed  $\pi$ -systems tend to have lower  $\lambda$  compared to oligomeric  $\pi$ -systems. The latter is characterised by single bonds connecting aromatic rings, which results in more molecular motions

comprising rotation around the single bonds. On the contrary, stiffer molecular structure would result in lower molecular geometric variation upon charge transfer.<sup>[124]</sup>

**Table 2.5: Reorganization energy ( $\lambda$ ), transfer integrals ( $J_T$ ) and charge carrier mobility ( $\mu$ ) of the investigated compounds.**

$\mu$  is referred to BC TFTs.

Compound	$\lambda$ (meV)	$J_T$ (meV)	$\mu$ (cm <sup>2</sup> V <sup>-1</sup> s <sup>-1</sup> )
<b>DN4T</b>	152	61, 99, 33	2.0
<b>isoDN4T</b>	213	17, 33, 33	$3.3 \times 10^{-3}$
<b>tBu-DNTT</b>	143	63, 26, 26	1.9
<b>tBu-DBTTT</b>	145	52, 30, 57	1.0
<b>tBu-BTBT-1</b>	309	19, 20, 20	0.25
<b>tBu-BTBT-1</b>	263	8, 26, 26	0.10

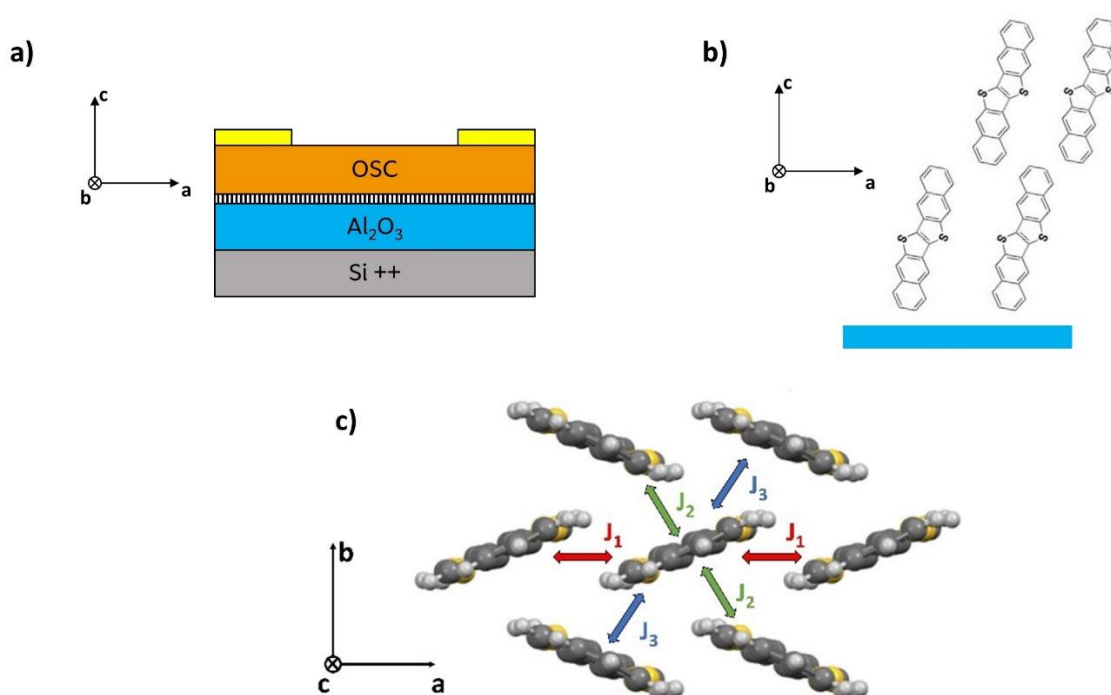
At last, **isoDN4T** exhibits  $\lambda$  of 213 meV, that is larger than the one of **DN4T** and smaller than those of *tert*-butyl-thienyl derivatives of BTBT. Nevertheless, **isoDN4T** reveals mobility 3 orders of magnitude lower compared to **DN4T** and 2 orders of magnitude lower compared to *tert*-butyl-thienyl derivatives of BTBT. This aspect is discussed later (**Paragraph 2.6.2.2**).

In TFTs the molecules tend to crystallize by orienting the longest molecular axis of the  $\pi$ -system parallel to the dielectric surface. With this orientation the charge transport takes place within the *ab* plane, named herringbone layer plane if the OSC adopt a HB packing motif (see **Figure 2.22**). The reported transfer integrals values are referred to HOMO wavefunctions overlap between adjacent molecules along the *ab* plane, as depicted in **Figure 22-c**. Severe anisotropy of the electronic interaction along the *ab* plane together with poor overlap of the HOMO wavefunctions generally limit the charge transport leading to lower charge carrier mobility.

The HOMO transfer integrals were found to be in the range of 10<sup>1</sup>-10<sup>2</sup> meV (**Table 2.5**) in agreement with the class of thienoacenes.<sup>[52]</sup> Particularly, **DN4T**, **tBu-DNTT** and **tBu-DBTTT** exhibit the largest transfer integrals, with values of (61,99,33) meV, (63,26,26) meV and (52,30,57) meV, respectively.

The computed transfer integrals reflect a moderate anisotropy of electronic interactions within adjacent molecules, with a variance percentage between

47% and 57%. The other compounds show smaller transfer integrals with values between 8 and 33 meV, with variance percentage of 48% for **isoDN4T** and 69% for **tBu-BTBT-2**. Only **tBu-BTBT-1** reveals an almost perfect isotropy of electronic interactions, giving a variance percentage of 5% of the computed transfer integrals. Notably, the highest charge carrier mobilities extracted in TFTs, are exhibited by that compounds which show the lowest reorganization energies together with large values of transfer integrals. These results confirm that an extended HOMO wavefunctions overlap, along with small molecular geometry variation upon charge transfer, are necessary to boost charge carrier mobility in OSCs.<sup>[52]</sup>



**Figure 2.22: Molecular arrangement with respect to  $a$ ,  $b$  and  $c$  directions.** a) schematic illustration of a TFT with the active layer along the  $ab$  plane. (b) Example of the molecular arrangement of DNTT onto the dielectric (in light blue), with the molecules standing approximately upright with respect to the substrate. (c) Schematic illustration of transfer integrals within adjacent molecules along the  $ab$  plane.

## 2.6.2 DN4T and isoDN4T vs DNTT, isoDNTT and L-DBTTA

In order to define structure-properties relationships for **DN4T** and **isoDN4T**, their crystalline packing and electronic parameters, were compared to those of **DNTT**, **isoDNTT** and **L-DBTTA**. These values, taken both from the literature and from the present work, are reported in **Table 2.6**.

**Table 2.6: Crystalline packing, ionization energy (IE), and mobility ( $\mu$ ) of DN4T, isoDN4T, DNTT, isoDNTT and L-DBTTA.**

(\*) = Measurements performed in this work

HB = herringbone, S-HB = sandwich herringbone

Compound	Packing	IE (eV)	$\mu$ (cm <sup>2</sup> V <sup>-1</sup> s <sup>-1</sup> )	Ref.
<b>DN4T</b>	HB	5.27 (*)	2.0 (*)	[130]
<b>isoDN4T</b>	HB	5.23 (*)	$3.3 \times 10^{-3}$ (*)	[130]
<b>DNTT</b>	HB	5.42(*)	2.3 (*)	[28,157,158]
<b>isoDNTT</b>	S-HB	5.58	( $10^{-3}$ - $10^{-2}$ )	[157]
<b>L-DBTTA</b>	Stacked	5.16	0.15	[129,130]

### 2.6.2.1 Packing motif

**DN4T** and **isoDN4T** show the same herringbone packing motif as **DNTT** and **isoDNTT** (sandwich herringbone for the latter). On the contrary, by comparing **DN4T** and **isoDN4T** with **L-DBTTA**, we observe that the introduction of an additional external naphthalene ring to the same central core leads to a herringbone motif packing, instead of a stacked arrangement. In herringbone arrangement, charge transport is facilitated by edge-to-face interactions leading to efficient charge transport. Among the most encountered packing motif in organic semiconductor crystals, herringbone packing has shown to give rise to high mobility, along with brick-wall packing, if compared to slipped  $\pi$ -stacking and slipped-stack packing motifs.

### 2.6.2.2 Mobility of DN4T and isoDN4T

*The electronic structures were calculated by Marco Bardini (Université de Mons) using density functional theory (DFT) to optimize geometries in gas phase at the B3LYP 6-311G\* level.*

Notably, **isoDN4T** TFTs show mobility 3 orders of magnitude lower compared to **DN4T** TFTs. This big difference may be related to different interactions within the molecules in the crystalline arrangement. If we consider the short contacts within neighbouring molecules (which are defined as any intermolecular contact shorter than the sum of the van der Waals radii of the involved atoms), **DN4T** is characterized by C-H $\cdots\pi$ , S $\cdots$ C and S $\cdots$ S interactions. On the contrary, **isoDN4T** exhibits only C-H $\cdots\pi$  interactions, as displayed in **Figure 2.23**, reflecting a larger distance between the sulphur atoms of adjacent molecules if compared to **DN4T**. This would result in less efficient charge transfer within neighbouring molecules. In addition, as

already mentioned, sulphur atoms have higher electron density compared to carbon and hydrogen atoms. The larger electron densities on the sulphur atoms in the HOMO (i.e., larger HOMO coefficient on the sulphur atoms), increases the effective overlap of the HOMOs of neighbouring molecules. In contrast, nodal planes or small HOMO coefficients on the sulphur atoms would reduce intermolecular orbitals overlap, which would reduce the efficiency of charge transport.<sup>[27]</sup>

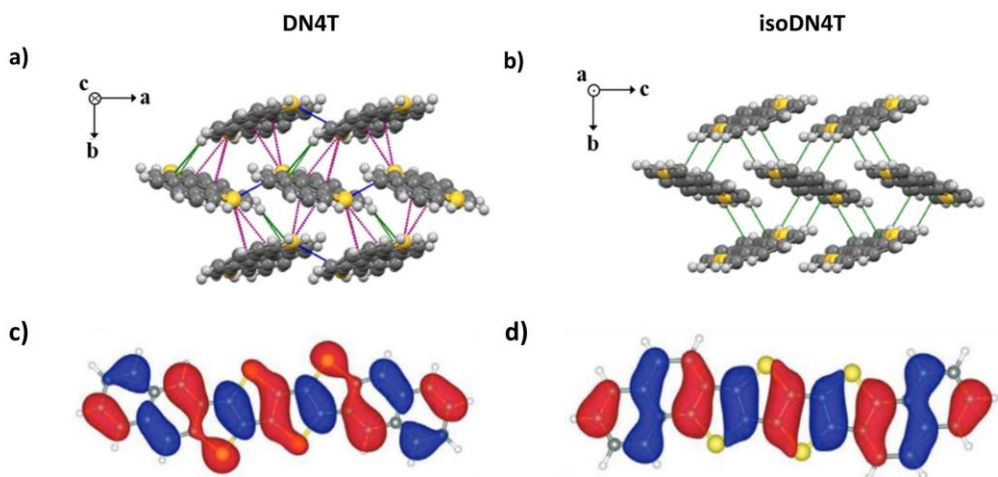
This is confirmed by the calculation of the coefficients of the HOMO orbitals of the two isomers, highlighting a larger electron density on the sulphur atoms of **DN4T** (**Figure 2.23**) compared to **isoDN4T**. Likewise, **DNTT** and **L-DBTTA** exhibit larger HOMO coefficients on the sulphur atoms compared to **isoDNTT**.<sup>[130,157]</sup>

Notably, the same decrease of  $\approx 2$ -3 orders of magnitude has been observed in **DNTT** and **isoDNTT**,<sup>[157]</sup> suggesting the smaller coefficients of HOMO on the sulphur atoms as one of the main reasons of lower mobility in **isoDN4T** and **isoDNTT**. In case of **L-DBTTA**, the lower mobility ( $0.15 \text{ cm}^2 \text{ V}^{-1} \text{ s}^{-1}$ ) compared to **DN4T** and **DNTT** has been attributed to the stacked packing motif which results in 1D transfer integrals distribution, detrimental to charge transport.<sup>[130]</sup>

The dynamic disorder in the OSC layer (i.e., electron-phonon coupling) plays a central role in charge transport. Thus, the low mobility of **isoDN4T** may be related also to a detrimental influence of the coupling of crystal vibrational modes with charge motion. This would also help to explain the lower mobility of **isoDN4T** compared to **tBu-BTBT-1** and **tBU-BTBT-2**. The latter show small transfer integrals and large reorganization energy, as **isoDN4T**. Nonetheless, the *tert*-butyl-thienyl derivatives exhibit carrier mobility of 2 orders of magnitude higher than **isoDN4T**. The morphological characterization of the thin films unveiled no substantial difference to justify this large mobility difference between the compounds. In the case of **tBu-BTBT-1** the higher mobility can be linked to the isotropic transfer integrals. It has been shown that OSCs with balanced transfer integrals in the different crystalline directions are more resilient to dynamic disorder.<sup>[58]</sup> In the case of **tBu-BTBT-2** and in order to deeply understand the reason behind the low mobility of **isoDN4T**, an experimental and computational study of the electron phonon-coupling of the investigated compounds would be required.

In summary, the annealing of terminal naphthene moieties (**DN4T** and **isoDN4T**) instead of benzene moieties to the same central motif of four thienyl rings enables a favourable HB packing which promotes balanced 2D electronic interactions within adjacent molecules. This is reflected in higher mobility in **DN4T**, while in **isoDN4T** is characterized by lower mobility

attributed to the lower electronic density of the HOMO. On the other hand, the two additional thienyl rings in the central motif of **DN4T** compared to **DNTT**, do not lead to significant variation of crystal packing motif, transfer integrals distribution and electronic density of the HOMO, resulting in similar charge carrier mobility of  $\approx 2 \text{ cm}^2 \text{ V}^{-1} \text{ s}^{-1}$ .



**Figure 2.23: Short contacts between adjacent molecules in the crystalline arrangement and calculated HOMO of DN4T and isoDN4T.**

Short contacts in (a) **DN4T** and (b) **isoDN4T** crystalline structures are displayed as distances less or equal to the sum of van der Waals radii ( $\text{S} \cdots \text{S}$  in blue,  $\text{C} \cdots \text{S}$  in purple,  $\text{C-H} \cdots \pi$  in green). Shape of the HOMO orbital of (c) **DN4T** and (d) **isoDN4T**.

### 2.6.2.3 Charge carrier injection

**DN4T** and **isoDN4T** show IE values in line with the class of thienoacenes ( $4.9 \text{ eV} < \text{IE} < 5.8 \text{ eV}$ ).<sup>[52]</sup> Particularly, **DN4T** and **isoDN4T** show IE of 5.3 eV which suggest rather facile charge injection from the OSCs to the gold contacts. The contacts work function was determined by using UPS, giving values of 4.7 eV for bare Au and of 5.2 eV for PFBT/Au (see **Chapter 3**).

The ratio between the contact resistance and the total resistance of the devices ( $R_c/R_{\text{tot}}$ ) equals to the ratio of the voltage drop at the contact and the applied source-drain voltage ( $V_c/V_d$ )<sup>[86]</sup>, revealing if the voltage drop at the contact is negligible compared to the voltage drop over the channel. For **DN4T** and **isoDN4T**, the voltage drop at the contacts is lower than 10% of the applied drain voltage for both TC and BC devices, confirming a facile charge injection from the gold electrodes to the OSCs. It is worth to underline that the energy barrier which a charge must overcome on injection from the metal contact to the OSC is not controlled just by the energy difference between the

metal's work function and the IE of the organic semiconductor. Moreover, at the interface several factors like charge carrier's transfer, interface dipole, band banding, depletion region, etc.,<sup>[152]</sup> must be considered to have a precise and reliable energy value.

### 2.6.3 C<sub>8</sub>-DN4T and C<sub>10</sub>-DN4T vs C<sub>8</sub>-DNTT and DN4T

Charge carrier mobility, threshold voltage (extracted from the best performing devices) and ionization energy of **C<sub>8</sub>-DN4T**, **C<sub>10</sub>-DN4T**, **C<sub>8</sub>-DNTT** (see **Figure A1.6** in the **Appendix**) and **DN4T** are compared (**Table 2.7**), in order to understand the effect of the functionalization of DN4T molecular core with alkyl side chains.

**Table 2.7: Ionization energy, threshold voltage and charge carrier mobility of C<sub>8</sub>-DN4T, C<sub>10</sub>-DN4T and C<sub>8</sub>-DNTT.**

V<sub>th</sub> and  $\mu$  and RcW values are referred to devices fabricated on optimized substrate temperature.

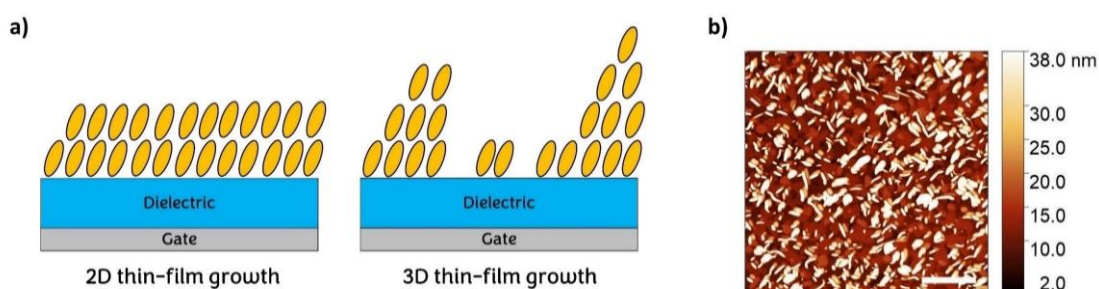
Compound	IE (eV)	V <sub>th</sub> (V)	$\mu$ (cm <sup>2</sup> V <sup>-1</sup> s <sup>-1</sup> )	RcW (k $\Omega$ cm)
<b>C<sub>8</sub>-DN4T</b>	4.95	-0.4	2.3	1.2
<b>C<sub>10</sub>-DN4T</b>	4.97	-0.4	2.5	0.8
<b>C<sub>8</sub>-DNTT</b>	4.92	-0.4	4.8	0.8
<b>DN4T</b>	5.27	-1.2	2.0	1.8

In this case, all the devices are referred to this work and were produced using the same fabrication parameters, allowing a fair comparison between the compounds. Due to the inability to solve the crystal structure of **C<sub>8</sub>-DN4T** and **C<sub>10</sub>-DN4T**, the discussion is focused on the electrical performances of the devices only. Transfer and output characteristics of **C<sub>8</sub>-DNTT** are reported in **Chapter 3**.

#### 2.6.3.1 Charge carrier mobility and thin-films morphology

The main differences between the alkylated DN4Ts and **C<sub>8</sub>-DNTT** is the higher charge carrier mobility of the latter (4.8 cm<sup>2</sup>V<sup>-1</sup>s<sup>-1</sup>), approximately twice compared to the alkylated DN4Ts (2.3-2.5 cm<sup>2</sup>V<sup>-1</sup>s<sup>-1</sup>). This difference may be linked to the dissimilar thin-film morphology. The growth process of the alkylated DN4T molecules is characterized by a 3D growth mode (Volmer-Weber type), which has shown to be a reason of poor charge transport due to

the formation of severe grain boundaries acting as deep energetic traps.<sup>[143]</sup> On the contrary, **C<sub>8</sub>-DNTT** shows a 2D growth mode, forming a typical terrace structure (covered by small single crystals) with terrace steps height that matches the unit cell long axis. The competition between molecule-molecule and molecule-substrate interaction determines the growth mode for the first layers onto the substrate. Therefore, the thin-film morphology of **C<sub>8</sub>-DNTT** (see **Figure 2.24**) reflects a stronger interaction between the molecule and the TDPA/Al<sub>2</sub>O<sub>3</sub> substrate, while for **C<sub>8</sub>-DN4T** and **C<sub>10</sub>-DN4T**, molecule-molecule interaction dominates, leading to a 3D thin-film morphology which disfavours charge carrier transport.



**Figure 2.24: Thin-film growth mode.**

(a) Schematic illustration of 2D and 3D thin-film growth. (b) AFM topography image of **C<sub>8</sub>-DNTT** thin film deposited onto TDPA/Al<sub>2</sub>O<sub>3</sub> through vacuum deposition at substrate temperature of 100 °C (deposition rate of 0.1 Ås<sup>-1</sup> and nominal thickness of ca. 25 nm). Scale bar: 1 μm.

Nonetheless, the alkylation of **DN4T** leads to increased charge carrier mobilities compared to the parent molecule. The increment of charge carrier mobility from 2.0 cm<sup>2</sup>V<sup>-1</sup>s<sup>-1</sup> in **DN4T** up to 2.3-2.5 cm<sup>2</sup>V<sup>-1</sup>s<sup>-1</sup> in **C<sub>8</sub>-** and **C<sub>10</sub>-DN4T** may be attributed to the decrease of thermal motions due to weak interaction within the alkyl chains of adjacent molecules. As already reported for **BTBT**, **DNTT** and their alkylated derivatives, the introduction of alkyl chains attached along the long axis of their conjugated core suppresses the amplitude of vibrations along the unit cell long axis thanks to a large number of weak interactions between the alkyl chains of neighbouring molecules.<sup>[58,159]</sup>

We suppose that also for **C<sub>8</sub>-DN4T** and **C<sub>10</sub>-DN4T**, the alkylation of the aromatic ring results in lower dynamic disorder of the crystal lattice, enabling a more extended charge delocalization.

This would lead to two main expected effects: increase of the charge carrier mobility and reduction of the IE in crystalline OSCs compared to the parent and non-alkylated compounds. The solution of the crystalline structure of **C<sub>8</sub>-DN4T** and **C<sub>10</sub>-DN4T** would be needed to confirm the hypothesis of a closer packing of the aromatic core which can reduce the detrimental effect of dynamic disorder.

### 2.6.3.2 Charge carrier injection

The ionization energy is almost identical for all the alkylated derivatives (4.9 eV), highlighting a reduction of IE if compared to the parent compounds (5.3 eV for **DN4T** and 5.4 eV for **DNTT**). Considering that IE is the energy required to remove one electron from the HOMO of a molecule, its value strongly depends on crystal packing that influences electronic delocalization.<sup>[159]</sup> Hence, IE of an isolated molecule in vacuum may differ from its value in the solid state, where intermolecular delocalization and electrostatic interaction within neighbouring molecules can lead to energy variation of the energy levels. As mentioned above, the introduction of alkyl chains may suppress the amplitude of lattice vibrations (thanks to weak interactions within adjacent molecules), enhancing charge carrier delocalization and leading to IE reduction. In the first-place alkyl substituents are weak electron donors. Lower IE in alkylated DN4T compared to the parent molecule is reflected in better charge carrier injection. This is confirmed by the lower  $V_{th}$  (close to 0 V) and  $R_C W$  ( $< 1.2 \text{ k}\Omega\text{cm}$ ) in alkylated DN4T, compared to the parent molecule which shows  $V_{th}$  0.8 V higher and  $R_C W$  up to  $1.0 \text{ k}\Omega\text{cm}$  higher.

## 2.6.4 Tert-butyl substituted thienoacenes

### 2.6.4.1 Effect of $\pi$ -extension on charge injection

In order to understand the effect of the  $\pi$ -core extension on charge injection properties in TFTs, ionization energy obtained by PYS, threshold voltage and contact resistance, both extracted from TFTs, of *tert*-butyl substituted thienoacenes are compared (**Table 2.8**). The extension of the  $\pi$ -core obtained by an annealed approach and an oligomeric approach led to IE reduction for all the synthesized compounds if compared to **tBu-BTBT** (IE = 5.7 eV). Particularly, ionization energy is  $\approx 0.3 \text{ eV}$  lower for **tBu-DNTT**,  $\approx 0.4 \text{ eV}$  lower for **tBu-DBTTT** and **tBu-BTBT-1**, and  $\approx 0.5 \text{ eV}$  lower for **tBu-BTBT-2**.

**Table 2.8: Ionization energy (IE), threshold voltage ( $V_{th}$ ) and mobility ( $\mu$ ) of *tert*-butyl substituted thienoacenes.**

(#) Measurements performed in this work.

(\*) Not reported

(§) TLM not applicable

(SD) Devices fabricated through solution shearing technique

Compound	IE (eV)	$V_{th}$ (V)	$R_cW$ (k $\Omega$ cm)	Ref.
<b>tBu-BTBT</b>	5.7	$\approx -70$ (SD)	*	[133]
		-69 (SD)	*	[134]
		-3.1	§	#
<b>tBu-DNTT</b>	5.37	-1.7	4.4	#
<b>tBu-DBTTT</b>	5.31	-1.3	2.9	#
<b>tBu-BTBT-1</b>	5.34	-1.7	4.4	#
<b>tBu-BTBT-2</b>	5.23	-1.5	4.8	#

OSCs with ionization energy in the range of 5.1-5.4 eV are considered the most optimal for device applications since this IE range ensures a good compromise between facile charge injection and chemical stability against oxidation.<sup>[160]</sup> In the first place, this IE range minimize the Schottky barrier at the interface between gold electrodes and OSC. Lower IE may lead to easy oxidation of the compounds and to oxygen doping that disfavour charge transport in devices.<sup>[161,162]</sup> Several examples of reduced ionization energy have been reported, both for extended  $\pi$ -units, obtained both from a annealed approach<sup>[27,122,163]</sup> and oligomeric approach.<sup>[135,164]</sup> An example of the effect of the extended  $\pi$ -conjugated core has been already shown in for **DNTT**, **DN4T** and **isoDN4T**. **DN4T** and **isoDN4T** possess two additional thienyl rings in the central motif compared to **DNTT**. The IE shifted from 5.42 eV in **DNTT** to 5.27 and 5.23 eV in **DN4T** and **isoDN4T**, respectively, confirming the IE reduction caused by the extended  $\pi$ -core.

In this case, the IE reduction turns into lower  $V_{th}$  for all the synthesized compounds when employed in TFTs, compared to those fabricated with **tBu-BTBT**. Particularly, considering TFTs fabricated by vacuum deposition with a BC geometry, TFTs based on **tBu-BTBT** show  $V_{th}$  of -3.1 V. Because of the  $\pi$ -core extension,  $V_{th}$  is found to be 1.4 V lower in TFTs based on **tBu-DNTT** and on **tBu-BTBT-1**, 1.8 V lower in TFTs based on **tBu-DBTTT**, and 1.6 V lower in TFTs based on **tBu-BTBT-2**.

Moreover, the improved charge carrier injection is furtherly confirmed by the low contact resistance extracted for the *tert*-butyl thienoacene derivatives with an extended  $\pi$ -system, which exhibit  $R_cW$  lower than 5 k $\Omega$ cm. On the

contrary, it was not possible to extract  $R_{\text{C}}W$  from devices based on **tBu-BTBT**, since TFTs with channel length smaller than 215  $\mu\text{m}$  did not show drain current modulation upon the application of a gate bias - preventing the application of TLM. No field-effect response in small channel length devices may be related to high contact resistance, that is expected due to the deep ionization energy of **tBu-BTBT**.

In conclusion, the reduction of IE is reflected in a facile charge carrier injection, which in turns leads to the lowering of  $V_{\text{th}}$  for all the synthesized compounds. This allows the extraction of charge carrier mobility over a larger applied gate voltage, ensuring a high reliability of the extracted field-effect mobilities and hindering potential over- (or under-) estimations.

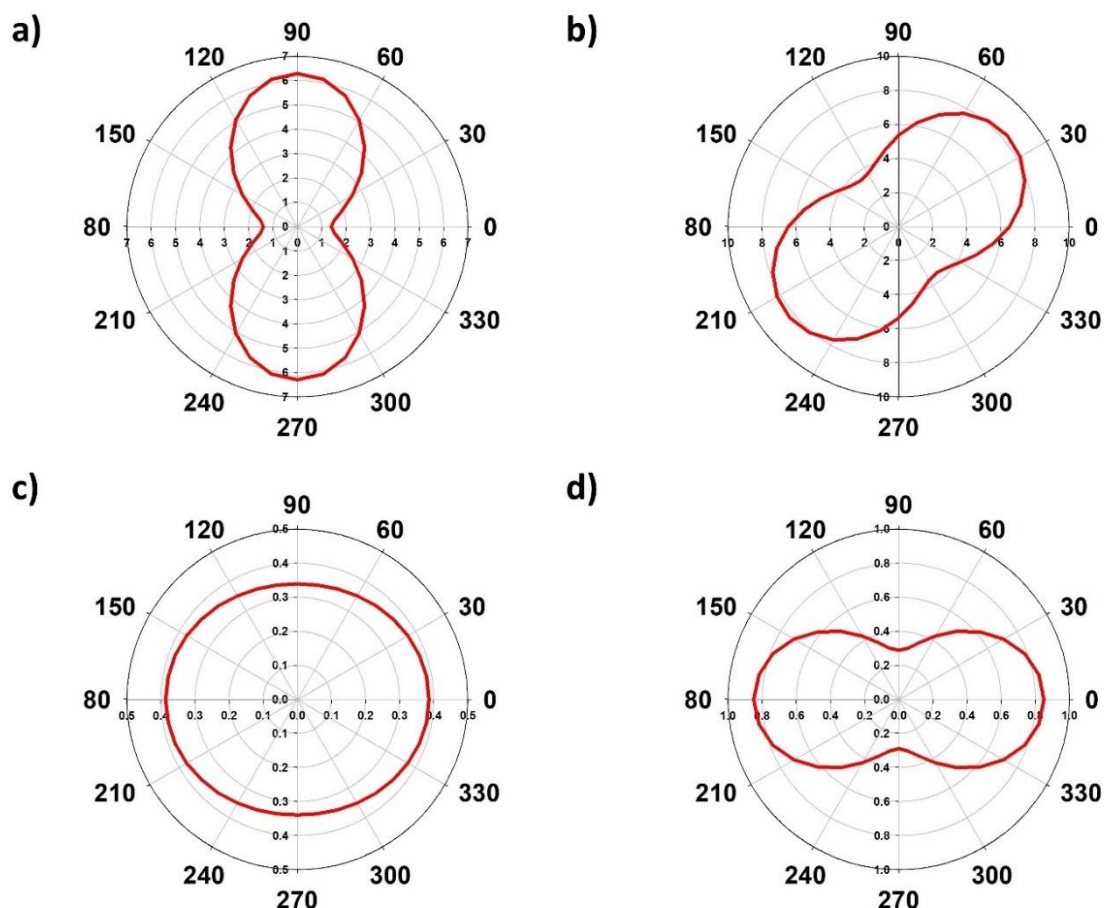
#### 2.6.4.2 Calculated charge mobility anisotropy

*Hole mobility anisotropy simulations were provided by Dr. Vincent Lamaur (Université de Mons). The simulations were performed by using a kinetic Monte Carlo approach (kMC) assuming a purely hopping regime.*

The high mobility of **tBu-BTBT** (up to  $\approx 7 \text{ cm}^2\text{V}^{-1}\text{s}^{-1}$  in single crystal FETs) has been attributed to the large and balanced transfer integrals, which are reflected in an almost perfect mobility isotropy obtained by Kinetic Monte Carlo (kMC) simulations with calculated mobility of  $\approx 4 \text{ cm}^2\text{V}^{-1}\text{s}^{-1}$ . These simulations enable the calculation of charge carrier mobility anisotropy along the herringbone (HB) plane of charge transport (*ab* plane in **Figure 2.22**).

By calculating the field-effect mobility anisotropy for the tert-butyl substituted thienoacenes (**Figure 2.25**), it is clear that solely **tBu-BTBT-1** shows isotropic charge properties, but low simulated mobility (about  $0.35 \text{ cm}^2\text{V}^{-1}\text{s}^{-1}$ ). On the contrary, **tBu-DNTT** and **tBu-DBTTT** show charge transport anisotropy along with higher simulated mobility (with maximum values of about 6 and  $8 \text{ cm}^2\text{V}^{-1}\text{s}^{-1}$  respectively) while **tBu-BTBT-2** exhibits both severe mobility anisotropy and low simulated mobility (maximum values of about  $0.8 \text{ cm}^2\text{V}^{-1}\text{s}^{-1}$ ).

These results indicate that the functionalization of the aromatic cores with *tert*-butyl groups does not ensure isotropic electronic interaction within neighbouring molecules. Actually, the degree of anisotropy of charge transport depends on several factors, such as the  $\pi$ -core structure, the packing motif of OSC in solid state and the  $\pi$ -core substituents, all of which contribute to the type and strength of electronic interactions.



**Figure 2.25: Mobility anisotropy plots.**

(a) **tBu-DNTT-tBu**, (b) **tBu-DBTTT-tBu**, (c) **tBu-th-BTBT-th-tBu** and (d) **tBu-th-BTBT-th-th-tBu** Plots are obtained from kMC simulations.

The experimental mobility values extracted from TFTs, reflect the trend obtained from the computational calculations. Despite the significant large values of transfer integrals and simulated charge carrier mobility, **tBu-DNTT** and **tBu-DBTTT** reveal poor charge transport isotropy, limiting the achievement of higher mobility. On the contrary, **tBu-BTBT-1** shows mobility isotropy, but better electrical performances are hindered by the reduced HOMO wavefunctions overlap. At last, **tBu-BTBT-2** exhibits both severe mobility anisotropy along with small transfer integrals values, reflected in the lowest experimental charge carrier mobility extracted in TFTs. It has to be highlighted that, both DFT and kMC calculations were performed considering a pure hopping regime that can model charge transport properties for organic semiconductors with low mobility ( $\mu \ll 1 \text{ cm}^2\text{V}^{-1}\text{s}^{-1}$ ).

Moreover, the two computational approaches were based on molecular crystals structure solved at low temperature, which may not consider the dynamic disorder present at higher temperature and the complexity of polycrystalline thin films, where the presence of different crystalline domains, grain boundaries and traps may further limit the comparison between the computational and experimental data. Notwithstanding, the mobility values extracted from polycrystalline thin-film devices are consistent with the trend shown in computational calculations, stressing the prominence to maximize the charge transport isotropy and the overlap of the HOMO levels to enhance charge carrier mobility.

## 2.7 Summary

I presented two isomers and the alkylated derivatives of a new class of thienoacenes bearing a central tetrathienyl core annealed with two external naphthalene rings that were employed in organic TFTs. The evaluation of the electrical characteristics revealed **DN4T**, **C<sub>8</sub>-DN4T** and **C<sub>10</sub>-DN4T** as high performance OSCs, with charge carrier mobility up to  $2.1 \text{ cm}^2 \text{ V}^{-1} \text{ s}^{-1}$  for the parent molecule and up to  $2.5 \text{ cm}^2 \text{ V}^{-1} \text{ s}^{-1}$  for the alkylated derivatives. In addition, I presented the electrical performances evaluation of four new *tert*-butyl substituted thienoacenes. The compounds have an extended  $\pi$ -system compared to **tBu-BTBT**, that ensures a better charge delocalization. This was confirmed by the lower ionization energy that in turns is reflected in lower  $V_{\text{th}}$  ( $< 1.7 \text{ V}$ ) in TFTs, along with small contact resistance ( $< 5 \text{ k}\Omega\text{cm}$ ). Among the compounds, **tBu-DNTT** was revealed as high performance OSC, with mobility exceeding  $1.9 \text{ cm}^2 \text{ V}^{-1} \text{ s}^{-1}$ . Structure-properties relationships were established, highlighting how several factors contribute to the final devices' performances. Herringbone packing motif, extended  $\pi$ -system, IE close to the electrodes work function, large and balanced transfer integrals and low reorganization energy are key parameters in OSCs design to obtain high performance materials for TFTs applications.

The impact of thin-film morphology on the device performances was evaluated through atomic force microscopy. All the compounds showed a typical 2D growth forming a terrace structure pattern, except for **C<sub>8</sub>-DN4T** and **C<sub>10</sub>-DN4T** that exhibited a 3D growth. This crystalline growth should disfavour charge transport along the active channel due to the presence of large number of grain boundaries. The crystal structure solution of **C<sub>8</sub>-DN4T** and **C<sub>10</sub>-DN4T** would be needed to confirm the proposed structure-properties relationship for the alkylated derivatives.

Moreover, considering the solubility enabled by the functionalization with alkyl side chains and with *tert*-butyl substitutions, solution processing could be employed to fabricate TFTs based on alkylated DN4Ts and *tert*-butyl substituted thienoacenes, with the view to optimize the thin-film morphology and induce a 2D crystalline growth in case of alkylated DN4Ts. For this purpose, solution-sharing technique could be used to fabricate TFTs. This technique allows the production of single crystalline domain within the first few active layer (removing the grain boundaries effects in the devices) that have shown charge carrier mobility higher than  $10 \text{ cm}^2 \text{ V}^{-1} \text{ s}^{-1}$  for alkylated thienoacenes.<sup>[165,166]</sup>



# Chapter 3

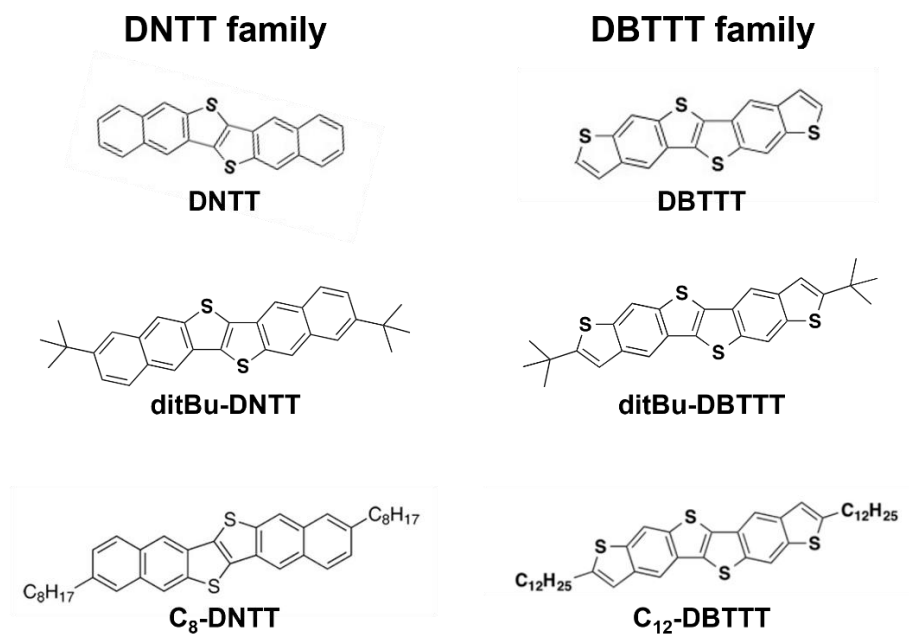
## Elucidating the influence of the molecular structure of thienoacenes organic semiconductors on contact resistance

### 3.1 Introduction

The role of contact resistance in organic semiconductors-based devices has gained considerable attention within the scientific community. This is because the performance of the final device is influenced by both charge carrier injection and charge transport through the semiconductor layer. The effect of contact resistance on the development of OFETs is twofold. Firstly, a high contact resistance can lead to inaccuracies in the determination of device parameters, which can have significant consequences on material development by producing incorrect structure-property relationships or leading to the rejection of potentially valuable organic semiconductors.<sup>[72]</sup> Secondly, high contact resistance places limitations on the maximum transit frequency that can be achieved through device miniaturization.<sup>[89,167]</sup> This limitation is particularly pertinent in the development of organic TFTs for low-power, high-frequency applications since reducing device size requires a corresponding increase in operating frequency. Therefore, it is essential to minimize contact resistance to enhance the performance of organic TFTs, establish accurate structure-property relationships, and maximize their potential in high-frequency applications. Several methodologies have been developed to address this issue, including the use of high charge carrier density in the electrolyte gate insulator,<sup>[168,169]</sup> contact doping,<sup>[73,74]</sup> mono- or bi-layer OSC films,<sup>[42,82]</sup> thin dielectric thickness, and transferred platinum contacts.<sup>[46]</sup> Although a few examples of width-normalized contact resistance ( $R_cW$ ) have been reported in OFETs to be below 100  $\Omega\text{cm}$ ,<sup>[89]</sup> the majority of reported  $R_cW$  values for state-of-the-art OSCs fall within the range of 100  $\Omega\text{cm}$  to 10  $\text{k}\Omega\text{cm}$ .<sup>[72]</sup>

This chapter aims to investigate the influence of molecular structure, specifically with regards to the molecular core substituents, on contact resistance in staggered and coplanar device geometries. While other factors that affect contact resistance have been extensively studied, little attention has been paid to this aspect. Therefore, we examined the charge transport

and contact resistance properties of **DNTT** and **DBTTT**, as well as their *tert*-butyl derivatives, namely **tBu-DNTT** and **tBu-DBTTT**, and alkylated derivatives, namely **C<sub>8</sub>-DNTT** and **C<sub>12</sub>-DBTTT**. In this chapter, we refer to the DNTT family as **DNTT**, **tBu-DNTT** and **C<sub>8</sub>-DNTT**, and the DBTTT family as **DBTTT**, **tBu-DBTTT** and **C<sub>12</sub>-DBTTT** (Scheme 3.1).



**Scheme 3.1**

## 3.2 Crystal structures

The crystal structures of the parent and alkylated molecules of the DNTT and DBTTT families have been reported in the literature.<sup>[60,128,170,171]</sup> In **Chapter 2**, the crystal structures of tert-butyl derivatives were presented, and therefore, we focus here solely on the crystalline characteristics of the parent and alkylated compounds.

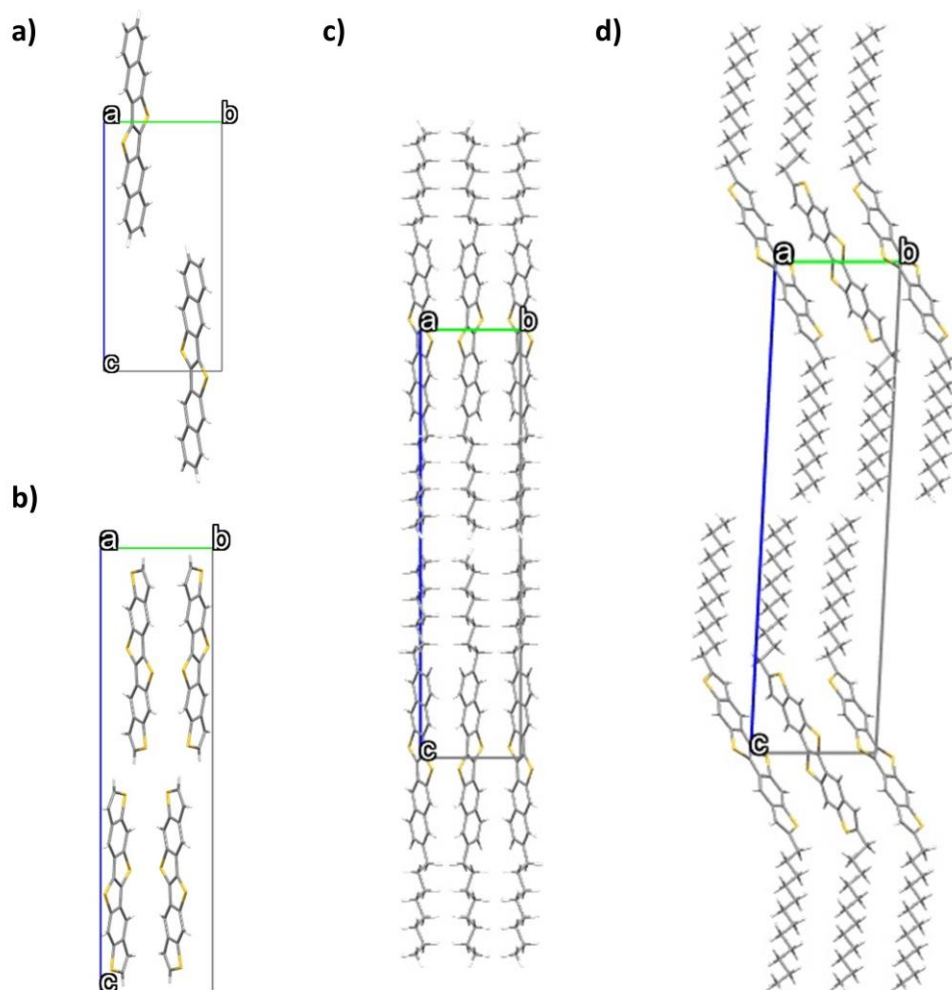
All the compounds display a characteristic layer-by-layer herringbone packing motif, where the HB angle between adjacent molecules ranges from 51.1° to 56.4°. The monoclinic space groups  $P 2_1$ ,  $P 2_1/c$  and  $P 2_1/a$  accommodate **DNTT**, **DBTTT**, and **C<sub>12</sub>-DBTTT**, respectively, while **C<sub>8</sub>-DNTT** belongs to the triclinic space group  $P -1$  (**Figure 3.1**).<sup>§§</sup> The parent molecules consist of one unique molecule in the asymmetric unit ( $Z' = 1$ ), whereas the alkylated derivatives exhibit half a molecule in the asymmetric unit ( $Z' = 0.5$ ). Notably, **DBTTT** displays four molecules in the unit cell ( $Z = 4$ ) where the length of the  $c$  axis (longest axis) corresponds to the length of two **DBTTT** molecules (**Table 3.1**).

**Table 3.1:** Crystallographic data of DNTT, DBTTT, C<sub>8</sub>-DNTT and C<sub>12</sub>-DBTTT.

Compound	DNTT	C <sub>8</sub> -DNTT	DBTTT	C <sub>12</sub> -DBTTT
<b>Formula</b>	C <sub>22</sub> H <sub>12</sub> S <sub>2</sub>	C <sub>38</sub> H <sub>44</sub> S <sub>2</sub>	C <sub>18</sub> H <sub>8</sub> S <sub>4</sub>	C <sub>42</sub> H <sub>56</sub> S <sub>4</sub>
<b>Crystal system</b>	Monoclinic	Triclinic	Monoclinic	Monoclinic
<b>Space group</b>	$P 2_1$	$P -1$	$P 2_1/c$	$P 2_1/a$
<b>a (Å)</b>	6.187(4)	5.8734(4)	5.91290(10)	5.9874(4)
<b>b (Å)</b>	7.662(6)	8.9824(5)	7.8545(2)	7.8611(4)
<b>c (Å)</b>	16.208(11)	35.2165(19)	31.0943(8)	35.2165(19)
<b>α (deg)</b>	90	92.810(5)	90	90
<b>β (deg)</b>	92.49(2)	90.799(5)	91.5270(10)	99.860(7)
<b>γ (deg)</b>	90	93.613(5)	100.828(3)	90
<b>Volume [Å<sup>3</sup>]</b>	767.611	1851.73	90	1579.71
<b>Z</b>	2	2	4	2
<b>Z'</b>	1	0.5	1	0.5

<sup>§§</sup> The accuracy of assigning a  $P 2_1$  polar space group to **DNTT** and **DN4T** is currently ambiguous. This uncertainty arises from the fact that crystals belonging to polar space groups typically exhibit a growth pattern characterized by a single preferred direction, which is not observed in either **DNTT** or **DN4T**.

All the compounds exhibit C-H $\cdots\pi$ , S $\cdots$ C, and S $\cdots$ S interactions, with the latter found to enhance charge transfer within neighbouring molecules. The high efficiency of charge transport in these compounds is confirmed by reported charge carrier mobility exceeding  $2\text{ cm}^2\text{V}^{-1}\text{s}^{-1}$  in polycrystalline TFTs for all the compounds.<sup>[60,126,128,171]</sup>



**Figure 3.1: Crystalline packing of the parent and alkylated compounds.**  
a) DNTT, (b) DBTTT, (c) C<sub>8</sub>-DNTT, (d) C<sub>12</sub>-DBTTT.

### 3.3 Thin-film transistor fabrication

Thin film transistors with bottom-gate top-contact (TC) and bottom-gate bottom-contact (BC) geometry were fabricated as already reported in **Paragraph 2.1**. In this case, the substrate temperature was kept at the optimal value which gives the best charge carrier mobility for each respective compound. The OSC deposition rate was set at  $0.3 \text{ \AA s}^{-1}$ , except for the alkylated compounds that were deposited at rate of  $0.1 \text{ \AA s}^{-1}$  (**Table 3.2**). The OSCs were deposited with nominal thickness of 25 nm and 80 nm, monitored by a crystal quartz microbalance and confirmed by and AFM measurements.

**Table 3.2:** Fabrication parameters used for TC and BC TFTs.

Compound	T <sub>s</sub> (°C)	Deposition rate (Ås <sup>-1</sup> )
DNTT	70	0.3
tBu-DNTT	100	0.3
C <sub>8</sub> -DNTT	100	0.1
DBTTT	70	0.3
tBu-DBTTT	100	0.3
C <sub>12</sub> -DBTTT	100	0.1

## 3.4 Thin-films characterization

### 3.4.1 Topography

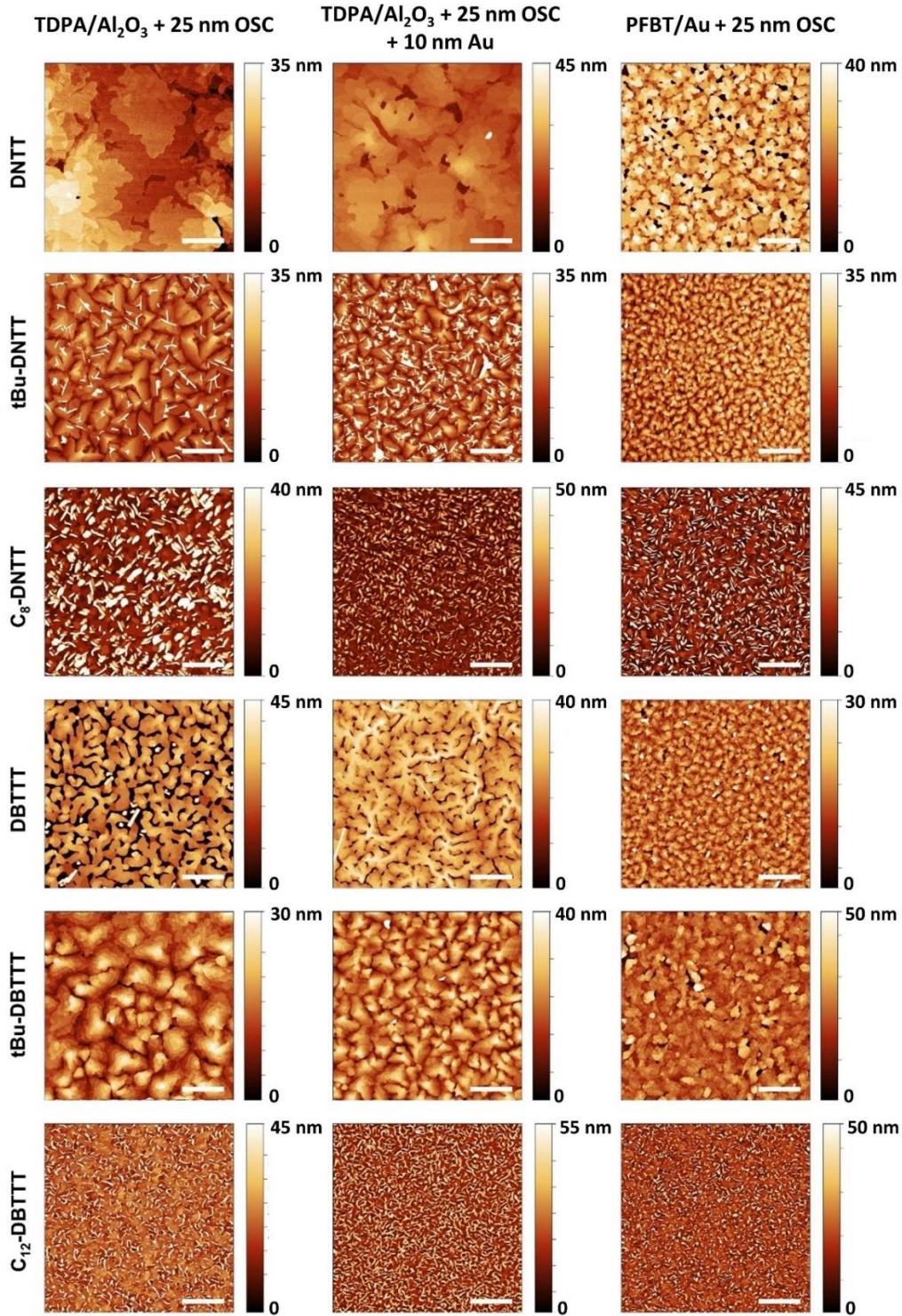
Atomic force microscopy in tapping mode was employed to analyse the thin-film topography of thienoacenes OSCs. Particularly AFM measurements were performed on the active layer and on the contact region of BC TFTs with 25-nm-thick OSCs (**Figure 3.2**, left and right column). Across the active layer, OSCs are deposited onto TDPA/Al<sub>2</sub>O<sub>3</sub> substrates. In this region the OSC morphology affects the charge carrier mobility, depending mainly on the OSC crystalline growth and on the formation of grain boundaries. While across the contacts, OSCs are deposited onto PFBT /Au surface. In this case the OSC morphology in this region influences charge carrier injection in BC devices. It is worth noting that the OSC morphology across the active layer of TC and BC devices are similar, since OSC is deposited onto TDPA/Al<sub>2</sub>O<sub>3</sub> substrate either way. Moreover, considering that in TC devices gold is thermally evaporated through shadow masks onto the OSC, the effect of gold deposition on thin-film morphology of OSCs was analysed. Specifically, AFM measurements were carried out on samples which consists of 25-nm-thick OSC deposited onto TDPA/Al<sub>2</sub>O<sub>3</sub> substrates, additionally coated with 10 nm of gold deposited at 0.5 Ås<sup>-1</sup> (**Figure 3.2**, centre column).

#### 3.4.1.1 Deposition onto TDPA/Al<sub>2</sub>O<sub>3</sub>

All the compounds deposited onto TDPA/Al<sub>2</sub>O<sub>3</sub> substrates exhibit a terraced topography characterised by the diffuse presence of grain boundaries. By analysing the AFM images, the average height steps of the terrace structures were extracted, giving values that match the length of the long unit cell axis of each respective compound, except for **DBTTT**. The latter has four molecules in the unit cell and its unit cell long axis correlates to the length of two molecules. Hence, the terrace height steps extracted from AFM images of **DBTTT** coincide to half of the unit cell long axis, that in turns corresponds to the length of one molecule.

The calculated height steps are in the range of 1.5 nm and 3.6 nm, depending on the length of the respective molecule (**Table 3.3**). These results suggest that for all the compounds, molecules pack with an upright orientation respect to the substrates when vacuum deposited. The parent compounds and the *tert*-butyl derivatives exhibit relatively flatter topography compared to the alkylated derivatives. The latter are characterised by the presence of several needle-shaped crystal aggregates that stand on the top of the terraced surfaces. **tBu-DNTT** shows a significant reduction of these crystalline

aggregates, while these aggregates are not exhibited for **DNTT**, **DBTTT** and **tBu-DBTTT**, that are characterised by smoother thin-film surfaces.



**Figure 3.2: AFM topography images of thin films.**

OSCs are deposited onto TDPA/ $\text{Al}_2\text{O}_3$  substrates (left column), onto TDPA/ $\text{Al}_2\text{O}_3$  substrate and covered with 10 nm of Au (center column), onto PFBT/Au surfaces (left column). Nominal thickness of OSCs films = 25 nm. Lateral scale bar = 1  $\mu\text{m}$ .

It is still unclear the role of these crystalline aggregates on the final device performances, especially in the case of TC devices where the gold contacts are deposited on top of them.

In addition, when gold is deposited on top of OSCs to fabricate source and drain contacts in TC device geometry, gold nanoclusters may penetrate the semiconductor film. These clusters can modify the dipole barrier at Au/OSC interface and consequently affect contact resistance.<sup>[172]</sup> Gold-cluster penetration into the OSC is generally denoted by the formation of craters and voids on the OSC thin film, with depth up to 30 nm.<sup>[173]</sup>

From the AFM topography images, it is clear that no deep voids (neither a pitted morphology) are formed upon the deposition of 10-nm-thick gold layer on the top of the OSCs. For all the compounds, the thin-film morphology of OSCs coated with gold resembles the morphology of the uncoated OSCs. This suggests a minor penetration of gold clusters into the OSCs compared to those reported in the literature.<sup>[173]</sup> Moreover, no relevant differences were observed within the parent molecules, the *tert*-butyl and the alkylated derivatives upon the gold layer deposition, indicating a similar mechanical response to gold cluster penetration into the OSCs films.

#### 3.4.1.2 Deposition onto PFBT/Au

The deposition of OSCs onto PFBT/Au surfaces led to a terrace structured topography for all the compounds, reflecting some features exhibited by the thin films deposited onto TDPA/Al<sub>2</sub>O<sub>3</sub>. Also in this case, the alkylated molecules unveil a large number of needle-shaped crystal aggregates on top of the films, in contrast with the parent compounds and the *tert*-butyl-substituted derivatives. Moreover, the average height steps of the terraced structures correspond to those obtained from AFM images of OSCs deposited on TDPA/Al<sub>2</sub>O<sub>3</sub>, suggesting that the molecules assume an upright orientation even on PFBT/Au substrates. Specifically, the height steps were found to be in the range of 1.5 nm and 3.6 nm, also in this case (**Table 3.3**).

The main difference between OSCs deposited onto TDPA/Al<sub>2</sub>O<sub>3</sub> substrates and onto PFBT/Au surfaces lies in the size of grain diameters. For all the compounds the grain diameter decreases passing from TDPA/Al<sub>2</sub>O<sub>3</sub> to PFBT/Au substrates. Particularly, the grain diameter decreases from 3370 nm to 560 nm for **DNTT**, from 620 nm to 380 nm for **tBu-DNTT-tBu**, from 550 nm to 330 nm for **C<sub>8</sub>-DNTT**, from 610 nm to 390 nm for **DBTTT**, from 1900 nm to 540 nm for **tBu-DBTTT-tBu** and from 450 nm to 340 nm for **C<sub>12</sub>-DBTTT** (**Table 3.3**). This discrepancy in grain diameter values between

TDPA/Al<sub>2</sub>O<sub>3</sub> and PFBT/Au substrates, is linked to the different nucleation processes occurring on the surfaces.

Based on the larger grain diameters observed on the TDPA/Al<sub>2</sub>O<sub>3</sub> substrate, it can be inferred that the TDPA-SAM promotes a lower nucleation density in comparison to the fluorinated surface provided by PFBT-SAM.<sup>[141]</sup> As a consequence, this would lead to the creation of fewer grains with larger diameters on the TDPA-SAM when compared to the PFBT-SAM.

At last, these findings support the idea that gold contacts that have undergone PFBT treatment ensure a similar OSC morphology throughout the contact-to-channel region, which is expected to facilitate charge injection in the BC device described in this study.

**Table 3.3: Averaged grain size extracted from AFM images of thin films deposited onto TDPA/Al<sub>2</sub>O<sub>3</sub> and PFBT/Au.**

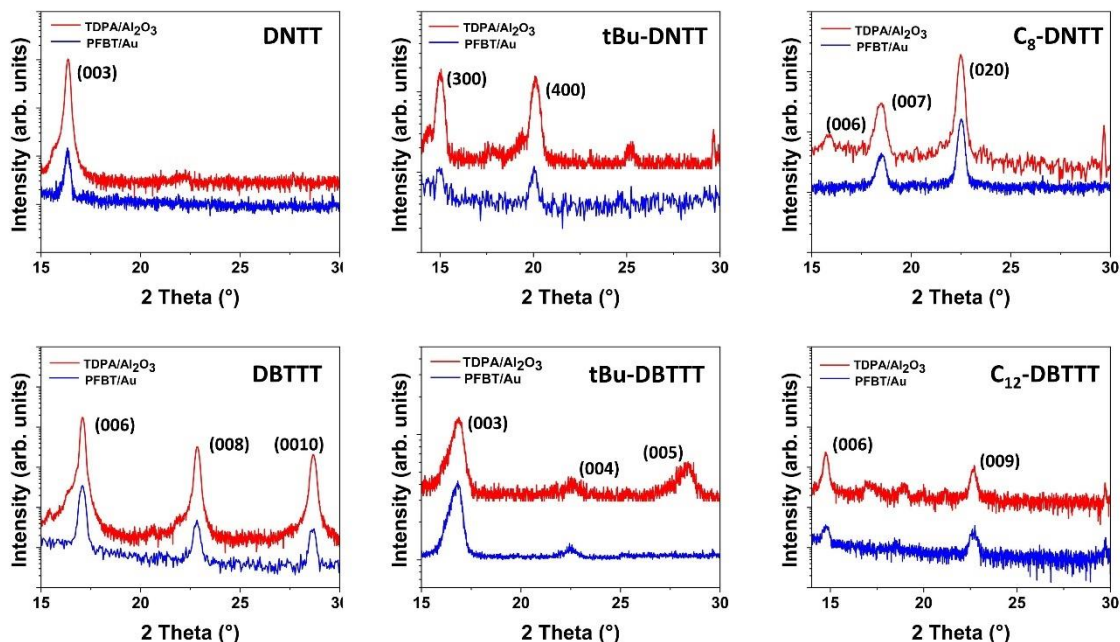
Compound	TDPA/Al <sub>2</sub> O <sub>3</sub> (nm)	PFBT/Au (nm)
DNTT	3370 ± 860	563 ± 80
tBu-DNTT	615 ± 110	378 ± 102
C <sub>8</sub> -DNTT	547 ± 115	327 ± 70
DBTTT	612 ± 183	388 ± 96
tBu-DBTTT	1983 ± 398	353 ± 160
C <sub>12</sub> -DBTTT	445 ± 77	338 ± 60

### 3.4.2 Crystallinity

The crystallinity of OSCs thin films deposited onto TDPA/Al<sub>2</sub>O<sub>3</sub> and PFBT/Au substrates was investigated by XRD. Considering the larger spot size required for the measurements, OSCs were deposited onto 2.5 × 2.5 cm<sup>2</sup> TDPA/Al<sub>2</sub>O<sub>3</sub> and PFBT/Au substrates using the same deposition parameter reported in **Paragraph 3.3**.

The XRD patterns collected from thin films deposited onto TDPA/Al<sub>2</sub>O<sub>3</sub> and PFBT/Au exhibit Bragg peaks at the same 2θ values for each respective compound (**Figure 3.3**). The peaks were indexed and assigned to the family planes {001} and {100}, depending on the molecule. These planes correspond to the herringbone layer planes, defined as those planes enclosed between the two short unit cell axis. By employing the Bragg law, the d-spacing (interlayer

distance) associated to the family planes was calculated, giving values ranging from 1.5 to 3.6 nm (see **Table 3.4**).



**Figure 3.3: XRD patterns of OSCs deposited onto TDPA/Al<sub>2</sub>O<sub>3</sub> and PFBT/Au substrates.**

The thin films have nominal thickness of 25 nm.

The d-spacing values match the length of the unit cell long axis and as well the terrace height steps extracted from AFM images, for each respective compound - except for **DBTTT**, where terrace height steps correspond to the half of the d-spacing and therefore to the half of unit cell long axis (as already explained). This confirm that the molecules adopt a layered structure both on TDPA/Al<sub>2</sub>O<sub>3</sub> and PFBT/Au, standing approximately upright with respect to the substrates and orienting their unit cell long axis towards the direction perpendicular to the substrate's surface.

In the case of **C<sub>8</sub>-DNTT** thin films, the XRD pattern exhibit a peak at  $2\theta = 22.5^\circ$ , that is associated to the reflection of (020) plane. This is likely attributed to the reflection of the 3D crystalline aggregates that are massively formed on the terraced structure of **C<sub>8</sub>-DNTT** thin films.

At last, the diffraction patterns collected from OSCs deposited onto PFBT/Au substrates show a lower relative intensity compared to the patterns collected from TDPA/Al<sub>2</sub>O<sub>3</sub> substrates. This is caused likely by the rougher and higher X-ray reflectivity of the underneath gold layer.<sup>[43]</sup>

**Table 3.4: Comparisons of the d-spacing, terrace height steps and unit cell long axis.**

d-spacing (d-XRD) is calculated from XRD patterns, terrace height steps (d-AFM) are obtained from AFM images, and unit cell long axis (L SCXRD) is obtained from the single crystal structure. In the table are shown the values extracted from TDPA/Al<sub>2</sub>O<sub>3</sub> and PFBT/Au substrates. The unit cell long axes are taken from the reported crystalline structures.

Compound	d XRD TDPA/Al <sub>2</sub> O <sub>3</sub> (Å)	d XRD PFBT/Au (Å)	d AFM TDPA/Al <sub>2</sub> O <sub>3</sub> (Å)	d AFM PFBT/Au (Å)	L SCXRD (Å)
<b>DNTT</b>	16.3	16.3	15.8 ± 1.8	15.7 ± 1.7	16.2
<b>tBu-DNTT</b>	17.9 ± 0.1	17.8 ± 0.3	17.3 ± 1.0	16.8 ± 2.1	17.6
<b>C<sub>8</sub>-DNTT</b>	33.5 ± 0.2	33.4 ± 0.2	33.5 ± 3.0	35.4 ± 4.5	34.1
<b>DBTTT</b>	31.1 ± 0.1	31.3 ± 0.4	15.3 ± 0.8	15.2 ± 1.5	31.4
<b>tBu-DBTTT</b>	15.8 ± 0.1	15.7 ± 0.3	16.3 ± 2.6	15.9 ± 2.4	16.0
<b>C<sub>12</sub>-DBTTT</b>	34.6 ± 0.2	34.8 ± 0.2	35.7 ± 4.0	35.8 ± 3.8	35.2

## 3.5 Thin-film transistors characteristics

The electrical characteristics were assessed by measuring TFTs, using the same measurement parameters mentioned in **Chapter 2**. Also in this chapter, all the reported transfer characteristics and extracted values are referred to the linear regime ( $V_d = -0.1$  V) and to devices with  $W/L = 480/215$   $\mu\text{m}$ , unless otherwise stated. Particularly, the transmission line method (TLM) used to extract contact resistance is valid only in the linear regime. TLM assumes a linear drop in voltage across the active channel, that is ensured by a uniform charge carrier density along the accumulation layer when operating the devices in linear regime. On the contrary, in saturation regime a step potential drop close to the drain contact (pinch-off) is present, invalidating the application of the method.

In the first part of this section the electrical characteristics of TFTs with 25-nm-thick OSC layer are reported, while in the second part the impact of OSC thickness on the electrical performances and contact resistance is investigated by analysing TFTs with 80-nm-thick OSC layer. Please note that the recorded output characteristics and the plots showing the extracted  $R_c W$  over the entire range of gate-overdrive voltage are reported in the **Appendix**.

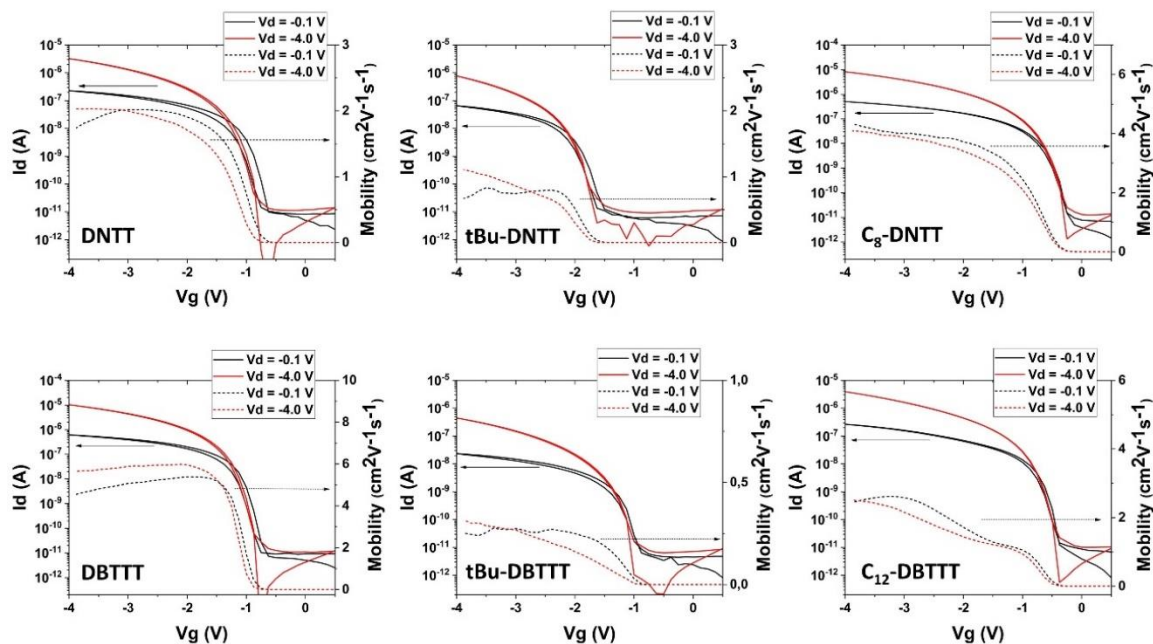
### 3.5.1 TFTs with 25-nm-thick OSC layer

#### 3.5.1.1 Electrical performances

By measuring the transfer characteristics, the electrical performances of TC TFTs with 25-nm-thick OSC layer were assessed. (**Figure 3.4**)

For both DNNT and DBTTT families, the parent molecules and the alkylated derivatives show high charge carrier mobility, with values of  $2.3 \text{ cm}^2\text{V}^{-1}\text{s}^{-1}$  for **DNNT**, of  $5.1 \text{ cm}^2\text{V}^{-1}\text{s}^{-1}$  for **DBTTT**, of  $3.7 \text{ cm}^2\text{V}^{-1}\text{s}^{-1}$  for **C<sub>8</sub>-DNNT** and of  $2.2 \text{ cm}^2\text{V}^{-1}\text{s}^{-1}$  for **C<sub>12</sub>-DBTTT**. Conversely, the *tert*-butyl derivatives exhibit lower mobility, with values of  $0.8 \text{ cm}^2\text{V}^{-1}\text{s}^{-1}$  and  $0.3 \text{ cm}^2\text{V}^{-1}\text{s}^{-1}$  for **tBu-DNNT** and **tBu-DBTTT**, respectively.

Likewise, TFTs based on parent molecules and alkylated derivatives show lower threshold voltage, ranging from  $-0.8$  V to  $-1.2$  V, than those based on *tert*-butyl derivatives, which show  $V_{th}$  ranging from  $-1.6$  V to  $-1.8$  V. The increased threshold voltage in *tert*-butyl derivative-based TFTs denotes a significant amount of trapping sites.



**Figure 3.4: Transfer characteristics of TC TFTs with 25-nm-thick OSC layer.** Solid lines and dashed lines are referred to drain current and mobility respectively. All TFTs have W/L = 480/215  $\mu\text{m}$ .

A method to evaluate the trap density is by measuring the subthreshold swing (SS, defined as the inverse slope of the logarithmic  $I_d$  as a function of  $V_g$  in the subthreshold regime) and use **Equation 1.17**.<sup>\*\*\*</sup> The  $N_{\text{bulk}}$  term (bulk trap density per unit volume and energy) cannot be ignored in the case of staggered devices since the injected charges must pass through the OSC's bulk in order to reach the accumulation channel. Thus, the subthreshold swing reflects both the contribution of the interfacial trap density and bulk trap density and thereby higher SS indicates a greater number of trap sites. As expected, the parent compounds and the alkylated derivatives are characterized by lower SS than *tert*-butyl derivatives. SS was found to be of 141 mV/dec and 163 mV/dec for **tBu-DNTT** and **tBu-DBTTT**, respectively. In contrast **DNTT** and **C<sub>8</sub>-DNTT** show SS of 109 and 112 mV/dec, respectively, while **DBTTT** and **C<sub>12</sub>-DBTTT** show SS of 116 and 122 mV/dec respectively (**Table 3.5**). In summary, the analysis of TC TFTs characteristics highlights the inferior electrical performances of *tert*-butyl derivatives compared to the parent and alkylated molecules, due to the lower charge carrier mobility, higher threshold voltage and larger number of trap sites.

<sup>\*\*\*</sup> **Equation 1.17**  $\rightarrow SS = \frac{KT \ln(10)}{q} \left( 1 + \frac{q^2 N_{it} + q\sqrt{\epsilon} N_{\text{bulk}}}{C_i} \right)$

Table 3.5: Electrical performance of TC TFTs with 25-nm-thick OSC layer.

Compound	$\mu$ ( $\text{cm}^2\text{V}^{-1}\text{s}^{-1}$ )	$V_{\text{th}}$ (V)	SS (mV/dec)
<b>DNTT</b>	$2.3 \pm 0.1$	$-1.0 \pm 0.1$	$109 \pm 5$
<b>tBu-DNTT</b>	$0.8 \pm 0.1$	$-1.8 \pm 0.1$	$141 \pm 4$
<b>C<sub>8</sub>-DNTT</b>	$3.7 \pm 0.2$	$-0.8 \pm 0.1$	$112 \pm 4$
<b>DBTTT</b>	$5.1 \pm 0.1$	$-1.2 \pm 0.1$	$116 \pm 3$
<b>tBu-DBTTT</b>	$0.3 \pm 0.1$	$-1.6 \pm 0.2$	$163 \pm 2$
<b>C<sub>12</sub>-DBTTT</b>	$2.2 \pm 0.1$	$-1.1 \pm 0.1$	$122 \pm 2$

Similarly, the electrical performances of BC TFTs were extracted from transfer characteristics (**Figure 3.5**). BC TFTs based on the parent compound unveil similar charge carrier mobility compared to the TC counterparts, with values of 2.3 and  $4.7 \text{ cm}^2\text{V}^{-1}\text{s}^{-1}$  for **DNTT** and **DBTTT** respectively. On the contrary, BC TFTs based on *tert*-butyl and alkylated derivatives exhibit slightly higher mobility compared to TC TFTs, with values of 1.4 and  $1.0 \text{ cm}^2\text{V}^{-1}\text{s}^{-1}$  for **tBu-DNTT** and **tBu-DBTTT**, respectively, and with values of 4.8 and  $3.3 \text{ cm}^2\text{V}^{-1}\text{s}^{-1}$  for **C<sub>8</sub>-DNTT** and **C<sub>12</sub>-DBTTT**, respectively.

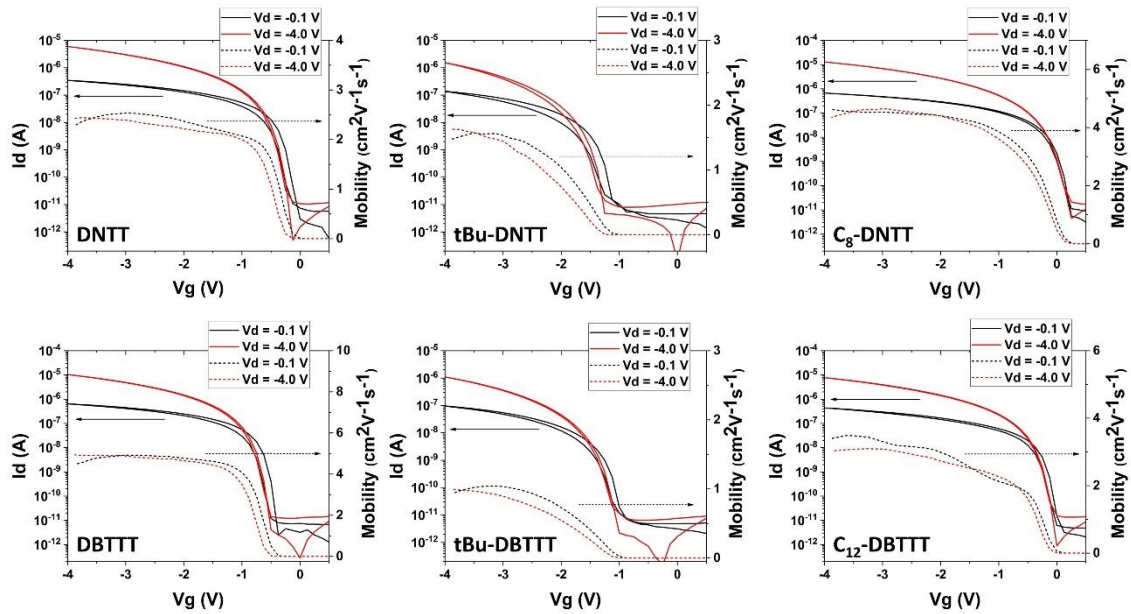


Figure 3.5: Transfer characteristics of BC TFTs with 25-nm-thick OSC layer. Solid lines and dashed lines are referred to drain current and mobility respectively. All TFTs have  $W/L = 480/215 \text{ }\mu\text{m}$ .

As already shown in **Chapter 2**, also in this case the adoption of a BC device geometry results in the lowering of threshold voltage for all the compounds. Passing from TC to BC device,  $V_{th}$  decreases up to 0.3 V for **DNTT**, up to 0.4 V for **C<sub>8</sub>-DNTT**, up to 0.5 V for **DBTTT** and **C<sub>12</sub>-DBTTT** and up to 0.1 V for the *tert*-butyl derivatives. Both a more facile charge injection in BC devices (see the section on contact resistance) and a smaller number of trap sites can be linked to the lower threshold voltage.

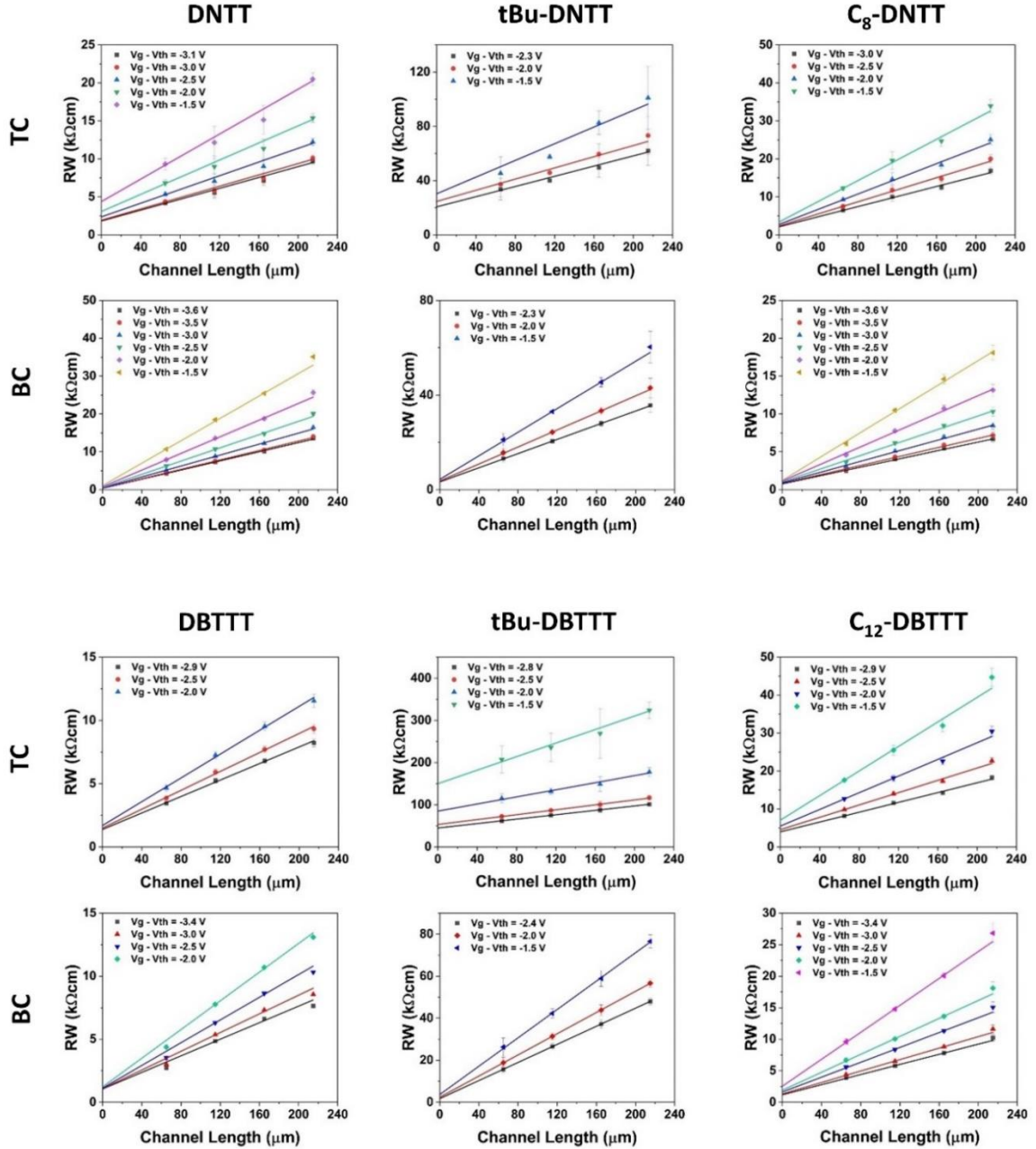
Depending on the compound, the subthreshold swing of BC TFTs is between 9 and 18 meV/dec lower than the TC counterparts (**Table 3.6**). This highlights a minor presence of traps in BC devices. Given that each compound was deposited onto TDPA/Al<sub>2</sub>O<sub>3</sub> dielectric using the same deposition parameters, TC and BC TFTs based on the same compound ought to exhibit a comparable nominal interfacial charge trap density. Device-to-device variation is expected. Yet, the systematic decreased subthreshold swing of BC TFTs raises the possibility that  $N_{bulk}$  is a contributing factor to the disparity in SS values. In TC TFTs trap sites may be present in the OSC volume between the contacts and the gate-induced carrier channel. In contrast, since charges are directly injected into the accumulation channel in BC TFT, this contribution is disregarded. Additionally, the parent compounds and the alkylated derivatives display lower SS than the *tert*-butyl derivatives, maintaining the trend seen in TC TFTs. This indicates a larger trap density of the latter. By setting  $N_{bulk} = 0$ ,  $N_{int}$  were extracted in BC devices. The *tert*-butyl derivatives exhibit the largest  $N_{it}$ , with values of  $1.35 \times 10^{12}$  and  $1.72 \times 10^{12}$  eV<sup>-1</sup> cm<sup>-2</sup> for **tBu-DNTT** and **tBu-DBTTT** respectively. The parent compounds unveil the lowest  $N_{it}$ , with values of  $6.19 \times 10^{11}$  and  $7.62 \times 10^{11}$  eV<sup>-1</sup> cm<sup>-2</sup> for **DNTT** and **DBTTT** respectively, followed by the alkylated derivatives, which show  $N_{it}$  of  $8.03 \times 10^{11}$  and  $9.61 \times 10^{11}$  eV<sup>-1</sup> cm<sup>-2</sup> for **C<sub>8</sub>-DNTT** and **C<sub>12</sub>-DBTTT** respectively (**Table 3.6**).

**Table 3.6: Electrical performance of BC TFTs with 25-nm-thick OSC layer.**

Compound	$\mu$ (cm <sup>2</sup> V <sup>-1</sup> s <sup>-1</sup> )	$V_{th}$ (V)	SS (mV/dec)	$N_{it}$ (10 <sup>12</sup> eV <sup>-1</sup> cm <sup>-2</sup> )
<b>DNTT</b>	$2.3 \pm 0.1$	$-0.7 \pm 0.1$	$100 \pm 8$	$0.62 \pm 0.04$
<b>tBu-DNTT</b>	$1.4 \pm 0.1$	$-1.7 \pm 0.1$	$128 \pm 4$	$1.34 \pm 0.10$
<b>C<sub>8</sub>-DNTT</b>	$4.8 \pm 0.3$	$-0.4 \pm 0.1$	$100 \pm 3$	$0.80 \pm 0.07$
<b>DBTTT</b>	$4.7 \pm 0.1$	$-0.7 \pm 0.1$	$98 \pm 5$	$0.76 \pm 0.12$
<b>tBu-DBTTT</b>	$1.0 \pm 0.1$	$-1.5 \pm 0.1$	$147 \pm 3$	$1.72 \pm 0.07$
<b>C<sub>12</sub>-DBTTT</b>	$3.3 \pm 0.2$	$-0.6 \pm 0.1$	$108 \pm 5$	$0.96 \pm 0.13$

### 3.5.1.2 Contact resistance

Contact resistance was evaluated by recording the transfer characteristics of TFTs with channel length of 65, 115, 165, 215  $\mu\text{m}$  and channel width of 480  $\mu\text{m}$  (transfer characteristics of devices with channel length of 65, 115 and 165  $\mu\text{m}$  are reported in the **Appendix – Figure A2.6**). The width-normalized total resistance (RW) was calculated for each gate-overdrive voltage ( $V_g - V_{th}$ ) and plotted as a function of the channel length (**Figure 3.6**).

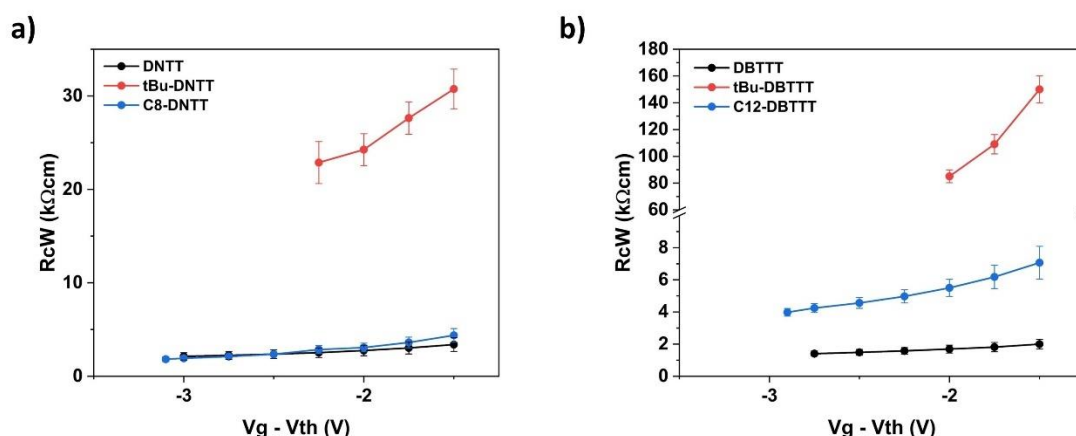


**Figure 3.6: Transmission line method applied to TC and BC TFTs with 25-nm-thick OSC layer.**

Linear fits to the width-normalized contact resistance as a function of the channel length at different values of gate-overdrive voltage.

Through a linear fitting (all the fits exhibit adjusted  $R^2 \geq 0.98$ ), the width-normalized contact resistance ( $R_C W$ ) as a function of the gate-overdrive voltage for BC and TC devices of each compound was obtained. As well, the intrinsic mobility ( $\mu_0$ ) was obtained from the slope of the linear fits (**Figure A2.12**, in the **Appendix**).

In TC devices, *tert*-butyl derivatives exhibit considerably higher  $R_C W$  compared to the respective parent molecules and alkylated derivatives over the entire range of gate-overdrive voltage (**Figure 3.7**).



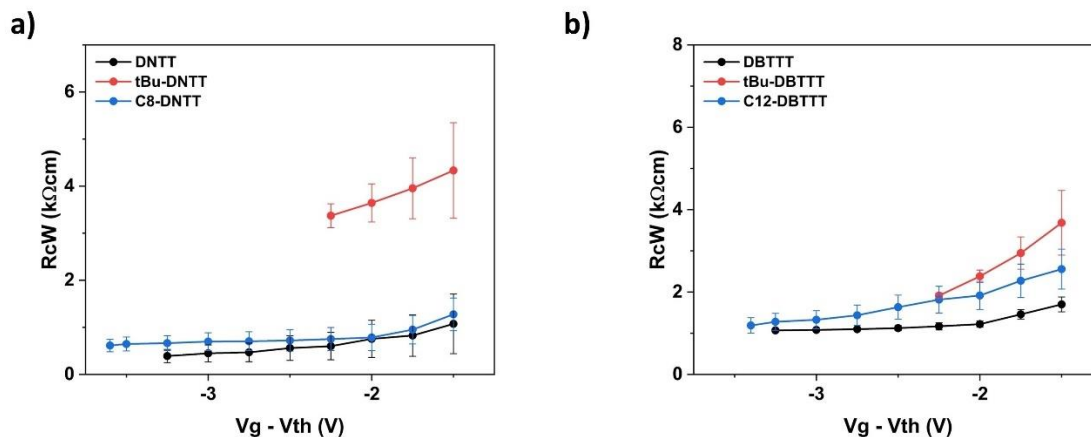
**Figure 3.7: Width-normalized contact as a function of the gate-overdrive voltage of TC TFTs with 25-nm-thick OSC layer.**

(a) DNTT, tBu-DNTT and C<sub>8</sub>-DNTT, (b) DBTTT, tBu-DBTTT and C<sub>12</sub>-DBTTT.

Specifically, for a gate-overdrive voltage of -2.0 V, **tBu-DNTT** and **tBu-DBTTT** show  $R_C W$  of 24.5  $k\Omega cm$  and of 85.0  $k\Omega cm$  respectively. These values are one order of magnitude higher than those extracted for **DNTT**, **C<sub>8</sub>-DNTT**, **DBTTT** and **C<sub>12</sub>-DBTTT** which show  $R_C W$  of 2.8, 3.1, 1.7 and 5.5  $k\Omega cm$ , respectively. In addition, the  $R_C W$  of *tert*-butyl derivatives of both families are more strongly modulated by the gate-overdrive voltage if compared to the respective parent and alkylated molecules. This can be primarily ascribed to the higher charge trap density of the former. Larger number of trap sites beneath the contact region delay charge carrier injection and as well prevent the extraction of charge carrier from the accumulation channel.<sup>[174,175]</sup> As a result, the number of mobile charge carriers and charge carrier mobility beneath the contacts are reduced. The applied gate voltage modulates both the mobile charge carrier density and charge carrier mobility that subsequently affect contact resistance.

In BC devices, all the compounds exhibit lower width-normalized  $R_C W$  compared to those extracted from TC devices over the whole range of gate-overdrive voltage. Specifically, for common fixed gate-overdrive voltage of -2.0 V,  $R_C W$  is of 0.8  $k\Omega cm$  for **DNTT**, of 3.7  $k\Omega cm$  for **tBu-DNTT**, of 0.8  $k\Omega cm$  for **C<sub>8</sub>-DNTT**, of 1.2  $k\Omega cm$  for **DBTTT**, of 2.4  $k\Omega cm$  for **tBu-DBTTT** and of 1.9  $k\Omega cm$  for **C<sub>12</sub>-DBTTT**.

$R_C W$  in BC TFTs is lower than 4.3  $k\Omega cm$  for all the compounds over the entire gate-overdrive voltage (**Figure 3.8**).



**Figure 3.8: Width-normalized contact as a function of the gate-overdrive voltage of BC TFTs with 25-nm-thick OSC layer.**

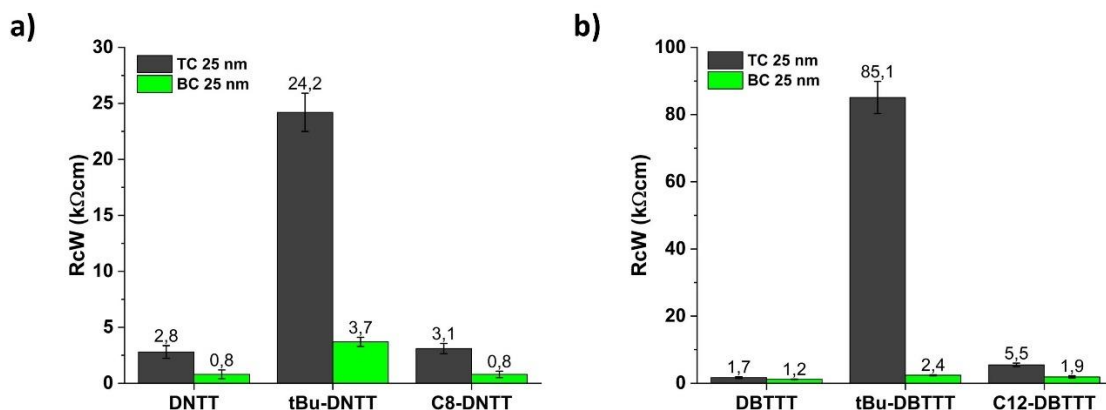
(a) **DNTT**, **tBu-DNTT** and **C<sub>8</sub>-DNTT**, (b) **DBTTT**, **tBu-DBTTT** and **C<sub>12</sub>-DBTTT**.

It is worth to emphasize two aspects. First off, *tert*-butyl derivatives have a greater  $R_C W$  than their respective parent molecules and alkylated derivatives. However, this difference in  $R_C W$  is larger TC TFTs, while it is milder in BC TFTs. Specifically, in TC TFTs,  $R_C W$  of **tBu-DNTT** is  $\approx 8$  times larger than **DNTT** and **C<sub>8</sub>-DNTT**, while and  $R_C W$  of **tBu-DBTTT** is  $\approx 50$  times larger than **DBTTT** and  $\approx 15$  times larger than **C<sub>12</sub>-DBTTT**. In contrast in BC TFTs,  $R_C W$  of **tBu-DNTT** is  $\approx 5$  times larger than **DNTT** and **C<sub>8</sub>-DNTT**, while and  $R_C W$  of **tBu-DBTTT** is  $\approx 2$  times larger than **DBTTT** and almost similar to **C<sub>12</sub>-DBTTT**. Second, the  $R_C W$  dependence on the applied gate-overdrive voltage of the *tert*-butyl derivatives is noticeably less pronounced, compared to the TC counterparts. This is explained by the lower charge trap density of BC TFTs, given that the contribution of the traps in the OSC bulk beneath the contact is neglected.

As already reported,<sup>[85]</sup> BC devices can show lower contact resistance along with better electrical performances compared to TC devices if conditions are

met. First, a dielectric layer with a thickness lower than 30 nm is required. For this purpose, materials with high dielectric constant must be employed as  $\text{AlO}_x$ ,  $\text{TiO}_x$  or  $\text{HfO}_x$ . Second, the formation of a PFBT-SAM on the surface of gold contacts is needed to ensure a uniform organic semiconductor morphology across the contact-channel interface and to minimize the energy barrier height between the contacts and the OSC. Particularly, it has been shown that TC TFTs based on **DPh-DNTT** exhibit  $R_cW$  up to 2 times lower compared to the TC counterparts. This has been obtained by fabricating TFTs with 3-nm-thick dielectric layer of  $\text{Al}_2\text{O}_3$ , additionally functionalized with a TDPA-SAM, and by using PFBT/Au contacts.<sup>[85]</sup>

A similar trend is unveiled in our experiments for TFTs based on parent molecules and alkylated derivatives. The width-normalized contact resistance extracted in BC devices is 1.3 times lower for **DNTT**, 2.8 times lower for **C<sub>8</sub>-DNTT**, 1.4 times lower for **DBTTT** and 2.9 times lower for **C<sub>12</sub>-DBTTT**, than the TC devices. Surprisingly, a dramatic reduction of  $R_cW$  in BC TFTs based on *tert*-butyl derivatives was observed, with values about 7- and 35-fold lower than TC based on **tBu-DNTT** and **tBu-DBTTT** respectively (**Figure 3.9**).

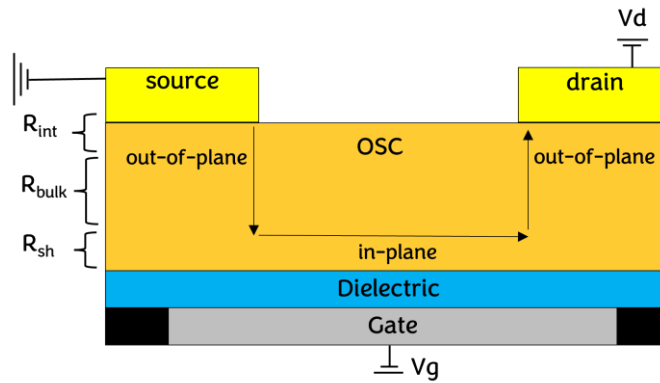


**Figure 3.9: Width-normalized contact resistance of TC and BC TFTs.** (a) **DNTT**, **tBu-DNTT-tBu** and **C<sub>8</sub>-DNTT**, (b) **DBTTT**, **tBu-DBTTT-tBu** and **C<sub>12</sub>-DBTTT**. Gate-overdrive voltage = -2.0 V

This significant variation in contact resistance between the two device geometries can be attributed to the involvement of the OSC resistance beneath the contacts, as well as the lower nominal injection barrier in BC TFTs due to the PFBT treatment of the gold contacts. In TC devices the contact resistance ( $R_c$ ) is given by the sum of the bulk resistance ( $R_{\text{bulk}}$ ), that is the resistance associated with the charge transport through the OSC

thickness, and the interface resistance ( $R_{\text{int}}$ ) that is the resistance associated with the injection barrier between the metal contact and the OSC. In BC devices, charges are injected into the accumulation channel straightaway, removing  $R_{\text{bulk}}$  contribution.

When considering the direction of current density in TFTs, two charge transport directions may be defined: in-plane and out-of-plane (**Figure 3.10**). The former is parallel to the OSC/dielectric interface, whereas the latter is perpendicular to the OSC/dielectric interface. The in-plane mobility ( $\mu_{\text{in}}$ ) is the mobility commonly extracted in OFETs by using the gradual channel approximation (please note that the term "charge carrier mobility" is always referred to the effective in-plane charge carrier mobility extracted from transfer characteristics using **equation 1.20**,<sup>+++</sup> unless otherwise stated). Consequently, the sheet resistance ( $R_{\text{sh}}$ ) is the resistance associated to charge transport through the gate-induced carrier channel, which can be limited by the presence of interfacial traps, grain boundaries and defects.



**Figure 3.10:** Schematic illustration of the in-plane and out-of-plane directions of charge transport in a staggered device.

On the other hand, poor out-of-plane charge carrier mobility ( $\mu_{\text{out}}$ ), which is typical in TFTs based on organic semiconductors, limits out-of-plane charge transport. As already shown, OSCs tend to pack standing approximately upright with respect to the dielectric when vacuum deposited. This molecular packing enhances the overlap of HOMO wavefunctions along the in-plane direction, which in turns boosts the in-plane mobility. Conversely, the HOMO wavefunctions overlap along the out-of-plane direction is strongly weakened

<sup>+++</sup> **Equation 1.20**  $\rightarrow \mu_{\text{eff},\text{lin}} = \frac{L}{w c_i V_d} \left. \frac{\partial I_d}{\partial V_g} \right|_{V_d}$

by the larger distance between the aromatic cores. Moreover, the introduction of substituents as in the case of *tert*-butyl and alkylated derivatives, further increases the distance between the molecular cores, resulting in poorer out-of-plane charge transport. At last, in TC TFTs charge transport along the out-of-plane direction also depends on the semiconductor thickness ( $t_{\text{osc}}$ ), wherein thicker OSC film leads to an increased  $R_{\text{bulk}}$ .

The results obtained from TC and BC devices based on the investigated compounds emphasize, first, the reduction in contact resistance when adopting a coplanar geometry. Second, they show that molecules with poor out-of-plane charge transport, such as *tert*-butyl and alkylated derivatives, are more influenced by device geometry than those with better out-of-plane charge transport (i.e., **DNTT** and **DBTTT**).

What remains unclear is the reason behind the significant difference in  $R_{\text{C}}W$  between the *tert*-butyl derivatives and the alkylated derivatives in TC TFTs. In fact, a higher  $R_{\text{bulk}}$  in alkylated derivatives than in *tert*-butyl derivatives is anticipated because the lengthy alkyl chains force a larger distance between the molecular cores in the out-of-plane direction. This would lead to high  $R_{\text{C}}W$ , contrary to our experimental findings, which show that  $R_{\text{C}}W$  in TC TFTs based on *tert*-butyl derivatives is one order of magnitude larger than in TC TFTs based on alkylated derivatives. The latter reveal  $R_{\text{C}}W$  of the same order of magnitude of the parent molecules.

Contact resistance in TC TFTs does not depend only on  $R_{\text{bulk}}$ , but also on  $R_{\text{int}}$ ,  $R_{\text{sh}}$  and on the extension of the charge injection area. The next paragraphs are focused on the study of these parameters to understand the reason behind the difference in  $R_{\text{C}}W$  between the core molecules, the alkylated derivatives and the *tert*-butyl derivatives.

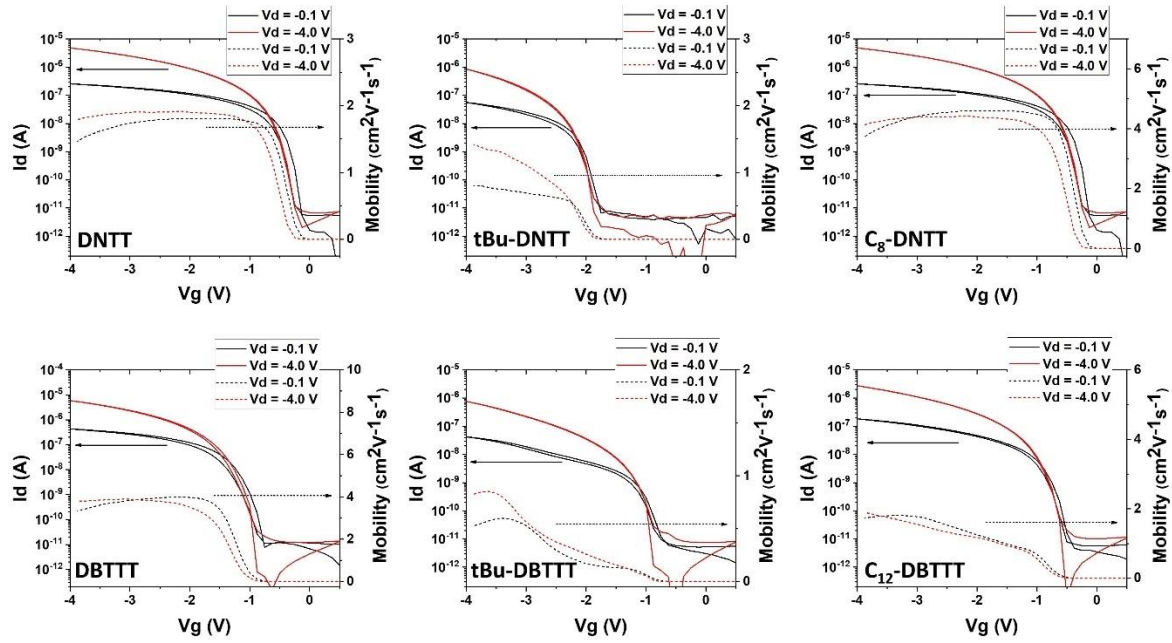
### 3.5.2 TFTs with 80-nm-thick OSC layer

#### 3.5.2.1 Electrical performances

The electrical performances of TC and BC TFTs with 80-nm-thick OSC layer were evaluated by recording transfer characteristics, depicted in **Figure 3.11** and **3.12**.

For TC devices with 80-nm-thick OSCs, the parent molecules and the alkylated derivatives exhibit higher charge carrier mobility and lower threshold voltage than the *tert*-butyl derivatives, as in the case of 25-nm-thick OSC. Specifically, the extracted mobility values are of  $1.8 \text{ cm}^2\text{V}^{-1}\text{s}^{-1}$  for **DNTT**,  $4.0 \text{ cm}^2\text{V}^{-1}\text{s}^{-1}$  for **DBTTT**,  $4.1 \text{ cm}^2\text{V}^{-1}\text{s}^{-1}$  for **C<sub>8</sub>-DNTT** and  $1.5 \text{ cm}^2\text{V}^{-1}\text{s}^{-1}$  for **C<sub>12</sub>-DBTTT**. TC TFTs based on **tBu-DNTT** and **tBu-DBTTT**, on the other hand,

show reduced charge carrier mobility of  $0.6 \text{ cm}^2\text{V}^{-1}\text{s}^{-1}$  and  $0.3 \text{ cm}^2\text{V}^{-1}\text{s}^{-1}$ , respectively. Threshold voltage is lower for the parent compound and alkylated derivatives, with values ranging from -0.8 V to -1.2 V, than for tert-butyl derivatives, with values ranging from -1.7 V to -2.0 V. (Table 3.7).



**Figure 3.11: Transfer characteristics of TC TFTs with 80-nm-thick OSC layer.**

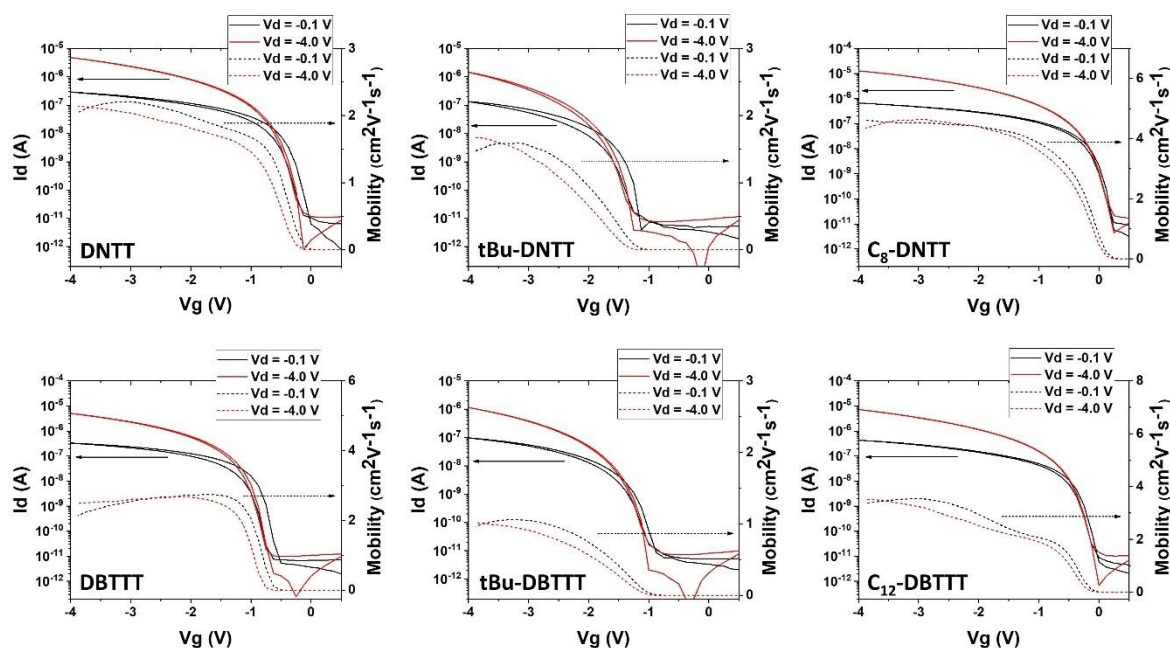
Solid lines and dashed lines are referred to drain current and mobility respectively. All TFTs have  $W/L = 480/215 \text{ }\mu\text{m}$ .

**Table 3.7: Electrical performance of TC TFTs with 80-nm-thick OSC layer.**

Compound	$\mu \text{ (cm}^2\text{V}^{-1}\text{s}^{-1}\text{)}$	$V_{th} \text{ (V)}$	SS (mV/dec)
DNTT	$1.8 \pm 0.1$	$-0.7 \pm 0.1$	$112 \pm 2$
tBu-DNTT	$0.7 \pm 0.1$	$-2.0 \pm 0.2$	$155 \pm 7$
C <sub>8</sub> -DNTT	$4.2 \pm 0.3$	$-0.6 \pm 0.2$	$122 \pm 3$
DBTTT	$4.0 \pm 0.2$	$-1.3 \pm 0.1$	$129 \pm 4$
tBu-DBTTT	$0.4 \pm 0.1$	$-1.7 \pm 0.1$	$190 \pm 9$
C <sub>12</sub> -DBTTT	$1.5 \pm 0.2$	$-1.2 \pm 0.1$	$143 \pm 11$

The primary difference between TC TFTs with 80-nm-thick OSC layers and those with 25-nm-thick layers is the former's larger subthreshold swing. For

all compounds except **DNTT**, SS was found to be between 10 and 27 meV/dec greater than the respective devices based on a 25-nm-thick OSC layer. (**Table 3.7**). This could be attributed to the increased number of trap sites formed as a result of the increased OSC thickness. In contrast, **DNTT**-based devices exhibit similar SS for the OSC thicknesses, suggesting that the OSC thickness has just a minor effect on the charge trap density for **DNTT**.



**Figure 3.12: Transfer characteristics of BC TFTs with 80-nm-thick OSC layer.**

Solid lines and dashed lines are referred to drain current and mobility respectively. All TFTs have  $W/L = 480/215 \mu\text{m}$ .

The same trend of mobility and threshold voltage within the investigate compounds showed in TC TFTs, was observed in BC devices with 80-nm-thick OSCs. As compared to *tert*-butyl derivatives, the parent molecules and alkylated derivatives displayed higher charge carrier mobility and lower  $V_{th}$ .

Particularly, the parent molecules exhibit charge carrier mobility up to  $2.4 \text{ cm}^2\text{V}^{-1}\text{s}^{-1}$  for **DNTT**, up to  $2.9 \text{ cm}^2\text{V}^{-1}\text{s}^{-1}$  for **DBTTT**, while the alkylated derivatives show charge carrier mobility up to  $4.9 \text{ cm}^2\text{V}^{-1}\text{s}^{-1}$  for **C8-DNTT** and up to  $3.2 \text{ cm}^2\text{V}^{-1}\text{s}^{-1}$  for **C12-DBTTT**. BC TFTs based on **tBu-DNTT-tBu** and **tBu-DBTTT-tBu** show charge carrier mobility of  $1.4 \text{ cm}^2\text{V}^{-1}\text{s}^{-1}$  and  $0.9 \text{ cm}^2\text{V}^{-1}\text{s}^{-1}$ , respectively. Threshold voltage was found to be in the range of -0.5 and -1.2 V for the parent and alkylated molecules, and in the range of -1.6 and -1.7 V for the *tert*-butyl derivatives.

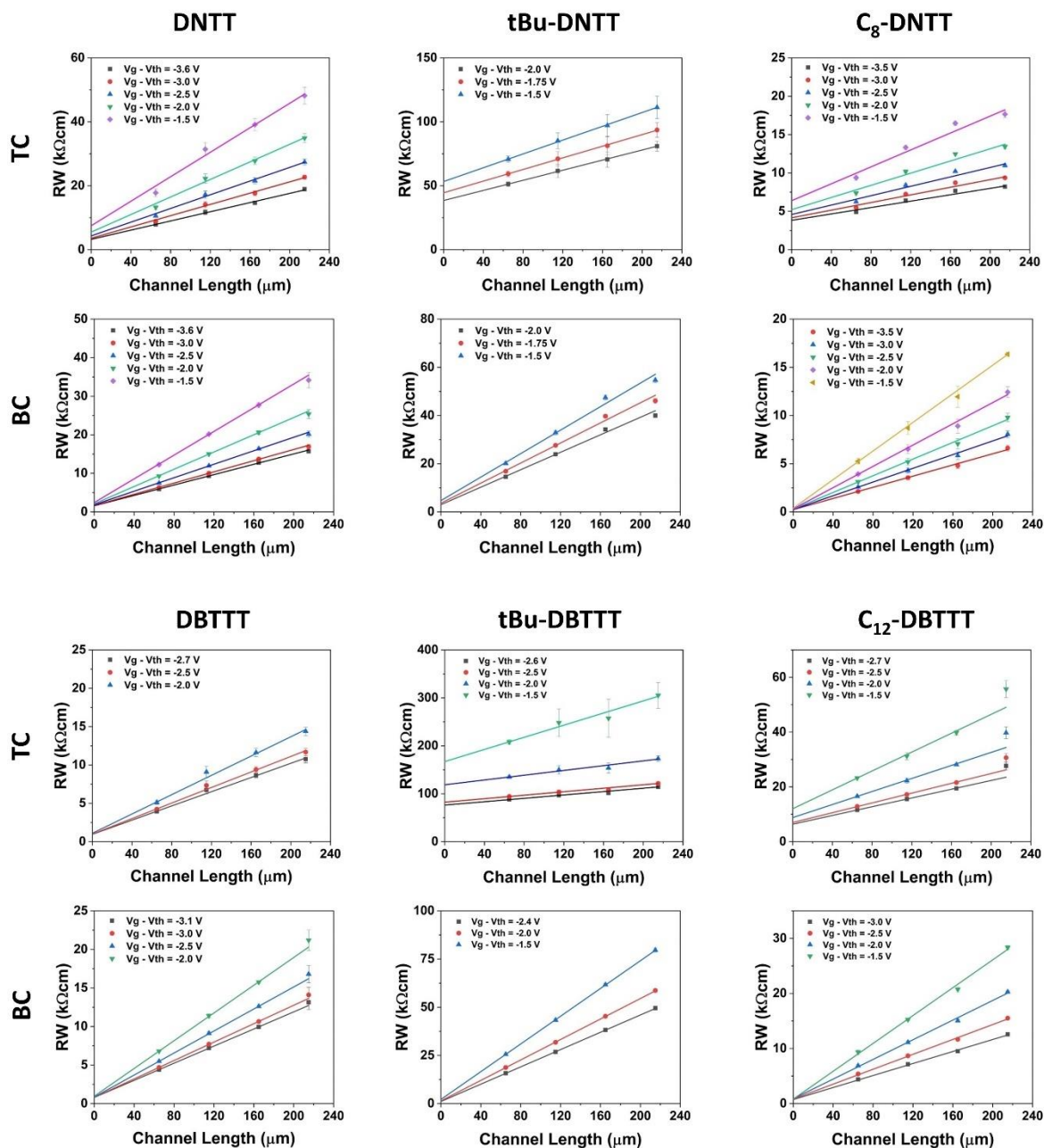
Interestingly, for each compound, the extracted SS from BC TFTs with 80-nm-thick OSC layer exhibit comparable values to those from BC TFTs with a 25-nm-thick OSC layer. The calculated interfacial trap density values (**Table 3.8**) unveil no significant difference between the two OSC thicknesses. This is consistent with the fact that the greater SS in TC devices is caused by the OSC bulk volume through which charges must pass to reach the gate-induced accumulation channel. Because the contact edge of BC TFTs is on the same plane as the accumulation channel, the increase in OSC thickness has no effect on the charge trap density.

**Table 3.8: Electrical performance of BC TFTs with 80-nm-thick OSC layer.**

Compound	$\mu$ (cm <sup>2</sup> V <sup>-1</sup> s <sup>-1</sup> )	V <sub>th</sub> (V)	SS (mV/dec)	N <sub>it</sub> (10 <sup>12</sup> eV <sup>-1</sup> cm <sup>-2</sup> )
<b>DNTT</b>	2.4 ± 0.1	-0.5 ± 0.1	97 ± 2	0.74 ± 0.05
<b>tBu-DNTT</b>	1.4 ± 0.1	-1.7 ± 0.1	136 ± 11	1.51 ± 0.27
<b>C<sub>8</sub>-DNTT</b>	4.9 ± 0.2	-0.4 ± 0.1	101 ± 6	0.82 ± 0.15
<b>DBTTT</b>	2.9 ± 0.2	-0.9 ± 0.1	107 ± 3	0.94 ± 0.08
<b>tBu-DBTTT</b>	0.9 ± 0.1	-1.6 ± 0.1	151 ± 4	1.81 ± 0.10
<b>C<sub>12</sub>-DBTTT</b>	3.2 ± 0.2	-0.8 ± 0.1	114 ± 4	1.08 ± 0.11

### 3.5.2.2 Contact resistance

The width-normalized contact resistance of TC and BC TFTs with 80-nm-thick OSC layer was evaluated with TLM by recording transfer characteristics for devices with channel length of 65, 115, 165 and 215  $\mu$ m (transfer characteristics of devices with channel length of 65, 115 and 165  $\mu$ m are reported in the **Appendix – Figure A2.7**) The width-normalized contact resistance was derived as a function of the gate-overdrive voltage, as in the case of devices with 25-nm-thick OSC afterwards (**Figure 3.13**).



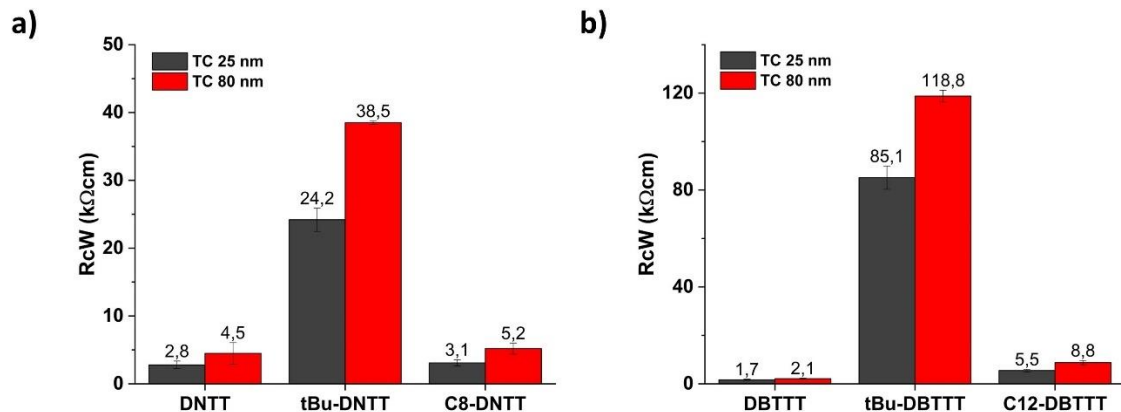
**Figure 3.13: Transmission line method applied to TC and BC TFTs with 80-nm-thick OSC layer.**

Linear fits to the width-normalized contact resistance as a function of the channel length at different values of gate-overdrive voltage.

Similarly, the intrinsic mobility ( $\mu_0$ ) was obtained from the slope of the linear fits (**Figure A2.12**, in the **Appendix**).

For all the compounds over the entire range of gate-overdrive voltage,  $R_cW$  increased in TC TFTs with an 80-nm-thick OSC layer as compared to TC TFTs with a 25-nm-thick OSC layer. Particularly, for gate-overdrive voltage of -2.0 V, the extracted  $R_cW$  is of 4.5 kΩcm for **DNTT**, 38.5 kΩcm for **tBu-**

**DNTT-tBu**, 5.2 k $\Omega$ cm for **C<sub>8</sub>-DNTT**, 2.1 k $\Omega$ cm for **DBTTT**, 118.8 k $\Omega$ cm for **tBu-DBTTT-tBu** and of 8.8 k $\Omega$ cm for **C<sub>12</sub>-DBTTT** ( $R_cW$  values are between 1.2 and 1.6 times higher than TC TFTs based on 25-nm-thick OSC layer, see **Figure 3.14**). The dependence of contact resistance on OSC thickness in staggered geometry results from the extra space that charges must traverse following injection from the source contact to reach the accumulation layer.<sup>[42,73,74]</sup> Moreover, the augmented thickness of the OSC layer lead to higher charge-trap density which disfavour charge transport in the out-of-plane direction.<sup>[79]</sup> As a result, an OSC layer thickness of 20 to 30 nm is commonly used in TC TFTs, as it ensures a minimal thickness to form a continuous film between the source and drain contacts while preventing a significant contribution of the OSC thickness to contact resistance. It is worth mentioning that when the OSC layer thickness increased from 25 nm to 80 nm (more than threefold),  $R_cW$  was found to be only between 1.2 and 1.6 times higher – depending on the compound – in TC TFTs with the thickest OSC layer. This indicates that  $R_cW$  depends nonlinearly on OSC thickness.<sup>[176]</sup>

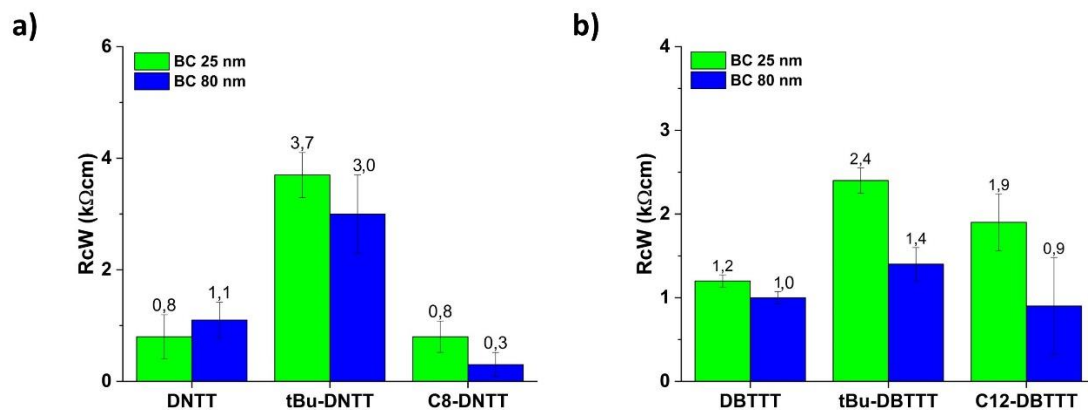


**Figure 3.14: Width-normalized contact resistance of TC TFTs with 80-nm-thick OSC layer.**

(a) **DNTT**, **tBu-DNTT** and **C<sub>8</sub>-DNTT**, (b) **DBTTT**, **tBu-DBTTT** and **C<sub>12</sub>-DBTTT**. Gate-overdrive voltage = -2.0 V.

In BC TFTs, the augmented OSC thickness is not reflected in an increased  $R_cW$ . On the contrary, compared to BC TFTs made with 25-nm-thick OSC, all the compounds exhibit similar or slightly reduced width-normalized contact resistance, over the entire range of gate-overdrive voltage. Specifically, for gate-overdrive voltage of -2.0 V, the extracted  $R_cW$  is 1.1 k $\Omega$ cm for **DNTT**, 3.0 k $\Omega$ cm for **tBu-DNTT-tBu**, 0.3 k $\Omega$ cm for **C<sub>8</sub>-DNTT**, 1.0

k $\Omega$ cm for **DBTTT**, 1.4 k $\Omega$ cm for **tBu-DBTTT-tBu** and of 0.9 k $\Omega$ cm for **C<sub>12</sub>-DBTTT** (Figure 3.15).



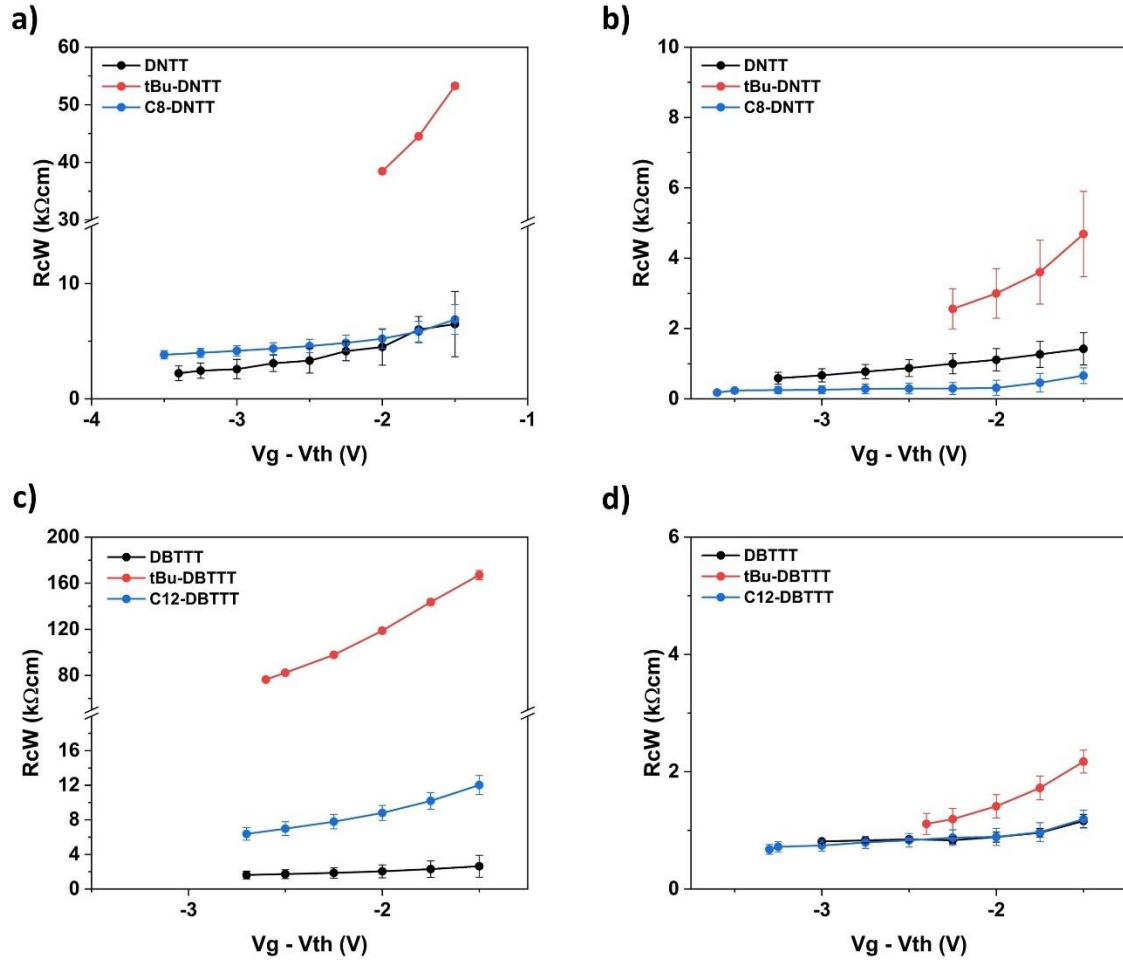
**Figure 3.15: Width-normalized contact resistance of BC TFTs with 80-nm-thick OSC layer.**

(a) **DNTT**, **tBu-DNTT** and **C<sub>8</sub>-DNTT**, (b) **DBTTT**, **tBu-DBTTT** and **C<sub>12</sub>-DBTTT**. Gate-overdrive voltage = -2.0 V

In case of coplanar geometry, charges are injected from the source contact into the accumulation layer straightaway, hindering the contribution of the OSC volume beneath the contacts to the contact resistance. Hence, the increase of semiconductor thickness does not result in higher contact resistance. On the contrary, this can lead to an improved OSC overlay along the contact-to-channel region and to an increased charge injection area, which may have a beneficial effect on the contact resistance. In coplanar geometry the charge injection area roughly corresponds to the product between the channel width and the OSC thickness. It is worth noting that OSC thickness larger than the thickness of the source contact does not lead to larger injection area, since (to first approximation) no charge exchange occurs above the contacts.<sup>[86,177]</sup>

At last, the fabrication of TC and BC TFTs with an 80-nm thick OSC layer confirmed the trend observed in devices with a 25-nm thick OSC layer (Figure 3.16). The contact resistance of the parent molecules and their alkylated derivatives for TC devices is similar, with values less than 9 k $\Omega$ cm. *Tert*-butyl derivatives, on the other hand, unveil  $R_C W$  values that are one or two orders of magnitude larger than the respective parent and alkylated molecules, with values of 38.5 k $\Omega$ cm and 118.8 k $\Omega$ cm for **tBu-DNTT** and **tBu-DBTTT**, respectively. For BC devices with 80-nm-thick OSC layer, all the compounds exhibit  $R_C W$  lower than 4 k $\Omega$ cm, as in the case of BC TFTs with

25-nm-thick OSC. In addition, the extracted  $R_cW$  values always lower than those extracted for TC devices with 80-nm-thick OSC layer, over the entire range of gate-overdrive voltage.



**Figure 3.16: Width-normalized contact as a function of the gate-overdrive voltage TFTs with 80-nm-thick OSC layer.**

$R_cW$  of DNTT, tBu-DNTT and C<sub>8</sub>-DNTT extracted from (a) TC TFTs and (b) BC TFTs.  $R_cW$  of DBTTT, tBu-DBTTT and C<sub>12</sub>-DBTTT extracted from (c) TC TFTs and (d) BC TFTs.

### 3.6 Out-of-plane charge transport

*Conductive atomic force microscopy measurements were performed in collaboration with Dr. Nicholas Turetta, at Supramolecular Science and Engineering Institute (ISIS) of Strasbourg, under the supervision of Prof. Paolo Samorì.*

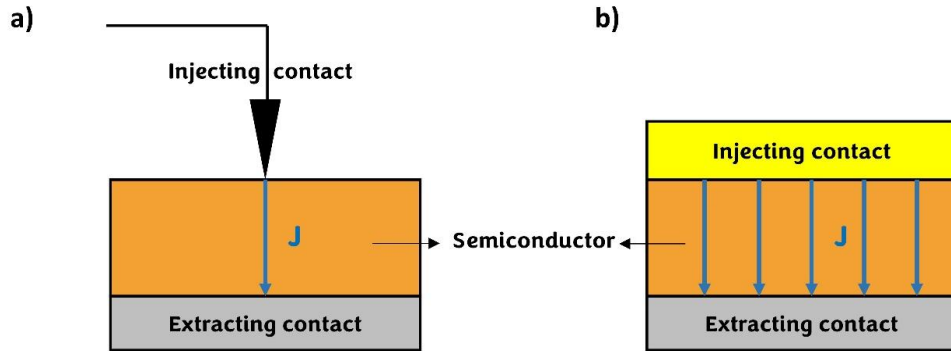
The out-of-plane charge transport properties of the investigated compounds were assessed by using conductive atomic force microscopy (C-AFM). C-AFM enables the simultaneous measurement of the topography and conductivity of a sample, by scanning the sample surface with a conductive tip which acts as a nanoscale electrical probe. Current density-voltage (J-V) characteristics are obtained via C-AFM on a single point of the material surface (with the extension of the probed area in the range of tens of nm<sup>2</sup>) and to record material surface current mapping at given bias. Since the surface current is mapped at fixed bias, C-AFM can be considered as a local probe for vertical charge transport.

Current density-voltage characteristics obtained by C-AFM can be fitted by the space-charge limited current (SCLC) model to extract the out-of-plane mobility. In a typical configuration, the semiconductor is sandwiched between two electrodes, with one of them being an injection blocking electrode.<sup>[178]</sup> SCLC implies unipolar injection of charge carriers from the other ohmic contact into the bulk of the semiconductor. At low bias voltage, the flow of current is characterized by an ohmic behaviour ( $J \propto V$ ). By increasing the applied bias voltage, charges accumulate around the electrode, leading to the formation of a space charge region, that is considered as a continuum distribution of charges rather than space localized charges. This “cloud” of charges is accumulated in proximity of the injection electrode, due to the inability of the material to transport the charges fast enough in the opposite direction.<sup>[52,179]</sup> Therefore, at a given applied external electric field an equilibrium stage is reached, and the concentration of injected charges is comparable or higher than the free charge carrier concentration. At this stage, the current density exhibits a quadratic dependence on the bias voltage ( $J \propto V^2$ ). In absence of active traps, SCLC can be modelled by the Mott-Gurney charge model, as follow:

$$J = \frac{9}{8} \varepsilon \varepsilon_0 \mu \frac{V^2}{L^3} \quad (3.1)$$

where  $\varepsilon$  is the relative dielectric constant of the OSC,  $\varepsilon_0$  is the vacuum permittivity,  $V$  is the applied voltage bias and  $L$  is the channel length (thickness of the OSC). In this case,  $\mu$  is referred to the charge carrier mobility along the thickness of the OSC and hence to the out-of-plane mobility. This

expression was first derived for J-V curves extracted from diodes with parallel-plane geometry and eventually applied for C-AFM<sup>[180–183]</sup> (**Figure 3.17**).



**Figure 3.17: Sample geometry for SCLC measurements.**

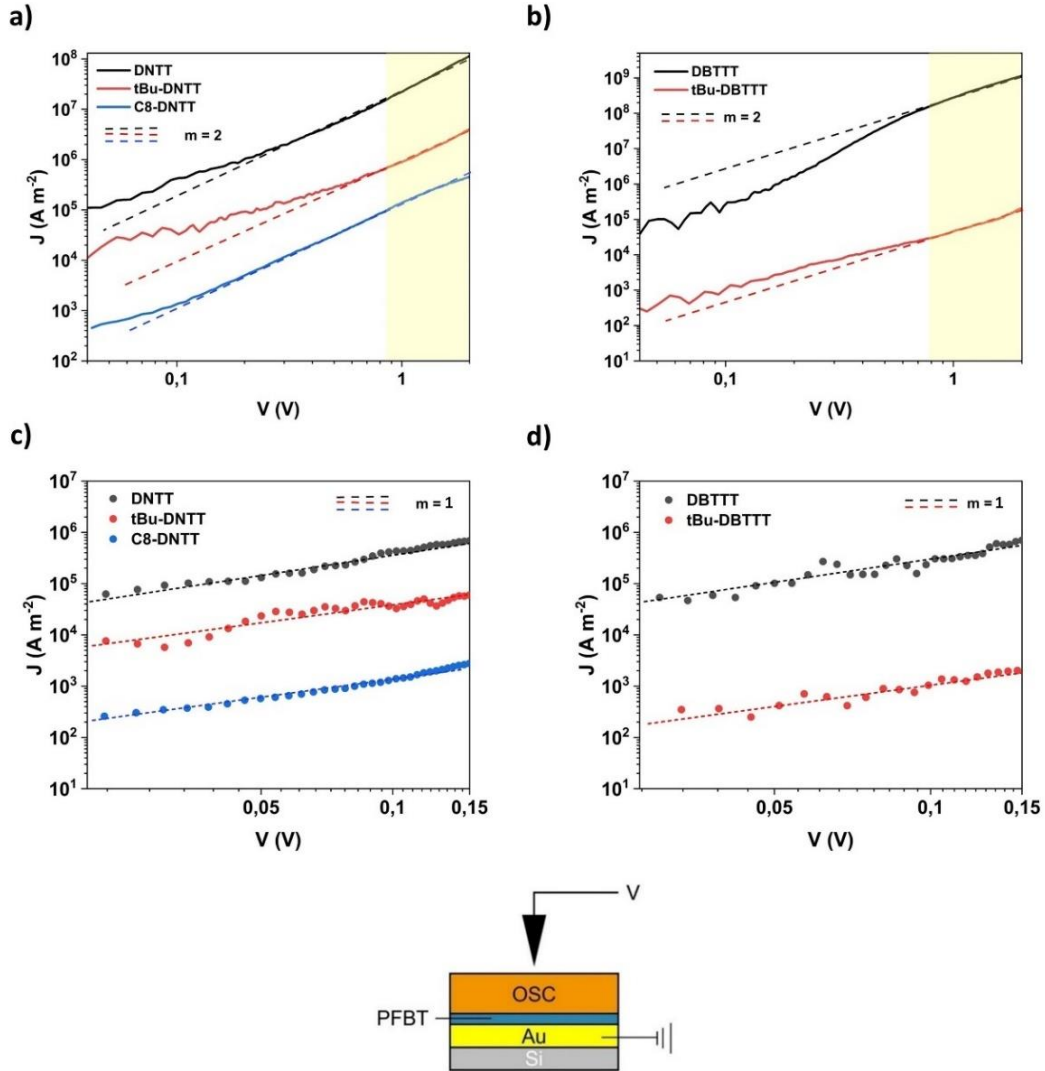
Schematic representation of (a) C-AFM set-up presenting a tip-plane geometry and (b) diode parallel-plane geometry. The current density direction is shown by blue arrows.

More accurate expressions for J-V current collected by C-AFM with the view to extract a more reliable  $\mu$  value have been presented.<sup>[184–186]</sup> Reid *et al.*,<sup>[184]</sup> proposed the introduction of empirical parameters and factors obtained from both finite element simulations and the comparison within J-V curves extracted from diodes and C-AFM. This model led to charge carrier mobility values 3 orders of magnitude lower compared to the ones obtained from Mott-Gurney model. However, the Reid model has been developed for thick semiconductor polymers and therefore could not be appropriate for nm-thick films, as in our case. In summary, considering that no accurate model has been yet established for nm-thick layers of small-molecule OSCs, the extracted values of mobility presented in this paragraph must be considered more qualitatively rather than quantitatively. Despite the selected model, the trend within analysed semiconductors is maintained, showing which one opposes the highest (or lowest) resistance along the out-of-plane direction.

### 3.6.1 Evaluation of the out-of-plane mobility

In a typical experimental set-up, Si/SiO<sub>2</sub> wafer is coated with 30-nm-thin layer of gold and consequently immersed in a PFBT solution in isopropanol, which results in the formation of a PFBT-SAM. Eventually, a thin layer of OSC ( $\approx 10$  nm) is vacuum-deposited onto the substrate (the extended

procedure is reported in **Chapter 5**). The Au surface is electrically grounded to the sample holder of the instrument where the voltage bias is applied by Pt/Ir tip, as depicted in **Figure 3.18**.



**Figure 3.18: J-V characteristics measured using C-AFM on thin films plotted in logarithmic scale.**

(a) J-V characteristics of **DNTT**, **tBu-DNTT** and **C<sub>8</sub>-DNTT** thin films, (b) J-V characteristics of **DBTTT** and **tBu-DBTTT** thin films. The highlighted region (between 0.8 and 2.0 V) indicates the SCLC regime, while the dashed lines serve as references displaying lines with power coefficient ( $m$ ) = 2. (c) J-V characteristics of **DNTT**, **tBu-DNTT**, **C<sub>8</sub>-DNTT** thin films and (d) J-V characteristics of **DBTTT** and **tBu-DBTTT** thin films for bias voltage < 0.15 V (here the dashed lines have a power coefficient  $m$  = 1). On the bottom: schematic representation of the experimental set-up employed for J-V characteristics measurement via C-AFM.

A set of at least 20 J-V curves were recorded in different region of the sample, by displacing the tip over a  $5 \times 5$  array of points separated by 200 nm in a  $1 \times 1 \mu\text{m}^2$  surface. The measurements were performed at controlled relative humidity ( $\text{RH} < 5\%$ ) to avoid potential chemical reactions, that may affect the electrical response of the materials.<sup>[187]</sup>

The contact area between the C-AFM tip and the surface of the organic semiconductors was estimated to  $\approx 78 \text{ nm}^2$ , by assuming  $\approx 0.5 \text{ nm}$  of tip indentation from the deflection error signal and a hemispherical shape at the apex of the C-AFM tip (with a nominal tip diameter of 25 nm).<sup>[184]</sup>

It is important to underline that the topography and the crystallinity of OSCs deposited onto Au/PFBT were analysed by AFM and XRD, confirming that all the compounds form crystalline films with the molecules standing approximately upright with respect to the substrate (see **Paragraph 3.4**). Therefore, the current-voltage characteristics collected via C-AFM refer to charge transport along the direction perpendicular to the  $\pi$ -stacking direction of neighbouring molecules.

Except for **C<sub>12</sub>-DBTTT**, the current density acquired from the thin films exhibit a quadratic dependence on the bias voltage for  $V > 0.8 \text{ V}$ , as depicted by the dashed lines and the yellow highlighted region in **Figure 3.18**. In this range, the Mott-Gurney model can be employed to extract the out-of-plane mobility of the compounds. Moreover, it is worth noting that the current density exhibits a linear dependence on the applied bias for  $V < 0.15 \text{ V}$ , indicating an ohmic injection of charge carriers.

As expected, the parent molecules exhibit the highest  $\mu_{\text{out}}$ , with value of  $0.22 \text{ cm}^2\text{V}^{-1}\text{s}^{-1}$ , both for **DNTT** and **DBTTT**. The *tert*-butyl derivatives show  $\mu_{\text{out}}$  3 orders of magnitude lower compared to the parent molecules, with values of  $2.8 \times 10^{-4}$  and  $1.1 \times 10^{-4} \text{ cm}^2\text{V}^{-1}\text{s}^{-1}$ , for **tBu-DNTT** and **tBu-DBTTT** respectively. At last, the extracted  $\mu_{\text{out}}$  for **C<sub>8</sub>-DNTT** is the lowest, giving value of  $3.2 \times 10^{-5} \text{ cm}^2\text{V}^{-1}\text{s}^{-1}$  ( $\mu_{\text{out}}$  values with relative standard deviations are displayed in **Table 3.9**). **C<sub>12</sub>-DBTTT** thin film did not show a detectable current response upon the application of bias voltage, most likely due to the poor charge transport that is hindered by the long alky chains. The current response shown by the sample was already close to the limit of the current amplifier sensitivity (0.1 pA) in **C<sub>8</sub>-DNTT** thin films. The spatial extension of the alkyl chains possessing four more carbon atoms may further reduce the out-of-plane mobility due to lower HOMO wavefunctions overlap. Therefore, we suppose that  $\mu_{\text{out}}$  of **C<sub>12</sub>-DBTTT** is lower than  $\mu_{\text{out}}$  of **C<sub>8</sub>-DNTT** ( $< 3.2 \times 10^{-5} \text{ cm}^2\text{V}^{-1}\text{s}^{-1}$ ).

The out-of-plane mobilities extracted for **DNTT** and **DBTTT** are of the same order of magnitude of those reported for rubrene ( $0.19 \text{ cm}^2\text{V}^{-1}\text{s}^{-1}$ ) obtained by using admittance spectroscopy measurements in diode with planar-parallel geometry.<sup>[188]</sup> Likewise, the out-of-plane mobility of **C8-DNTT** is similar to those reported for alkylated-NDIs ( $10^{-5}/10^{-6} \text{ cm}^2\text{V}^{-1}\text{s}^{-1}$ ), obtained by applying the SCLC model on J-V curves collected via C-AFM.<sup>[150]</sup> These results reflect the poorer charge transport along the thickness of OSC when the molecular core is functionalized with alkyl chains substituents.

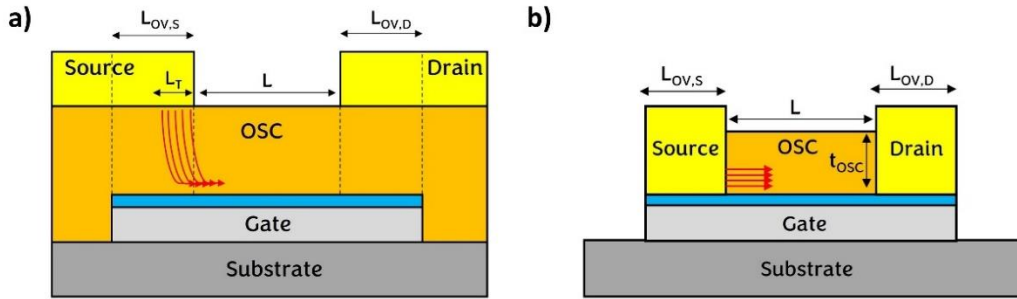
In conclusion, we found the same trend for both DNTT and DBTTT families, confirming that the more efficient charge transport along the out-of-plane direction is exhibited by the parent molecules, followed by the *tert*-butyl and alkylated derivatives.

**Table 3.9: Out-of-plane mobility ( $\mu_{\text{out}}$ ) obtained from J-V characteristics.** Out-of-plane mobility is extracted by using the Mott-Gurney model on averaged J-V curves in SCLC regime (bias voltage  $> 0.8 \text{ V}$ ).

Compound	$\mu_{\text{out}} (\text{cm}^2\text{V}^{-1}\text{s}^{-1})$
<b>DNTT</b>	$(2.2 \pm 0.2) \times 10^{-1}$
<b>tBu-DNTT</b>	$(2.8 \pm 0.1) \times 10^{-4}$
<b>C8-DNTT</b>	$(3.2 \pm 0.2) \times 10^{-5}$
<b>DBTTT</b>	$(2.2 \pm 0.1) \times 10^{-1}$
<b>tBu-DBTTT</b>	$(1.1 \pm 0.1) \times 10^{-4}$

### 3.7 Charge injection area

In first approximation, TC TFTs are characterized by larger contact injection area ( $A_{inj}$ ) than the BC counterpart. In BC TFTs injection occurs from the contact edge, with a contact injection area that roughly corresponds to the product between the channel width and the thickness of the OSC.<sup>[177]</sup> For TC TFTs, in principle, injection can involve all the contact area facing the gate. However, in the framework of current crowding model, not all the gate-to-contact overlap ( $L_{ov}$ ) contributes to the total injection area. A characteristic injection length has been defined, referred as transfer length ( $L_T$ ), which represents the effective length under the contacts through which 63% of charges are injected into the OSC (**Figure 3.19**).<sup>[81,94]</sup>



**Figure 3.19: Charge carrier injection in TC and BC TFTs.**

Schematic illustration of (a) injection underneath the contact in TC geometry and (b) injection through the contact edge in BC geometry. The red arrows represent the flow of the injected charges. In TC devices the 63% of charges are injected over a characteristic length denoted as transfer length ( $L_T$ ).

Therefore, in TC TFTs the contact injection area is expected to be about equal to the product of the channel width and the transfer length. Transfer length is obtained from TLM measurements by extrapolating the linear regression to  $RW = 0$ , considering that the point of intersection with the  $x$ -axis corresponds to  $-2L_T$ .<sup>[94]</sup>

In case TC TFTs based on investigated compounds (with 25-nm-thick OSC layer),  $L_T$  was extracted at gate-overdrive voltage of -2.0 V (**Figure 3.20**), giving values ranging from 13 to 101  $\mu\text{m}$ . Eventually, the contact injection area was calculated as the product between  $L_T$  and the channel width (**Table 3.10**).

**Table 3.10: Extracted transfer lengths ( $L_T$ ) and charge injection areas ( $A_{inj}$ ) for TC TFTs with 25-nm-thick OSC layer.**

Compound	$L_T$ ( $\mu\text{m}$ )	$A_{inj}$ ( $\mu\text{m}^2$ )
<b>DNTT</b>	13.7	$6.6 \times 10^3$
<b>tBu-DNTT</b>	48.5	$2.3 \times 10^4$
<b>C<sub>8</sub>-DNTT</b>	27.3	$1.3 \times 10^4$
<b>DBTTT</b>	17.9	$8.6 \times 10^3$
<b>tBu-DBTTT</b>	101.1	$4.9 \times 10^4$
<b>C<sub>12</sub>-DBTTT</b>	23.4	$1.1 \times 10^4$

The parent molecules unveil the smallest  $L_T$  of 13.7  $\mu\text{m}$  and 17.9  $\mu\text{m}$  for **DNTT** and **DBTTT** respectively, followed by the alkylated derivatives which exhibit  $L_T$  of 27.3  $\mu\text{m}$  and 23.4  $\mu\text{m}$  for **C<sub>8</sub>-DNTT** and **C<sub>12</sub>-DBTTT** respectively. At last, the longest  $L_T$  was extracted for *tert*-butyl derivatives, with values of 48.5  $\mu\text{m}$  and 101.1  $\mu\text{m}$  for **tBu-DNTT** and **tBu-DBTTT** respectively.

In order to compare the contact resistance independent of the contact area, the specific contact resistivity is defined ( $\rho_c$ ) as follow:<sup>[94,189]</sup>

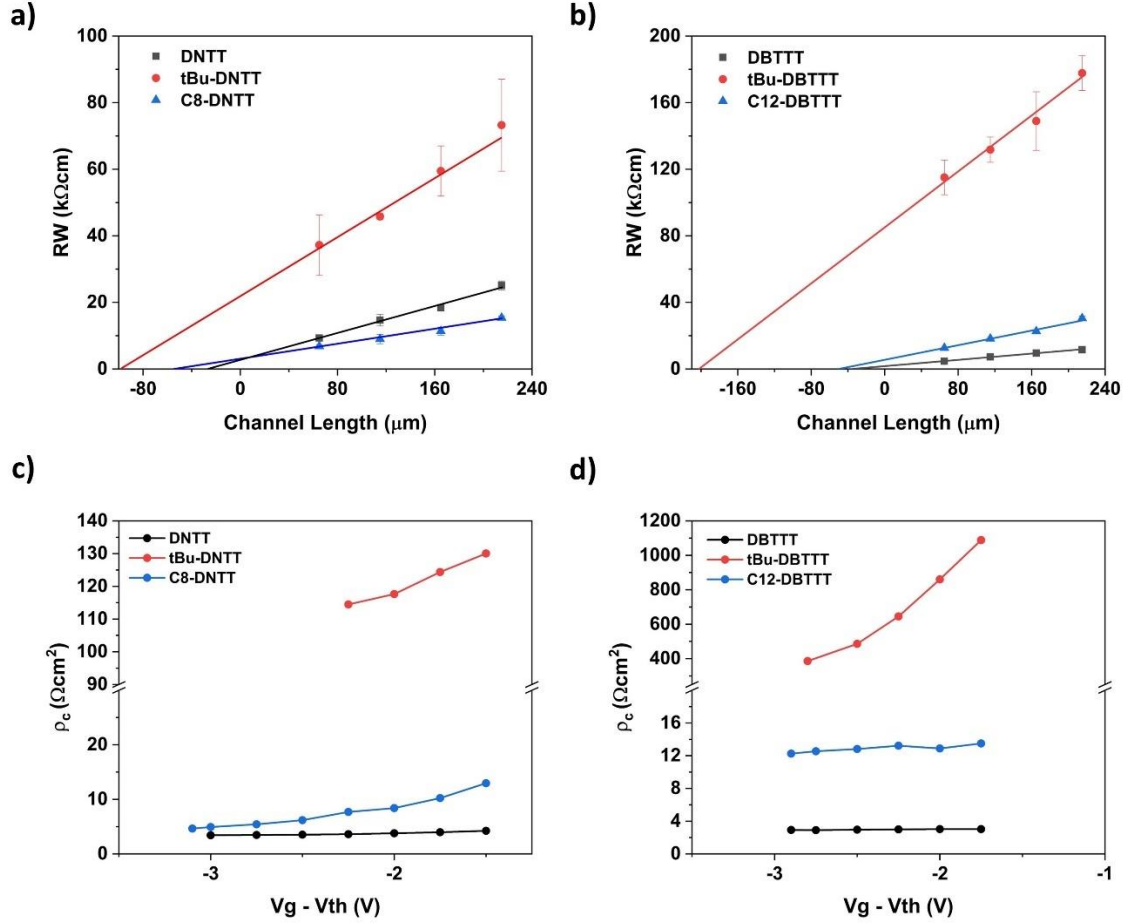
$$\rho_c = R_c W L_T \quad (3.2)$$

The above relationship is valid only if  $L_{ov} \geq 1.5 L_T$ , that is the case for all the analysed devices. The contact resistivity as a function of the gate-overdrive voltage was obtained for each compound and displayed in **Figure 3.20**. Specifically, considering a gate-overdrive voltage of -2.0 V, **DNTT**, **DBTTT** and **C<sub>8</sub>-DNTT** and **C<sub>12</sub>-DBTTT** exhibit contact resistivity of 3.8  $\Omega\text{cm}^2$ , 3.0  $\Omega\text{cm}^2$ , 8.4  $\Omega\text{cm}^2$  and 12.9  $\Omega\text{cm}^2$  respectively, while the *tert*-butyl derivatives exhibit contact resistivity of 106.1  $\Omega\text{cm}^2$  and 859.9  $\Omega\text{cm}^2$  for **tBu-DNTT** and **tBu-DBTTT** respectively.

By comparing the contact resistivity and the width-normalized contact resistance (the latter is not normalized to the transfer length), it is clear that the same trend is maintained. In fact, in both cases, the core and the alkylated molecules show values 1 or 2 orders of magnitude lower compared to the *tert*-butyl derivatives. These results suggest that, in TC TFTs presented in this work, the contact injection area does not play a major role in determining the contact resistance.

For BC TFTs,  $A_{inj}$  is estimated to be  $\approx 12 \mu\text{m}^2$ , that is 2 and 3 orders of magnitude lower compared to the contact injection areas extracted from TC TFTs. This difference is expected due to the small contact edge in BC devices

limited by the 25-nm-thick OSC layer. It is worth noting that transfer length was not calculated for BC TFTs, since in first approximation charge injection does not occur underneath the contacts in a coplanar geometry.<sup>[86,177]</sup> Thus, also in the case of BC TFTs, the achievement of lower contact resistance compared to the TC counterparts, is not limited by the reduced contact injection area.



**Figure 3.20: Transfer length extraction and contact resistivity in TC TFTs.** Total device resistance as a function of the channel length for (a) DNTT family and (b) DBTTT family, at gate-overdrive voltage of -2.0 V. The intersection of the linear regression with the  $x$ -axis ( $RW = 0$ ) corresponds to  $-2L_T$ . Calculated contact resistivity as a function of the gate-overdrive voltage for (c) DNTT family and (d) DBTTT family.

### 3.8 Study of the OSC/contact interface using ultraviolet photoelectron spectroscopy

*Ultraviolet photoelectron spectroscopy measurements were performed in collaboration with Christos Gatsios at the Humboldt University of Berlin, under the supervision of Prof. Norbert Koch.*

In a typical ultraviolet photoelectron spectroscopy (UPS) measurement, the sample is irradiated with monochromatic light of energy  $h\nu$ . When the excitation energy is sufficient the electrons can obtain enough kinetic energy to be excited from their initial bound states to the vacuum level where they can be detected by an electron spectrometer. The electrons that have surpassed their characteristic initial binding energies ( $E_B$ ) and work function of the material ( $WF$ ) reach the vacuum level with kinetic energies ( $E_k$ ). Since the total energy is conserved (neglecting inelastic scattering), the binding energies  $E_B$  of the initial electron states can be determined using the following equation:

$$E_k = h\nu - E_B - WF \quad (3.3)$$

The detector is calibrated by using a polycrystalline gold foil, in the way that the binding energy is referred to the fermi level ( $E_F = 0$  V) and not to the vacuum level, which may shift due to the presence of interfacial dipole. The distribution of bound states in the sample can be assessed by determining the kinetic energy distribution of the released photoelectrons. In a metal, the electrons with the highest kinetic energy originate the Fermi level. Conversely, in an organic semiconductor the electrons with the highest kinetic energy originate from the HOMO. It is commonly agreed that charge transport does not occur at the maximum of the density of states (DOS) of the HOMO, but rather at the low binding energy side that is characterized by a sufficient DOS at the onset to ensure charge transport. Consequently, the HOMO energy ( $E_{\text{HOMO}}$ ) can be extracted from UPS measurements, by considering the onset of the HOMO peak (that is the one at the lowest binding energy).<sup>[190]</sup>

Furthermore, UPS measurements are distinguished by a background signal at low kinetic energies caused by inelastic scattering processes of electrons that lose some of their energy as they leave the sample. The secondary electron cutoff (SECO) is the point at low kinetic energies where this background abruptly ceases. This means that electrons of lower kinetic energy than the energy of the SECO cannot escape from the sample surface. Thus, the position of the SECO provides details regarding the material's work function:

$$WF = E_{SECO} \quad (3.4)$$

The interfacial dipole is calculated as the difference between the work function of the metal ( $WF_m$ ) and the work function of the metal coated with the OSC ( $WF_{m+OSC}$ ):

$$\Delta = WF_m - WF_{m+OSC} \quad (3.5)$$

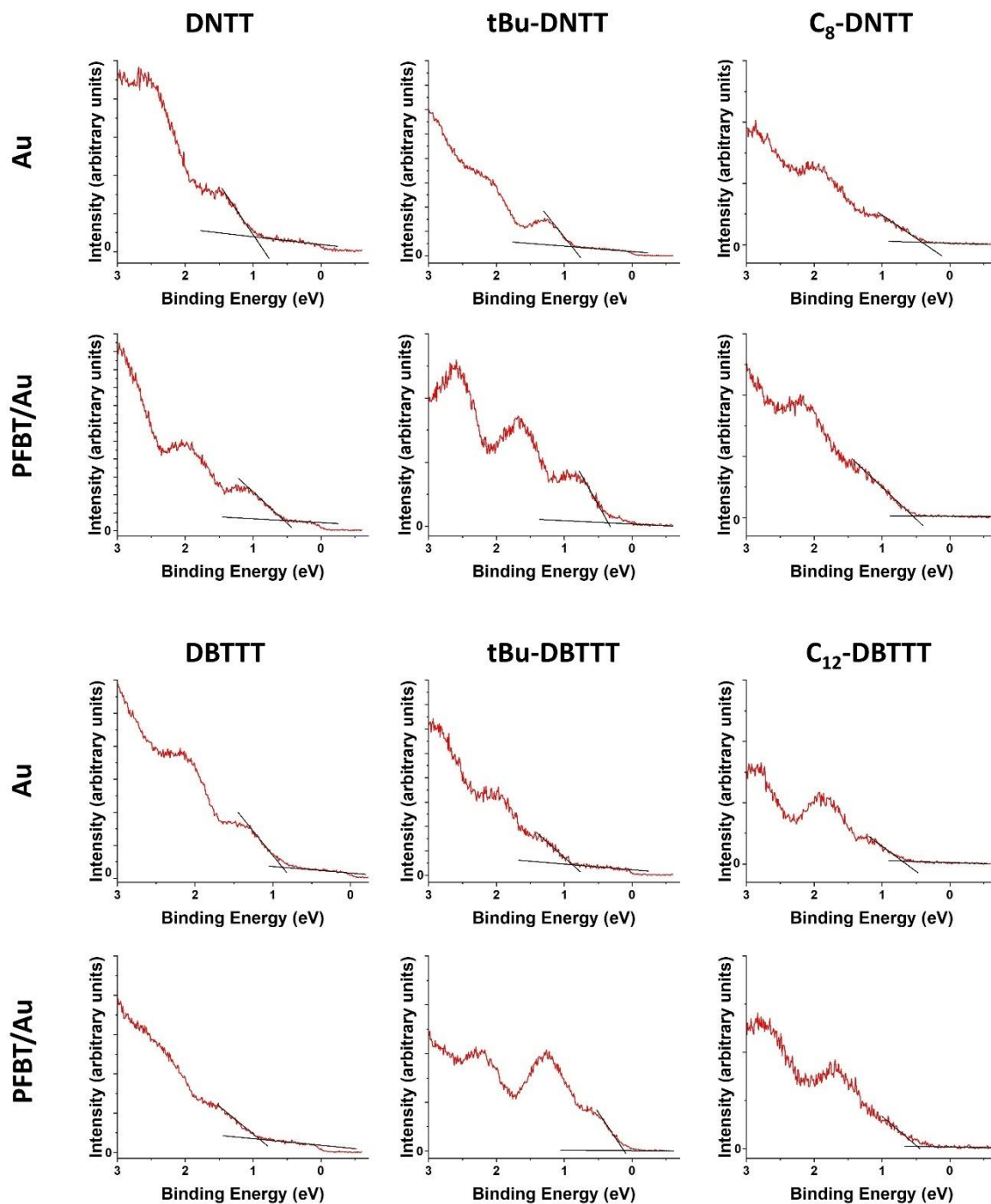
The thickness of the OSC deposited onto the metal is the one at which subsequent OSC deposition does not result in a change in HOMO energy, indicating that the effect of the interfacial dipole saturates, causing no further bend bending of the HOMO. Hence, the ionization energy is given by the sum of  $E_{HOMO}$  and the material work function:

$$IE = E_{HOMO} + WF_{m+OSC} \quad (3.6)$$

In a typical experimental setup, two substrates were prepared for each investigated organic semiconductor compound. The first substrate consisted of a Si/SiO<sub>2</sub> wafer coated with 30 nm of gold (hereinafter namely Au substrate), while the second substrate was the same except that it was immersed in a PFBT solution in isopropanol, resulting in the formation of a PFBT-SAM on the gold surface (hereinafter namely PFBT/Au surface). Each organic semiconductor compound was then thermally evaporated onto both substrates in an ultra-high vacuum, with different thicknesses monitored via a crystal quartz microbalance (the detailed preparation and measurement procedures are described in **Chapter 5**). As such, the OSC/Au interface reflects the OSC/contact interface of TC TFTs, while the OSC/PFBT-Au interface reflects the OSC/contact interface in BC TFTs.

### 3.8.1 Hole injection barrier and ionization energy

By depositing 20-Å-thick OSC layer onto the Au and PFBT/Au substrates, the hole injection barrier ( $\Phi_{B,p}$ ) of each compound with respect to the relative substrate was extracted from the onset of the HOMO peak (**Figure 3.21**). Compounds deposited onto Au substrates unveil  $\Phi_{B,p}$  between 0.48 and 0.96 eV. Specifically, for both the family a similar trend is observed: the parent compounds and the *tert*-butyl derivatives exhibit larger injection barrier, with values in the range of 0.85-0.96 eV, while the alkylated derivatives exhibit smaller injection barrier, with values of 0.48 eV and 0.77 eV for **C<sub>8</sub>-DNTT** and **C<sub>12</sub>-DBTTT** respectively (**Table 3.11**). If the effect of the resistance associated to the charge transport beneath the contacts in TC TFTs is discarded, smaller injection barrier would result in reduction of contact resistance.



**Figure 3.21: UPS spectra showing the valence region of thin film deposited onto Au and PFBT/Au substrates.**

The thin films were deposited with a nominal thickness of 20 Å. The black lines show the onset of the HOMO peaks.

The current density ( $J_{\text{int}}$ ) transported across the metal/OSC interface is influenced by the injection barrier, in both thermionic field emission ( $J_{\text{int,TFE}}$ ) and tunnelling ( $J_{\text{int,T}}$ ) mechanisms of charge carrier injection:<sup>[72]†††</sup>

$$J_{\text{int,TFE}} \propto \exp(-\Phi_B) \quad (3.7)$$

$$J_{\text{int,T}} \propto \exp(-\sqrt{\Phi_B}) \quad (3.8)$$

Notably, the *tert*-butyl derivatives compounds demonstrate  $R_{\text{cW}}$  values up to two orders of magnitude greater than their parent compounds, despite possessing comparable hole injection barriers ( $\Phi_{\text{B,p}}$  is of 0.96 eV for **DNTT**, 0.88 eV for **tBu-DNTT**, 0.85 eV for **DBTTT** and 0.87 eV for **tBu-DBTTT**). As such, in staggered TFTs, both the resistance associated to the OSC volume underneath the contacts and that at the metal/OSC interface contribute to the contact resistance, although the exact extent and relative significance of each component remain uncertain. This topic will be further elucidated in the subsequent section (**Paragraph 3.9**).

Upon deposition onto PFBT/Au substrates, all of the OSCs, with the exception of **C<sub>8</sub>-DNTT** and **DBTTT**, exhibit reduced values of  $\Phi_{\text{B,p}}$  when compared to those obtained from Au substrates. The hole injection barrier was observed to range between 0.15 and 0.84 eV, decreasing by up to 0.44 eV for **DNTT**, 0.53 eV for **tBu-DNTT**, 0.72 eV for **tBu-DBTTT**, and 0.27 eV for **C<sub>12</sub>-DBTTT**. In contrast, the injection barrier for **DBTTT** and **C<sub>8</sub>-DNTT** remains relatively unchanged (**Table 3.11**). Interestingly, *tert*-butyl derivatives display the largest reduction in the hole injection barriers, passing from Au to PFBT/Au substrates, along with the largest reduction of contact resistance, passing from TC to BC TFTs. However, this trend is observed across all compounds.

This highlights that the combination of a lower injection barrier at the metal/OSC interface, which minimizes interface resistance, and the fact that charges are directly injected into the accumulation channel collectively contribute to the reduced contact resistance of BC TFTs as compared to the TC counterpart. It should be noted, however, that the hole injection barrier is not the sole parameter governing the charge injection process and the resulting contact resistance in BC TFTs. If this were the case, **tBu-DBTTT**-based BC TFTs would display the lowest  $R_{\text{cW}}$ , as **tBu-DBTTT** shows the lowest hole injection barrier when deposited onto PFBT/Au substrates, compared to the other compounds. However, the BC TFTs based on **DNTT** and **C<sub>8</sub>-DNTT** exhibit the lowest  $R_{\text{cW}}$  values, indicating that additional

---

††† Thermionic field emission occurs when the height of the injection barrier is above the thermal energy, while tunneling may occur when the width of depleted region at the metal/OSC interface is smaller than the free path of carriers in the OSC.

factors play a role in determining the charge injection process and ultimately, the contact resistance observed in BC TFTs. This aspect is further explored in the next section (**Paragraph 3.9**).

The lower injection barrier can be ascribed both to the higher work function of the PFBT/Au and to the increased interfacial dipole (both are outcomes of the Fermi level pinning) as compared to that of Au substrate. The work function of PFBT/Au substrates was determined to be approximately 0.5 eV higher than that of Au substrates. The former exhibits a work function of  $(5.16 \pm 0.16)$  eV and the latter exhibits a work function of  $(4.67 \pm 0.06)$  eV, obtained from the SECO onset of the respective substrates (**Figure 3.22**).

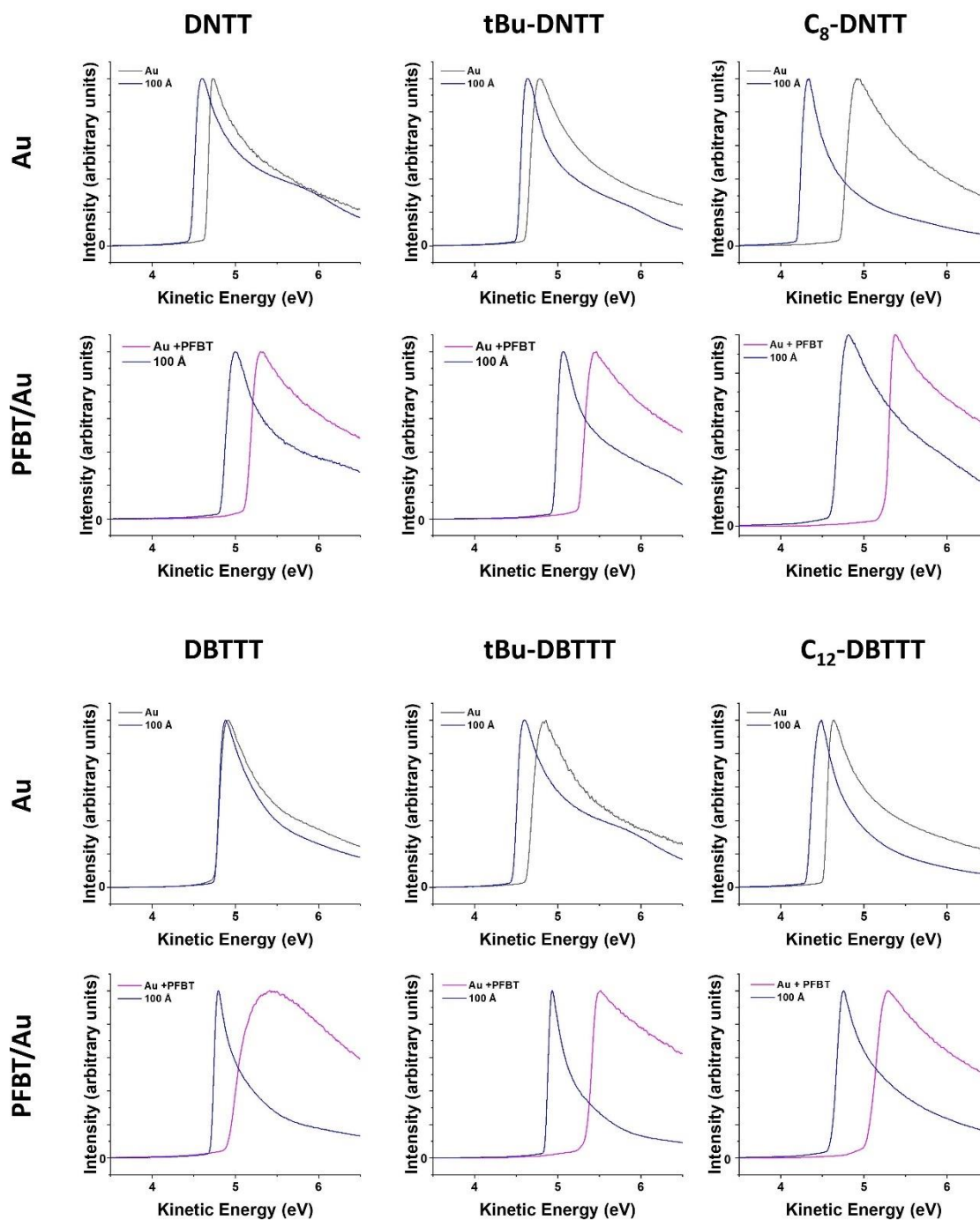
Furthermore,  $E_{\text{HOMO}}$  was determined as the thickness of the OSC layer was increased, for both Au and PFBT/Au substrates, until it reached a saturation value. This indicates that the depleted region was surpassed. The  $E_{\text{HOMO}}$  value did not exhibit any further variation beyond an OSC thickness of 100 Å for all the compounds.

Consequently, this specific OSC thickness was utilized to establish the interfacial dipole by extrapolating the work function of the metal coated with 100-Å-thick OSC layer ( $\text{WF}_{\text{m+OSC}}$ ) from the SECO (**Figure 3.22**) and using **equation 3.5**. Additionally, the ionization energy of each compound was determined by employing **equation 3.6**.

Effectively, the Schottky barriers, defined as the difference between the substrate work function and the ionization energy of the OSCs, were consistently lower in the case of OSCs deposited onto PFBT/Au substrates (ranging from 0.28 to 0.42 eV) in comparison to those deposited onto Au substrates (ranging from 0.34 to 0.92 eV). This finding confirms that minimizing the difference between the metal work function and the ionization energy of the OSC is a straightforward way to reduce contact resistance in organic TFTs. However, it should be noted that this method does not account for the band bending at the metal/OSC interface. Therefore, it cannot be assumed that the Schottky barrier is equivalent to the injection barrier.

### 3.8.2 Interfacial dipole

The interfacial dipole created at the interface between the OSCs and the PFBT/Au substrates is consistently greater in magnitude than those formed with the Au substrates. More specifically, the interfacial dipole was determined to range from 0.19 to 0.73 eV for the former and from 0.10 to 0.20 eV for the latter, with the exception of **DBTTT**, which did not exhibit the formation of an interfacial dipole when deposited onto Au (**Table 3.11**).



**Figure 3.22: Secondary electrons cut-offs used to determine work functions.** The black lines refer to Au substrates, the magenta lines refer to PFBT/Au substrates and the blue lines refer to the sample consisting of 100-Å-thick OSC layer deposited onto the respective substrate.

A higher interfacial dipole at the metal/OSC interface means that there is a greater separation of electrical charge across the interface. This dipole can have implications for device performance in organic electronics because it can

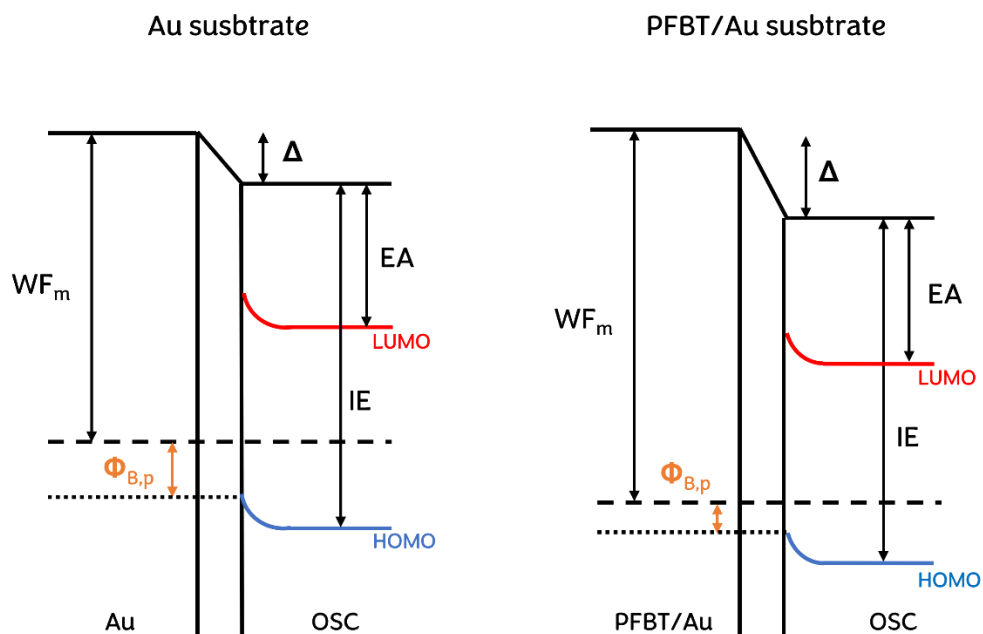
affect the energy levels of the charge carriers, as well as their ability to move across the interface. The specific impact of a higher interfacial dipole depends on the materials and device architecture used.<sup>[191–194]</sup>

In our case, the higher interfacial dipole in combination with higher work function of the metal appears to improve charge injection in TFTs, by contributing to reducing the hole injection barrier at the OSC/PFBT-Au interface (**Figure 3.23**). The two exceptions to the observed trend are **DBTTT** and **C<sub>8</sub>-DNTT**, which exhibit a higher interfacial dipole compared to that of the Au substrate, but do not result in a significant variation of the injection barrier. Interestingly, considering the deposition onto PFBT/Au substrates, the interfacial dipole values extracted for **DBTTT** and **C<sub>8</sub>-DNTT** are the smallest and largest, respectively, among all the investigated compounds. This observation suggests that a proper balance between the metal work function, the ionization energy of the OSC and the interfacial dipole is necessary to reduce the hole injection barrier.

**Table 3.11: Extracted values from UPS measurements.**

Hole injection barrier ( $\Phi_{B,p}$ ), interfacial dipole ( $\Delta$ ) and ionization energy (IE) of thin films deposited onto Au and PFBT/Au substrates.  $\Phi_{B,p}$  is determined from 20-Å-thick OSC layer, while  $\Delta$  and IE are determined from 100-Å-thick OSC layer.

Compound	Au			PFBT/Au		
	$\Phi_{B,p}$ (eV)	$\Delta$ (eV)	IE (eV)	$\Phi_{B,p}$ (eV)	$\Delta$ (eV)	IE (eV)
<b>DNTT</b>	0.96	0.18	5.42	0.52	0.29	5.44
<b>tBu-DNTT</b>	0.88	0.10	5.45	0.35	0.31	5.56
<b>C<sub>8</sub>-DNTT</b>	0.48	0.50	5.00	0.54	0.73	5.21
<b>DBTTT</b>	0.85	$\approx 0$	5.58	0.84	0.19	5.58
<b>tBu-DBTTT</b>	0.87	0.17	5.42	0.15	0.54	5.40
<b>C<sub>12</sub>-DBTTT</b>	0.77	0.20	5.14	0.50	0.45	5.25



**Figure 3.23: Schematic energy-level diagram of the bands alignment at Au and PFBT/Au substrates.**

This schematic representation is applicable to all the analysed compounds, except for **DBTTT** and **C<sub>8</sub>-DNTT**. Passing from Au to PFBT/Au substrate, the values of  $\Delta$  and  $WF_m$  were observed to increase, leading to a decrease in the hole injection barrier.

## 3.9 Discussion

The discussion of this chapter is divided into two parts: the first part focuses on the parameters that impact contact resistance in TC TFTs, and the second part focuses on the parameters affecting contact resistance in BC TFTs. A comprehensive outlook is presented, which considers both device geometries as well as the influence of the molecular structure of the OSCs.

### 3.9.1 Contact resistance in TC thin-film transistors

In the preceding sections, I presented the extraction and evaluation of various parameters that could potentially impact contact resistance in TC TFTs, including thin-film morphology, injection barrier, and out-of-plane charge transport (**Table 3.12**). We will now proceed to analyse how each parameter affects contact resistance, aiming to explain the lower contact resistance observed in alkylated derivatives (3.1 and 5.5 k $\Omega$ cm for **C<sub>8</sub>-DNTT** and **C<sub>12</sub>-DBTTT**, respectively) in comparison to the *tert*-butyl derivatives (24.2 and 85.1 k $\Omega$ cm for **tBu-DNTT** and **tBu-DBTTT**, respectively). In fact, it is expected that due to the lowest out-of-plane mobility of alkylated compounds compared to the analysed OSCs, they would exhibit a larger  $R_cW$  than the *tert*-butyl derivatives. However, our experimental results contradict this expectation. Specifically, we found that the  $R_cW$  in TC TFTs based on *tert*-butyl derivatives is one order of magnitude greater than in TC TFTs based on alkylated derivatives. Furthermore, the alkylated derivatives displayed  $R_cW$  of the same order of magnitude as the parent molecules (2.8 and 1.7 k $\Omega$ cm for **DNTT** and **DBTTT**, respectively).

**Table 3.12: Electrical performances and injection barriers of TC TFTs.**

Contact resistance ( $R_cW$ ), in-plane mobility ( $\mu_{in}$ ), (in-plane) intrinsic mobility ( $\mu_0$ ), out-of-plane mobility ( $\mu_{out}$ ) and hole injection barrier ( $\Phi_{B,p}$ ).

Compound	$R_cW$ (k $\Omega$ cm)	$\mu_{in}$ (cm <sup>2</sup> V <sup>-1</sup> s <sup>-1</sup> )	$\mu_0$ (cm <sup>2</sup> V <sup>-1</sup> s <sup>-1</sup> )	$\mu_{out}$ (cm <sup>2</sup> V <sup>-1</sup> s <sup>-1</sup> )	$\Phi_{B,p}$ (eV)
<b>DNTT</b>	2.8	2.3	2.7	$2.2 \times 10^{-1}$	0.96
<b>tBu-DNTT</b>	24.2	0.8	1.2	$2.8 \times 10^{-4}$	0.88
<b>C<sub>8</sub>-DNTT</b>	3.1	3.7	4.8	$3.2 \times 10^{-5}$	0.48
<b>DBTTT</b>	1.7	5.1	5.7	$2.2 \times 10^{-1}$	0.85
<b>tBu-DBTTT</b>	85.1	0.3	0.6	$1.1 \times 10^{-4}$	0.87
<b>C<sub>12</sub>-DBTTT</b>	5.5	2.2	2.5	n.a	0.77

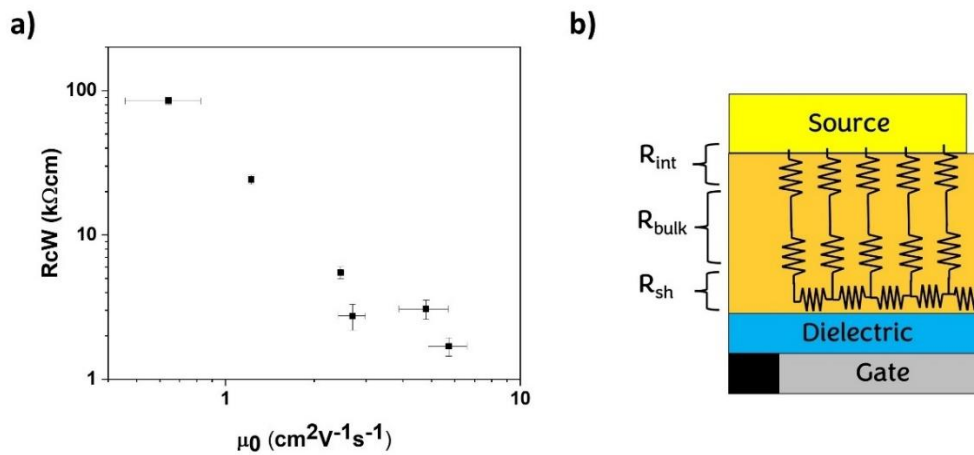
The investigation into thin-film morphology revealed no significant differences between the compounds that could explain the high contact resistance of the *tert*-butyl derivatives. All compounds exhibited a typical terraced structure morphology, which was characterized by the presence of grain boundaries. No direct correlation was found between grain size and contact resistance, and as well there was no correlation between the high presence of needle-shaped crystalline aggregates on top of the terraced structure (as observed in **C<sub>8</sub>-DNTT**, **C<sub>12</sub>-DBTTT** and **tBu-DNTT**) and contact resistance. Likewise, the calculated contact injection area was found to have negligible influence on determining contact resistance within the compounds. This was further emphasized by the fact that, despite the charge injection area being up to 2 orders of magnitude lower in BC TFTs compared to TC TFTs, the contact resistance is consistently lower in the former. We do not intend to imply that thin-film morphology and charge injection area can be disregarded when seeking to minimize contact resistance. However, in the case of our compounds and the selected device architecture, these parameters appear to have a minor impact on  $R_cW$ .

Let us now consider the interplay between the hole injection barrier, which controls the contact resistance at the metal/OSC interface ( $R_{int}$ ), and the out-of-plane mobility, which governs the bulk resistance ( $R_{bulk}$ ). The parent molecules and the *tert*-butyl derivatives have similar injection barriers, with **DNTT** exhibiting a slightly higher  $\Phi_{B,p}$  of 0.96 eV compared to **DBTTT** and the *tert*-butyl derivatives, which have  $\Phi_{B,p}$  in the range of 0.85-0.88 eV. Therefore, given a similar injection barrier, the higher contact resistance of the *tert*-butyl derivatives might be attributed to the three orders of magnitude lower out-of-plane mobility compared to the parent molecules. This hinders out-of-plane charge transport and contribute to the increased  $R_{bulk}$ . However, there are two unclear aspects. Firstly, increasing the OSC thickness from 25 nm to 80 nm (a three-fold increase) resulted in a 1.2 to 1.6 times increase in contact resistance, depending on the compound. Secondly, the alkylated derivatives exhibit even lower out-of-plane mobility than the *tert*-butyl derivatives but show contact resistance of the same order of magnitude as the parent compounds. Both of these factors indicate that while out-of-plane charge transport influence contact resistance, its impact is not predominant.<sup>[139]</sup>

Interestingly, we found a correlation between  $R_cW$  and intrinsic mobility ( $\mu_0$ ) extracted from TLM. It is worth noting that the extracted values of  $\mu_0$  are

slightly higher than the mobility values extracted from transfer characterisers ( $\mu_{in}$ ).<sup>§§§</sup>

Considering both the families,  $R_cW$  decreases as intrinsic mobility (and thus also  $\mu_{in}$ ) increases (**Figure 3.24**). This can be explained within the current crowding model. Considering the OSC volume beneath the contacts as a resistor network, charges are injected into the OSC and travel through the OSC thickness to reach the gate-induced charge accumulation channel. When charges are injected from the far contact edge, they encounter resistance when traveling along the OSC/dielectric interface ( $R_{sh}$ ) to reach the TFT channel (**Figure 3.24-b**).<sup>[81,195]</sup> This transport contributes to the device contact resistance. Lower mobility results in larger resistance to the charges traveling along this region ( $R_{sh} \propto 1/\mu_0$ ).



**Figure 3.24: Contact resistance vs intrinsic mobility.**

(a)  $R_cW$  as a function of the intrinsic mobility of TC TFTs. (b) Schematic illustration of the OSC volume beneath the source contact treated as a resistors network within the current crowding model.

Specifically,  $\mu_0$  is of 2.7 and 5.7  $cm^2 V^{-1} s^{-1}$  for **DNTT** and **DBTTT**, respectively, and of 1.2 and 0.6  $cm^2 V^{-1} s^{-1}$  for **tBu-DNTT** and **tBu-DBTTT**, respectively. This results in larger  $R_{sh}$  of the latter. It is worth reminding that TFTs based on *tert*-butyl derivatives exhibit larger charge trap density than those based on the parent compounds and alkylated derivatives. Alongside lower in-plane mobility the higher charge trap density compared to the parent compounds may further contribute to increasing the resistance associated with charge

<sup>§§§</sup>  $\mu_0$  is extracted from TLM  $\rightarrow RW = R_c + \frac{L}{W\mu_0 C_i(V_g - V_{th})}$ , where  $\frac{1}{\mu_0 C_i(V_g - V_{th})} = R_{sh}$   
 $\mu_{in}$  is extracted from transfer characteristics  $\rightarrow \mu_{in} = \frac{L}{W C_i V_d} \left. \frac{\partial I_d}{\partial V_g} \right|_{V_d}$

transport along the OSC/dielectric interface underneath the contact.<sup>[175]</sup> Therefore, the observed one-order-of-magnitude increase in  $R_{\text{C}}W$  for *tert*-butyl derivatives compared to the parent compounds can be primarily attributed to the poorer charge transport properties along the in-plane direction, rather than the larger bulk resistance.

At last, it was found that **C<sub>8</sub>-DNTT** exhibits a significantly lower charge injection barrier (0.48 eV), while **C<sub>12</sub>-DBTTT** has a slightly lower injection barrier (0.77 eV) in comparison to their parent compounds and *tert*-butyl derivatives. While the reduction in injection barrier is beneficial in minimizing  $R_{\text{int}}$  contribution and contact resistance, it is not the sole reason for the observed lower  $R_{\text{C}}W$  when compared to *tert*-butyl derivatives.

Although **C<sub>8</sub>-DNTT** has an injection barrier 0.40 eV lower than **tBu-DNTT**, the injection barrier of **C<sub>12</sub>-DBTTT** is only 0.10 eV lower than **tBu-DBTTT**. Nevertheless, **C<sub>12</sub>-DBTTT** still displays  $R_{\text{C}}W$  one order of magnitude lower than **tBu-DBTTT**, similar to the case of **C<sub>8</sub>-DNTT** and **tBu-DNTT**. Thus, also in this case, the lower  $R_{\text{C}}W$  of alkylated derivatives compared to their respective *tert*-butyl derivatives may also be attributed to their considerably higher in-plane mobility ( $\mu_0$  is of 5.7 and 2.5  $\text{cm}^2\text{V}^{-1}\text{s}^{-1}$  for **C<sub>8</sub>-DNTT** and **C<sub>12</sub>-DBTTT**, respectively). Clearly, the decrease in injection barrier assists in reducing the overall contact resistance, especially in case of **C<sub>8</sub>-DNTT**.

It is evident that the role of bulk charge transport cannot be dominant. If it were, the lower out-of-plane mobility of alkylated derivatives would result in larger  $R_{\text{C}}W$  than that of *tert*-butyl derivatives. This supports the idea that  $R_{\text{C}}W$  is primarily affected by in-plane charge transport along the OSC/dielectric interface beneath the contacts and the metal/OSC injection barrier, rather than the bulk charge transport.

In brief, these findings emphasize the significance of maximizing the in-plane mobility to decrease the resistance that hinders charge transport along the OSC/dielectric interface beneath the contacts, which in turn affect the overall contact resistance. The role of charge transport through the bulk of OSC is minor compared to the charge transport along the in-plane direction and the injection barrier. It is noteworthy that the bulk resistance resulting from out-of-plane charge transport is influenced by the overlap of the HOMO wavefunction in the out-of-plane direction. In this context, the molecular structure plays a critical role as the functionalization of the core with *tert*-butyl or alkyl chains increases the distance between molecular cores, thereby decreasing the transfer integrals. Despite poorer out-of-plane charge transport caused by the core functionalization, high contact resistance is not necessarily a consequence if in-plane charge transport is efficient (high mobility and low charge trap density) and the injection barrier is reduced.

However, when seeking to achieve the maximum reduction in contact resistance in TC TFTs, it is essential to minimize  $R_{\text{bulk}}$  as well. Albeit to a minor extent,  $R_{\text{bulk}}$  affects the contact resistance.

### 3.9.2 Contact resistance in BC thin-film transistors

The results of our study indicate that BC TFTs consistently exhibit lower contact resistance compared to the TC counterparts for all the analysed compounds and over the entire range of gate-overdrive voltage. This is mainly due to direct charge injection into accumulation channel in BC TFTs, removing the contribution of charge transport in the region underneath the contacts as in the case of TC TFTs. Consequently, contact resistance in BC TFTs is primarily regulated by the injection barrier at the metal/ OSC interface. Additionally, the use of PFBT-treated contacts in BC TFTs leads to an increased work function, up to 0.5 eV higher than bare gold, facilitating charge injection and contributing to the lowering of  $R_{\text{cW}}$ .

It is important to note that the morphology of the OSC across the contact-to-channel region is crucial in BC TFTs. Keeping the OSC morphology as similar as possible can help prevent charge trapping and inefficient charge injection.<sup>[85,141,142]</sup> The AFM images show that the morphology of all investigated compounds resembles that of the OSC deposited onto the TDPA/ $\text{Al}_2\text{O}_3$  substrate in the channel region.

We previously highlighted that **tBu-DBTTT** exhibits the lowest hole injection barrier (0.15 eV), followed by **tBu-DNTT** (0.35 eV). However, this does not necessarily correspond to the lowest contact resistance.  $R_{\text{cW}}$  was found to be of 3.7  $\text{k}\Omega\text{cm}$  for **tBu-DNTT** and 2.4  $\text{k}\Omega\text{cm}$  for **tBu-DBTTT**. The parent compounds and alkylated derivatives show lower  $R_{\text{cW}}$ , between 0.8 and 1.9  $\text{k}\Omega\text{cm}$  despite exhibiting higher injection barriers, which range from 0.50 to 0.84 eV (see **Table 3.13**). This can be attributed to the formation of a region depleted of charges due to band bending at the metal/OSC interface, which contributes to the overall contact resistance.

The resistivity of the depleted region has been shown to be proportional to  $1/\mu$  in drift diffusion simulations of BC devices based on pentacene at a given injection barrier.<sup>[86]</sup> The relationship between  $R_{\text{cW}}$  and  $1/\mu$  is not proportional in our case due to the compounds having different injection barriers and possibly different extension of the depleted region.

**Table 3.13: Contact resistance, charge carrier mobility and hole injection barrier of BC TFTs.**

Contact resistance ( $R_cW$ ), charge carrier mobility ( $\mu$ ) and hole injection barrier ( $\Phi_{B,p}$ ).

Compound	$R_cW$ ( $k\Omega cm$ )	$\mu$ ( $cm^2V^{-1}s^{-1}$ )	$\Phi_{B,p}$ (eV)
DNTT	0.8	2.3	0.52
tBu-DNTT	3.7	1.4	0.35
C <sub>8</sub> -DNTT	0.8	4.8	0.54
DBTTT	1.2	4.7	0.84
tBu-DBTTT	2.4	1.0	0.15
C <sub>12</sub> -DBTTT	1.9	3.3	0.50

Nonetheless, the lower  $R_cW$  of the parent compounds and alkylated derivatives can be attributed to their higher mobility (between 2.3 and 4.8  $cm^2V^{-1}s^{-1}$ ) compared to the *tert*-butyl derivatives (mobility of 1.4 and 1.0 for **tBu-DNTT** and **tBu-DBTTT**, respectively). Hence, despite their lower injection barrier, an efficient charge carrier injection in *tert*-butyl derivatives is hindered by the higher resistivity of the depleted region caused by their lower mobility.

In conclusion, within the coplanar device geometry, the variation in molecular structures resulting from molecular core functionalization does not influence contact resistance, since charges are directly injected into the accumulation channel. Primarily, to achieve a lower contact resistance in BC TFTs, it is necessary to minimize the injection barrier and maximize the charge carrier mobility, which in turns reduces the resistance associated to the depleted region at the metal/OSC interface.

### 3.10 Summary

In this chapter, the impact of the molecular structure of DNTT and DBTTT families on the contact resistance of organic TFTs was examined, with a particular emphasis on the device geometry, injection barrier at the metal/OSC interface, and out-of-plane and in-plane charge transport properties.

In the context of BC TFTs, the lowest contact resistance is shown by **DNTT** and **C<sub>8</sub>-DNTT**, despite their larger injection barrier compared to the *tert*-butyl derivatives. The observed effect is attributed to the formation of a depleted region at the metal/OSC interface, which contributes to contact resistance. The resistance opposed by the depleted region is lowered when mobility increases. Thus, although a lower injection barrier is beneficial for minimizing contact resistance, it is also important to maximize the charge carrier mobility. As such, compounds with a good balance between a low injection barrier and high in-plane mobility exhibit the lowest  $R_{\text{C}}W$ . Considering that in BC TFTs charges are directly injected into the accumulation channel, the variation of the molecular structure due to the core functionalization appears to have no influence on the contact resistance.

In the case of TC TFTs, it was found that the bulk charge transport through the thickness of the OSC influences contact resistance, but its impact is not dominant. The alkylated compounds showed out-of-plane mobilities 4 orders of magnitude lower than the parent compound due to the larger distance between the molecular cores along the out-of-plane direction. Yet  $R_{\text{C}}W$  of **C<sub>8</sub>-DNTT** and **C<sub>12</sub>-DBTTT** is comparable to those of the parent compounds. In contrast, *tert*-butyl derivatives showed  $R_{\text{C}}W$  one order of magnitude higher than the alkylated derivatives, despite their higher out-of-plane mobility. The comparison of the various factors affecting contact resistance revealed that  $R_{\text{C}}W$  is primarily determined by the resistance opposing charge transport along the OSC/dielectric interface beneath the contacts (governed by in-plane mobility and charge trap density) and the injection barrier at the metal/OSC interface. Thus, in TC TFTs, a larger distance between the molecular cores due to the introduction of substituents does not necessarily result in high contact resistance if the injection barrier is reduced and in-plane charge transport is efficient.

At last, the study found that BC TFTs consistently exhibit lower contact resistance compared to TC counterparts for all the analysed compounds. This is attributed to the direct injection of charges into the accumulation channel in BC TFTs. In contrast to TC TFTs, where the resistance to charge transport beneath the contacts contributes to the contact resistance, this contribution

is discarded in BC TFTs. The reduction in contact resistance was mild for the parent compounds and alkylated derivatives, with  $R_cW$  between 1.3 and 2.9 times lower in BC TFTs, compared to TC TFTs. However, BC TFTs based on **tBu-DNTT** showed up to 7 times lower  $R_cW$ , and BC TFTs based on **tBu-DBTTT** showed up to 35 times lower  $R_cW$  compared to the TC counterparts. This emphasizes the advantageous impact of employing a coplanar device geometry in terms of electrical performance and charge injection properties.



# Chapter 4

## Exploring the effect of vibrational strong coupling on perylene crystallization in a Fabry-Perot cavity

### 4.1 Introduction

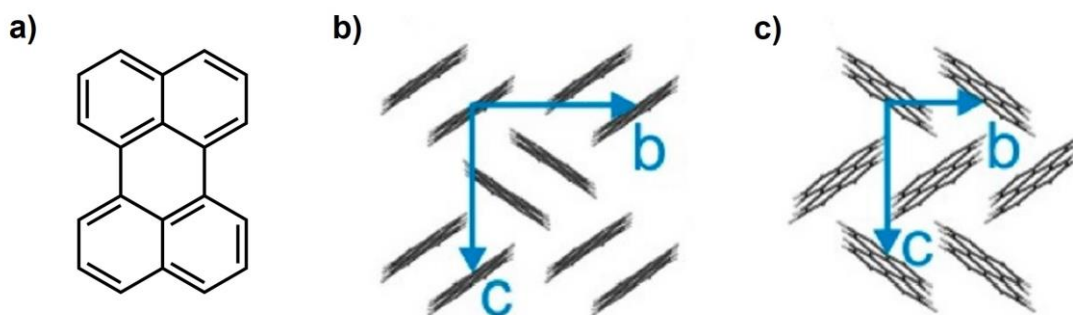
The coupling of molecular vibrations to optical cavity vacuum fields has shown to alter molecular and material properties i.e., by modifying the reactivity of organic reactions<sup>[105,114,196,197]</sup>. The alteration of chemical reactivity has been attributed to a reshaping of the Morse potential of the coupled bond modified by vibrational strong coupling (VSC), predicting a shortening or strengthening of the coupled bond and hence a change of its energy.<sup>[196,198]</sup> Therefore, if the energy and the strength of a bond involved in intermolecular interactions would be altered by coupling with the vacuum field, VSC may influence crystal nucleation as well as crystal growth.

The modification of the supramolecular assembly of a conjugated polymer<sup>[119]</sup> and of two structural isomers of phenyleneethynylene,<sup>[120]</sup> as well as the selective crystallization of a pseudo-polymorphic form of zeolite imidazolate frameworks,<sup>[118]</sup> serve as initial examples confirming the impact of VSC on supramolecular chemistry. It is worth noting that the reported supramolecular assembly modifications have been obtained through cooperative VSC (i.e., the optical mode couples with a vibrational mode of the solvent that resonates with a vibrational mode of the solute). The underlying mechanism of this phenomenon is not yet fully understood and may be related to changes in dispersive forces and/or the stabilization of one molecular assembly over another when the investigate system is strongly coupled with the vacuum field.

Controlling the crystal packing and polymorphism is crucial for optimizing the physical properties and electrical characteristics of OSC-based devices. Hence, the development of methods to induce selective crystallization, preventing the concomitant growth of polymorphic forms, may offer new opportunities to maximize the electrical performances of OSCs. In this context, perylene has been selected as a model case since it is readily available, well-known molecule and it represents the core of the perylene-based organic semiconductor molecules. Two crystals forms of perylene are reported, historically named alpha and beta (**Figure 4.1**)<sup>[199]</sup>. Crystallization

techniques have been utilized using both solution-based and sublimation methods, typically resulting in the concomitant growth of both polymorphic forms.<sup>[199,200]</sup> However, selective growth of each polymorph has also been reported.<sup>[201–203]</sup> Specifically,  $\beta$ -crystal-based OFETs exhibit hole mobility of  $1.1 \times 10^{-1} \text{ cm}^2\text{V}^{-1}\text{s}^{-1}$ , up to 10-fold higher than those based on the mixed-phase crystals and  $\alpha$ -phase crystal.<sup>[204]</sup> This finding reinforces the significance of controlling the packing of OSC and polymorphism to enhance device performance.

Accordingly, in this chapter, we endeavour to investigate the potential impact of vibrational strong coupling on perylene crystal growth and polymorphism through crystallization experiments conducted in a Fabry-Perot (FP) cavity.



**Figure 4.1: Polymorphic forms of perylene.**

(a) Molecular structure of perylene, (b) crystalline arrangement of the  $\alpha$ -form, (c) crystalline arrangement of the  $\beta$ -form.

## 4.2 Perylene crystallization

### 4.2.1 Crystal structures

Extensive research has been conducted on the packing motifs of perylene polymorphs.<sup>[199]</sup> The  $\alpha$ -form is characterized by a dimeric sandwich-herringbone motif, whereas the  $\beta$ -form has a monomeric  $\gamma$ -herringbone structure (**Figure 4.1**).<sup>[205]</sup> Both polymorphs belong to monoclinic space groups ( $P 2_1/c$  for the  $\alpha$ -form and  $P 2_1/a$  for the  $\beta$ -form), with a single unique molecule in the asymmetric unit (**Table 4.1**). The  $\alpha$ -form is mainly characterized by  $\pi$ - $\pi$  dimer interactions and C-H $\cdots$ H interactions, whereas the  $\beta$ -form is mainly characterized by  $\pi$ - $\pi$  in-stack interactions and C-H $\cdots\pi$  interactions. Therefore, it is of interest to investigate whether vibrational strong coupling between cavity optical modes and the aromatic C-H stretching or C=C stretching of perylene could potentially influence crystal growth and polymorphism.

**Table 4.1: Crystallographic data of perylene polymorphs.**

	$\alpha$ -form	$\beta$ -form
Formula	$C_{20}H_{12}$	
Crystal system	Monoclinic	Monoclinic
Space group	$P 2_1/c$	$P 2_1/a$
<b>a</b> (Å)	10.270	11.277
<b>b</b> (Å)	10.839	10.826
<b>c</b> (Å)	11.278	10.263
$\alpha$ (deg)	90	90
$\beta$ (deg)	100.53	100.55
$\gamma$ (deg)	90	90
<b>Z</b>	4	4
<b>Z'</b>	1	1

## 4.2.2 Crystallization experiments

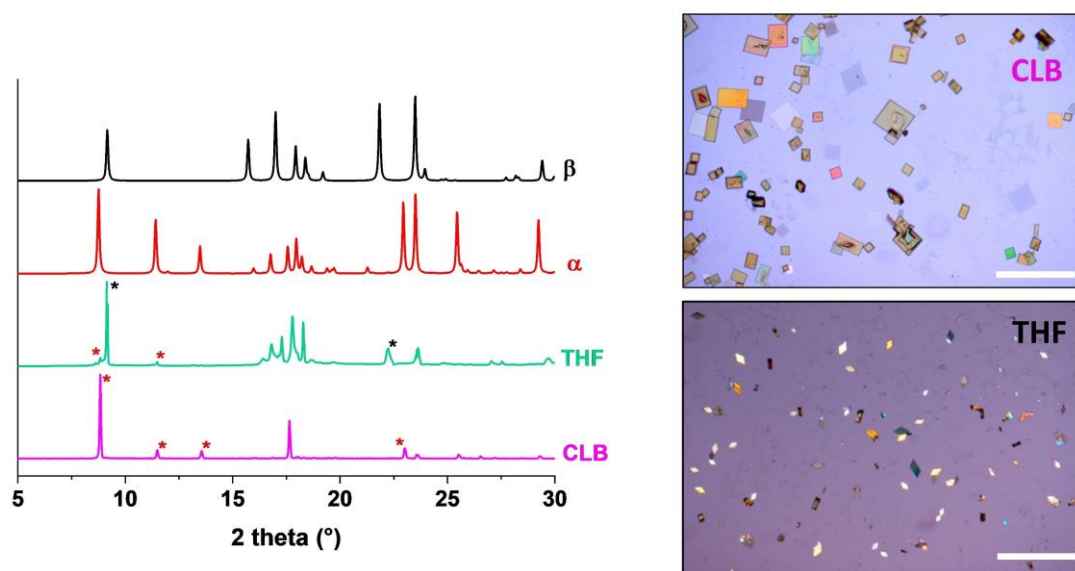
Perylene polymorphs exhibit different macroscopic habits, with  $\alpha$ -crystals appearing as rectangular shapes  $\beta$ -crystals appearing as rhombic shapes. This renders them readily distinguishable under an optical microscope. Crystallization experiments were conducted to verify the correlation between crystal habit and the underlying crystalline structure. Both polymorphic forms were selectively grown using a solution-dropping method in accordance with established protocols.<sup>[203]</sup>

Perylene was dissolved in chlorobenzene (CLB) with a concentration of 4 mg/mL and dropped onto a quartz substrate to obtain square-shaped crystals, upon solvent evaporation at room temperature. The rectangular crystals exhibit edge lengths ranging from 10 to 100  $\mu\text{m}$ . Likewise, rhomboidal-shaped crystals were obtained by the same procedure but using a 4 mg/mL perylene solution in tetrahydrofuran (THF). The rhomboidal crystals exhibit edge length ranging from 20 to 80  $\mu\text{m}$ . Also, a small number of rectangular-shaped crystals were observed, indicating the simultaneous crystallization of the  $\alpha$ -form. However, the amount of the rectangular-shaped crystals was considerably lower compared to those of rhomboidal shape (as illustrated in **Figure 4.2**).

X-ray diffraction was performed on the collected crystals and compared to the simulated powder XRD patterns of the  $\alpha$ - and  $\beta$ -forms (XRD patterns were simulated using Mercury distributed by Cambridge Crystallographic Data Center, referencing PERLEN04 for the  $\alpha$ -form and PERLEN01 for the  $\beta$ -form). The diffraction peaks from the rectangular perylene crystals obtained from chlorobenzene corresponds to the calculated XRD pattern of the  $\alpha$ -form (highlighted with red asterisks in **Figure 4.2**). The diffraction pattern from the rhombohedral perylene crystals from THF is consistent with the simulated  $\beta$ -phase (highlighted with black asterisks in **Figure 4.2**). Nonetheless, peaks of low intensity were detected at  $2\theta = 8.7^\circ$  and  $2\theta = 11.4^\circ$ , which are attributed to the minor presence of the rectangular-shaped crystals ( $\alpha$ -form) observed from the optical micrographs. This confirms that the rectangular-shaped crystals correspond to the  $\alpha$ -form, whereas the rhomboidal-shaped crystals correspond to the  $\beta$ -form.

Both polymorphs exhibit strong preferred orientations along (100). The two phases are easily distinguishable, as the  $\alpha$ -(100) and  $\beta$ -(100) reflections appeared at  $2\theta = 8.7^\circ$  and  $9.1^\circ$ , respectively, without overlap. Furthermore, the  $\alpha$ -form exhibit (110) and (11-1) reflections at  $2\theta = 11.4$  and  $13.5$ , respectively, where no reflections of the  $\beta$ -form are unveiled.

It is worth noting that THF has a boiling point of 66 °C, whereas chlorobenzene has a boiling point of 132 °C. Consequently, when solutions are deposited onto quartz substrates, THF evaporates at a faster rate than chlorobenzene (i.e., 50  $\mu$ L of perylene solution in THF evaporates in approximately 3 minutes, while 50  $\mu$ L of perylene solution in chlorobenzene evaporates in approximately 40 minutes at room temperature). The formation of  $\beta$ -crystals from a THF solution during rapid solvent evaporation suggests that  $\beta$ -crystal formation is kinetically driven rather than thermodynamically. This is consistent with the findings of Yago *et al.*,<sup>[201]</sup> who reported that fast cooling of a saturated solution of perylene in toluene (30 °C/min) selectively precipitates the  $\beta$ -polymorph, while slow cooling (1 °C/min) favours the growth of the  $\alpha$ -polymorph.

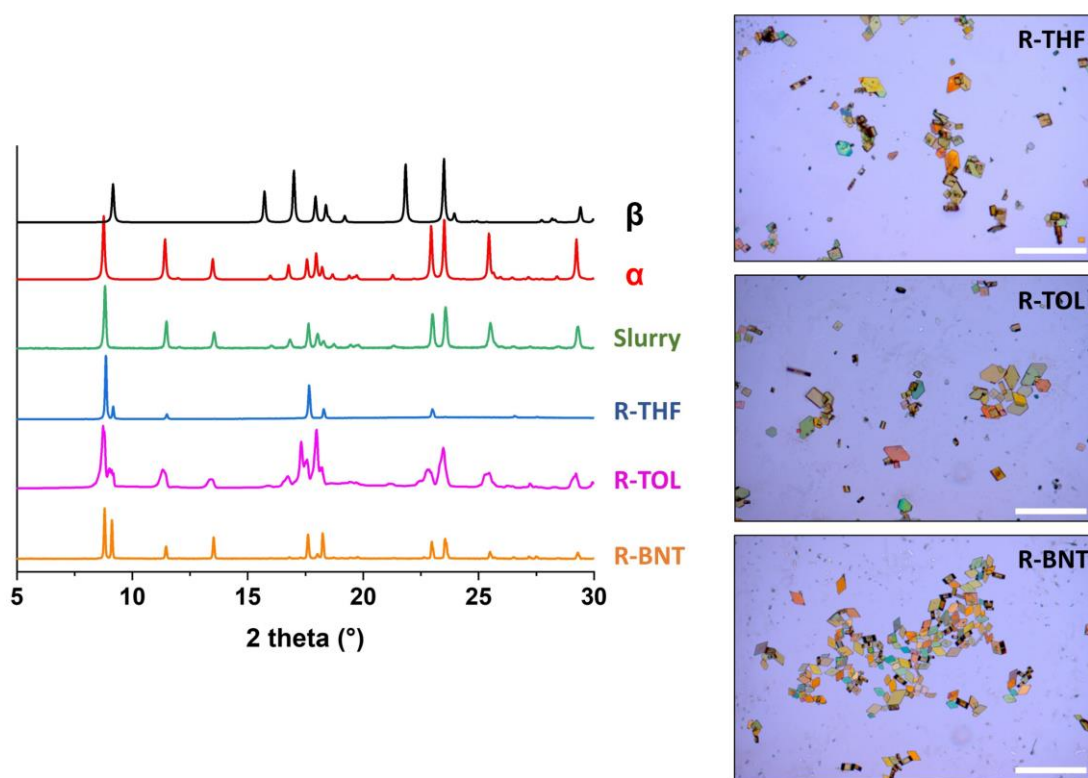


**Figure 4.2: XRD patterns and optical micrographs of  $\alpha$ - and  $\beta$ -form of perylene.**

On the left: XRD patterns obtained from solution-dropping method.  $\alpha$  and  $\beta$  refer to the simulated patterns, THF refers to crystals obtained by solution-dropping method of 4 mg/mL solution in THF and CLB refers to crystals obtained by solution-dropping method of 4 mg/mL solution in THF. The black and red asterisks highlight the peaks attributed to the  $\beta$ - and  $\alpha$ -form, respectively. On the right: optical micrograph (scale bar = 200  $\mu$ m).

In addition, recrystallization experiments were conducted, whereby three solutions were prepared: (a) perylene was dissolved in THF at a concentration of 10 mg/mL through stirring and heating at 50 °C for 30 min (namely R-THF), (b) perylene was dissolved in toluene at a concentration of 10 mg/mL

through stirring and heating at 70 °C for 30 min (namely R-TOL), and (c) perylene was dissolved in benzonitrile at a concentration of 10 mg/mL through stirring and heating at 70 °C for 30 min (namely R-BNT). The solutions were cooled at a rate of  $\approx 1$  °C/min until they reached room temperature. The resulting crystals at the bottom of the vials were collected and subjected to XRD analysis (see **Figure 4.3**). All recrystallization experiments yielded both polymorphic forms, as indicated by the presence of peaks at  $2\theta = 8.7^\circ$  and  $9.1^\circ$ , corresponding to the  $\alpha$ - and  $\beta$ -form, respectively. At last, slurry experiments were conducted by preparing a 10 mg/mL chlorobenzene solution of perylene, which was stirred and maintained at room temperature. After 4 days, XRD analysis was performed on the slurry, which exhibited peaks corresponding to the  $\alpha$ -form.



**Figure 4.3: Recrystallization and slurry experiments.**

On the left: XRD patterns obtained from recrystallization and slurry experiments.  $\alpha$  and  $\beta$  refer to the simulated patterns, R-THF refers to recrystallization of 10 mg/mL solution in THF cooled from 50 °C to room temperature, R-TOL refers to recrystallization of 10 mg/mL solution in toluene cooled from 70 °C to room temperature, R-BNT refers to recrystallization of 10 mg/mL solution in benzonitrile cooled from 70 °C to room temperature. On the right: optical micrographs (scale bar = 200  $\mu\text{m}$ ).

Considering the thermal properties, the  $\beta$ -form undergoes an irreversible phase transition to the  $\alpha$ -form, with the latter remaining stable up to the melting point. Differential scanning calorimetry has been reported by Hsieh *et al.*,<sup>[204]</sup> determining the phase transition of the  $\alpha$ - and  $\beta$ -form. During heating, the  $\alpha$ -crystals displayed a single endothermic phase transition corresponding to their melting point of 277 °C. On the other hand, the  $\beta$ -crystals displayed two endothermic transitions during heating: one corresponding to the melting process at 277 °C and the other occurring between 100 and 140 °C, indicating a phase transition towards a more stable  $\alpha$ -phase. X-ray diffraction study of the  $\beta$ -to- $\alpha$  phase transition by Botoshansky *et al.*<sup>[199]</sup> also showed that the  $\beta$ -to- $\alpha$  phase transition occurs between 100 and 140 °C. Exothermic transition between 100 and 140 °C has not been observed during the subsequent cooling process, indicating that the  $\alpha$ -crystal does not change back to the  $\beta$ -crystal during cooling.

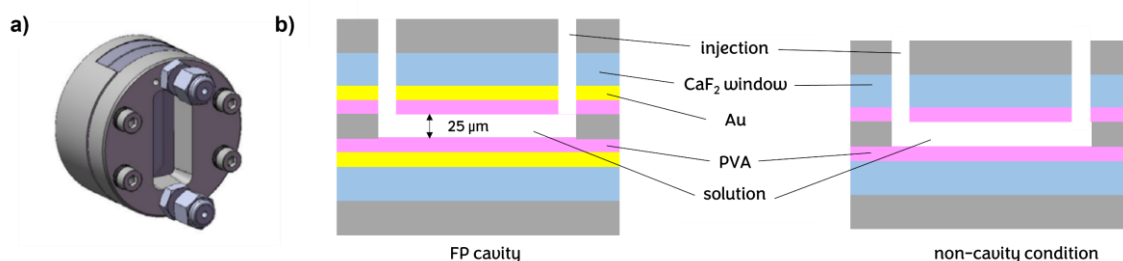
To summarize, the results of the crystallization experiments indicate that the solution-dropping method using a high boiling point solvent (chlorobenzene) favours the formation of the  $\alpha$ -form, whereas the solution-dropping method using a lower boiling point solvent (THF) leads to the preferential formation of the  $\beta$ -form. Recrystallization experiments carried out by cooling saturated solutions at a rate of 1°C/min resulted in the formation of both polymorphs, while prolonged slurry maturation yielded the selective formation of the  $\alpha$ -form. These findings, in conjunction with the reported thermal properties, suggest that the  $\alpha$ -form is the thermodynamically stable form, whereas the  $\beta$ -form is considered to be metastable.

## 4.3 Crystallization in Fabry-Perot cavity

### 4.3.1 Fabry-Perot cavity fabrication

In order to investigate the impact of VSC on perylene crystallization, a microfluidic optical Fabry-Perot (FP) cavity was utilized. The FP cavity comprises two parallel  $\text{CaF}_2$  windows coated with 10 nm of Au and a 100 nm thick layer of spin-coated polyvinyl alcohol (PVA) for protection. The two mirrors were assembled into a microfluidic cell with a 25  $\mu\text{m}$  thick Mylar spacer between them. Within this setup, a solution can be injected between the two mirrors, and the distance between the mirrors can be precisely adjusted by tightening or loosening the four screws that hold the cell (**Figure 4.4**). This allows for the achievement of VSC between FP optical modes and molecular vibrations. A comprehensive description of the FP cavity is provided in **Chapter 5**.

It should be noted that in the following section non-cavity experiments were conducted in the same microfluidic cell as described previously, but without the gold coating of the  $\text{CaF}_2$  windows. In the non-cavity condition, the experiment is performed in a micro-confined space (the volume between the  $\text{CaF}_2$  windows), but without the possibility to strongly couple molecular vibrations with the vacuum field.



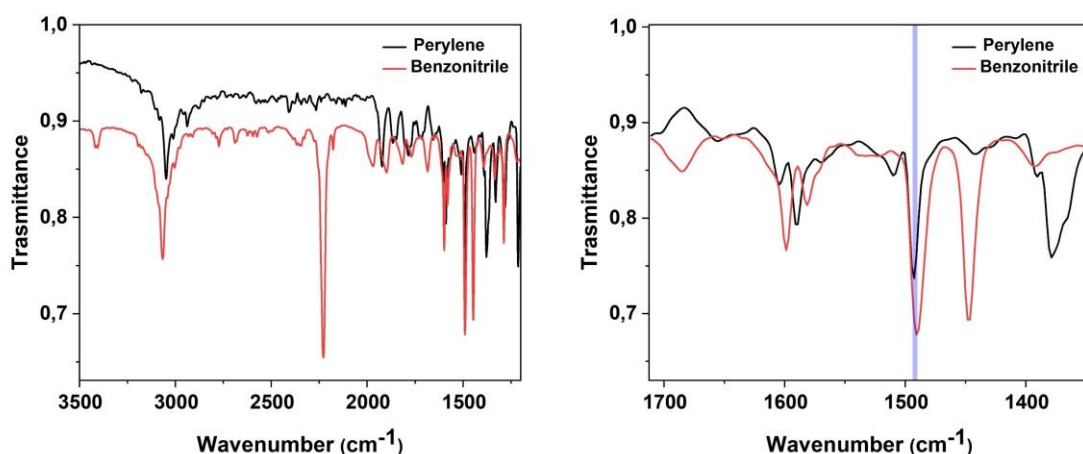
**Figure 4.4: Fabry-Perot cavity.**

(a) Assembled Microfluidic cell, (b) schematic illustration of the FP cavity and of the microfluidic cell employed for off-cavity experiments.

### 4.3.2 Results and discussion

*VSC experiments were performed in collaboration with Dr. Kripa Joseph, at Supramolecular Science and Engineering Institute (ISIS) of Strasbourg, under the supervision of Prof. Thomas Ebbsen.*

Due to the limited solubility of perylene in the selected solvents (THF, chlorobenzene and benzonitrile) it was not possible to directly achieve VSC between optical cavity modes and molecular vibrations of the solute. To overcome this limitation, we employed cooperative VSC, which involves coupling the solute through the solvent if there are overlapping vibrational bands between them. In particular, benzonitrile and perylene have an overlapping vibrational band at  $1492\text{ cm}^{-1}$ , which corresponds to the aromatic C=C stretching (**Figure 4.5**).



**Figure 4.5: Fourier transformed infrared spectra of perylene and benzonitrile.**

On the right: perylene and benzonitrile spectra in the region between  $1710$  and  $1350\text{ cm}^{-1}$ , highlighting the overlap of the vibrational bands at  $1492\text{ cm}^{-1}$  (marked with a blue line).

In typical experiments, a  $10\text{ mg/mL}$  solution of perylene in benzonitrile was prepared by stirring and heating the solution at  $70\text{ }^{\circ}\text{C}$  for  $30\text{ min}$ . Subsequently, the solution was introduced into the pre-heated FP cavity at  $70\text{ }^{\circ}\text{C}$  by coupling a heating jacket to the assembled microfluidic cell. By modulating the distance between the mirrors, two different scenarios under two different VSC conditions were achieved (**Figure 4.6**):

1. VSC of the solvent band at  $2228\text{ cm}^{-1}$  ( $\text{C}\equiv\text{N}$  stretching) with the  $18^{\text{th}}$  mode of the cavity, along with cooperative VSC of the solvent (and perylene) band at  $1492\text{ cm}^{-1}$  (aromatic C=C stretching) with the  $12^{\text{th}}$  mode of the cavity, namely **VSC1** hereinafter,
2. VSC of the solvent band at  $1445\text{ cm}^{-1}$  (aromatic C=C stretching) with the  $12^{\text{th}}$  mode of the cavity, namely **VSC2** hereinafter.

VSC was confirmed by the formation of polaritonic states separated by an energy called Rabi splitting ( $\hbar\Omega_R$ ), which is higher than the full width at half maximum of both the coupled optical mode ( $\nu_o$ ) and the vibrational band ( $\nu_s$ ). In **VSC1**, VSC of the vibrational mode at 2228  $\text{cm}^{-1}$  resulted in Rabi splitting of 51  $\text{cm}^{-1}$ , with  $\nu_o$  and  $\nu_s$  being 19  $\text{cm}^{-1}$  and 13  $\text{cm}^{-1}$ , respectively; while VSC of the vibrational mode at 1492  $\text{cm}^{-1}$  resulted in Rabi splitting of 28  $\text{cm}^{-1}$ , with  $\nu_o$  and  $\nu_s$  being 19  $\text{cm}^{-1}$  and 11  $\text{cm}^{-1}$ , respectively. In **VSC2**, Rabi splitting was found to be 26  $\text{cm}^{-1}$ , with  $\nu_o$  and  $\nu_s$  being 14  $\text{cm}^{-1}$  and 6  $\text{cm}^{-1}$ , respectively.

In **VSC1**, selective coupling of only the vibrational band at 1492  $\text{cm}^{-1}$  was not possible without coupling other vibrational modes of the solvent, due to the small free spectral range (FSR) of 124.2  $\text{cm}^{-1}$ . FSR is the difference in frequency between two adjacent resonance modes of the system. FSR is related to the refractive index of the medium and the distance between the mirrors using the following equation:<sup>[196]</sup>

$$FSR = \frac{10^4 m}{2 n L_m} \quad (4.1)$$

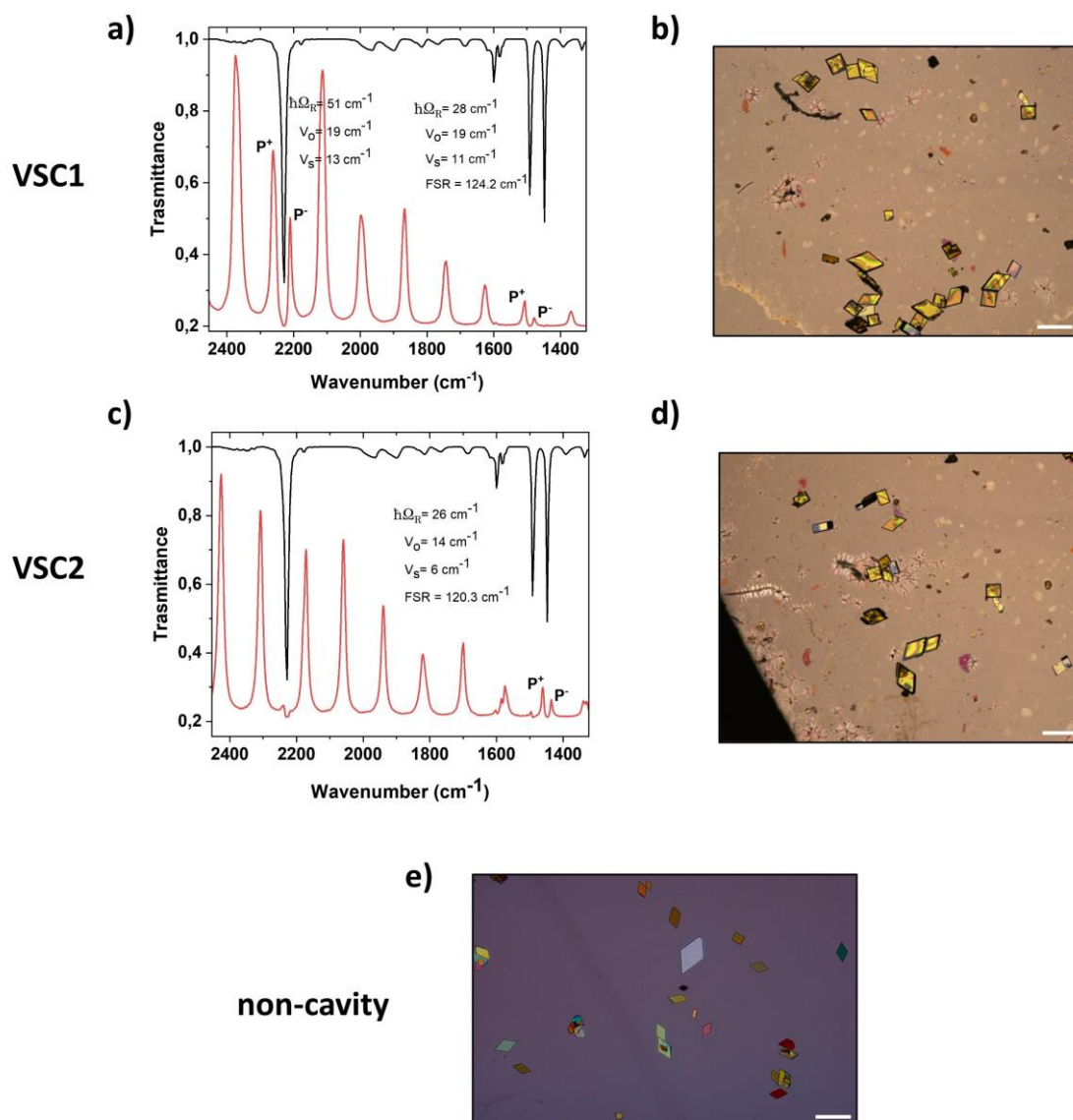
where  $m$  is the mode order,  $n$  is the refractive index of the medium and  $L_m$  is the distance between the mirrors. However, attempting to increase the free spectral range (FSR) by using a thinner spacer to achieve selective coupling conditions resulted in a decrease in the volume of solution injected into the cavity. This ultimately led to the formation of few or no crystals during the crystallization experiment.

As a control, non-cavity experiments were conducted using the same recrystallization method described above, but without the gold coating on the  $\text{CaF}_2$  windows. The experimental setup involved injecting a 10 mg/mL solution of perylene in benzonitrile at 70°C into the microfluidic cell, which was pre-heated at 70°C.

After establishing the VSC conditions as described in **VSC1** and **VSC2**, as well as in the case the non-cavity experiment, the microfluidic cell was cooled gradually from 70°C to 25°C at a rate of 1 °C/min. In all the recrystallization experiments (**VSC1**, **VSC2**, and non-cavity condition), rectangular and rhomboidal shaped platelet crystals were obtained, referred to as  $\alpha$  and  $\beta$  form, respectively (**Figure 4.6**). This is consistent with the recrystallization results presented in **Paragraph 4.2.2**, where a 10 mg/mL solution of perylene in benzonitrile was cooled from 70°C to room temperature in a vial, resulting in the formation of both polymorphs.

The polymorphic ratio was determined by categorizing the formed crystals according to their crystal habit and counting them in three independent replicates. The results indicated that the  $\alpha$ -form constituted (27±6) % of the

crystals in **VSC1**,  $(20 \pm 5)$  % in **VSC2**, and  $(15 \pm 2)$  % in the non-cavity condition. There was no significant difference in the edge length of the crystals, which ranged from 10 to 150  $\mu\text{m}$ .



**Figure 4.6: Recrystallization experiments conducted in the microfluidic cell.**

On the top: (a) On-resonance FP cavity where the vibrational mode at  $2228 \text{ cm}^{-1}$  of benzonitrile is coupled with the 18<sup>th</sup> optical mode and the vibrational mode at  $1492 \text{ cm}^{-1}$  of benzonitrile and perylene are coupled with the 12<sup>th</sup> optical mode (**VSC1**), and (b) the respective optical micrograph of formed crystals upon cavity cooling. (c) On-resonance FP cavity where the vibrational mode at  $1445 \text{ cm}^{-1}$  of benzonitrile is coupled with the 12<sup>th</sup> optical mode (**VSC2**), and (d) the respective optical micrograph of formed crystals upon cavity cooling. (e) Optical micrograph of crystals obtained in a non-cavity condition. Scale bar = 200  $\mu\text{m}$ .

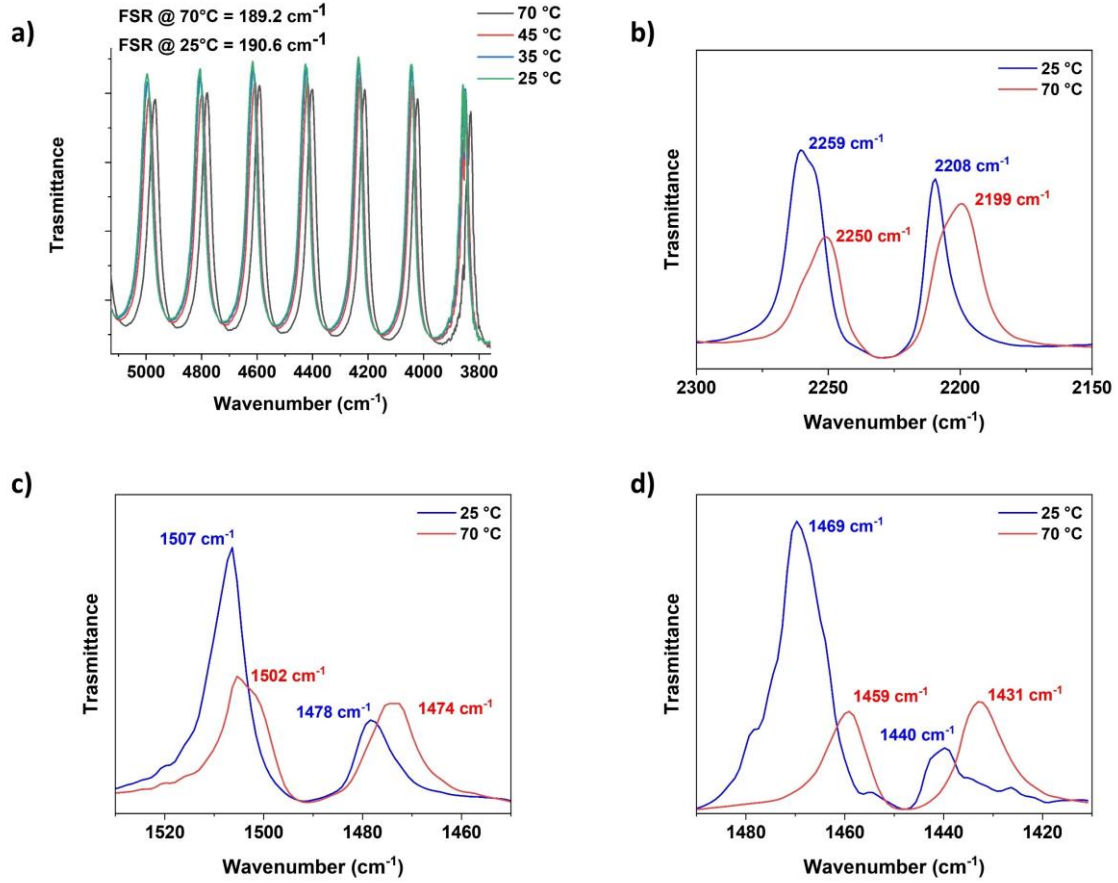
A slight increase in the ratio of the  $\alpha$ -form to the  $\beta$ -form was observed when transitioning from off-cavity conditions to **VSC2** and **VSC1**. However, since the difference between the polymorphic ratio values obtained from **VSC1** and **VSC2** compared to non-cavity conditions was small ( $\alpha$ -form increase of 5 % in **VSC1** and of 12 % in **VSC2**, compared to non-cavity condition), we cannot draw any straightforward conclusions.

In addition, the higher standard deviation of  $\alpha$ -form to the  $\beta$ -form ratio in **VSC1** and **VSC2** compared to the non-cavity condition indicates a greater variability in the polymorphic ratio across different experimental replicates in the former. This variability may be linked to variations in the free spectral range (FSR) of the FP cavity, which can be affected by changes in the refractive index due to crystal formation and the thermal expansion of the device system holding the gold coated  $\text{CaF}_2$  windows. To investigate this, we calculated the FSR of an empty FP cavity (filled with air) with a 25  $\mu\text{m}$  Mylar spacer between the mirrors. The FSR increased from 189.2 to 190.6  $\text{cm}^{-1}$  as the cavity was cooled from 70  $^{\circ}\text{C}$  to 25  $^{\circ}\text{C}$ , indicating that the reason of the increased FSR is linked to the variation of the distance between the cavity mirrors (**Figure 4.7a**).

Changes in the FSR resulted in modifications to the resonance conditions of polaritonic states in both **VSC1** and **VSC2**. The energy levels of these states were found to change as the FP cavity was cooled. Specifically, in **VSC1**, where polaritonic states were formed through the coupling of the  $\text{C}\equiv\text{N}$  stretching and the 18<sup>th</sup> optical mode,  $\text{P}^+$  and  $\text{P}^-$  energies increased by 9  $\text{cm}^{-1}$  when the temperature was lowered from 70  $^{\circ}\text{C}$  to 25  $^{\circ}\text{C}$ . Similarly, the polaritonic states formed through the coupling of the  $\text{C}=\text{C}$  stretching at 1492  $\text{cm}^{-1}$  and the 12<sup>th</sup> optical mode,  $\text{P}^+$  and  $\text{P}^-$ , respectively, increased by 5 and 4  $\text{cm}^{-1}$  as the temperature decreased. Finally, in the case of **VSC2**,  $\text{P}^+$  and  $\text{P}^-$  shifted to higher wavenumbers by up to 10 and 9  $\text{cm}^{-1}$  respectively, as the FP cavity was cooled to 25  $^{\circ}\text{C}$  (**Figure 4.7**).

In conclusion, the recrystallization experiments showed a slight increase in the ratio of the  $\alpha$ -form to the  $\beta$ -form under VSC conditions compared to non-cavity condition. Additionally, there was a higher variability in the polymorphic ratio observed during crystallization experiments under VSC. These findings suggest that VSC may have an effect on the crystallization outcome. However, the effect of VSC is likely weakened and variable due to the change of the FRS which in turns shifts the energy of polaritonic states during crystallization. It is important to note that previous studies reporting modifications in supramolecular assemblies induced by VSC were conducted at a fixed room temperature. Therefore, to confirm the influence of VSC on the polymorphic ratio in a systematic and reliable manner, crystallization

experiments should be conducted at a constant temperature of the FP cavity to prevent variations in the energy of polaritonic states throughout the experiment.



**Figure 4.7: Shift of the optical cavity modes due to temperature change.**

(a) Evolution of the optical cavity modes of an empty FP cavity when cooled from 70 °C to 25 °C. (b),(c) Shifts of the polaritonic states obtained in VSC1, referring to the coupling between the benzonitrile vibration at 2228  $\text{cm}^{-1}$  and the 18<sup>th</sup> optical mode and to the cooperative VSC between the vibration at 1492  $\text{cm}^{-1}$  and the 12<sup>th</sup> optical mode. (d) Shifts of the polaritonic states obtained in VSC2, referring to the coupling between the benzonitrile vibration at 1445  $\text{cm}^{-1}$  and the 12<sup>th</sup> optical mode

## 4.4 Summary

In this chapter the impact of VSC on the crystallization of perylene was investigated. First, the formation of the two polymorphic forms of perylene was studied using conventional crystallization methods such as solution-dropping, recrystallization and slurry techniques. The results indicate that both polymorphs grew concurrently in recrystallization experiments, whereas selective crystallization of either the  $\alpha$ -form or  $\beta$ -form was achieved through solution-dropping method. The  $\alpha$ -form was identified as the more stable thermodynamic form, which was obtained through slurry crystallization.

To examine the impact of VSC, recrystallization experiments were conducted in a FP cavity using two different conditions: cooperative VSC of the aromatic C=C stretching of benzonitrile that is resonant with perylene vibrational band and VSC of the aromatic C=C stretching solvent vibrational band that is not resonant with perylene vibrational modes. The experiments under VSC resulted in a slightly higher ratio of the  $\alpha$ -form to the  $\beta$ -form compared to the non-cavity condition. However, the FSR changed during the experiment due to the change in temperature of the microfluidic cell, causing a variation of the resonance conditions of the polaritonic states. This could potentially result in instability of the system and compromise the reproducibility of the results.

The study attempted to recrystallize perylene in a FP cavity but highlighted the limitation of the experimental setup due to the temperature changes of the FP cavity microfluidic cell. Therefore, alternative crystallization methods that can be conducted at room temperature, such as antisolvent crystallization, should be used in future experiments to fully explore the potential of VSC on crystal growth while avoiding issues with FSR changes.



# Chapter 5

## Materials and methods

### 5.1 OSC materials

DNTT (> 99% sublimed grade) and perylene (> 99.5 % sublimed grade) were purchased from Sigma-Aldrich, **C<sub>8</sub>-DN4T** (> 99% sublimed grade) was purchased from Lumtec. **DN4T**,<sup>[130]</sup> **isoDN4T**,<sup>[130]</sup> **tBu-BTBT-1**,<sup>[206]</sup> **tBu-BTBT-2**,<sup>[206]</sup> **tBu-BTBT**<sup>[133]</sup> and **C<sub>12</sub>-DBTTT**<sup>[171]</sup> were provided by Prof. Yves Geerts (Université Libre de Bruxelles), and their synthesis and purification are reported elsewhere.

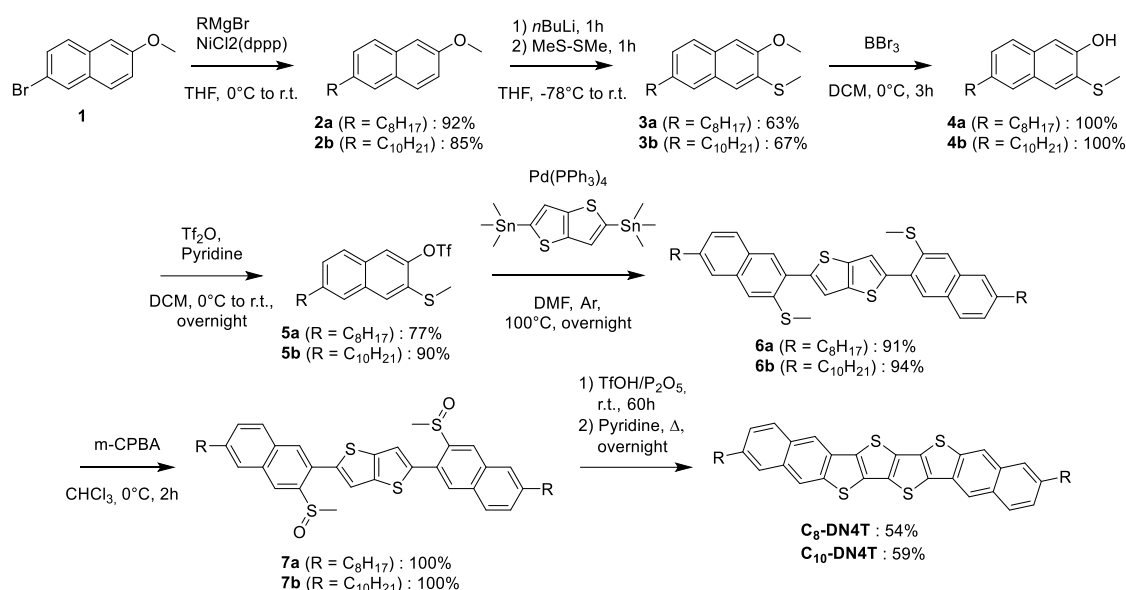
The synthetic routes and purification procedures for **C<sub>8</sub>-DN4T**, **C<sub>10</sub>-DN4T**, **tBu-DNTT** and **tBu-DBTTT** have not been published yet (manuscripts in preparation) and are reported in the following sections.

*The synthesis and purification of **C<sub>8</sub>-DN4T** and **C<sub>10</sub>-DN4T** were performed by Dr. Remy Jouclas, while the synthesis and purification of **tBu-DNTT** and **tBu-DBTTT** were performed by Dr. Antoine Leliege, in the laboratory of Prof. Yves Geerts (Université Libre de Bruxelles).*

#### 5.1.1 Synthesis of **C<sub>8</sub>-DN4T** and **C<sub>10</sub>-DN4T**

The synthesis followed the synthetic scheme previously published by Niimi *et. al.*<sup>[207]</sup> for the synthesis of dialkyl-DNTT. Introduction of the side alkyl chains was performed at the first step through a Kumada cross-coupling between the commercially available 6-bromo-2-methoxynaphthalene **1** and the corresponding commercial Grignard reagents to afford intermediates **2a-b**. Introduction of the thiomethyl group dedicated to the final thiophene-forming cyclization was performed by selective *ortho*-lithiation directed by the methoxy group. Subsequent conversion of the latter to triflate was carried out by demethylation in presence of boron tribromide followed by triflation with triflic anhydride to afford triflates **5a-b** in good yields for the 2 steps. The end of the synthesis was performed following the previously published synthetic scheme of **DN4T**<sup>[130]</sup> involving the use of commercial 2,5-bis-trimethylstannylthieno[3,2-b]thiophene and triflates **5a-b** in order to place the center of the tetrathienyl core. Cyclization of the resulting disulfides **6a-b** was performed upon oxidation into disulfoxydes in presence of *m*-CPBA with quantitative yields, prior to 2-steps cyclization in triflic acid in presence of phosphorus pentoxide followed by demethylation of the resulting triflate

salts in refluxed pyridine to afford **C<sub>8</sub>-DN4T** and **C<sub>10</sub>-DN4T** in moderate yields, with overall yields ranging from 22 to 28%. Purification of the final compounds was performed by recrystallization in 1,2,4-trichlorobenzene, giving NMR grade pure compounds as shiny gold powders composed of nano- to micrometric flake aggregates. Finally, analytical grade powders could be obtained by careful thermal sublimation of the obtained powders at 10<sup>-6</sup> mbar and 380°C.

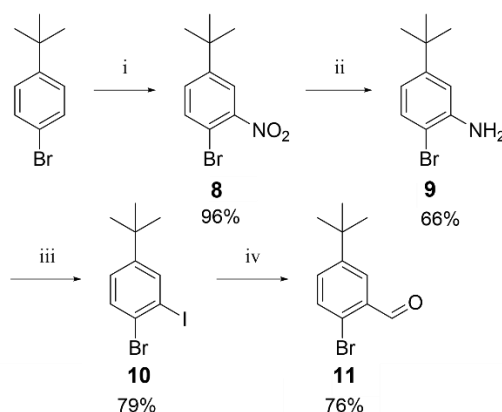


**Scheme 5.1**

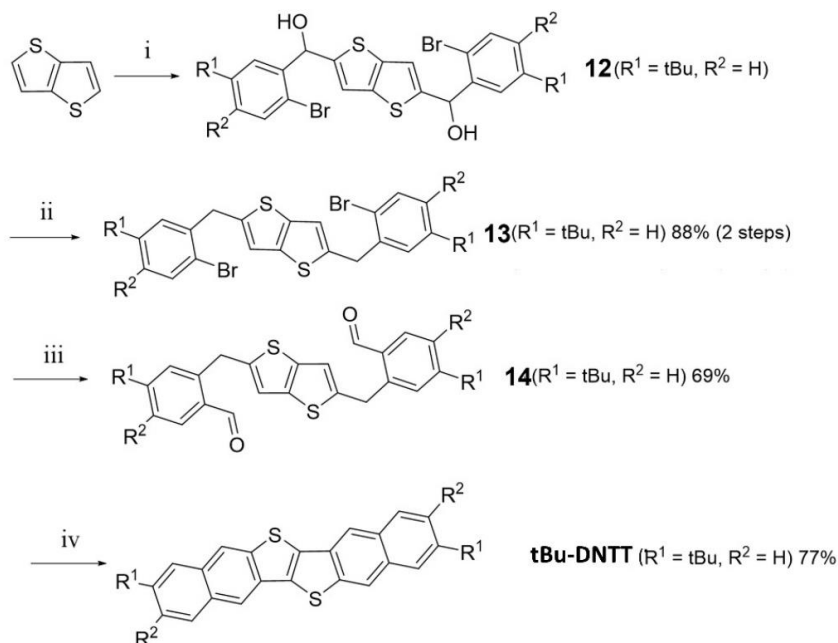
### 5.1.2 Synthesis of **tBu-DNTT**

**Scheme 5.2** shows the synthesis of the benzaldehydes **11** required for preparation of **tBu-DNTT**. The *tert*-butyl compound **11** is prepared in four steps starting from the commercial 1-bromo-4-(*tert*-butyl)benzene. The three first steps leading to the iodo compound **10** are described in a literature procedure and have been repeated.<sup>[208]</sup> The iodo compound **10** has been obtained in 38% yield from the starting compound 1-bromo-4-(*tert*-butyl)benzene. The *tert*-butyl compound **11** has not been reported, yet. It has been synthesized, at -78°C in THF, by iodine–magnesium exchange with *i*PrMgCl followed by trapping with DMF, in 76% yield. **tBu-DNTT** has been obtained by the synthetic route shown in **Scheme 5.3**, inspired by the one developed by Park *et al.* for the **DBTTT**.<sup>[128]</sup> **tBu-DNTT** is synthesized in four steps from the thieno[3,2-*b*]thiophene and **11**. The two first steps of **Scheme 5.3** afford dibromo compounds **13** in an 88 % yield. The dialdehyde derivatives **14** has been obtained in 69 % yield. Finally, the cyclization, followed by a dehydration and an aromatization gives rise, after purification by

sublimation, to **tBu-DNTT** in 82 % yield. Starting from thieno[3,2-b]thiophene the yield of **tBu-DNTT** is 47 %. The crude product was purified by sublimation (330 °C under a pressure of 10<sup>-6</sup> mbar), a yellow solid was obtained.



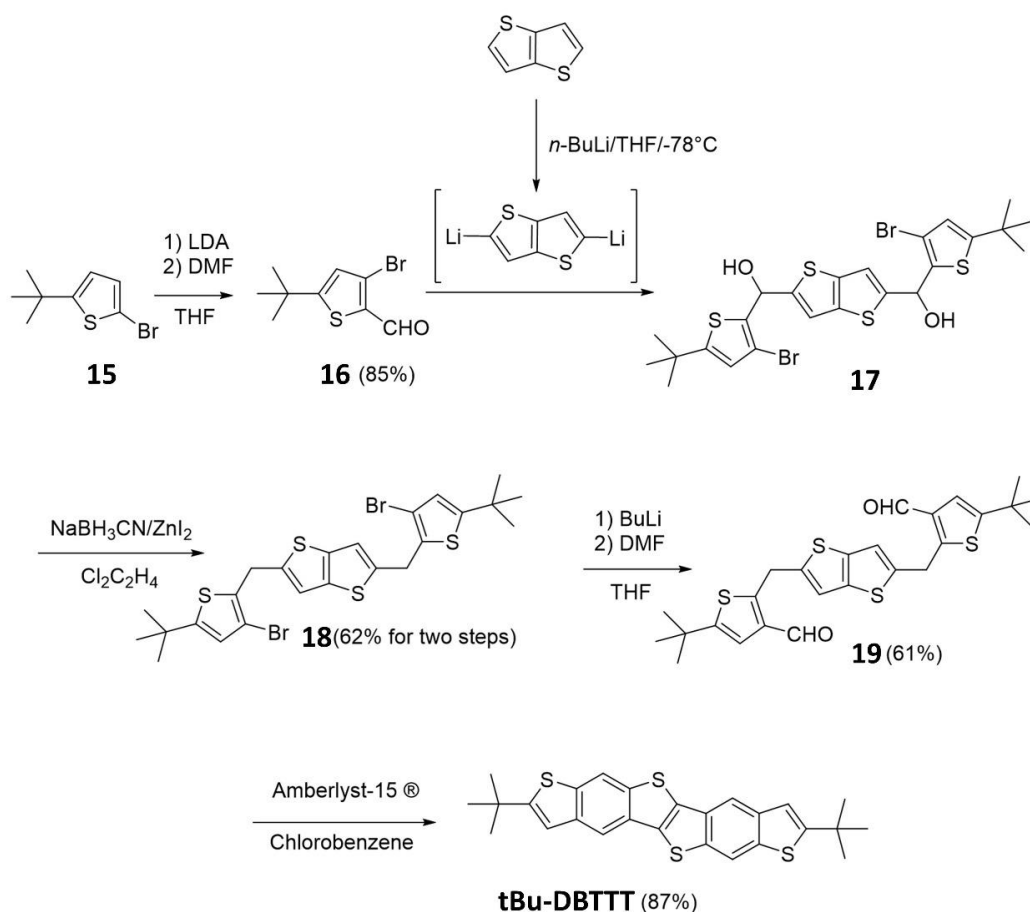
**Scheme 5.2:** i) HNO<sub>3</sub>, H<sub>2</sub>SO<sub>4</sub> (96% yield); ii) Na<sub>2</sub>S<sub>2</sub>O<sub>4</sub>, 2-methoxyethanol/water (66% yield); iii) NaNO<sub>2</sub>, HCl then KI, water (79% yield); iv) iPrMgCl then DMF, THF (76% yield).



**Scheme 5.3:** i) *n*-BuLi then 2-bromo-5-(tert-butyl)benzaldehyde (**11**) leading to the diol **12**, THF; ii) NaBH<sub>3</sub>CN, ZnI<sub>2</sub>, 1,2-dichloroethane; iii) *n*-BuLi then DMF, THF; iv) Amberlyst 15 ®, chlorobenzene.

### 5.1.3 Synthesis of tBu-DBTTT

**tBu-DBTTT** was obtained by a similar synthetic route developed by Park *et al.* for the **DBTTT**.<sup>[128]</sup> Compound **16** was synthesized from **15** by a halogen dance reaction at low temperature using LDA. The carbaldehyde **16** was then obtained by condensation of DMF on the lithium derivative. The final compound **tBu-DBTTT** is synthesized with a good yield from the thieno[3,2-*b*]thiophene (33% in four steps). Selective deprotonation at the  $\alpha$  position of the thieno[3,2-*b*]thiophene with *n*-BuLi, followed by the condensation with carbaldehyde **16**, gave diol **17**. This compound was reduced without more purification in presence of NaBH<sub>3</sub>CN and ZnI<sub>2</sub> for give the dibromo compound **18**. Compound **19** was obtained from compound **11** after lithium/bromine exchange with *n*-BuLi at low temperatures, followed by the addition of DMF. **tBu-DBTTT** was obtained by using Amberlyst-15® as a cyclization and aromatization agent in a Bradsher reaction on dialdehyde **12**. The final compound was purified by recrystallization to afford a white solid.



Scheme 5.4

## 5.2 Thin-film transistors fabrication and electrical measurements

All the thin film transistors were fabricated on highly doped silicon wafers with 30 nm of  $\text{Al}_2\text{O}_3$  (Christian-Albrecht University of Kiel, Institute for Electrical Engineering and Information Technology). The  $\text{Al}_2\text{O}_3$  substrates were exposed to oxygen plasma (Diener Electronic; oxygen flow rate 20 sccm, pressure 0.50 mbar, plasma power 100 W, duration 2 min) and then immersed overnight in 1.5 mM solution of n-tetradecylphosphonic acid (TDPA, Sigma-Aldrich) in 2-propanol (Acros Organics) to obtain a 1.5-nm-thick self-assembled monolayer (SAM). Subsequently, the substrates were rinsed first in 2-propanol then in deionized water and finally in 2-propanol again and dried on a hot plate at 100 °C for 10 min. Thus, the  $\text{Al}_2\text{O}_3$ /SAM dielectric has a capacitance of 185.5 nF cm<sup>-2</sup>. In the case of BC devices, gold bottom contacts were deposited by vacuum sublimation (UNIVEX 300, Leybold GmbH; pressure of  $\sim 10^{-5}$  mbar, deposition rate of 0.5 Å s<sup>-1</sup> and nominal thickness of ca. 50 nm monitored by a quartz crystal microbalance) through a shadow mask onto the gate-dielectric substrates at room temperature. Afterwards, the substrates were immersed in a 10 mM solution of pentafluorobenzenethiol (PFBT, Alfa Aesar) in 2-propanol for 30 min, obtaining a SAM on the gold bottom contacts, then rinsed with 2-propanol and dried. OSCs were evaporated in vacuum (pressure of  $\sim 10^{-6}$  mbar) through a shadow mask onto the substrates which were held at desired temperatures, obtaining the final devices with a channel width of 480 µm and channel length of 65, 115, 165 and 215 µm. In case of TC devices, OSCs were deposited by vacuum sublimation (pressure of  $\sim 10^{-6}$  mbar) on the  $\text{Al}_2\text{O}_3$ /SAM dielectric substrates, heated at desired temperatures, before the gold contacts deposition through a shadow mask (pressure of  $\sim 10^{-5}$  mbar, deposition rate of 0.5 Å s<sup>-1</sup>, nominal thickness of ca. 50 nm), obtaining the final devices with a channel width of 480 µm and channel length of 65, 115, 165 and 215 µm. The electrical measurements (Agilent 4155C Semiconductor Parameter Analyzer) were carried out in ambient air and at room temperature.

## 5.3 Ultraviolet photoelectron spectroscopy measurements

Ultraviolet photoelectron spectroscopy measurements were conducted using a UHV (ultra-high vacuum) system with a pressure of  $10^{-10}$  mbar. A Helium discharge lamp was used to produce the monochromatized He I<sub>a</sub> line (21.22 eV) for all measurements. The spectra were recorded at room temperature using a hemispherical SPECS Phoibos 100 analyzer. Prior to the

measurements, a polycrystalline gold foil was utilized to calibrate the detector and determine the energy resolution. The pass energy was set at 5 eV, providing an energy resolution of 120 meV for the valence region spectra. The work function values were determined from the secondary electron cutoff (SECO) spectra, measured with a sample bias of -10 V and a pass energy of 2 eV, which allowed for an energy resolution of 78 meV.

Before the UPS measurements, the molecules were deposited onto Au and PFBT/Au substrates by thermal evaporation under ultra-high vacuum conditions ( $10^{-8}$  mbar). The Au substrates were obtained by thermal evaporation of 30 nm layer of Au under high vacuum conditions ( $10^{-6}$  mbar) onto Si/SiO<sub>2</sub> substrates at a rate of  $0.5 \text{ \AA s}^{-1}$ . The PFBT/Au substrates were obtained by immersing the Au substrate in a 10 mM solution of PFBT (Alfa Aesar) in 2-propanol for 30 minutes, followed by rinsing with 2-propanol and drying. OSC films were grown onto the substrates, with the nominal thickness being monitored via a quartz crystal microbalance.

## 5.4 Atomic force microscopy

### 5.4.1 Topography imaging

The thin films morphologies were evaluated through atomic force microscopy (AFM, Bruker Dimension Icon) in tapping mode with Olympus OMCL-AC240TS-R3 tips.

### 5.4.2 Conductive atomic force microscopy

C-AFM measurements were performed on thin films of OSCs that were deposited on PFBT/Au substrates via vacuum sublimation (UNIVEX 300, Leybold GmbH; pressure of  $\sim 10^{-6}$  mbar, nominal thickness of approximately 10 nm monitored by a quartz crystal microbalance). The PFBT/Au substrates were prepared as described earlier for UPS measurements. The Au surface was grounded to the instrument's sample holder for electrical conductivity. C-AFM measurements were conducted using a Bruker Dimension Icon setup in contact mode, in air with a relative humidity level below 5%. Pt/Ir coated SCM-PIT-V2 tips were utilized for the measurements (tip stiffness:  $k = 3 \text{ N/m}$ ).

## 5.5 Thin-films X-Ray Diffraction

Thin film for X-Ray diffraction analysis were obtained by depositing OSCs onto TDPA/Al<sub>2</sub>O<sub>3</sub> substrates and onto PFBT/Au substrates with a nominal thickness of  $\approx 25$  nm, as described in section 5.2 and 5.3 respectively. X-ray diffraction was performed by using Rigaku SmartLab. The diffractometer is equipped with a Cu K $\alpha$  source. The measurements were carried out at a tube voltage of 40 kV (tube current of 50 mA), with scanning steps of 0.04° at scanning speed of 1.5°/min.

## 5.6 Photoelectron Yield Spectroscopy

Thin films used for X-ray diffraction measurements were employed for PYS measurements as well. Photoelectron yield curves were acquired utilizing a Riken Keiki spectrophotometer (model AC-2) with an energy increment of 0.05 eV and UV spot intensity of 10 nW.

## 5.7 Optical Microscopy

Optical microscope images were taken with a Zeiss Axiotron equipped with Zeiss Mikroscope Objektiv Epiplan-Neofluar lenses and with AxioCam MRc. Polarized optical microscope images were taken with Leica DM4500 P, equipped with N PLAN EPI POL lenses.

## 5.8 Powder X-Ray diffraction

The XRD patterns were obtained in Bragg–Brentano geometry, over the 2 $\theta$  range of 3–40°, with a step size of 0.01° and a speed of 10.0°/min, using a Rigaku MiniFlex 600 diffractometer with Cu K $\alpha$  radiation generated from a copper sealed tube with 40 kV and 15 mA.

## 5.9 Fabry-Perot cavity fabrication

CaF<sub>2</sub> windows and demountable microfluidic cells were purchased from Specac. The CaF<sub>2</sub> windows were sputtered with 10 nm of Au using Emitech K575X metal sputterer, followed by spin-coating a 100 nm thick insulating layer with a solution of PVA in water (4% w/w) at 4000 rpm. The Au mirrors were separated by a 25  $\mu$ m Mylar spacer (Specac) and assembled into the microfluidic cell. The temperature of the microfluidic cell was controlled by

using a heating jacket (Specac). All spectroscopic data were acquired via a tuned area of the cavity using a 2 mm diameter aperture. For non-cavity experiments, CaF<sub>2</sub> windows were prepared by spin-coating PVA onto them.

## 5.10 Fourier transformed infrared spectroscopy

The FT-IR spectroscopy data were recorded with a Bruker Vertex 70 FT-IR spectrometer in transmission mode. The spectra were acquired with 2 cm<sup>-1</sup> resolution and averaged over at least 38 scans.

## 5.11 Quantum calculations

### 5.11.1 Transfer integrals

The optimization of geometry, computation of electronic structure, and estimation of reorganization energies of neutral isomers were carried out using the B3LYP functional and a 6-31G(d,p) basis set at the Density Functional Theory (DFT) level with the Gaussian 16-A03 package.<sup>[209]</sup> The transfer integrals between closely situated neighbours in the frozen crystal structure were calculated using the reported experimental crystal structures as input. To estimate these parameters at the DFT B3LYP/DZ level of theory within a fragment orbital approach, the ADF package was utilized.<sup>[210,211]</sup> In practice, a 3×3×3 supercell was created for each molecule and electronic couplings were computed among all pairs of close neighbours, which included molecules in the unit cell at the center of the system. Any molecule B for which at least one atom was within a 5 Å range of any atom of molecule A was considered a close neighbour to a given molecule A.

### 5.11.2 Reorganization energies

The nuclear relaxation energy associated with the transition from neutral to charged geometry was evaluated using a displaced harmonic oscillator model. The individual contributions of each intramolecular vibrational mode were determined, while neglecting Duchinsky rotation effects<sup>[63]</sup> :

$$E_{rel} = \sum_i \frac{g^2(i)}{\hbar\omega_i} = \sum_i S_i \hbar\omega_i \quad (5.1)$$

with the index i running over all intramolecular vibrational modes of energy  $\hbar\omega_i$ .  $g(i)$  is the local electron-phonon coupling constant associated to the

normal coordinate  $Q_i$  that has been computed numerically and  $S_i$  the corresponding Huang-Rhys factor.

$$g^2(i) = \frac{V^2(i)}{2M_i\hbar\omega^3} \text{ and } V^2(i) = \left(\frac{\partial^2 E}{\partial Q_i^2}\right)_{Q=0} \quad (5.2)$$

with  $M_i$  the effective mass of mode  $i$ .

### 5.11.3 Mobility Anisotropy

Mobility anisotropy plots were computed using a hopping regime and a Kinetic Monte Carlo algorithm that employs the first reaction method.<sup>[212]</sup> Initially, a single charge was localized at a specific site or molecular unit at  $t=0$ , and hopping rates were subsequently determined based on the transfer integrals and reorganization energies computed at the quantum-chemical level. Random waiting times were generated for each hopping process, and the process with the shortest waiting time was chosen. The simulation clock was then advanced by the chosen waiting time, and the distance travelled by the charge was incremented by the distance between the centers of mass of the involved molecules in the charge transfer. This cycle was repeated until the simulation clock reached a time limit of  $10^{-9}$  s. Finally, the mobility was determined using the following equation:

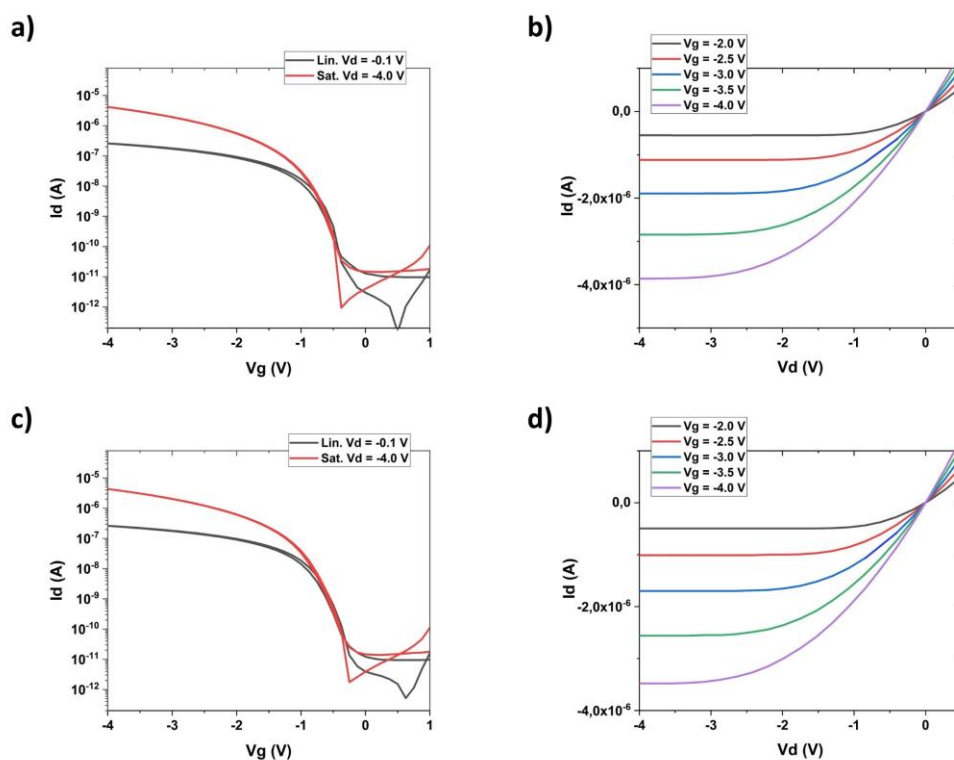
$$\mu = \frac{d}{t E} \quad (5.3)$$

Where  $E$  is the amplitude of the electric field (set to 1000 V/cm). Mobilities were computed for different directions of the electric with regard to the unit cell vector  $a$ , from  $\theta=0^\circ$  to  $\theta=350^\circ$ .

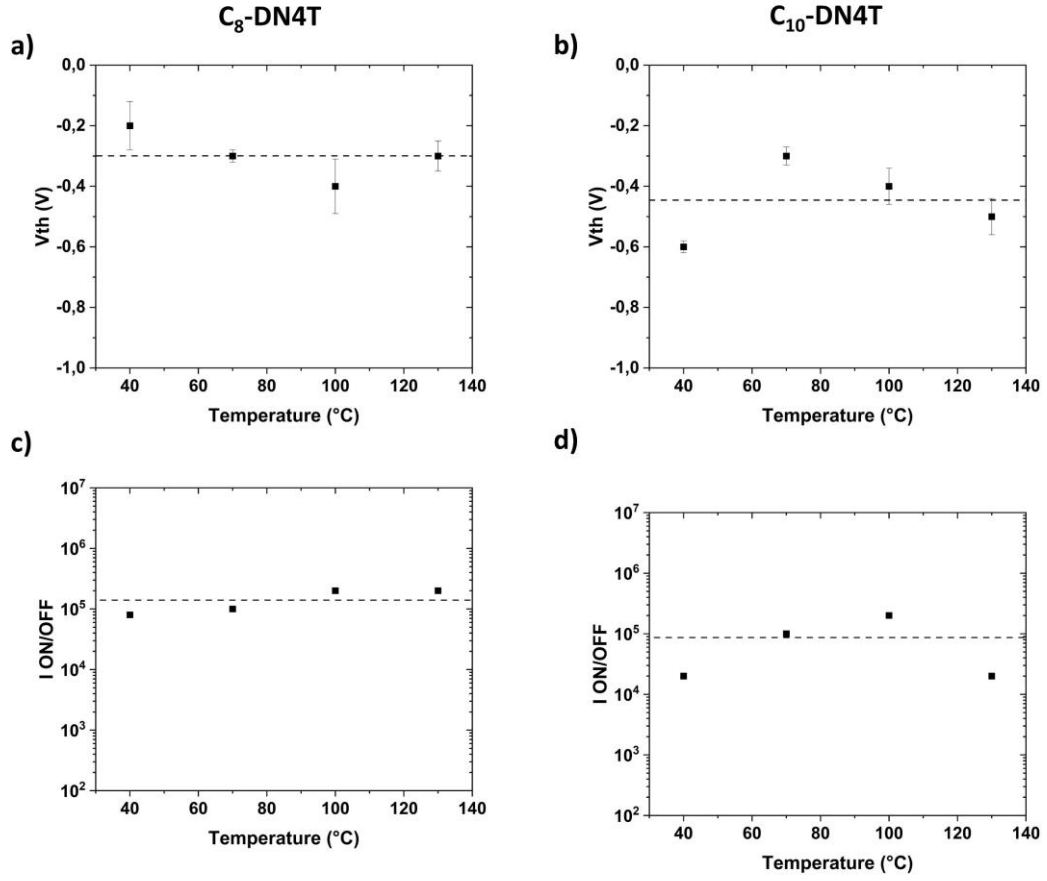


# Appendix

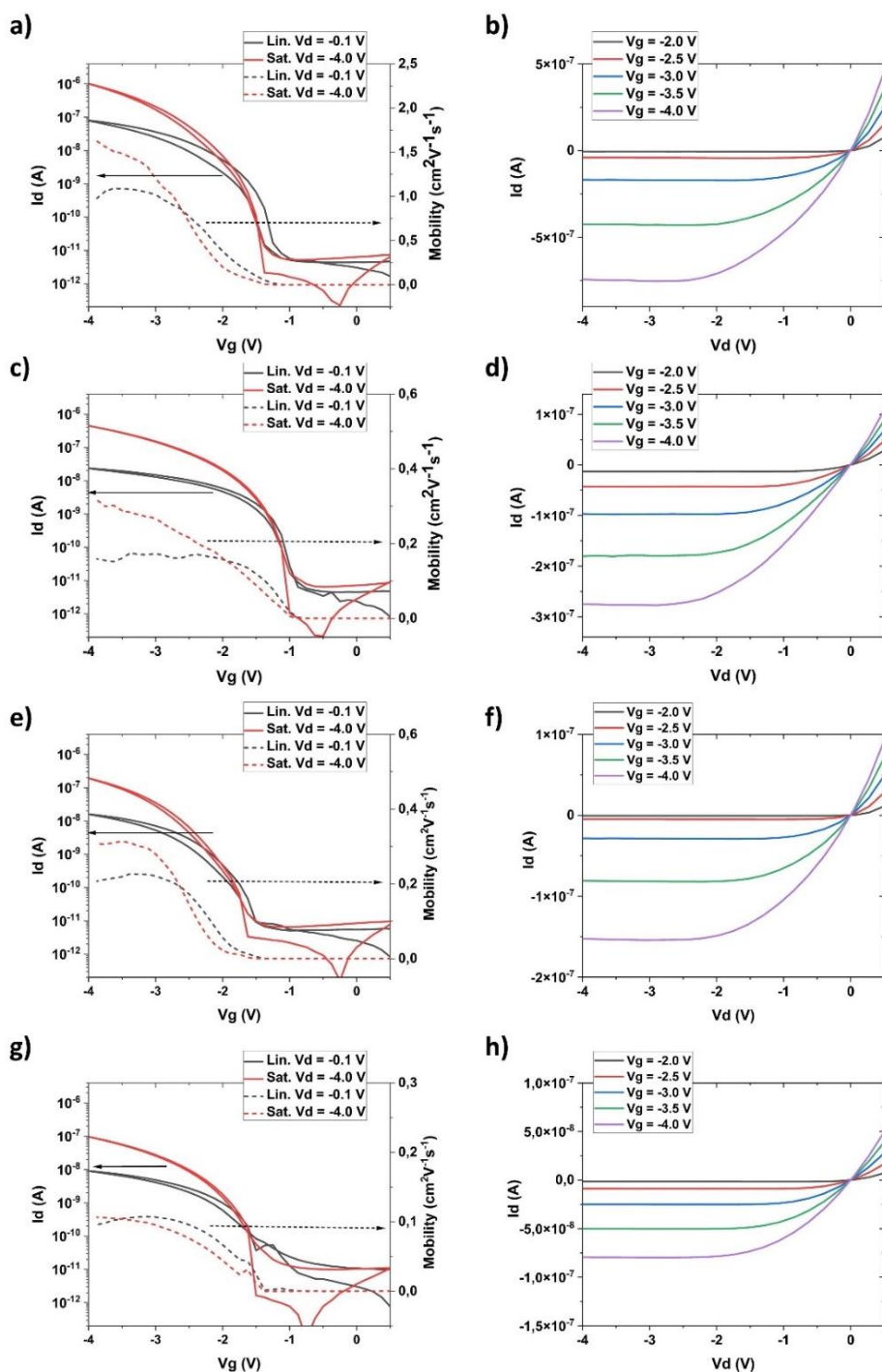
## A.1 Appendix referred to Chapter 2: “Charge transport and charge injection properties of new thienoacene derivatives in thin-film transistors”



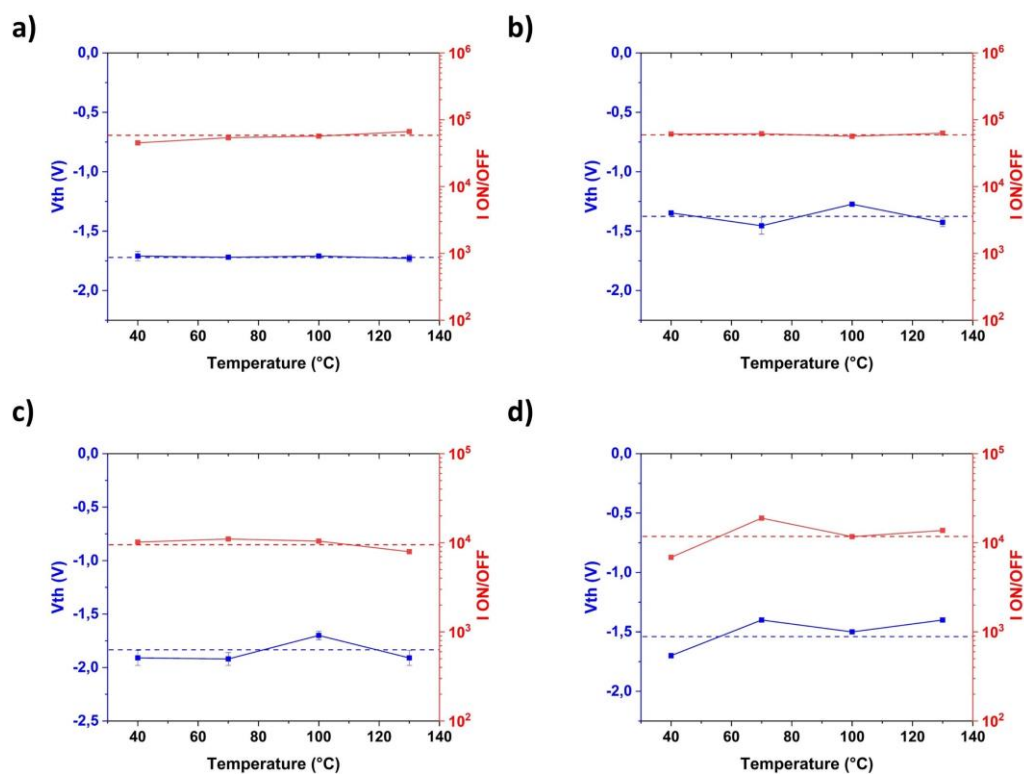
**Figure A1.1:** Transfer and output characteristics of **C<sub>8</sub>-DN4T** and **C<sub>10</sub>-DN4T** TC devices. On the top: representative transfer (on the left) and output (on the right) characteristics of BC TFTs based on (a),(b) **C<sub>8</sub>-DN4T** and (c),(d) **C<sub>10</sub>-DN4T** at substrate temperature of 100 °C. TFTs have W/L = 480/215  $\mu\text{m}$ .



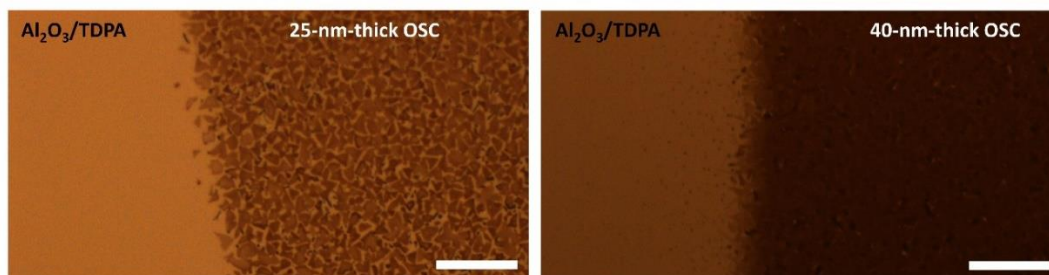
**Figure A1.2:** Threshold voltage and on/off current ratio vs substrate temperature for  $C_8$ -DN4T and  $C_{10}$ -DN4T. Threshold voltage and on/off current ratio as a function of the substrate temperature in (a),(c)  $C_8$ -DN4T and (b),(d)  $C_{10}$ -DN4T based BC TFTs. The values are referred to the linear regime and to devices with  $W/L = 480/215$   $\mu m$ . The dot lines indicate the averaged values of  $V_{th}$  and  $I_{ON/OFF}$ .



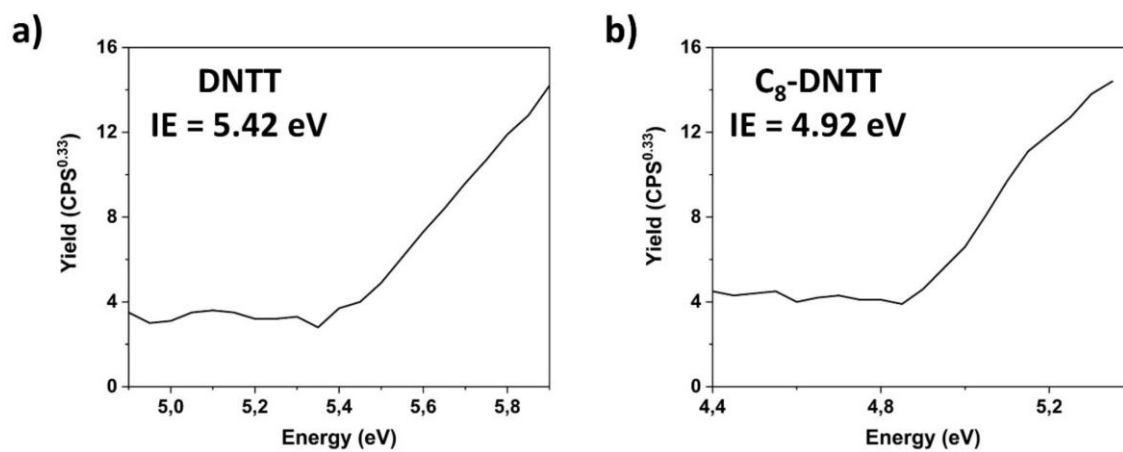
**Figure A1.3:** Transfer (left) and output (right) characteristics of the best performing TC TFTs based on *tert*-butyl theienoacene derivatives. (a, b) **tBu-DNTT**, (c, d) **tBu-DBTTT**, (e, f) **tBu-BTBT-1** and (g, h) **tBu-BTBT-2**. In transfer characteristics, solid lines and dashed lines are referred to drain current and mobility respectively. All TFTs have  $W/L = 480/215 \mu\text{m}$ .



**Figure A1.4:** Threshold voltage and on/off current ratio vs the substrate temperature for BC TFTs based on *tert*-butyl thienoacene derivatives. (a) **tBu-DNTT**, (b) **tBu-DBTTT**, (c) **tBu-BTBT-1** and (d) **tBu-BTBT-2**. The values are referred to the linear regime and to devices with  $W/L = 480/215 \mu\text{m}$ . The dot lines indicate the averaged values of  $V_{th}$  and  $I_{ON/OFF}$ .



**Figure A1.5:** Optical micrographs of 25-nm-thick (on the left) and 40-nm-thick (on the right) layer of **tBu-BTBT** deposited onto  $\text{Al}_2\text{O}_3/\text{TDPA}$  at substrate temperature of  $70^{\circ}\text{C}$ . Scale bar =  $20 \mu\text{m}$ .



**Figure A1.6:** PYS measurements performed on thin films of (a) **DNTT** and (b) **C<sub>8</sub>-DNTT**

**Table A1.1:** Electrical performance of **DN4T** and **isoDN4T** TFTs, in linear ( $V_d = -0.1$  V) and saturation ( $V_d = -4.0$  V) regime.

Compound	Geometry	Substrate T (°C)	$\mu$ (cm <sup>2</sup> V <sup>-1</sup> s <sup>-1</sup> )		$V_{th}$ (V)		$I_{ON/OFF}$	
			Linear	Saturation	Linear	Saturation	Linear	Saturation
DN4T	TC	40	$0.9 \pm 0.03$	$0.8 \pm 0.01$	$-2.3 \pm 0.01$	$-1.9 \pm 0.01$	$\sim 5 \times 10^5$	$\sim 7 \times 10^5$
		60	$1.7 \pm 0.03$	$1.6 \pm 0.01$	$-2.0 \pm 0.05$	$-1.6 \pm 0.03$	$\sim 2 \times 10^6$	$\sim 6 \times 10^5$
		80	$1.7 \pm 0.08$	$1.5 \pm 0.01$	$-2.4 \pm 0.07$	$-2.2 \pm 0.01$	$\sim 7 \times 10^5$	$\sim 4 \times 10^6$
		100	$2.1 \pm 0.03$	$1.9 \pm 0.05$	$-1.9 \pm 0.04$	$-1.9 \pm 0.05$	$\sim 9 \times 10^5$	$\sim 2 \times 10^6$
		120	$1.9 \pm 0.22$	$1.8 \pm 0.19$	$-1.9 \pm 0.10$	$-1.6 \pm 0.13$	$\sim 1 \times 10^6$	$\sim 3 \times 10^6$
		140	$1.9 \pm 0.05$	$1.7 \pm 0.05$	$-2.1 \pm 0.13$	$-1.8 \pm 0.17$	$\sim 9 \times 10^5$	$\sim 2 \times 10^6$
	BC	40	$1.3 \pm 0.02$	$1.1 \pm 0.01$	$-1.3 \pm 0.02$	$-1.1 \pm 0.01$	$\sim 1 \times 10^5$	$\sim 2 \times 10^5$
		60	$1.4 \pm 0.07$	$1.3 \pm 0.06$	$-1.1 \pm 0.04$	$-0.9 \pm 0.04$	$\sim 1 \times 10^5$	$\sim 3 \times 10^5$
		80	$1.6 \pm 0.11$	$1.5 \pm 0.11$	$-1.3 \pm 0.02$	$-1.1 \pm 0.02$	$\sim 6 \times 10^5$	$\sim 5 \times 10^5$
		100	$2.0 \pm 0.02$	$1.8 \pm 0.02$	$-1.2 \pm 0.01$	$-1.0 \pm 0.01$	$\sim 3 \times 10^5$	$\sim 5 \times 10^5$
		120	$1.5 \pm 0.10$	$1.4 \pm 0.10$	$-1.2 \pm 0.05$	$-1.0 \pm 0.04$	$\sim 4 \times 10^5$	$\sim 4 \times 10^5$
		140	$1.3 \pm 0.11$	$1.1 \pm 0.10$	$-1.4 \pm 0.05$	$-1.2 \pm 0.05$	$\sim 1 \times 10^6$	$\sim 5 \times 10^5$
isoDN4T	TC	40	$(3.6 \pm 0.06) \times 10^{-3}$	$(3.3 \pm 0.04) \times 10^{-3}$	$-2.0 \pm 0.05$	$-1.6 \pm 0.05$	$\sim 6 \times 10^3$	$\sim 3 \times 10^4$
		60	$(3.6 \pm 0.08) \times 10^{-3}$	$(3.2 \pm 0.06) \times 10^{-3}$	$-1.9 \pm 0.07$	$-1.6 \pm 0.07$	$\sim 7 \times 10^3$	$\sim 2 \times 10^4$
		80	$(3.7 \pm 0.01) \times 10^{-3}$	$(3.6 \pm 0.01) \times 10^{-3}$	$-1.8 \pm 0.07$	$-1.6 \pm 0.06$	$\sim 4 \times 10^3$	$\sim 2 \times 10^4$
		100	$(4.2 \pm 0.01) \times 10^{-3}$	$(4.2 \pm 0.01) \times 10^{-3}$	$-1.7 \pm 0.01$	$-1.5 \pm 0.01$	$\sim 4 \times 10^3$	$\sim 3 \times 10^4$
		120	$(4.1 \pm 0.05) \times 10^{-3}$	$(4.0 \pm 0.01) \times 10^{-3}$	$-1.8 \pm 0.03$	$-1.5 \pm 0.02$	$\sim 4 \times 10^3$	$\sim 2 \times 10^4$
		140	$(3.5 \pm 0.04) \times 10^{-3}$	$(3.4 \pm 0.11) \times 10^{-3}$	$-2.2 \pm 0.04$	$-1.9 \pm 0.03$	$\sim 3 \times 10^3$	$\sim 2 \times 10^4$
	BC	40	$(2.9 \pm 0.08) \times 10^{-3}$	$(2.5 \pm 0.10) \times 10^{-3}$	$-1.4 \pm 0.13$	$-0.8 \pm 0.01$	$\sim 4 \times 10^3$	$\sim 6 \times 10^4$
		60	$(3.2 \pm 0.24) \times 10^{-3}$	$(3.0 \pm 0.22) \times 10^{-3}$	$-1.1 \pm 0.01$	$-0.8 \pm 0.01$	$\sim 7 \times 10^2$	$\sim 3 \times 10^3$
		80	$(3.3 \pm 0.05) \times 10^{-3}$	$(3.0 \pm 0.04) \times 10^{-3}$	$-1.2 \pm 0.01$	$-0.7 \pm 0.02$	$\sim 9 \times 10^2$	$\sim 2 \times 10^3$
		100	$(3.3 \pm 0.10) \times 10^{-3}$	$(3.1 \pm 0.04) \times 10^{-3}$	$-1.0 \pm 0.01$	$-0.7 \pm 0.02$	$\sim 6 \times 10^2$	$\sim 3 \times 10^3$
		120	$(3.5 \pm 0.04) \times 10^{-3}$	$(3.4 \pm 0.02) \times 10^{-3}$	$-0.8 \pm 0.04$	$-0.5 \pm 0.05$	$\sim 1 \times 10^3$	$\sim 3 \times 10^3$
		140	$(3.2 \pm 0.09) \times 10^{-3}$	$(3.0 \pm 0.02) \times 10^{-3}$	$-1.1 \pm 0.03$	$-0.7 \pm 0.03$	$\sim 2 \times 10^3$	$\sim 4 \times 10^3$

**Table A1.2:** Electrical performance of **C<sub>8</sub>-DN4T** and **C<sub>10</sub>-DN4T** TFTs, in linear ( $V_d = -0.1$  V) and saturation ( $V_d = -4.0$  V) regime.

Compound	Geometr y	Substrat e T (°C)	$\mu$ (cm <sup>2</sup> V <sup>-1</sup> s <sup>-1</sup> )		$V_{th}$ (V)		$I_{ON/OFF}$	
			Linear	Saturatio n	Linear	Saturatio n	Linear	Saturatio n
<b>C<sub>8</sub>-DN4T</b>	<b>BC</b>	40	1.1 ± 0.09	1.2 ± 0.07	-0.2 ± 0.08	-0.2 ± 0.08	~ 8 × 10 <sup>4</sup>	~ 1 × 10 <sup>5</sup>
		70	1.5 ± 0.09	1.4 ± 0.24	-0.3 ± 0.02	-0.3 ± 0.02	~ 1 × 10 <sup>5</sup>	~ 1 × 10 <sup>5</sup>
		100	2.3 ± 0.21	2.2 ± 0.22	-0.4 ± 0.09	-0.3 ± 0.07	~ 2 × 10 <sup>5</sup>	~ 4 × 10 <sup>5</sup>
		130	1.9 ± 0.04	1.9 ± 0.02	-0.3 ± 0.05	-0.8 ± 0.05	~ 2 × 10 <sup>5</sup>	~ 1 × 10 <sup>5</sup>
	<b>TC</b>	40	1.3 ± 0.16	1.2 ± 0.15	-0.9 ± 0.02	-0.8 ± 0.02	~ 4 × 10 <sup>4</sup>	~ 6 × 10 <sup>5</sup>
		70	1.4 ± 0.01	1.4 ± 0.01	-0.9 ± 0.01	-0.8 ± 0.01	~ 5 × 10 <sup>4</sup>	~ 7 × 10 <sup>5</sup>
		100	2.0 ± 0.02	2.0 ± 0.02	-0.8 ± 0.07	-0.8 ± 0.06	~ 9 × 10 <sup>4</sup>	~ 1 × 10 <sup>6</sup>
		130	1.6 ± 0.02	1.5 ± 0.02	-0.9 ± 0.04	-0.2 ± 0.04	~ 5 × 10 <sup>4</sup>	~ 7 × 10 <sup>5</sup>
<b>C<sub>10</sub>-DN4T</b>	<b>BC</b>	40	0.2 ± 0.01	0.2 ± 0.01	-0.6 ± 0.02	-0.6 ± 0.02	~ 2 × 10 <sup>4</sup>	~ 3 × 10 <sup>4</sup>
		70	1.0 ± 0.03	1.1 ± 0.03	-0.3 ± 0.03	-0.3 ± 0.06	~ 1 × 10 <sup>5</sup>	~ 4 × 10 <sup>5</sup>
		100	2.5 ± 0.05	2.5 ± 0.05	-0.4 ± 0.06	-0.4 ± 0.06	~ 4 × 10 <sup>5</sup>	~ 2 × 10 <sup>6</sup>
		130	1.0 ± 0.03	1.0 ± 0.03	-0.5 ± 0.06	-0.5 ± 0.06	~ 2 × 10 <sup>4</sup>	~ 4 × 10 <sup>5</sup>
	<b>TC</b>	40	0.1 ± 0.01	0.1 ± 0.01	-1.6 ± 0.07	-1.4 ± 0.03	~ 2 × 10 <sup>3</sup>	~ 1 × 10 <sup>4</sup>
		70	0.8 ± 0.07	0.8 ± 0.07	-0.9 ± 0.05	-0.8 ± 0.05	~ 2 × 10 <sup>4</sup>	~ 3 × 10 <sup>5</sup>
		100	1.8 ± 0.12	1.8 ± 0.12	-0.8 ± 0.04	-0.8 ± 0.04	~ 7 × 10 <sup>4</sup>	~ 1 × 10 <sup>6</sup>
		130	0.7 ± 0.01	0.7 ± 0.01	-1.1 ± 0.04	-1.0 ± 0.03	~ 2 × 10 <sup>4</sup>	~ 2 × 10 <sup>5</sup>

**Table A1.3:** Electrical performances of BC and TC TFTs based on **tBu-DNTT**, in linear ( $V_d = -0.1$  V) and saturation ( $V_d = -4.0$  V) regime.

Compound	Geometry	Substrate T (°C)	$\mu$ (cm <sup>2</sup> V <sup>-1</sup> s <sup>-1</sup> )		$V_{th}$ (V)		$I_{ON/OFF}$	
			Linear	Saturation	Linear	Saturation	Linear	Saturation
<b>tBu-DNTT</b>	<b>TC</b>	40	0.22 ± 0.04	0.28 ± 0.10	-2.0 ± 0.12	-2.0 ± 0.06	5 × 10 <sup>3</sup>	1 × 10 <sup>5</sup>
		70	0.53 ± 0.14	0.83 ± 0.20	-2.0 ± 0.06	-2.0 ± 0.03	2 × 10 <sup>4</sup>	7 × 10 <sup>5</sup>
		100	0.87 ± 0.14	1.0 ± 0.11	-2.0 ± 0.07	-2.0 ± 0.06	2 × 10 <sup>4</sup>	5 × 10 <sup>5</sup>
		130	0.44 ± 0.08	0.59 ± 0.14	-2.0 ± 0.10	-2.0 ± 0.07	1 × 10 <sup>4</sup>	2 × 10 <sup>5</sup>
	<b>BC</b>	40	1.4 ± 0.08	1.3 ± 0.07	-1.7 ± 0.04	-1.7 ± 0.04	5 × 10 <sup>4</sup>	1 × 10 <sup>6</sup>
		70	1.7 ± 0.03	1.6 ± 0.02	-1.7 ± 0.02	-1.7 ± 0.02	5 × 10 <sup>4</sup>	1 × 10 <sup>6</sup>
		100	1.8 ± 0.07	1.7 ± 0.05	-1.7 ± 0.01	-1.7 ± 0.01	6 × 10 <sup>4</sup>	4 × 10 <sup>6</sup>
		130	1.8 ± 0.01	1.7 ± 0.01	-1.7 ± 0.03	-1.7 ± 0.01	7 × 10 <sup>4</sup>	2 × 10 <sup>6</sup>

**Table A1.4:** Electrical performances of BC and TC TFTs based on **tBu-DBTTT**, in linear ( $V_d = -0.1$  V) and saturation ( $V_d = -4.0$  V) regime.

Compound	Geometry	Substrate T (°C)	$\mu$ (cm <sup>2</sup> V <sup>-1</sup> s <sup>-1</sup> )		$V_{th}$ (V)		$I_{ON/OFF}$	
			Linear	Saturation	Linear	Saturation	Linear	Saturation
<b>tBu-DBTTT</b>	<b>TC</b>	40	0.09 ± 0.03	0.19 ± 0.03	-1.5 ± 0.03	-1.5 ± 0.03	2 × 10 <sup>4</sup>	1 × 10 <sup>5</sup>
		70	0.17 ± 0.01	0.24 ± 0.01	-1.5 ± 0.03	-1.4 ± 0.06	3 × 10 <sup>4</sup>	9 × 10 <sup>4</sup>
		100	0.16 ± 0.02	0.17 ± 0.02	-1.5 ± 0.04	-1.3 ± 0.21	1 × 10 <sup>4</sup>	1 × 10 <sup>5</sup>
		130	0.11 ± 0.03	0.19 ± 0.05	-1.5 ± 0.08	-1.3 ± 0.15	2 × 10 <sup>4</sup>	2 × 10 <sup>5</sup>
	<b>BC</b>	40	0.7 ± 0.03	0.2 ± 0.01	-1.4 ± 0.01	-0.6 ± 0.02	6 × 10 <sup>4</sup>	9 × 10 <sup>5</sup>
		70	1.0 ± 0.01	1.1 ± 0.03	-1.5 ± 0.07	-0.3 ± 0.06	6 × 10 <sup>4</sup>	1 × 10 <sup>6</sup>
		100	1.0 ± 0.03	2.5 ± 0.05	-1.3 ± 0.02	-0.4 ± 0.06	6 × 10 <sup>4</sup>	1 × 10 <sup>6</sup>
		130	0.5 ± 0.13	1.0 ± 0.03	-1.4 ± 0.03	-0.5 ± 0.06	6 × 10 <sup>4</sup>	9 × 10 <sup>5</sup>

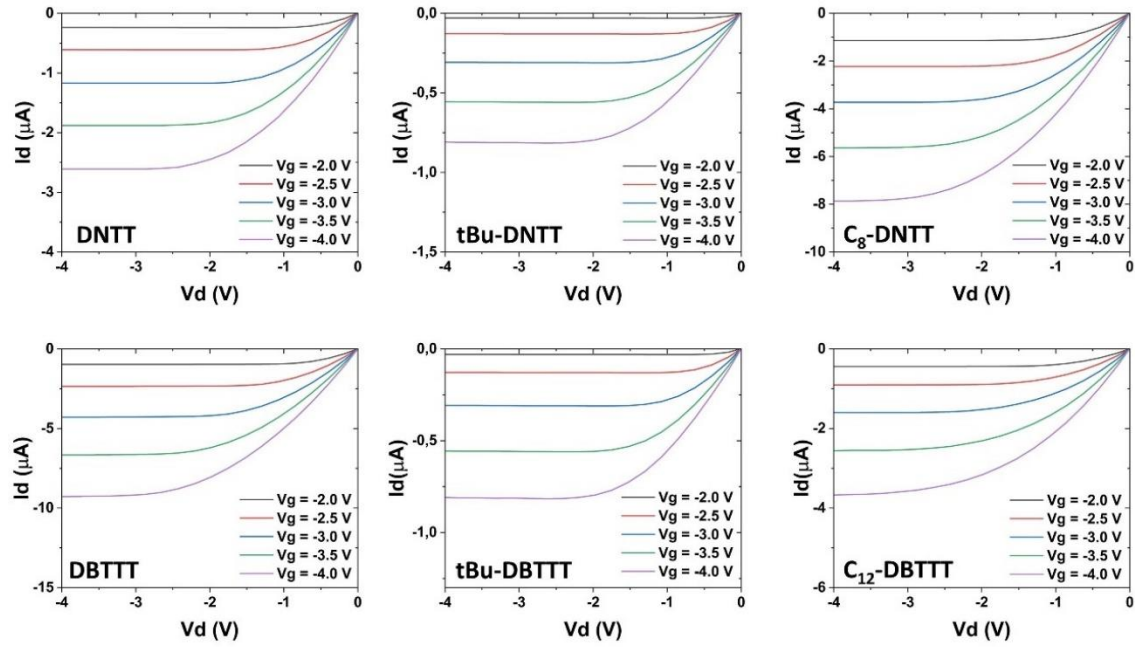
**Table A1.5:** Electrical performances of BC and TC TFTs based on **tBu-BTBT-1**, in linear ( $V_d = -0.1$  V) and saturation ( $V_d = -4.0$  V) regime.

Compound	Geometry	Substrate T (°C)	$\mu$ (cm <sup>2</sup> V <sup>-1</sup> s <sup>-1</sup> )		$V_{th}$ (V)		$I_{ON/OFF}$	
			Linear	Saturation	Linear	Saturation	Linear	Saturation
<b>tBu-BTBT-1</b>	<b>TC</b>	40	0.04 ± 0.007	0.05 ± 0.005	-2.3 ± 0.07	-2.3 ± 0.1	9 × 10 <sup>2</sup>	1 × 10 <sup>4</sup>
		70	0.05 ± 0.004	0.08 ± 0.008	-2.1 ± 0.15	-2.1 ± 0.19	1 × 10 <sup>3</sup>	3 × 10 <sup>4</sup>
		100	0.18 ± 0.019	0.26 ± 0.026	-2.1 ± 0.14	-2.1 ± 0.16	5 × 10 <sup>3</sup>	1 × 10 <sup>5</sup>
		130	0.14 ± 0.018	0.18 ± 0.018	-2.2 ± 0.17	-2.2 ± 0.18	4 × 10 <sup>3</sup>	6 × 10 <sup>4</sup>
	<b>BC</b>	40	0.20 ± 0.005	0.18 ± 0.006	-1.9 ± 0.07	-1.9 ± 0.07	1 × 10 <sup>4</sup>	2 × 10 <sup>5</sup>
		70	0.23 ± 0.007	0.22 ± 0.005	-1.9 ± 0.06	-1.9 ± 0.09	1 × 10 <sup>4</sup>	1 × 10 <sup>5</sup>
		100	0.25 ± 0.008	0.22 ± 0.005	-1.7 ± 0.04	-1.7 ± 0.05	1 × 10 <sup>4</sup>	1 × 10 <sup>5</sup>
		130	0.19 ± 0.033	0.21 ± 0.002	-1.9 ± 0.07	-1.9 ± 0.11	8 × 10 <sup>3</sup>	3 × 10 <sup>5</sup>

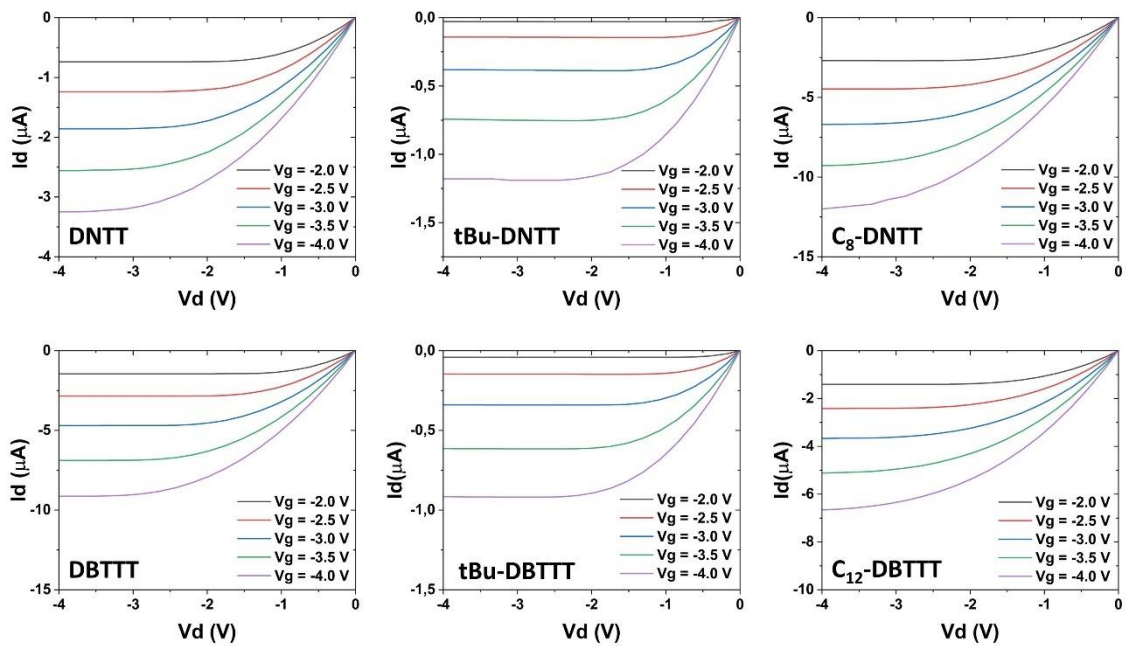
**Table A1.6:** Electrical performances of BC and TC TFTs based on **tBu-BTBT-2**, in linear ( $V_d = -0.1$  V) and saturation ( $V_d = -4.0$  V) regime.

Compound	Geometry	Substrate T (°C)	$\mu$ (cm <sup>2</sup> V <sup>-1</sup> s <sup>-1</sup> )		$V_{th}$ (V)		$I_{ON/OFF}$	
			Linear	Saturation	Linear	Saturation	Linear	Saturation
<b>tBu-BTBT-2</b>	<b>TC</b>	40	0.05 ± 0.005	0.05 ± 0.001	-1.8 ± 0.14	-1.8 ± 0.06	3 × 10 <sup>3</sup>	1 × 10 <sup>4</sup>
		70	0.08 ± 0.002	0.07 ± 0.001	-1.8 ± 0.04	-1.7 ± 0.05	2 × 10 <sup>3</sup>	2 × 10 <sup>4</sup>
		100	0.07 ± 0.003	0.09 ± 0.004	-1.8 ± 0.01	-1.8 ± 0.03	3 × 10 <sup>3</sup>	2 × 10 <sup>5</sup>
		130	0.06 ± 0.007	0.06 ± 0.005	-1.8 ± 0.08	-1.8 ± 0.02	3 × 10 <sup>3</sup>	2 × 10 <sup>4</sup>
	<b>BC</b>	40	0.05 ± 0.001	0.05 ± 0.001	-1.7 ± 0.02	-1.6 ± 0.01	7 × 10 <sup>3</sup>	1 × 10 <sup>5</sup>
		70	0.08 ± 0.002	0.08 ± 0.002	-1.4 ± 0.02	-1.4 ± 0.02	2 × 10 <sup>4</sup>	9 × 10 <sup>5</sup>
		100	0.10 ± 0.003	0.09 ± 0.001	-1.5 ± 0.01	-1.4 ± 0.01	1 × 10 <sup>4</sup>	7 × 10 <sup>4</sup>
		130	0.09 ± 0.001	0.08 ± 0.001	-1.4 ± 0.02	-1.4 ± 0.02	1 × 10 <sup>4</sup>	2 × 10 <sup>6</sup>

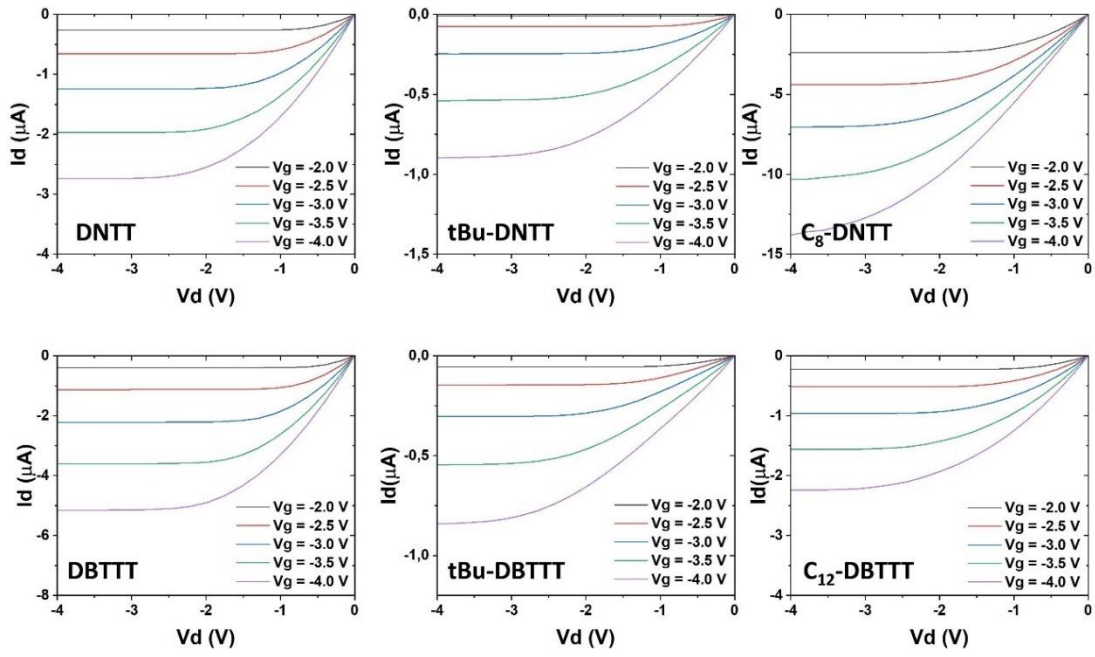
## A.2 Appendix referred to Chapter 3: “Elucidating the influence of the molecular structure of thienoacenes organic semiconductors on contact resistance”.



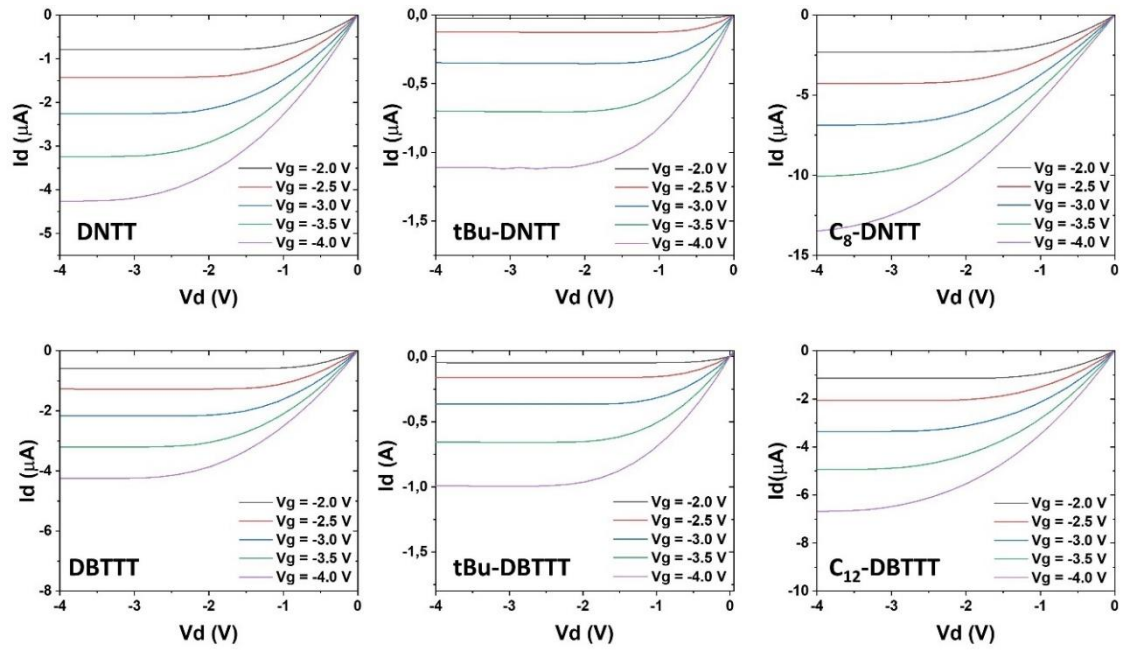
**Figure A2.1:** Output characteristics of TC TFTs with 25-nm-thick OSC layer. All TFTs have  $W/L = 480/215 \mu\text{m}$ .



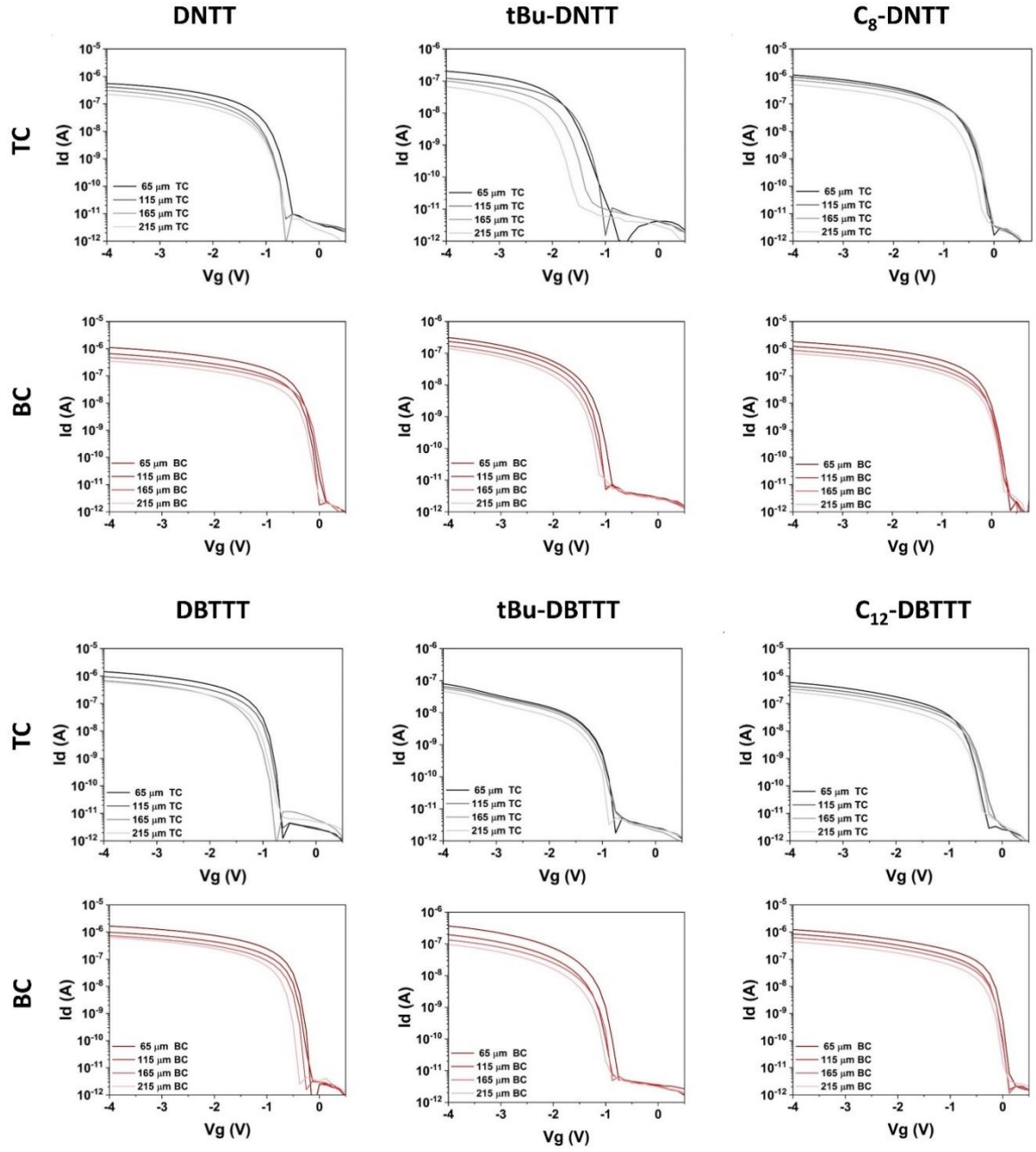
**Figure A2.2:** Output characteristics of BC TFTs with 25-nm-thick OSC layer. All TFTs have  $W/L = 480/215 \mu\text{m}$ .



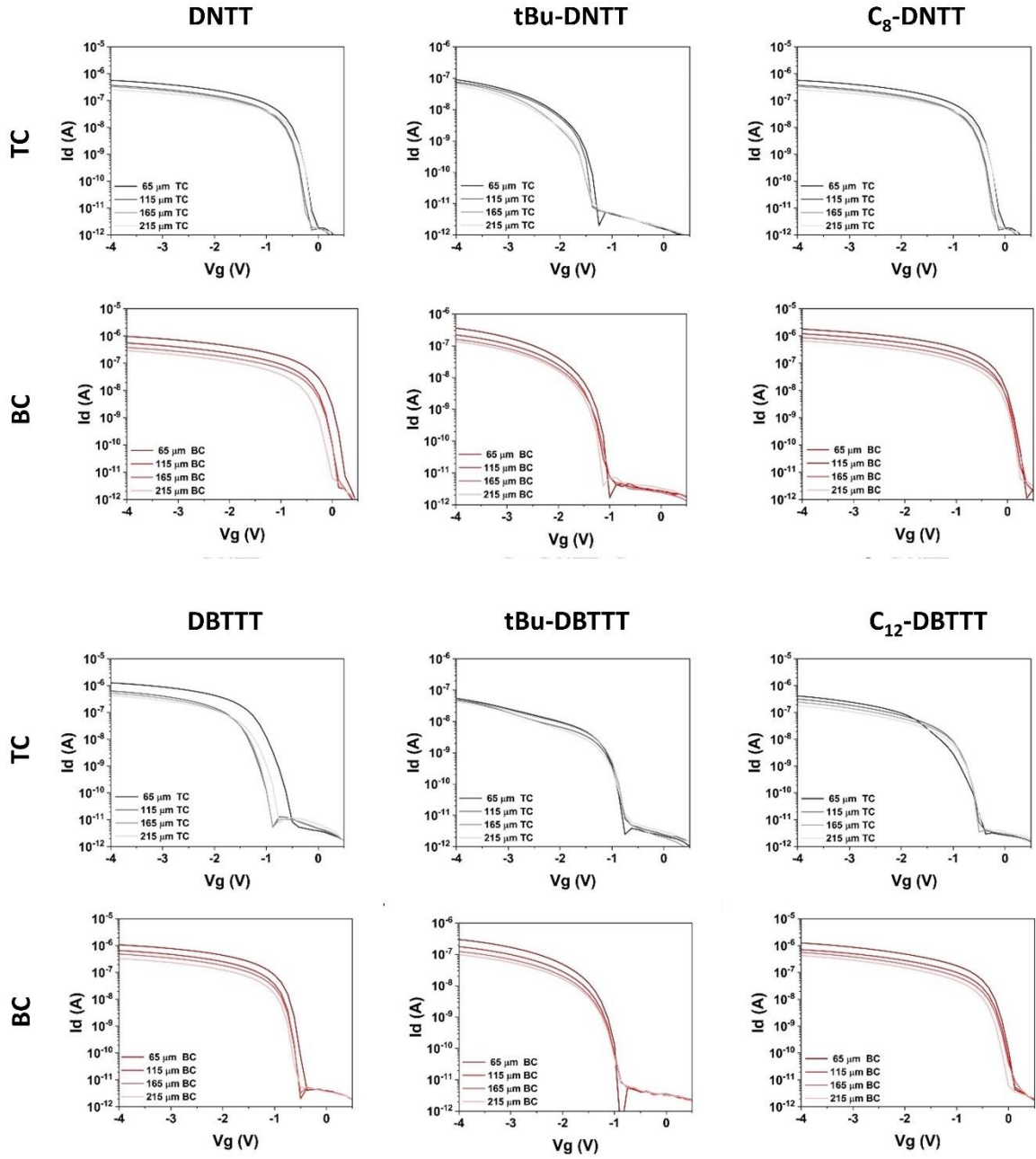
**Figure A2.4:** Output characteristics of TC TFTs with 80-nm-thick OSC layer. All TFTs have  $W/L = 480/215 \mu\text{m}$ .



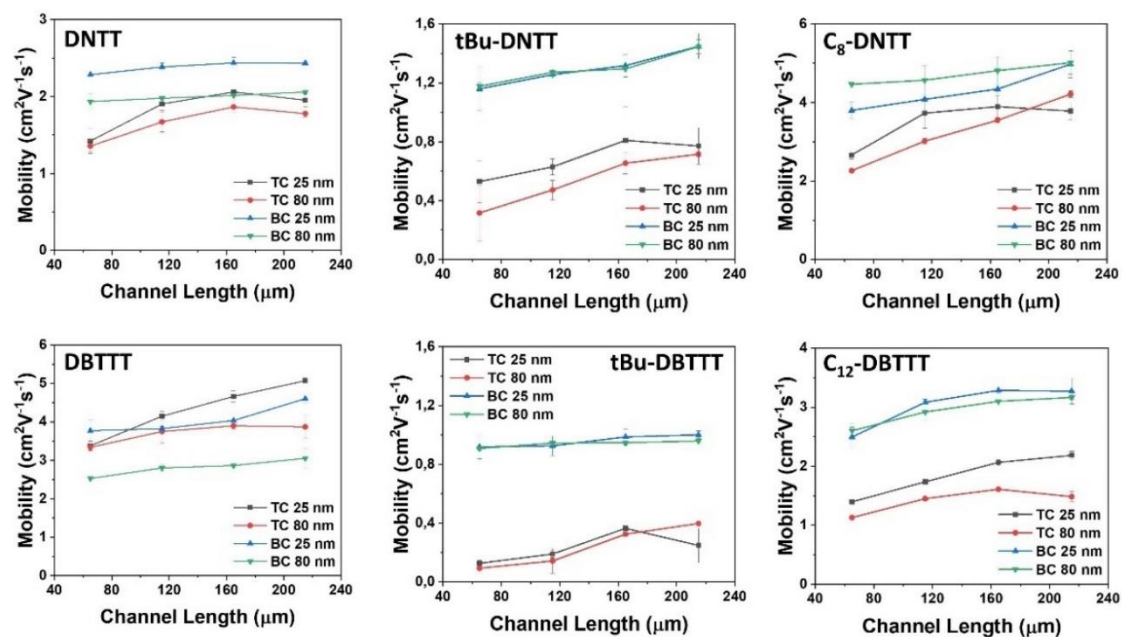
**Figure A2.5:** Output characteristics of BC TFTs with 80-nm-thick OSC layer. All TFTs have  $W/L = 480/215 \mu\text{m}$ .



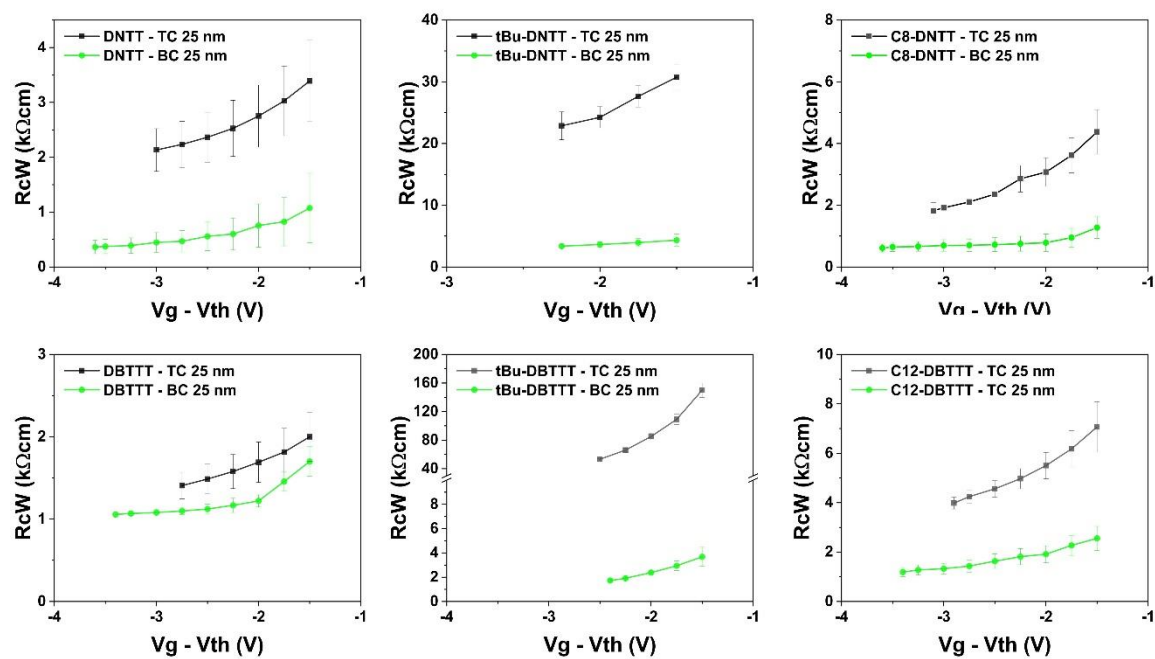
**Figure A2.6:** Transfer characteristics of TC and BC TFTs with 25-nm-thick OSC layer at different channel length.



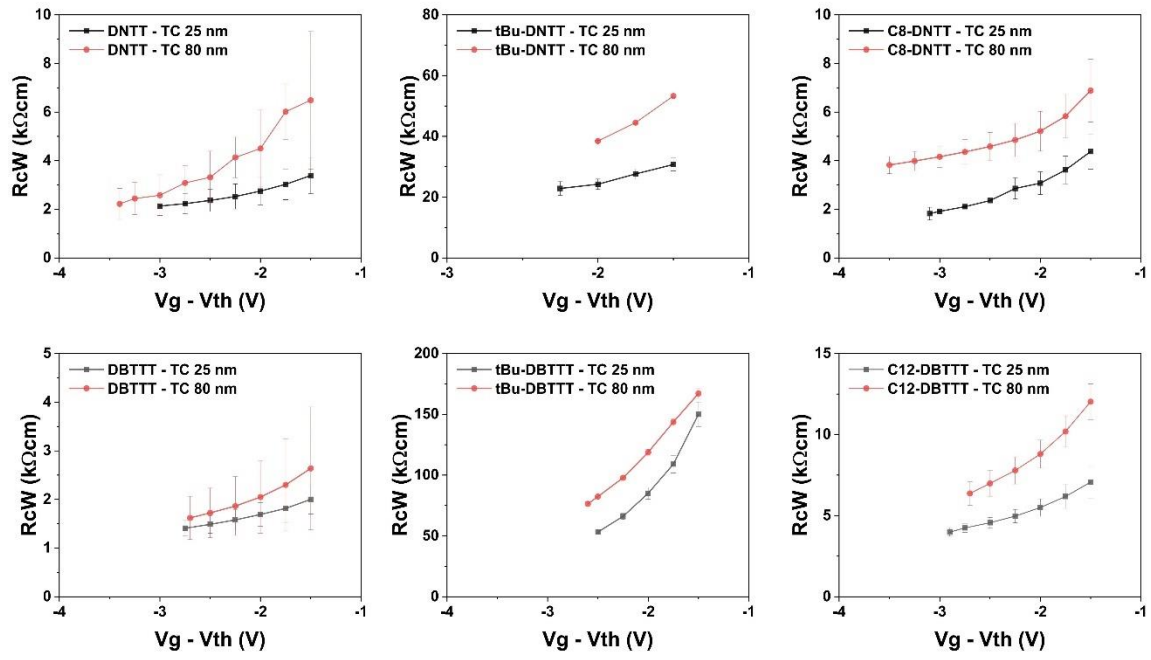
**Figure A2.7:** Transfer characteristics of TC and BC TFTs with 80-nm-thick OSC layer at different channel length.



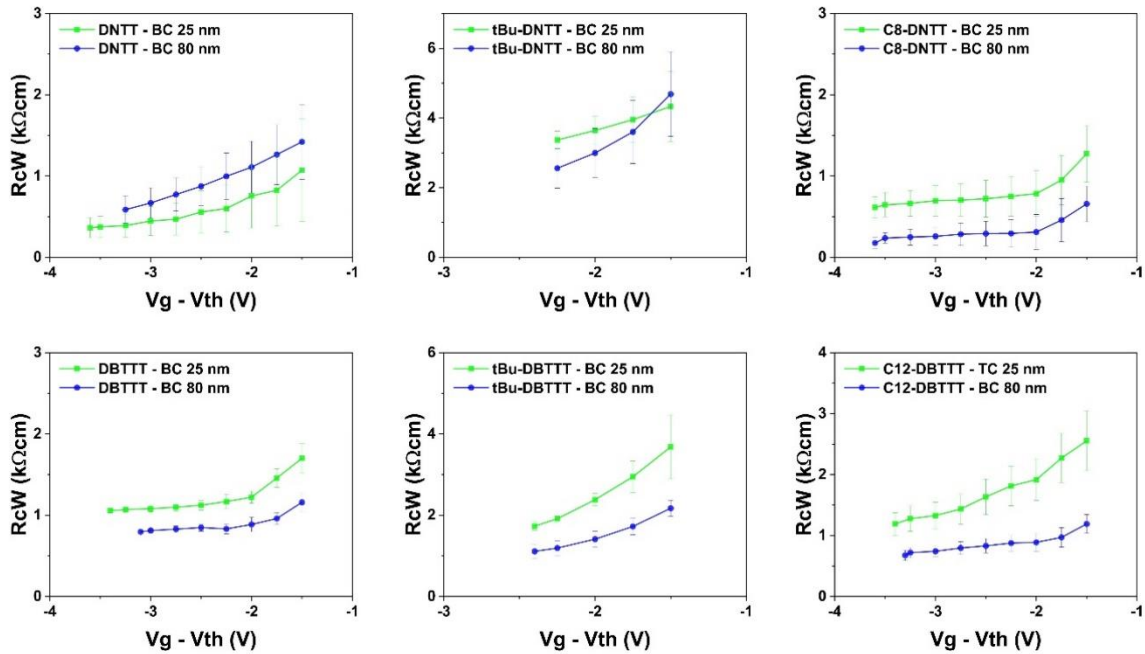
**Figure A2.8:** Effective mobility extracted from TC and BC TFTs as a function of the channel length.



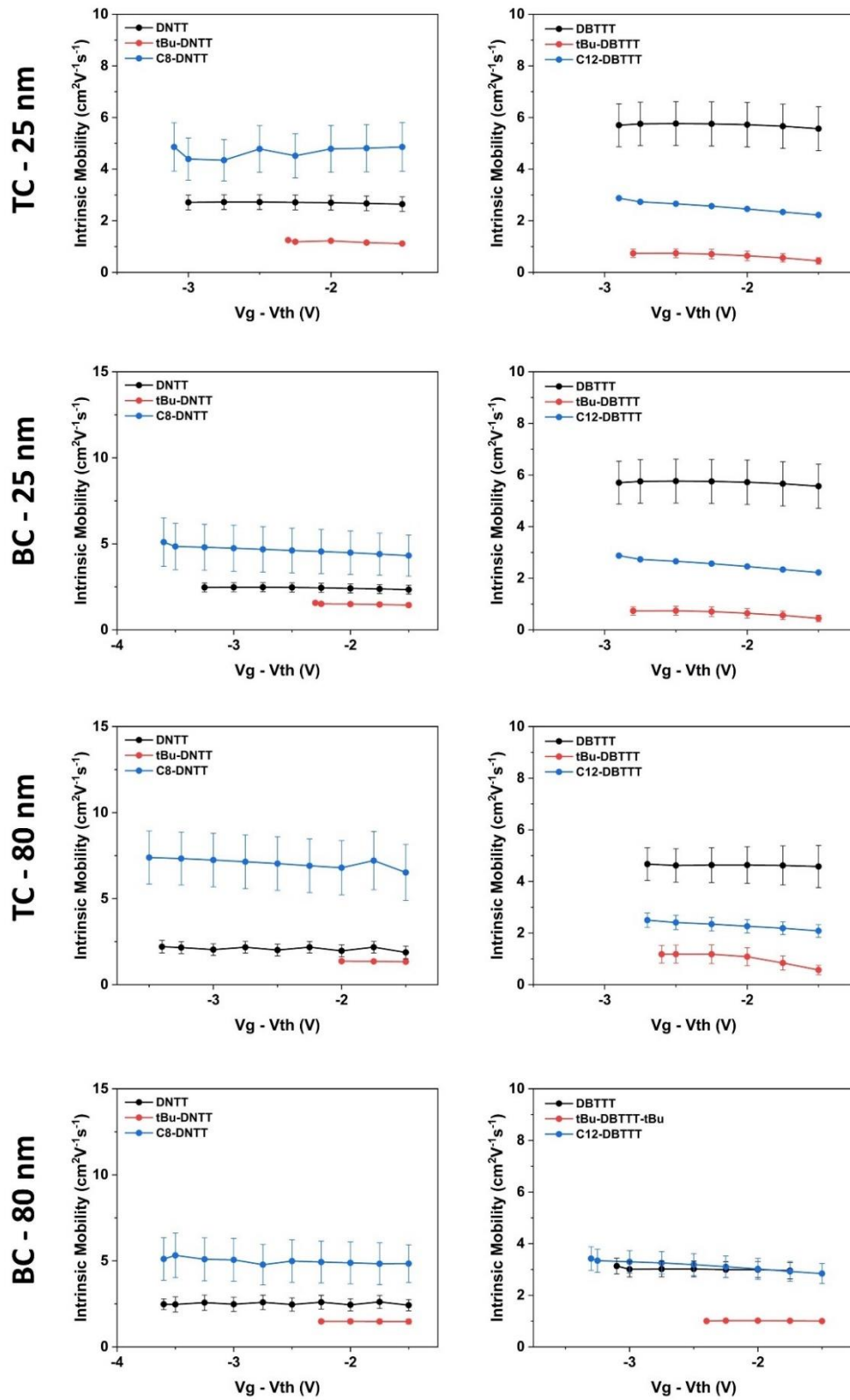
**Figure A2.9:**  $R_cW$  vs gate-overdrive voltage of TC and BC TFTs with 25-nm thick OSC layer.



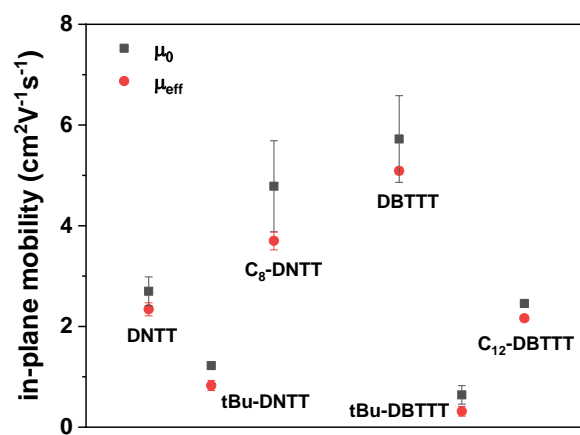
**Figure A2.10:** RcW vs gate-overdrive voltage of TC TFTs with 25- and 80-nm-thick OSC layer.



**Figure A2.11:** RcW vs gate-overdrive voltage of BC TFTs with 25- and 80-nm-thick OSC layer.



**Figure A2.12:** Intrinsic mobility values extracted by using TLM of TC and BC TFTs with 25- and 80-nm-thick OSC layer.



**Figure A2.13:** Intrinsic mobility values extracted from TLM ( $\mu_0$ ) and effective mobility values extracted from TFTs with 25-nm-thick OSC layer.



# Chapter 6

## Conclusions

New classes of thienoacenes OSCs were processed and successfully integrated in TFTs, allowing the determination of their electrical performances. The charge transport and charge injection properties were analysed in relation to the crystalline and molecular structures of the OSCs. Additionally, a novel approach to influencing the crystal growth of OSCs through vacuum field coupling was explored.

In **Chapter 2**, thienoacenes with various molecular cores and substitutions were used as active materials in TFTs. The structure-properties relations for high-performance OSCs were established, highlighting the importance of factors such as the herringbone packing motif, layer-by-layer growth of the thin films, extended  $\pi$ -system, ionization energy close to the electrodes' work function, large and balanced transfer integrals, and low reorganization energy. A novel class of thienoacenes was presented, with **DN4T**, **C<sub>8</sub>-DN4T**, and **C<sub>10</sub>-DN4T** showing charge carrier mobility up to  $2.1 \text{ cm}^2\text{V}^{-1} \text{ s}^{-1}$  for the parent molecule and up to  $2.5 \text{ cm}^2\text{V}^{-1} \text{ s}^{-1}$  for the alkylated derivatives.

Furthermore, the electrical performance of four newly synthesized thienoacenes with *tert*-butyl substitutions, which have an extended  $\pi$ -system compared to **tBu-BTBT**, were evaluated. The lower ionization energy observed in these compounds was attributed to their extended charge delocalization, which resulted in a lower threshold voltage and smaller contact resistance in TFTs compared to those based on **tBu-BTBT**. Among the compounds, **tBu-DNTT** was identified as a high-performance OSC, with mobility exceeding  $1.9 \text{ cm}^2\text{V}^{-1}\text{s}^{-1}$ . In **Chapter 2**, the contact resistance of the analysed compounds was also investigated, highlighting a significant discrepancy in  $R_{\text{cW}}$  values between TC devices based on **DN4T** and **isoDN4T**. This was unexpected due to the almost identical injection barrier of the two isomers.

Driven by this finding, in **Chapter 3**, the impact of the molecular structure of DNTT and DBTTT families on the contact resistance of organic TFTs was explored, with a focus on the device geometry, injection barrier at the metal/OSC interface, and out-of-plane and in-plane charge transport properties. Our findings indicate that in BC devices the molecular structure do not significantly influence contact resistance. Efficient charge carrier injection is achieved when the injection barrier at the contact/OSC interface is minimized and the OSC exhibits high in-plane charge carrier mobility, thus

reducing the resistance opposed to charge transport at the depleted region formed at the contact/OSC interface. Among the analysed compounds, **DNTT** and **C<sub>8</sub>-DNTT** exhibited the lowest contact resistance (0.8 kΩcm) due to their good balance between low injection barrier ( $\approx 0.5$  eV) and high in-plane mobility (2.3 and 4.8 cm<sup>2</sup>V<sup>-1</sup>s<sup>-1</sup>, respectively). In TC TFTs, where charges must travel through the OSC thickness to achieve the accumulation channel, it was found that the resistance associated with bulk charge transport is not a dominant factor for determining the overall contact resistance. Instead, the primary factors determining the contact resistance are the resistance opposing charge transport along the OSC/dielectric interface beneath the contacts (which is influenced by in-plane mobility and charge trap density) and the injection barrier at the metal/OSC interface. Therefore, in TC TFTs, if the injection barrier is reduced and in-plane charge transport is efficient, a larger distance between the molecular cores due to the introduction of substituents does not necessarily lead to high contact resistance. At last, the study determined that BC TFTs consistently exhibit lower contact resistance than TC TFTs for all the compounds analysed. BC TFTs showed a modest reduction in contact resistance for the parent compounds and alkylated derivatives, with  $R_{\text{C}}W$  between 1.3 and 2.9 times lower compared to TC TFTs. However, BC TFTs based on **tBu-DNTT** showed up to 7 times lower  $R_{\text{C}}W$ , and BC TFTs based on **tBu-DBTTT** showed up to 35 times lower  $R_{\text{C}}W$  compared to the TC counterparts. This underlines the advantages of using a coplanar device geometry, which improves electrical performance and charge injection properties.

In the **Chapter 4**, we explored the effect of light-matter coupling on perylene crystal growth and polymorphism. Recrystallization experiments were carried out in an FP cavity under two different conditions: cooperative VSC of the aromatic C=C stretching of benzonitrile that is resonant with perylene vibrational band, and VSC of the aromatic C=C stretching solvent vibrational band that is not resonant with perylene vibrational modes. The results indicated a slightly higher ratio of the  $\alpha$ -form to the  $\beta$ -form compared to the non-cavity condition. However, the FSR varied during the experiment due to the temperature changes in the microfluidic cell, potentially resulting in an unstable system and reducing the reproducibility of the results. The study showed that the experimental setup using an FP cavity was limited by temperature changes in the microfluidic cell. Thus, to fully explore the potential of VSC on crystal growth and avoid FSR changes, alternative crystallization technique that can be conducted at room temperature (such as antisolvent crystallization) should be considered for future experiments.

In conclusion, this thesis sheds light on the molecular design of thienoacenes OSCs, while offering new perspectives on contact resistance of organic thin-

film transistors and the manipulation of OSC crystallization. The potential of organic semiconductors in logic operators hinges on their ability to overcome the dynamic and static disorder that frequently hinders their electrical performance, making them less efficient than their inorganic counterparts. The various experimental chapters presented in this thesis are aimed at addressing significant challenges in organic electronics. To achieve efficient charge transport, a rational molecular design is essential. Therefore, it is crucial to establish a correlation between the chemical and crystalline structure of OSCs and their electrical properties, which would be beneficial for the future growth of this field.

Emerging fields such as coupling with the vacuum field, chiral induced spin selectivity, and bioelectronics can benefit from the wealth of knowledge accumulated by the scientific community in the past decades regarding OSCs for logic operators. The ability to fine-tune molecular properties through synthetic design is still crucial for creating custom OSCs for specific applications. In this framework, this thesis contributes to further understanding of structure-properties relations, minimization of contact resistance, and exploration of new methods for manipulating OSC crystallization, providing valuable insights for scientists developing novel OSCs toward the progress of organic electronics.



# Résumé

## Introduction

Le domaine des semi-conducteurs organiques (Organic SemiConductors - OSC) a été largement étudié et développé au cours des dernières décennies, en raison de ses potentielles applications technologiques en électronique imprimée.<sup>[213]</sup> L'origine des propriétés semi-conductrices de ces matériaux provient de leur conjugaison moléculaire par le biais d'orbitales hybrides  $sp^2$ , formant à la fois des liaisons  $\sigma$ - et  $\pi$ . Alors que dans les premières, les électrons sont localisés ; les électrons sont délocalisés dans les secondes, permettant des voies de conduction aux charges électriques. À l'état solide, les molécules d'OSC sont maintenues ensemble par des interactions intermoléculaires faibles de type Van der Waals (VdW), de sorte que le recouvrement des orbitales moléculaires de molécules voisines permet le transport de charges dans le cristal (ou le film polycristallin). Par conséquent, les propriétés électriques des OSC dépendent fortement de l'organisation supramoléculaire à l'état solide. Les OSC sont notamment employés dans les transistors à effet de champ (Field-Effect Transistors - FET), qui sont des dispositifs à trois électrodes où le flux de courant est modulé par un champ électrique. Les FET sont largement utilisés dans l'industrie électronique pour fabriquer des circuits intégrés, à la base des appareils et des dispositifs de l'électronique moderne. A l'heure actuelle, la technologie des FET de l'industrie électronique est principalement basée sur des semi-conducteurs inorganiques en raison de leurs performances électriques supérieures. Les OSC offrent toutefois une technologie alternative de semi-conducteurs présentant des avantages tels que la flexibilité,<sup>[8]</sup> une mise en œuvre à températures plus faibles que celles requises par leurs homologues inorganiques,<sup>[9]</sup> le dépôt en solution via des solvants organiques classiques offrant la possibilité d'applications rentables sur de grandes surfaces<sup>[9]</sup> et une conception moléculaire sur mesure (chimie de synthèse).<sup>[214]</sup> Cependant, la mobilité des porteurs de charge dans les OSC est entravée par un désordre dynamique empêchant une délocalisation complète de la fonction d'onde des charges. Une conception rationnelle des OSC est donc nécessaire pour assurer un arrangement bien défini des molécules au sein du cristal et d'ainsi permettre de maximiser le recouvrement des orbitales moléculaires de molécules voisines (larges intégrales de transfert) tout en minimisant les réarrangements géométriques de molécules impliquées dans (faible énergie de réorganisation) le transport de charge.<sup>[52]</sup>

L'objectif de cette thèse est d'étudier les relations structure-propriétés de semi-conducteurs organiques basés sur le thiénoacène afin d'esquisser des lignes directrices pour améliorer leur conception moléculaire. Le couplage lumière-matière pour influencer la croissance cristalline et le polymorphisme des OSC a également été exploré.

## Résultats et discussion

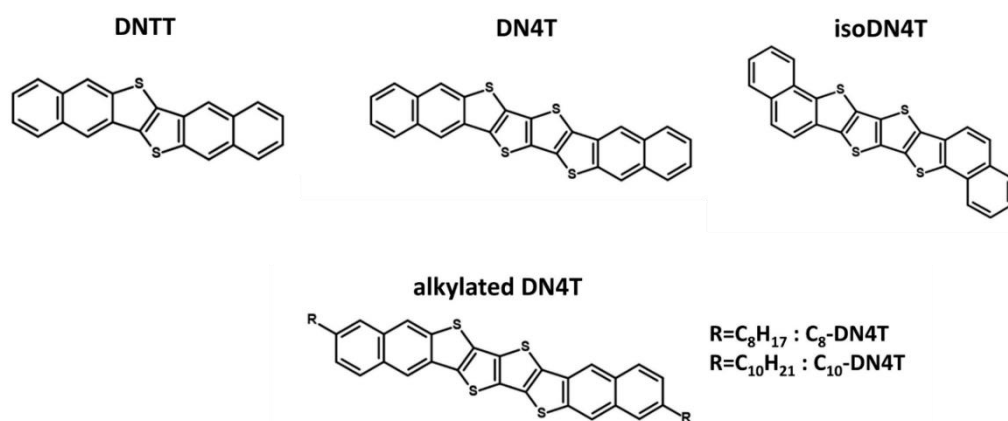
Cette thèse de doctorat commence par une brève introduction sur les semi-conducteurs organiques, mettant l'accent sur les aspects structurels, les transistors à effet de champ organiques et l'effet du couplage lumière-matière sur le transport de charge dans les OSC. Trois chapitres se rapportant au travail expérimental effectué pendant le doctorat sont ensuite présentés. Le résumé de chaque chapitre est présenté ci-dessous.

- *Evaluation des propriétés de transport et d'injection de charges de nouveaux dérivés de thiénoacènes dans des transistors en films minces*

Les propriétés de transport de charge de deux nouveaux semi-conducteurs isomères à base de thiénoacène, DN4T et isoDN4T, sont présentées (**Figure 1**). L'objectif est de comprendre si l'intégration d'un motif central de quatre cycles thiényles fusionnés entre deux fragments naphtyles conduit à une mobilité élevée des porteurs de charge dans les transistors à couche mince (Thin-Film Transistors, TFT), tout en préservant un arrangement « herringbone » des molécules à l'état cristallin. Le désordre dynamique, résultant des modes de vibration moléculaire, limite fortement l'obtention d'une mobilité élevée dans les semi-conducteurs organiques. Dans les OSC présentant une structure « herringbone », les modes de vibration ayant un mouvement de translation des molécules le long de leur axe long, sont majoritairement responsables des variations du recouvrement orbitalaire et donc de la réduction de mobilité.<sup>[58,60]</sup> Toutefois, ces modes de vibration nuisibles peuvent être mitigés dans les OSC présentant des structures moléculaires qui s'écartent de la linéarité.<sup>[215]</sup> Dans le cas du DN4T et de l'isoDN4T, l'intégration de quatre cycles thiényles fusionnés entre deux fragments naphtyles accentue la non-linéarité de la forme moléculaire par rapport au DNTT (**Figure R.1**). Ce dernier a été choisi comme référence pour les études de physique des dispositifs électroniques en raison de sa grande mobilité des porteurs de charge ( $> 2 \text{ cm}^2\text{V}^{-1}\text{s}^{-1}$ ).<sup>[126]</sup> Dans cette optique, les performances électriques du DN4T et de l'isoDN4T sont étudiées dans des transistors à couche mince et comparées à celles des OSC les plus performants du domaine. Les TFT sont fabriqués par dépôt en phase vapeur sous vide, en

optimisant la température du substrat et la géométrie du dispositif. Les meilleures performances électriques sont obtenues pour les dispositifs qui présentent une architecture « bottom contact » (BC) des électrodes des transistors et une température de substrat de 100 °C durant l'évaporation. Plus précisément, les TFT à base de DN4T présentent une mobilité des porteurs de charge allant jusqu'à  $2.1 \text{ cm}^2\text{V}^{-1}\text{s}^{-1}$  alors que ceux basés sur l'isoDN4T présentent seulement une mobilité des porteurs de charge 3 ordres de grandeur plus faible jusqu'à  $0.003 \text{ cm}^2\text{V}^{-1}\text{s}^{-1}$ . Cette différence de mobilité est attribuée à plusieurs facteurs. Tout d'abord, la comparaison des structures cristallines des deux isomères révèle un plus petit nombre de contacts courts dans l'isoDN4T. De plus, les calculs de chimie quantique mettent en évidence des intégrales de transfert plus importantes ainsi qu'une énergie de réorganisation plus faible pour le DN4T, comparé à l'isoDN4T.

Dans ce chapitre, nous présentons également l'évaluation des performances électriques de dérivés alkylés de DN4T, à savoir le C<sub>8</sub>-DN4T et le C<sub>10</sub>-DN4T (**Figure R.1**).

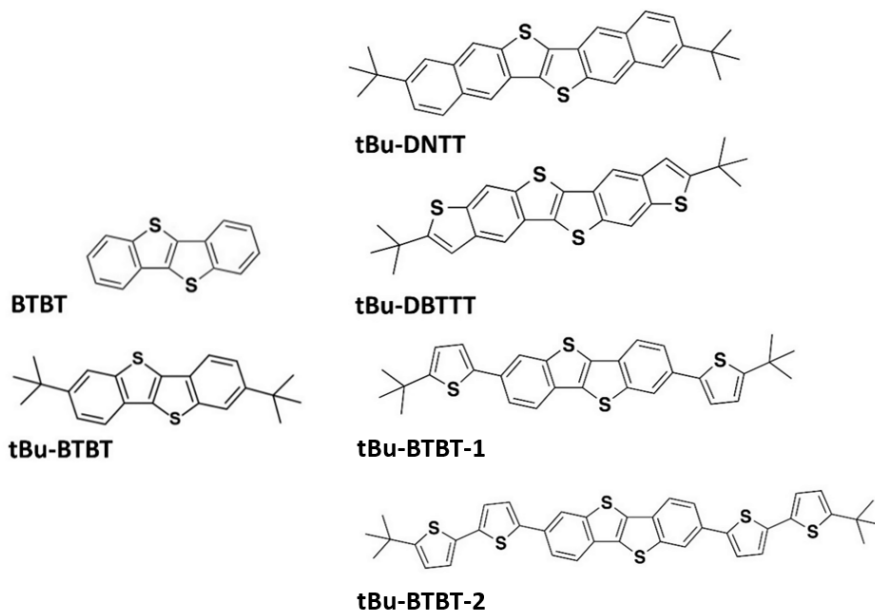


**Figure R.1:** Structures moléculaires du DNTT, DN4T, isoDN4T et des dérivés alkylés du DN4T.

Ces derniers sont supposés avoir une mobilité des porteurs de charge plus élevée par rapport au cœur aromatique de base, le DN4T. En effet, l'introduction de chaînes alkyles latérales permet de réduire l'impact de certains modes de vibration.<sup>[58,60]</sup> Les TFT basés sur C<sub>8</sub>-DN4T et C<sub>10</sub>-DN4T présentent une mobilité allant jusqu'à  $2.4 \text{ cm}^2\text{V}^{-1}\text{s}^{-1}$  et  $2.5 \text{ cm}^2\text{V}^{-1}\text{s}^{-1}$  respectivement, légèrement supérieures à celle du DN4T. L'obtention de meilleures performances est entravée par la mauvaise morphologie des films minces, caractérisée par un mode de croissance 3D. Ce mode de croissance

s'est avéré être une raison du mauvais transport de charge en raison de la formation de nombreux joints de grains agissant comme des pièges énergétiques profonds.<sup>[143]</sup>

Enfin, les performances électriques ainsi que l'injection de charges dans les TFTs basés sur des dérivés de thiénoacènes substitués par des groupes périphériques stériques sont étudiées. Les composés étudiés sont des dérivés tert-butyl de DNTT et DBTTT, à savoir tBu-DNTT et tBu-DBTTT, et des dérivés tert-butyl-thiényle de BTBT, à savoir tBu-BTBT-1 et tBu-BTBT-2 (**Figure R.2**). Ces composés ont été sélectionnés en raison de leur cœur aromatique  $\pi$  étendu par rapport au tBu-BTBT. En effet, ce dernier a montré une mobilité élevée des porteurs de charge dans les TFT (jusqu'à  $2.4 \text{ cm}^2\text{V}^{-1}\text{s}^{-1}$ ), qui a été attribuée au transport de charge presque isotrope au sein du plan des couches « herringbone ». <sup>[133]</sup> Malgré sa mobilité intrinsèque élevée, le tBu-BTBT présente une énergie d'ionisation profonde (5.7 eV) qui défavorise l'injection de porteurs de charge à partir de contacts métalliques en or dans les transistors. Cela se traduit par une tension de seuil élevée et des non-idéalités des dispositifs électroniques fabriqués à partir de ce dernier. Le cœur aromatique  $\pi$  étendu des composés étudiés dans ce chapitre devrait réduire l'énergie d'ionisation, en raison d'une meilleure délocalisation des porteurs de charge. <sup>[124]</sup> Ceci est confirmé par mesures spectroscopiques (spectroscopie de photoémission - photoelectron spectroscopy in air) réalisées sur films minces des composés étudiés, mettant en évidence des énergies d'ionisation comprises entre 5.23 et 5.37 eV. Ces valeurs se traduisent par une tension de seuil modérée dans les TFT, ce qui garantit des dispositifs plus fiables et idéaux. Le tBu-DNTT présente la plus grande mobilité parmi les composés étudiés, avec des valeurs dépassant  $1.9 \text{ cm}^2\text{V}^{-1}\text{s}^{-1}$ , suivi par tBu-DBTTT ( $1.0 \text{ cm}^2\text{V}^{-1}\text{s}^{-1}$ ), tBu-BTBT-1 ( $0.25 \text{ cm}^2\text{V}^{-1}\text{s}^{-1}$ ) et enfin tBu-BTBT-2 ( $0.10 \text{ cm}^2\text{V}^{-1}\text{s}^{-1}$ ). Les calculs de chimie quantique confirment les meilleures propriétés de transport de charge des dérivés tert-butyl de DNTT et DBTTT, présentant des intégrales de transfert plus grandes ainsi que des énergies de réorganisation plus faibles par rapport aux dérivés tert-butyl-thiényle de BTBT. Additionnellement, les simulations de Monte Carlo mettent en évidence une anisotropie du transport de charge pour tous les composés, à l'exception de tBu-BTBT-1. En conclusion, l'élargissement du cœur aromatique  $\pi$  assure une injection plus facile des porteurs de charge dans les TFT par rapport à ceux basés sur le tBu-BTBT. Plus particulièrement, le tBu-DNTT se révèle être un OSC de haute performance, avec une mobilité dépassant  $1.9 \text{ cm}^2\text{V}^{-1}\text{s}^{-1}$ .

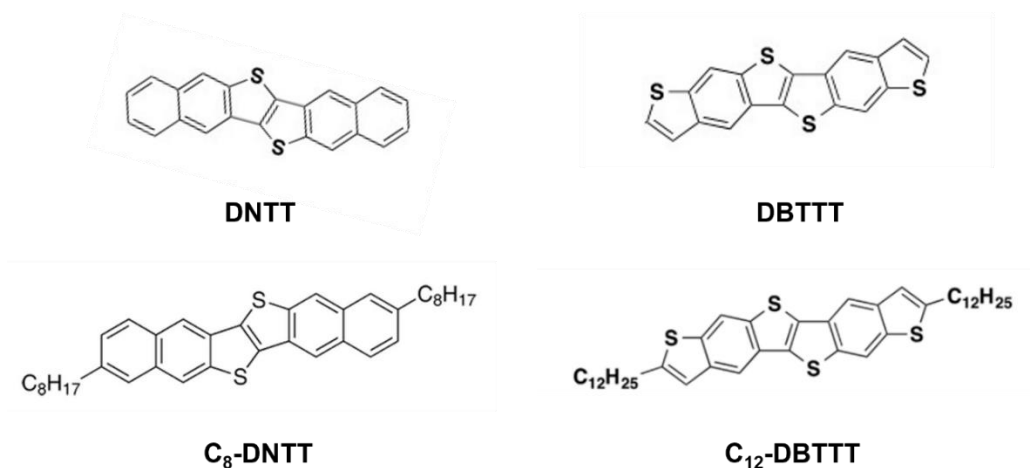


**Figure R.2:** Structures moléculaires des dérivés de thiénoacènes substitués par des groupes périphériques stériques étudiés au chapitre 2 : tBu-DNTT, tBu-DBTTT, dBu-BTBT-1 et tBu-BTBT-2. Les structures du BTBT et du tBu-BTBT sont également présentées.

- *Résistance de contact dans les transistors en couches minces à base de dérivés de thiénoacène*

Ces dernières années, la résistance de contact a fait l'objet d'un intérêt accru dans le domaine de la recherche sur les OSC. En effet, les performances des dispositifs sont souvent limitées par l'injection de porteurs de charge plutôt que par le transport de charge le long de la couche active.<sup>[72]</sup> Une résistance de contact élevée peut conduire à une non-idéalité des dispositifs et ainsi affecter l'extraction des paramètres, conduisant à des sur-(ou sous-)estimations des performances électriques. Cela peut ainsi mener à une interprétation incorrecte des relations structure-propriétés, qui à son tour affecte la conception moléculaire de futurs OSC. Il est également à noter qu'une résistance de contact élevée limite la fréquence de transit dans les TFT organiques, en particulier pour les dispositifs miniaturisés dont la longueur de canal est inférieure à quelques dizaines de micromètres.<sup>[167]</sup> Ce chapitre se concentre sur le rôle de la structure moléculaire des OSC et en particulier sur l'impact des substituants du cœur moléculaire sur la résistance de contact dans des dispositifs à géométrie top contact (TC) et bottom contact (BC) afin de les comparer. En effet, cet aspect a été peu étudié par rapport aux autres

facteurs ayant un lien direct avec la résistance de contact, tels que la barrière Schottky et le matériau utilisé pour l'électrode. Les composés choisis dans ce travail sont le DNTT et le DBTTT, ainsi que leurs dérivés tert-butyle et alkylés, à savoir tBu-DNTT, tBu-DBTTT, C<sub>8</sub>-DNTT et C<sub>12</sub>-DBTTT (**Figure R.2 et R.3**).



**Figure R.3:** Structures moléculaires des composés utilisés dans le chapitre 3, à savoir le DNTT, le DBTTT et leurs dérivés alkylés, le C<sub>8</sub>-DNTT et le C<sub>12</sub>-DBTTT.

La fabrication de TFT basés sur ces composés, permet l'extraction de la résistance de contact normalisée en largeur ( $R_cW$ ). Nous avons observé que les dispositifs présentant une géométrie coplanaire (BC) ne sont pas significativement affectés par les substituants du coeur moléculaire, montrant pour tous les composés des  $R_cW$  inférieures à 5 k $\Omega$ cm. Au contraire, dans les dispositifs TC, les dérivés tert-butyle présentent des  $R_cW$  supérieures de 2 ordres de grandeur par rapport aux molécules de base et à leurs dérivés alkylés. Cet écart important de  $R_cW$  est attendu entre les molécules de base et les dérivés tert-butyle, car la présence de substituants sur les coeurs moléculaires augmente la distance entre les coeurs moléculaires selon l'axe long des molécules, ce qui entrave la mobilité hors du plan. Par conséquent, même dans le cas des dérivés alkylés, une faible mobilité hors du plan est attendue en raison du faible recouvrement orbitalaire des molécules voisines (selon l'axe z) causé par l'extension spatiale des chaînes alkyles. En revanche, les dérivés alkylés présentent une faible résistance de contact, similaire à celle des molécules de base. La combinaison des résultats expérimentaux obtenus par plusieurs techniques (microscopie à force atomique pour la conductivité électrique, spectrométrie photoélectronique UV, diffraction des Rayons-X, et études physiques de dispositifs électroniques) nous a permis de mettre en évidence que la plus faible

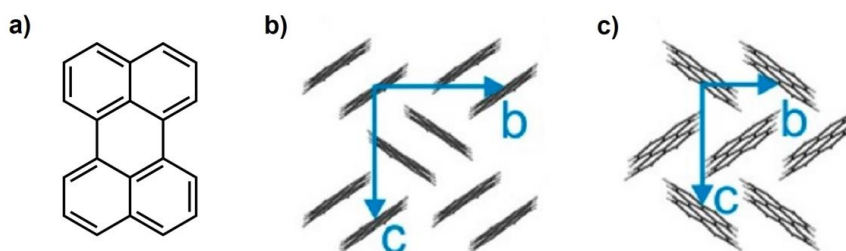
résistance de contact observée pour les composés alkylés (comparé à leurs homologues tert-butyl) pouvait être le résultat de leur plus grande mobilité des porteurs de charge "dans le plan" dans la région sous les contacts. La densité de porteurs de charge plus élevée compense la faible mobilité hors du plan, ce qui conduit à une faible résistance de contact dans les dispositifs TC pour les dérivés alkylés. Ce travail met en évidence la contribution mutuelle de la mobilité hors du plan (qui dépend fortement de la structure moléculaire de l'OSC) et de la densité de porteurs de charge dans la détermination de la résistance de contact dans les TFT à configuration TC.

- *Exploration de l'effet du couplage fort vibratoire sur la cristallisation du pérylène dans une cavité Fabry-Perot*

Le couplage des vibrations moléculaires ou des transitions électroniques aux niveaux énergétiques du champ de vide des cavités optiques s'est avéré capable de modifier de multiples propriétés de molécules et matériaux. On peut citer par exemple la modification de la réactivité de réactions organiques<sup>[196]</sup> ainsi que l'augmentation du courant électrique dans des semi-conducteurs organiques<sup>[112]</sup>. L'effet sur la réactivité chimique a été attribué à un remodelage du potentiel de Morse de la liaison couplée modifiée par le couplage fort vibrationnel (Vibrational Strong Coupling, VSC), prédisant un raccourcissement ou un renforcement de la liaison couplée et donc un changement de son énergie. Par conséquent, si l'énergie et la force d'une liaison impliquée dans des interactions intermoléculaires sont modifiées par le couplage avec le champ du vide, le VSC peut influencer la germination des cristaux ainsi que leur croissance. Comme premiers exemples, la modification de l'agrégation supramoléculaire d'un polymère conjugué<sup>[119]</sup> et l'influence sur le pseudo-polymorphisme des structures imidazolate de zéolite<sup>[118]</sup> confirment l'influence des VSC dans la chimie supramoléculaire. De plus, l'arrangement cristallin et le polymorphisme ont fortement affecté la mobilité des porteurs de charge dans les OSC. Le développement de méthodes pour induire une cristallisation sélective, empêchant la croissance concomitante de plusieurs polymorphes peut donc offrir de nouvelles opportunités pour maximiser la mobilité des porteurs de charge dans les OSC.

Ce chapitre se concentre sur la cristallisation du pérylène dans une cavité Fabry-Perot (FP), afin d'explorer l'effet du VSC sur la croissance cristalline et le polymorphisme. Les conditions expérimentales pour obtenir la cristallisation du pérylène à l'intérieur d'une cavité FP ont été établies, montrant une formation concomitante des formes  $\alpha$  et  $\beta$  (**Figure R.4**), dans les expériences de recristallisation. Le VSC coopératif est obtenu en couplant la vibration moléculaire du solvant (benzonitrile) avec les modes optiques de

la cavité. Malheureusement, le rapport entre les deux polymorphes n'est pas modifié de manière significative par le VSC. Nous avons observé des décalages des modes optiques de la cavité qui peuvent être une raison d'instabilité et un problème pour la reproductibilité des expériences. En résumé, pour éviter ces décalages causés par le changement de température de la cavité, des expériences de cristallisation à température constante doivent être réalisées. Ce n'est que dans ce cas que l'on pourra explorer le potentiel du VSC à influencer la croissance cristalline et le polymorphisme des OSC.



**Figure R.4:** (a) Structure moléculaire du pérylène, (b) arrangement moléculaire dans la phase  $\alpha$ , (c) arrangement moléculaire dans la phase  $\beta$ . La direction d'observation est perpendiculaire au plan  $(bc)$ .

## Conclusions

Les relations entre la structure moléculaire, l'arrangement cristallin à l'état solide et les propriétés électriques des OSC sont explorées au cours de ce travail. Grâce à la fabrication de transistors en couches minces, aux calculs de chimie quantique et à une approche multi-technique, des relations structure-propriétés sont mises en évidence. Une attention particulière est accordée à l'effet de la structure moléculaire et cristalline sur les propriétés de transport de charge, l'injection de charges et la résistance de contact. Enfin, une approche innovante pour influencer la croissance cristalline et le polymorphisme des OSC est présentée. Cette dernière met en évidence les limites de l'expérience de recristallisation dans une cavité Fabry-Perot et expose des lignes directrices pour de futurs montages expérimentaux. En conclusion, cette thèse tente de répondre à certains défis dans le développement de nouveaux OSC à haute performance, tout en apportant de nouvelles perspectives sur la conception moléculaire, leur utilisation dans les transistors à couche mince et une manière innovante d'influencer la croissance cristalline.



# References

- [1] A. Tsumura, H. Koezuka, T. Ando, 'Macromolecular electronic device: Field-effect transistor with a polythiophene thin film', *Appl. Phys. Lett.* **1986**, *49*, 1210–1212.
- [2] C. W. Tang, 'Two-layer organic photovoltaic cell', *Appl. Phys. Lett.* **1986**, *48*, 183–185.
- [3] V. Y. Merritt, H. J. Hovel, 'Organic solar cells of hydroxy squarylium', *Appl. Phys. Lett.* **1976**, *29*, 414–415.
- [4] Z. B. Henson, K. Müllen, G. C. Bazan, 'Design strategies for organic semiconductors beyond the molecular formula', *Nature Chem* **2012**, *4*, 699–704.
- [5] C. Kunkel, J. T. Margraf, K. Chen, H. Oberhofer, K. Reuter, 'Active discovery of organic semiconductors', *Nat Commun* **2021**, *12*, 2422.
- [6] A. Operamolla, G. M. Farinola, 'Molecular and Supramolecular Architectures of Organic Semiconductors for Field-Effect Transistor Devices and Sensors: A Synthetic Chemical Perspective', *Eur. J. Org. Chem.* **2011**, *2011*, 423–450.
- [7] P. Yu, Y. Zhen, H. Dong, W. Hu, 'Crystal Engineering of Organic Optoelectronic Materials', *Chem* **2019**, *5*, 2814–2853.
- [8] U. Zschieschang, H. Klauk, 'Organic transistors on paper: a brief review', *J. Mater. Chem. C* **2019**, *7*, 5522–5533.
- [9] J. W. Ward, Z. A. Lampton, O. D. Jurchescu, 'Versatile Organic Transistors by Solution Processing', *ChemPhysChem* **2015**, *16*, 1118–1132.
- [10] H. Klauk, Ed. , *Organic Electronics: Materials, Manufacturing and Applications*, Wiley, 2006.
- [11] C. K. Chiang, C. R. Fincher, Y. W. Park, A. J. Heeger, H. Shirakawa, E. J. Louis, S. C. Gau, A. G. MacDiarmid, 'Electrical Conductivity in Doped Polyacetylene', *Phys. Rev. Lett.* **1977**, *39*, 1098–1101.
- [12] H. Kim, W. Park, Y. Kim, M. Filatov, C. H. Choi, D. Lee, 'Relief of excited-state antiaromaticity enables the smallest red emitter', *Nat Commun* **2021**, *12*, 5409.
- [13] A. Troisi, G. Orlandi, 'Band Structure of the Four Pentacene Polymorphs and Effect on the Hole Mobility at Low Temperature', *J. Phys. Chem. B* **2005**, *109*, 1849–1856.
- [14] S. Griggs, A. Marks, H. Bristow, I. McCulloch, 'n-Type organic semiconducting polymers: stability limitations, design considerations and applications', *J. Mater. Chem. C* **2021**, *9*, 8099–8128.
- [15] R. Noriega, J. Rivnay, K. Vandewal, F. P. V. Koch, N. Stingelin, P. Smith, M. F. Toney, A. Salleo, 'A general relationship between disorder, aggregation and charge transport in conjugated polymers', *Nature Mater* **2013**, *12*, 1038–1044.
- [16] K. Gu, J. W. Onorato, C. K. Luscombe, Y. Loo, 'The Role of Tie Chains on the Mechano-Electrical Properties of Semiconducting Polymer Films', *Adv. Electron. Mater.* **2020**, *6*, 1901070.
- [17] S. Fratini, M. Nikolka, A. Salleo, G. Schweicher, H. Sirringhaus, 'Charge transport in high-mobility conjugated polymers and molecular semiconductors', *Nat. Mater.* **2020**, *19*, 491–502.
- [18] H. Sirringhaus, P. J. Brown, R. H. Friend, M. M. Nielsen, K. Bechgaard, B. M. W. Langeveld-Voss, A. J. H. Spiering, R. A. J. Janssen, E. W. Meijer, P.

- Herwig, D. M. de Leeuw, 'Two-dimensional charge transport in self-organized, high-mobility conjugated polymers', *Nature* **1999**, *401*, 685–688.
- [19] R. D. McCullough, S. Tristram-Nagle, S. P. Williams, R. D. Lowe, M. Jayaraman, 'Self-orienting head-to-tail poly(3-alkylthiophenes): new insights on structure-property relationships in conducting polymers', *J. Am. Chem. Soc.* **1993**, *115*, 4910–4911.
- [20] B. H. Hamadani, D. J. Gundlach, I. McCulloch, M. Heeney, 'Undoped polythiophene field-effect transistors with mobility of  $1\text{cm}^2\text{V}^{-1}\text{s}^{-1}$ ', *Appl. Phys. Lett.* **2007**, *91*, 243512.
- [21] G. Schweicher, Y. Olivier, V. Lemaire, Y. H. Geerts, 'What Currently Limits Charge Carrier Mobility in Crystals of Molecular Semiconductors?', *Isr. J. Chem.* **2014**, *54*, 595–620.
- [22] D. J. Gundlach, Y. Y. Lin, T. N. Jackson, S. F. Nelson, D. G. Schlom, 'Pentacene organic thin-film transistors-molecular ordering and mobility', *IEEE Electron Device Lett.* **1997**, *18*, 87–89.
- [23] A. A. Günther, J. Widmer, D. Kasemann, K. Leo, 'Hole mobility in thermally evaporated pentacene: Morphological and directional dependence', *Appl. Phys. Lett.* **2015**, *106*, 233301.
- [24] C. D. Sheraw, T. N. Jackson, D. L. Eaton, J. E. Anthony, 'Functionalized Pentacene Active Layer Organic Thin-Film Transistors', *Adv. Mater.* **2003**, *15*, 2009–2011.
- [25] G. Giri, S. Park, M. Vosgueritchian, M. M. Shulaker, Z. Bao, 'High-Mobility, Aligned Crystalline Domains of TIPS-Pentacene with Metastable Polymorphs Through Lateral Confinement of Crystal Growth', *Adv. Mater.* **2014**, *26*, 487–493.
- [26] V. Podzorov, E. Menard, A. Borissov, V. Kiryukhin, J. A. Rogers, M. E. Gershenson, 'Intrinsic Charge Transport on the Surface of Organic Semiconductors', *Phys. Rev. Lett.* **2004**, *93*, 086602.
- [27] K. Takimiya, S. Shinamura, I. Osaka, E. Miyazaki, 'Thienoacene-Based Organic Semiconductors', *Adv. Mater.* **2011**, *23*, 4347–4370.
- [28] K. Takimiya, I. Osaka, T. Mori, M. Nakano, 'Organic Semiconductors Based on [1]Benzothieno[3,2-*b*] [1]benzothiophene Substructure', *Acc. Chem. Res.* **2014**, *47*, 1493–1502.
- [29] H. Ebata, T. Izawa, E. Miyazaki, K. Takimiya, M. Ikeda, H. Kuwabara, T. Yui, 'Highly Soluble [1]Benzothieno[3,2-*b*]benzothiophene (BTBT) Derivatives for High-Performance, Solution-Processed Organic Field-Effect Transistors', *J. Am. Chem. Soc.* **2007**, *129*, 15732–15733.
- [30] P. Darmawan, T. Minari, Y. Xu, S.-L. Li, H. Song, M. Chan, K. Tsukagoshi, 'Optimal Structure for High-Performance and Low-Contact-Resistance Organic Field-Effect Transistors Using Contact-Doped Coplanar and Pseudo-Staggered Device Architectures', *Adv. Funct. Mater.* **2012**, *22*, 4577–4583.
- [31] E. G. Bittle, J. I. Basham, T. N. Jackson, O. D. Jurchescu, D. J. Gundlach, 'Mobility overestimation due to gated contacts in organic field-effect transistors', *Nat Commun* **2016**, *7*, 10908.
- [32] H. Minemawari, T. Yamada, H. Matsui, J. Tsutsumi, S. Haas, R. Chiba, R. Kumai, T. Hasegawa, 'Inkjet printing of single-crystal films', *Nature* **2011**, *475*, 364–367.
- [33] Y. Yuan, G. Giri, A. L. Ayzner, A. P. Zoombelt, S. C. B. Mannsfeld, J. Chen, D. Nordlund, M. F. Toney, J. Huang, Z. Bao, 'Ultra-high mobility transparent organic thin film transistors grown by an off-centre spin-coating method', *Nat Commun* **2014**, *5*, 3005.

- [34] T. Yamamoto, K. Takimiya, 'Facile Synthesis of Highly  $\pi$ -Extended Heteroarenes, Dinaphtho[2,3-*b*:2',3'-*f*]chalcogenopheno[3,2-*b*]chalcogenophenes, and Their Application to Field-Effect Transistors', *J. Am. Chem. Soc.* **2007**, *129*, 2224–2225.
- [35] M. Sugiyama, T. Uemura, M. Kondo, M. Akiyama, N. Namba, S. Yoshimoto, Y. Noda, T. Araki, T. Sekitani, 'An ultraflexible organic differential amplifier for recording electrocardiograms', *Nat Electron* **2019**, *2*, 351–360.
- [36] K. Kuribara, H. Wang, N. Uchiyama, K. Fukuda, T. Yokota, U. Zschieschang, C. Jaye, D. Fischer, H. Klauk, T. Yamamoto, K. Takimiya, M. Ikeda, H. Kuwabara, T. Sekitani, Y.-L. Loo, T. Someya, 'Organic transistors with high thermal stability for medical applications', *Nat Commun* **2012**, *3*, 723.
- [37] S. Yuvaraja, A. Nawaz, Q. Liu, D. Dubal, S. G. Surya, K. N. Salama, P. Sonar, 'Organic field-effect transistor-based flexible sensors', *Chem. Soc. Rev.* **2020**, *49*, 3423–3460.
- [38] U. Kraft, T. Zaki, F. Letzkus, J. N. Burghartz, E. Weber, B. Murmann, H. Klauk, 'Low-Voltage, High-Frequency Organic Transistors and Unipolar and Complementary Ring Oscillators on Paper', *Adv. Electron. Mater.* **2019**, *5*, 1800453.
- [39] C.-H. Kim, S. Sung, M.-H. Yoon, 'Synaptic organic transistors with a vacuum-deposited charge-trapping nanosheet', *Sci Rep* **2016**, *6*, 33355.
- [40] M. J. Mirshojaeian Hosseini, Y. Yang, A. J. Prendergast, E. Donati, M. Faezipour, G. Indiveri, R. A. Nawrocki, 'An organic synaptic circuit: toward flexible and biocompatible organic neuromorphic processing', *Neuromorph. Comput. Eng.* **2022**, *2*, 034009.
- [41] R. Hofmockel, U. Zschieschang, U. Kraft, R. Rödel, N. H. Hansen, M. Stolte, F. Würthner, K. Takimiya, K. Kern, J. Pflaum, H. Klauk, 'High-mobility organic thin-film transistors based on a small-molecule semiconductor deposited in vacuum and by solution shearing', *Organic Electronics* **2013**, *14*, 3213–3221.
- [42] B. Peng, Z. He, M. Chen, P. K. L. Chan, 'Ultrahigh On-Current Density of Organic Field-Effect Transistors Facilitated by Molecular Monolayer Crystals', *Adv Funct Materials* **2022**, *32*, 2202632.
- [43] J. W. Borchert, 'On the Minimization of Contact Resistance in Organic Thin-Film Transistors', *PhD Thesis* **2020**.
- [44] M. Geiger, R. Lingstädt, T. Wollandt, J. Deuschle, U. Zschieschang, F. Letzkus, J. N. Burghartz, P. A. Aken, R. T. Weitz, H. Klauk, 'Subthreshold Swing of 59 mV decade<sup>-1</sup> in Nanoscale Flexible Ultralow-Voltage Organic Transistors', *Adv Elect Materials* **2022**, *8*, 2101215.
- [45] J. W. Borchert, U. Zschieschang, F. Letzkus, M. Giorgio, R. T. Weitz, M. Caironi, J. N. Burghartz, S. Ludwigs, H. Klauk, 'Flexible low-voltage high-frequency organic thin-film transistors', *Sci. Adv.* **2020**, *6*, eaaz5156.
- [46] J. Zeng, D. He, J. Qiao, Y. Li, L. Sun, W. Li, J. Xie, S. Gao, L. Pan, P. Wang, Y. Xu, Y. Li, H. Qiu, Y. Shi, J.-B. Xu, W. Ji, X. Wang, 'Ultralow contact resistance in organic transistors via orbital hybridization', *Nat Commun* **2023**, *14*, 324.
- [47] A. Kitaigorodsky, *Molecular Crystals and Molecules*, Academic Press Inc., 1973.
- [48] C. Wang, H. Dong, L. Jiang, W. Hu, 'Organic semiconductor crystals', *Chem. Soc. Rev.* **2018**, *47*, 422–500.
- [49] C. Wang, H. Dong, W. Hu, Y. Liu, D. Zhu, 'Semiconducting  $\pi$ -Conjugated Systems in Field-Effect Transistors: A Material Odyssey of Organic Electronics', *Chem. Rev.* **2012**, *112*, 2208–2267.

- [50] C. Wang, H. Dong, H. Li, H. Zhao, Q. Meng, W. Hu, 'Dibenzothiophene Derivatives: From Herringbone to Lamellar Packing Motif', *Crystal Growth & Design* **2010**, *10*, 4155–4160.
- [51] K. Zhou, H. Dong, H. Zhang, W. Hu, 'High performance n-type and ambipolar small organic semiconductors for organic thin film transistors', *Phys. Chem. Chem. Phys.* **2014**, *16*, 22448–22457.
- [52] G. Schweicher, G. Garbay, R. Jouclas, F. Vibert, F. Devaux, Y. H. Geerts, 'Molecular Semiconductors for Logic Operations: Dead-End or Bright Future?', *Adv. Mater.* **2020**, *32*, 1905909.
- [53] A. F. Paterson, T. D. Anthopoulos, 'Enabling thin-film transistor technologies and the device metrics that matter', *Nat Commun* **2018**, *9*, 5264.
- [54] H. Klauk, 'Organic thin-film transistors', *Chem. Soc. Rev.* **2010**, *39*, 2643.
- [55] A. F. Paterson, S. Singh, K. J. Fallon, T. Hodsdon, Y. Han, B. C. Schroeder, H. Bronstein, M. Heeney, I. McCulloch, T. D. Anthopoulos, 'Recent Progress in High-Mobility Organic Transistors: A Reality Check', *Adv. Mater.* **2018**, *30*, 1801079.
- [56] J. Rivnay, S. C. B. Mannsfeld, C. E. Miller, A. Salleo, M. F. Toney, 'Quantitative Determination of Organic Semiconductor Microstructure from the Molecular to Device Scale', *Chem. Rev.* **2012**, *112*, 5488–5519.
- [57] W. L. Kalb, S. Haas, C. Krellner, T. Mathis, B. Batlogg, 'Trap density of states in small-molecule organic semiconductors: A quantitative comparison of thin-film transistors with single crystals', *Phys. Rev. B* **2010**, *81*, 155315.
- [58] S. Illig, A. S. Eggeman, A. Troisi, L. Jiang, C. Warwick, M. Nikolka, G. Schweicher, S. G. Yeates, Y. Henri Geerts, J. E. Anthony, H. Sirringhaus, 'Reducing dynamic disorder in small-molecule organic semiconductors by suppressing large-amplitude thermal motions', *Nat Commun* **2016**, *7*, 10736.
- [59] A. S. Eggeman, S. Illig, A. Troisi, H. Sirringhaus, P. A. Midgley, 'Measurement of molecular motion in organic semiconductors by thermal diffuse electron scattering', *Nature Mater* **2013**, *12*, 1045–1049.
- [60] G. Schweicher, G. D'Avino, M. T. Ruggiero, D. J. Harkin, K. Broch, D. Venkateshvaran, G. Liu, A. Richard, C. Ruzié, J. Armstrong, A. R. Kennedy, K. Shankland, K. Takimiya, Y. H. Geerts, J. A. Zeitler, S. Fratini, H. Sirringhaus, 'Chasing the "Killer" Phonon Mode for the Rational Design of Low-Disorder, High-Mobility Molecular Semiconductors', *Adv. Mater.* **2019**, *31*, 1902407.
- [61] D. P. McMahon, A. Troisi, 'Evaluation of the External Reorganization Energy of Polyacenes', *J. Phys. Chem. Lett.* **2010**, *1*, 941–946.
- [62] U. Purushotham, G. N. Sastry, 'Conjugate acene fused buckybowls: evaluating their suitability for p-type, ambipolar and n-type air stable organic semiconductors', *Phys. Chem. Chem. Phys.* **2013**, *15*, 5039.
- [63] V. Coropceanu, J. Cornil, D. A. da Silva Filho, Y. Olivier, R. Silbey, J.-L. Brédas, 'Charge Transport in Organic Semiconductors', *Chem. Rev.* **2007**, *107*, 926–952.
- [64] O. Ostroverkhova, 'Organic Optoelectronic Materials: Mechanisms and Applications', *Chem. Rev.* **2016**, *116*, 13279–13412.
- [65] S. Fratini, D. Mayou, S. Ciuchi, 'The Transient Localization Scenario for Charge Transport in Crystalline Organic Materials', *Adv. Funct. Mater.* **2016**, *26*, 2292–2315.
- [66] R. A. Marcus, 'Electron Transfer Reactions in Chemistry: Theory and Experiment (Nobel Lecture)', *Angew. Chem. Int. Ed. Engl.* **1993**, *32*, 1111–1121.

- [67] S. Fratini, S. Ciuchi, D. Mayou, G. T. de Laissardière, A. Troisi, ‘A map of high-mobility molecular semiconductors’, *Nature Mater* **2017**, *16*, 998–1002.
- [68] J. R. Brews, B. Laboratories, ‘A charge-sheet model of the MOSFET’, *Solid-State Electronics* **1977**, *21*, 345–355.
- [69] G. Horowitz, ‘Organic Field-Effect Transistors’, *Adv. Mater.* **1998**, *10*, 365–377.
- [70] Y. Xu, Y. Li, S. Li, F. Balestra, G. Ghibaudo, W. Li, Y. Lin, H. Sun, J. Wan, X. Wang, Y. Guo, Y. Shi, Y. Noh, ‘Precise Extraction of Charge Carrier Mobility for Organic Transistors’, *Adv. Funct. Mater.* **2020**, *30*, 1904508.
- [71] H. Klauk, ‘Will We See Gigahertz Organic Transistors?’, *Adv. Electron. Mater.* **2018**, *4*, 1700474.
- [72] M. Waldrip, O. D. Jurchescu, D. J. Gundlach, E. G. Bittle, ‘Contact Resistance in Organic Field-Effect Transistors: Conquering the Barrier’, *Adv. Funct. Mater.* **2020**, *30*, 1904576.
- [73] A. Yamamura, S. Watanabe, M. Uno, M. Mitani, C. Mitsui, J. Tsurumi, N. Isahaya, Y. Kanaoka, T. Okamoto, J. Takeya, ‘Wafer-scale, layer-controlled organic single crystals for high-speed circuit operation’, *Sci. Adv.* **2018**, *4*, eaao5758.
- [74] T. Matsumoto, W. Ou-Yang, K. Miyake, T. Uemura, J. Takeya, ‘Study of contact resistance of high-mobility organic transistors through comparisons’, *Organic Electronics* **2013**, *14*, 2590–2595.
- [75] D. Boudinet, M. Benwadih, S. Altazin, R. Gwoziecki, J. M. Verilhac, R. Coppard, G. Le Blevenec, I. Chartier, G. Horowitz, ‘Influence of the semiconductor layer thickness on electrical performance of staggered n- and p-channel organic thin-film transistors’, *Organic Electronics* **2010**, *11*, 291–298.
- [76] D. Gupta, M. Katiyar, D. Gupta, ‘An analysis of the difference in behavior of top and bottom contact organic thin film transistors using device simulation’, *Organic Electronics* **2009**, *10*, 775–784.
- [77] C. H. Kim, Y. Bonnassieux, G. Horowitz, ‘Fundamental Benefits of the Staggered Geometry for Organic Field-Effect Transistors’, *IEEE Electron Device Lett.* **2011**, *32*, 1302–1304.
- [78] C.-H. Kim, Y. Bonnassieux, G. Horowitz, ‘Compact DC Modeling of Organic Field-Effect Transistors: Review and Perspectives’, *IEEE Trans. Electron Devices* **2014**, *61*, 278–287.
- [79] Y. Xu, C. Liu, W. Scheideler, S. Li, W. Li, Y.-F. Lin, F. Balestra, G. Ghibaudo, K. Tsukagoshi, ‘Understanding Thickness-Dependent Charge Transport in Pentacene Transistors by Low-Frequency Noise’, *IEEE Electron Device Lett.* **2013**, *34*, 1298–1300.
- [80] C. Chiang, S. Martin, J. Kanicki, Y. Ugai, T. Yukawa, S. Takeuchi, ‘Top-Gate Staggered Amorphous Silicon Thin-Film Transistors: Series Resistance and Nitride Thickness Effects’, *Jpn. J. Appl. Phys.* **1998**, *37*, 5914.
- [81] T. J. Richards, H. Sirringhaus, ‘Analysis of the contact resistance in staggered, top-gate organic field-effect transistors’, *Journal of Applied Physics* **2007**, *102*, 094510.
- [82] T. Sawada, A. Yamamura, M. Sasaki, K. Takahira, T. Okamoto, S. Watanabe, J. Takeya, ‘Correlation between the static and dynamic responses of organic single-crystal field-effect transistors’, *Nat Commun* **2020**, *11*, 4839.
- [83] U. Kraft, K. Takimiya, M. J. Kang, R. Rödel, F. Letzkus, J. N. Burghartz, E. Weber, H. Klauk, ‘Detailed analysis and contact properties of low-voltage organic thin-film transistors based on dinaphtho[2,3-b:2',3'-f]thieno[3,2-b]thiophene (DNTT) and its didecyl and diphenyl derivatives’, *Organic Electronics* **2016**, *35*, 33–40.

- [84] M. Chen, B. Peng, R. A. Sporea, V. Podzorov, P. K. L. Chan, 'The Origin of Low Contact Resistance in Monolayer Organic Field-Effect Transistors with van der Waals Electrodes', *Small Science* **2022**, 2, 2100115.
- [85] J. W. Borchert, B. Peng, F. Letzkus, J. N. Burghartz, P. K. L. Chan, K. Zojer, S. Ludwigs, H. Klauk, 'Small contact resistance and high-frequency operation of flexible low-voltage inverted coplanar organic transistors', *Nat Commun* **2019**, 10, 1119.
- [86] M. Gruber, E. Zojer, F. Schürerer, K. Zojer, 'Impact of Materials versus Geometric Parameters on the Contact Resistance in Organic Thin-Film Transistors', *Adv. Funct. Mater.* **2013**, 23, 2941–2952.
- [87] K. Zojer, E. Zojer, A. F. Fernandez, M. Gruber, 'Impact of the Capacitance of the Dielectric on the Contact Resistance of Organic Thin-Film Transistors', *Phys. Rev. Applied* **2015**, 4, 044002.
- [88] S. Luan, G. W. Neudeck, 'An experimental study of the source/drain parasitic resistance effects in amorphous silicon thin film transistors', *Journal of Applied Physics* **1992**, 72, 766–772.
- [89] J. W. Borchert, R. T. Weitz, S. Ludwigs, H. Klauk, 'A Critical Outlook for the Pursuit of Lower Contact Resistance in Organic Transistors', *Advanced Materials* **2022**, 34, 2104075.
- [90] G. de Tournadre, F. Reisdorffer, R. Rödel, O. Simonetti, H. Klauk, L. Giraudet, 'High voltage surface potential measurements in ambient conditions: Application to organic thin-film transistor injection and transport characterization', *Journal of Applied Physics* **2016**, 119, 125501.
- [91] P. V. Pesavento, K. P. Puntambekar, C. D. Frisbie, J. C. McKeen, P. P. Ruden, 'Film and contact resistance in pentacene thin-film transistors: Dependence on film thickness, electrode geometry, and correlation with hole mobility', *Journal of Applied Physics* **2006**, 99, 094504.
- [92] C. Rolin, E. Kang, J.-H. Lee, G. Borghs, P. Heremans, J. Genoe, 'Charge carrier mobility in thin films of organic semiconductors by the gated van der Pauw method', *Nat Commun* **2017**, 8, 14975.
- [93] A. Kahn, N. Koch, W. Gao, 'Electronic structure and electrical properties of interfaces between metals and pi-conjugated molecular films', *J. Polym. Sci. B Polym. Phys.* **2003**, 41, 2529–2548.
- [94] D. K. Schroder, *Semiconductor Material and Device Characterization*, John Wiley & Sons, Inc., 2005.
- [95] H. Ishii, K. Sugiyama, E. Ito, K. Seki, 'Energy Level Alignment and Interfacial Electronic Structures at Organic/Metal and Organic/Organic Interfaces', *Adv. Mater.* **1999**, 11, 605–625.
- [96] Z. Zhang, J. T. Yates, 'Band Bending in Semiconductors: Chemical and Physical Consequences at Surfaces and Interfaces', *Chem. Rev.* **2012**, 112, 5520–5551.
- [97] M. Hertzog, M. Wang, J. Mony, K. Börjesson, 'Strong light–matter interactions: a new direction within chemistry', *Chem. Soc. Rev.* **2019**, 48, 937–961.
- [98] P. A. M. Dirac, 'The quantum theory of the emission and absorption of radiation', *Proc. R. Soc. London Ser. A Math. Phys. Character* **1927**, 114, 243–265.
- [99] K. Nagarajan, A. Thomas, T. W. Ebbesen, 'Chemistry under Vibrational Strong Coupling', *J. Am. Chem. Soc.* **2021**, 143, 16877–16889.
- [100] F. J. Garcia-Vidal, C. Ciuti, T. W. Ebbesen, 'Manipulating matter by strong coupling to vacuum fields', *Science* **2021**, 373, eabd0336.

- [101] E. T. Jaynes, F. W. Cummings, 'Comparison of quantum and semiclassical radiation theories with application to the beam maser', *Proc. IEEE* **1963**, *51*, 89–109.
- [102] M. Tavis, F. W. Cummings, 'Exact Solution for an N -Molecule—Radiation-Field Hamiltonian', *Phys. Rev.* **1968**, *170*, 379–384.
- [103] S. Wang, Strong Light-Molecule Coupling: Routes to New Hybrid Material, PhD thesis, Université de Strasbourg, 2015.
- [104] T. W. Ebbesen, 'Hybrid Light–Matter States in a Molecular and Material Science Perspective', *Acc. Chem. Res.* **2016**, *49*, 2403–2412.
- [105] J. Lather, P. Bhatt, A. Thomas, T. W. Ebbesen, J. George, 'Cavity Catalysis by Cooperative Vibrational Strong Coupling of Reactant and Solvent Molecules', *Angew. Chem. Int. Ed.* **2019**, *58*, 10635–10638.
- [106] J. A. Hutchison, T. Schwartz, C. Genet, E. Devaux, T. W. Ebbesen, 'Modifying Chemical Landscapes by Coupling to Vacuum Fields', *Angew. Chem. Int. Ed.* **2012**, *51*, 1592–1596.
- [107] J. A. Hutchison, A. Liscio, T. Schwartz, A. Canaguier-Durand, C. Genet, V. Palermo, P. Samorì, T. W. Ebbesen, 'Tuning the Work-Function Via Strong Coupling', *Adv. Mater.* **2013**, *25*, 2481–2485.
- [108] X. Zhong, T. Chervy, S. Wang, J. George, A. Thomas, J. A. Hutchison, E. Devaux, C. Genet, T. W. Ebbesen, 'Non-Radiative Energy Transfer Mediated by Hybrid Light-Matter States', *Angew. Chem. Int. Ed.* **2016**, *55*, 6202–6206.
- [109] X. Zhong, T. Chervy, L. Zhang, A. Thomas, J. George, C. Genet, J. A. Hutchison, T. W. Ebbesen, 'Energy Transfer between Spatially Separated Entangled Molecules', *Angew. Chem. Int. Ed.* **2017**, *56*, 9034–9038.
- [110] S. Hou, M. Khatoniar, K. Ding, Y. Qu, A. Napolov, V. M. Menon, S. R. Forrest, 'Ultralong-Range Energy Transport in a Disordered Organic Semiconductor at Room Temperature Via Coherent Exciton-Polariton Propagation', *Adv. Mater.* **2020**, *32*, 2002127.
- [111] D. M. Coles, N. Somaschi, P. Michetti, C. Clark, P. G. Lagoudakis, P. G. Savvidis, D. G. Lidzey, 'Polariton-mediated energy transfer between organic dyes in a strongly coupled optical microcavity', *Nature Mater* **2014**, *13*, 712–719.
- [112] E. Orgiu, J. George, J. A. Hutchison, E. Devaux, J. F. Dayen, B. Doudin, F. Stellacci, C. Genet, J. Schachenmayer, C. Genes, G. Pupillo, P. Samorì, T. W. Ebbesen, 'Conductivity in organic semiconductors hybridized with the vacuum field', *Nature Mater* **2015**, *14*, 1123–1129.
- [113] K. Nagarajan, J. George, A. Thomas, E. Devaux, T. Chervy, S. Azzini, K. Joseph, A. Jouaiti, M. W. Hosseini, A. Kumar, C. Genet, N. Bartolo, C. Ciuti, T. W. Ebbesen, 'Conductivity and Photoconductivity of a p-Type Organic Semiconductor under Ultrastrong Coupling', *ACS Nano* **2020**, *14*, 10219–10225.
- [114] K. Hirai, R. Takeda, J. A. Hutchison, H. Uji-i, 'Modulation of Prins Cyclization by Vibrational Strong Coupling', *Angew. Chem. Int. Ed.* **2020**, *59*, 5332–5335.
- [115] Y. Pang, A. Thomas, K. Nagarajan, R. M. A. Vergauwe, K. Joseph, B. Patrahaui, K. Wang, C. Genet, T. W. Ebbesen, 'On the Role of Symmetry in Vibrational Strong Coupling: The Case of Charge-Transfer Complexation', *Angew. Chem.* **2020**, *132*, 10522–10526.
- [116] R. M. A. Vergauwe, A. Thomas, K. Nagarajan, A. Shalabney, J. George, T. Chervy, M. Seidel, E. Devaux, V. Torbeev, T. W. Ebbesen, 'Modification of Enzyme Activity by Vibrational Strong Coupling of Water', *Angew. Chem.* **2019**, *131*, 15468–15472.

- [117] J. Lather, J. George, 'Improving Enzyme Catalytic Efficiency by Co-operative Vibrational Strong Coupling of Water', *J. Phys. Chem. Lett.* **2021**, *12*, 379–384.
- [118] K. Hirai, H. Ishikawa, T. Chervy, J. A. Hutchison, H. Uji-i, 'Selective crystallization *via* vibrational strong coupling', *Chem. Sci.* **2021**, *12*, 11986–11994.
- [119] K. Joseph, S. Kushida, E. Smarsly, D. Ihiawakrim, A. Thomas, G. L. Paravicini-Bagliani, K. Nagarajan, R. Vergauwe, E. Devaux, O. Ersen, U. H. F. Bunz, T. W. Ebbesen, 'Supramolecular Assembly of Conjugated Polymers under Vibrational Strong Coupling', *Angew Chem Int Ed* **2021**, *60*, 19665–19670.
- [120] K. Sandeep, K. Joseph, J. Gautier, K. Nagarajan, M. Sujith, K. G. Thomas, T. W. Ebbesen, 'Manipulating the Self-Assembly of Phenyleneethynylenes under Vibrational Strong Coupling', *J. Phys. Chem. Lett.* **2022**, *13*, 1209–1214.
- [121] S. Kumar, S. Biswas, U. Rashid, K. S. Mony, R. M. A. Vergauwe, V. Kaliginedi, A. Thomas, 'Extraordinary Electrical Conductance of Non-conducting Polymers Under Vibrational Strong Coupling', *arXiv* **2023**.
- [122] M. Watanabe, Y. J. Chang, S.-W. Liu, T.-H. Chao, K. Goto, Md. M. Islam, C.-H. Yuan, Y.-T. Tao, T. Shinmyozu, T. J. Chow, 'The synthesis, crystal structure and charge-transport properties of hexacene', *Nature Chem* **2012**, *4*, 574–578.
- [123] X. Gao, Y. Hu, 'Development of n-type organic semiconductors for thin film transistors: a viewpoint of molecular design', *J. Mater. Chem. C* **2014**, *2*, 3099–3117.
- [124] K. Takimiya, M. Nakano, H. Sugino, I. Osaka, 'Design and elaboration of organic molecules for high field-effect-mobility semiconductors', *Synthetic Metals* **2016**, *217*, 68–78.
- [125] R. Acharya, D. Günder, T. Breuer, G. Schmitz, H. Klauk, G. Witte, 'Stability of organic thin-film transistors based on ultrathin films of dinaphtho[2,3-*b*:2',3'-*f*]thieno[3,2-*b*]thiophene (DNTT)', *J. Mater. Chem. C* **2021**, *9*, 270–280.
- [126] U. Zschieschang, F. Ante, D. Kälblein, T. Yamamoto, K. Takimiya, H. Kuwabara, M. Ikeda, T. Sekitani, T. Someya, J. B.- Nimoth, H. Klauk, 'Dinaphtho[2,3-*b*:2',3'-*f*]thieno[3,2-*b*]thiophene (DNTT) thin-film transistors with improved performance and stability', *Organic Electronics* **2011**, *12*, 1370–1375.
- [127] E. Bestelink, U. Zschieschang, I. Bandara R M, H. Klauk, R. A. Sporea, 'The Secret Ingredient for Exceptional Contact-Controlled Transistors', *Adv Elect Materials* **2022**, *8*, 2101101.
- [128] J.-I. Park, J. W. Chung, J.-Y. Kim, J. Lee, J. Y. Jung, B. Koo, B.-L. Lee, S. W. Lee, Y. W. Jin, S. Y. Lee, 'Dibenzothiopheno[6,5-*b*:6',5'-*f*]thieno[3,2-*b*]thiophene (DBTTT): High-Performance Small-Molecule Organic Semiconductor for Field-Effect Transistors', *J. Am. Chem. Soc.* **2015**, *137*, 12175–12178.
- [129] J. Huang, H. Luo, L. Wang, Y. Guo, W. Zhang, H. Chen, M. Zhu, Y. Liu, G. Yu, 'Dibenzoannelated Tetrathienoacene: Synthesis, Characterization, and Applications in Organic Field-Effect Transistors', *Org. Lett.* **2012**, *14*, 3300–3303.
- [130] R. Jouclas, J. Liu, M. Volpi, L. Silva de Moraes, G. Garbay, N. McIntosh, M. Bardini, V. Lemaure, A. Vercoeur, C. Gatsios, F. Modesti, N. Turetta, D. Beljonne, J. Cornil, A. R. Kennedy, N. Koch, P. Erk, P. Samorì, G. Schweicher, Y. H. Geerts, 'Dinaphthotetrathienoacenes: Synthesis, Characterization, and Applications in Organic Field-Effect Transistors', *Advanced Science* **2022**, *9*, 2105674.

- [131] M. Abe, T. Mori, I. Osaka, K. Sugimoto, K. Takimiya, 'Thermally, Operationally, and Environmentally Stable Organic Thin-Film Transistors Based on Bis[1]benzothieno[2,3-*d*:2',3'-*d'*]naphtho[2,3-*b*:6,7-*b'*]dithiophene Derivatives: Effective Synthesis, Electronic Structures, and Structure–Property Relationship', *Chem. Mater.* **2015**, *27*, 5049–5057.
- [132] T. Mori, T. Nishimura, T. Yamamoto, I. Doi, E. Miyazaki, I. Osaka, K. Takimiya, 'Consecutive Thiophene-Annulation Approach to  $\pi$ -Extended Thienoacene-Based Organic Semiconductors with [1]Benzothieno[3,2-*b*] [1]benzothiophene (BTBT) Substructure', *J. Am. Chem. Soc.* **2013**, *135*, 13900–13913.
- [133] G. Schweicher, V. Lemaire, C. Niebel, C. Ruzié, Y. Diao, O. Goto, W. Lee, Y. Kim, J. Arlin, J. Karpinska, A. R. Kennedy, S. R. Parkin, Y. Olivier, S. C. B. Mannsfeld, J. Cornil, Y. H. Geerts, Z. Bao, 'Bulky End-Capped [1]Benzothieno[3,2-*b*]benzothiophenes: Reaching High-Mobility Organic Semiconductors by Fine Tuning of the Crystalline Solid-State Order', *Adv. Mater.* **2015**, *27*, 3066–3072.
- [134] H. Chung, D. Dudenko, F. Zhang, G. D'Avino, C. Ruzié, A. Richard, G. Schweicher, J. Cornil, D. Beljonne, Y. Geerts, Y. Diao, 'Rotator side chains trigger cooperative transition for shape and function memory effect in organic semiconductors', *Nat Commun* **2018**, *9*, 278.
- [135] A. Yamamoto, Y. Murata, C. Mitsui, H. Ishii, M. Yamagishi, M. Yano, H. Sato, A. Yamano, J. Takeya, T. Okamoto, 'Zigzag-Elongated Fused  $\pi$ -Electronic Core: A Molecular Design Strategy to Maximize Charge-Carrier Mobility', *Adv. Sci.* **2018**, *5*, 1700317.
- [136] C. Mitsui, T. Okamoto, M. Yamagishi, J. Tsurumi, K. Yoshimoto, K. Nakahara, J. Soeda, Y. Hirose, H. Sato, A. Yamano, T. Uemura, J. Takeya, 'High-Performance Solution-Processable N-Shaped Organic Semiconducting Materials with Stabilized Crystal Phase', *Adv. Mater.* **2014**, *26*, 4546–4551.
- [137] T. Okamoto, C. Mitsui, M. Yamagishi, K. Nakahara, J. Soeda, Y. Hirose, K. Miwa, H. Sato, A. Yamano, T. Matsushita, T. Uemura, J. Takeya, 'V-Shaped Organic Semiconductors With Solution Processability, High Mobility, and High Thermal Durability', *Adv. Mater.* **2013**, *25*, 6392–6397.
- [138] S. Casalini, C. A. Bortolotti, F. Leonardi, F. Biscarini, 'Self-assembled monolayers in organic electronics', *Chem. Soc. Rev.* **2017**, *46*, 40–71.
- [139] A. Fischer, H. Zündorf, F. Kaschura, J. Widmer, K. Leo, U. Kraft, H. Klauk, 'Nonlinear Contact Effects in Staggered Thin-Film Transistors', *Phys. Rev. Applied* **2017**, *8*, 054012.
- [140] A. A. Virkar, S. Mannsfeld, Z. Bao, N. Stingelin, 'Organic Semiconductor Growth and Morphology Considerations for Organic Thin-Film Transistors', *Adv. Mater.* **2010**, *22*, 3857–3875.
- [141] M. R. Niazi, R. Li, M. Abdelsamie, K. Zhao, D. H. Anjum, M. M. Payne, J. Anthony, D.-M. Smilgies, A. Amassian, 'Contact-Induced Nucleation in High-Performance Bottom-Contact Organic Thin Film Transistors Manufactured by Large-Area Compatible Solution Processing', *Adv. Funct. Mater.* **2016**, *26*, 2371–2378.
- [142] D. J. Gundlach, J. E. Royer, S. K. Park, S. Subramanian, O. D. Jurchescu, B. H. Hamadani, A. J. Moad, R. J. Kline, L. C. Teague, O. Kirillov, C. A. Richter, J. G. Kushmerick, L. J. Richter, S. R. Parkin, T. N. Jackson, J. E. Anthony, 'Contact-induced crystallinity for high-performance soluble acene-based transistors and circuits', *Nature Mater* **2008**, *7*, 216–221.
- [143] A. Virkar, S. Mannsfeld, J. H. Oh, M. F. Toney, Y. H. Tan, G. Liu, J. C. Scott, R. Miller, Z. Bao, 'The Role of OTS Density on Pentacene and C<sub>60</sub> Nucleation,

- Thin Film Growth, and Transistor Performance', *Adv. Funct. Mater.* **2009**, *19*, 1962–1970.
- [144] R. Ruiz, D. Choudhary, B. Nickel, T. Toccoli, K.-C. Chang, A. C. Mayer, P. Clancy, J. M. Blakely, R. L. Headrick, S. Iannotta, G. G. Malliaras, 'Pentacene Thin Film Growth', *Chem. Mater.* **2004**, *16*, 4497–4508.
- [145] H. Ishii, in *Compendium of Surface and Interface Analysis* (Ed.: The Surface Science Society of Japan), Springer Singapore, Singapore, 2018, pp. 457–463.
- [146] K. Takimiya, I. Osaka, T. Mori, M. Nakano, 'Organic Semiconductors Based on [1]Benzothieno[3,2-b][1]benzothiophene Substructure', *Acc. Chem. Res.* **2014**, *47*, 1493–1502.
- [147] A. Babuji, F. Silvestri, L. Pithan, A. Richard, Y. H. Geerts, N. Tessler, O. Solomeshch, C. Ocal, E. Barrena, 'Effect of the Organic Semiconductor Side Groups on the Structural and Electronic Properties of Their Interface with Dopants', *ACS Appl. Mater. Interfaces* **2020**, *12*, 57578–57586.
- [148] Y. Yamaguchi, Y. Kojiguchi, S. Kawata, T. Mori, K. Okamoto, M. Tsutsui, T. Koganezawa, H. Katagiri, T. Yasuda, 'Solution-Processable Organic Semiconductors Featuring S-Shaped Dinaphthothienothiophene (S-DNTT): Effects of Alkyl Chain Length on Self-Organization and Carrier Transport Properties', *Chem. Mater.* **2020**, *32*, 5350–5360.
- [149] M. C. Gwinner, R. D. Pietro, Y. Vaynzof, K. J. Greenberg, P. K. H. Ho, R. H. Friend, H. Sirringhaus, 'Doping of Organic Semiconductors Using Molybdenum Trioxide: a Quantitative Time-Dependent Electrical and Spectroscopic Study', *Adv. Funct. Mater.* **2011**, *21*, 1432–1441.
- [150] Y. Hu, D. X. Cao, A. T. Lill, L. Jiang, C.-A. Di, X. Gao, H. Sirringhaus, T.-Q. Nguyen, 'Effect of Alkyl-Chain Length on Charge Transport Properties of Organic Semiconductors and Organic Field-Effect Transistors', *Adv. Electron. Mater.* **2018**, *4*, 1800175.
- [151] B. H. Hamadani, D. Natelson, 'Temperature-dependent contact resistances in high-quality polymer field-effect transistors', *Appl. Phys. Lett.* **2004**, *84*, 443–445.
- [152] D. Natali, M. Caironi, 'Charge Injection in Solution-Processed Organic Field-Effect Transistors: Physics, Models and Characterization Methods', *Adv. Mater.* **2012**, *24*, 1357–1387.
- [153] V. Lemaire, D. A. da Silva Filho, V. Coropceanu, M. Lehmann, Y. Geerts, J. Pirls, M. G. Debije, A. M. van de Craats, K. Senthilkumar, L. D. A. Siebbeles, J. M. Warman, J.-L. Brédas, J. Cornil, 'Charge Transport Properties in Discotic Liquid Crystals: A Quantum-Chemical Insight into Structure–Property Relationships', *J. Am. Chem. Soc.* **2004**, *126*, 3271–3279.
- [154] E. F. Valeev, V. Coropceanu, D. A. da Silva Filho, S. Salman, J.-L. Brédas, 'Effect of Electronic Polarization on Charge-Transport Parameters in Molecular Organic Semiconductors', *J. Am. Chem. Soc.* **2006**, *128*, 9882–9886.
- [155] L. Viani, Y. Olivier, S. Athanasopoulos, D. A. da Silva Filho, J. Hulliger, J.-L. Brédas, J. Gierschner, J. Cornil, 'Theoretical Characterization of Charge Transport in One-Dimensional Collinear Arrays of Organic Conjugated Molecules', *ChemPhysChem* **2010**, *11*, 1062–1068.
- [156] N. E. Gruhn, D. A. da Silva Filho, T. G. Bill, M. Malagoli, V. Coropceanu, A. Kahn, J.-L. Brédas, 'The Vibrational Reorganization Energy in Pentacene: Molecular Influences on Charge Transport', *J. Am. Chem. Soc.* **2002**, *124*, 7918–7919.
- [157] T. Yamamoto, S. Shinamura, E. Miyazaki, K. Takimiya, 'Three Structural Isomers of Dinaphthothieno[3,2-b]thiophenes: Elucidation of Physicochemical

- Properties, Crystal Structures, and Field-Effect Transistor Characteristics', *BCSJ* **2010**, *83*, 120–130.
- [158] R. S. Sánchez-Carrera, S. Atahan, J. Schrier, A. Aspuru-Guzik, 'Theoretical Characterization of the Air-Stable, High-Mobility Dinaphtho[2,3-b:2'3'-f]thieno[3,2-b]-thiophene Organic Semiconductor', *J. Phys. Chem. C* **2010**, *114*, 2334–2340.
- [159] Y. Tsutsui, G. Schweicher, B. Chattopadhyay, T. Sakurai, J. Arlin, C. Ruzié, A. Aliev, A. Ciesielski, S. Colella, A. R. Kennedy, V. Lemaure, Y. Olivier, R. Hadji, L. Sanguinet, F. Castet, S. Osella, D. Dudenko, D. Beljonne, J. Cornil, P. Samori, S. Seki, Y. H. Geerts, 'Unraveling Unprecedented Charge Carrier Mobility through Structure Property Relationship of Four Isomers of Didodecyl[1]benzothieno[3,2- b ][1]benzothiophene', *Adv. Mater.* **2016**, *28*, 7106–7114.
- [160] U. Zschieschang, F. Ante, T. Yamamoto, K. Takimiya, H. Kuwabara, M. Ikeda, T. Sekitani, T. Someya, K. Kern, H. Klauk, 'Flexible Low-Voltage Organic Transistors and Circuits Based on a High-Mobility Organic Semiconductor with Good Air Stability', *Adv. Mater.* **2010**, *22*, 982–985.
- [161] S. Uttiya, L. Miozzo, E. M. Fumagalli, S. Bergantin, R. Ruffo, M. Parravicini, A. Papagni, M. Moret, A. Sassella, 'Connecting molecule oxidation to single crystal structural and charge transport properties in rubrene derivatives', *J. Mater. Chem. C* **2014**, *2*, 4147–4155.
- [162] M. Barf, F. S. Benneckendorf, P. Reiser, R. Bäuerle, W. Köntges, L. Müller, M. Pfannmöller, S. Beck, E. Mankel, J. Freudenberger, D. Jänsch, J. Tisserant, R. Lovrincic, R. R. Schröder, U. H. F. Bunz, A. Pucci, W. Jaegermann, W. Kowalsky, K. Müllen, 'Compensation of Oxygen Doping in p-Type Organic Field-Effect Transistors Utilizing Immobilized n-Dopants', *Adv Materials Technologies* **2021**, *6*, 2000556.
- [163] K. Takimiya, I. Osaka, T. Mori, M. Nakano, 'Organic Semiconductors Based on [1]Benzothieno[3,2- b ][1]benzothiophene Substructure', *Acc. Chem. Res.* **2014**, *47*, 1493–1502.
- [164] C. Niebel, Y. Kim, C. Ruzié, J. Karpinska, B. Chattopadhyay, G. Schweicher, A. Richard, V. Lemaure, Y. Olivier, J. Cornil, A. R. Kennedy, Y. Diao, W.-Y. Lee, S. Mannsfeld, Z. Bao, Y. H. Geerts, 'Thienoacene dimers based on the thieno[3,2-b]thiophene moiety: synthesis, characterization and electronic properties', *J. Mater. Chem. C* **2015**, *3*, 674–685.
- [165] B. Peng, K. Cao, A. H. Y. Lau, M. Chen, Y. Lu, P. K. L. Chan, 'Crystallized Monolayer Semiconductor for Ohmic Contact Resistance, High Intrinsic Gain, and High Current Density', *Adv. Mater.* **2020**, *32*, 2002281.
- [166] B. Peng, S. Huang, Z. Zhou, P. K. L. Chan, 'Solution-Processed Monolayer Organic Crystals for High-Performance Field-Effect Transistors and Ultrasensitive Gas Sensors', *Adv. Funct. Mater.* **2017**, *27*, 1700999.
- [167] U. Zschieschang, J. W. Borchert, M. Giorgio, M. Caironi, F. Letzkus, J. N. Burghartz, U. Waizmann, J. Weis, S. Ludwigs, H. Klauk, 'Roadmap to Gigahertz Organic Transistors', *Adv. Funct. Mater.* **2020**, *30*, 1903812.
- [168] D. Braga, M. Ha, W. Xie, C. D. Frisbie, 'Ultralow contact resistance in electrolyte-gated organic thin film transistors', *Appl. Phys. Lett.* **2010**, *97*, 193311.
- [169] J. Lenz, F. Del Giudice, F. R. Geisenhof, F. Winterer, R. T. Weitz, 'Vertical, electrolyte-gated organic transistors show continuous operation in the MA cm<sup>-2</sup> regime and artificial synaptic behaviour', *Nat. Nanotechnol.* **2019**, *14*, 579–585.

- [170] W. Xie, K. Willa, Y. Wu, R. Häusermann, K. Takimiya, B. Batlogg, C. D. Frisbie, 'Temperature-Independent Transport in High-Mobility Dinaphtho-Thieno-Thiophene (DNTT) Single Crystal Transistors', *Adv. Mater.* **2013**, *25*, 3478–3484.
- [171] H.-Y. Chen, G. Schweicher, M. Planells, S. M. Ryno, K. Broch, A. J. P. White, D. Simatos, M. Little, C. Jellett, S. J. Cryer, A. Marks, M. Hurhangee, J.-L. Brédas, H. Sirringhaus, I. McCulloch, 'Crystal Engineering of Dibenzothiophenothieno[3,2-*b*]thiophene (DBTTT) Isomers for Organic Field-Effect Transistors', *Chem. Mater.* **2018**, *30*, 7587–7592.
- [172] Y. Xu, C. Liu, H. Sun, F. Balestra, G. Ghibaudo, W. Scheideler, Y.-Y. Noh, 'Metal evaporation dependent charge injection in organic transistors', *Organic Electronics* **2014**, *15*, 1738–1744.
- [173] C.-H. Wang, C.-W. Su, S. W. Chan, L.-J. Fan, M.-C. Chen, Y.-W. Yang, 'Damaging Effect of Hot Metal Atoms on Organic Semiconducting Films during Top Contact Formation', *J. Phys. Chem. C* **2015**, *119*, 14593–14602.
- [174] Y. Liang, H.-C. Chang, P. Paul Ruden, C. Daniel Frisbie, 'Examination of Au, Cu, and Al contacts in organic field-effect transistors via displacement current measurements', *Journal of Applied Physics* **2011**, *110*, 064514.
- [175] C. Liu, Y. Xu, Y. Li, W. Scheideler, T. Minari, 'Critical Impact of Gate Dielectric Interfaces on the Contact Resistance of High-Performance Organic Field-Effect Transistors', *J. Phys. Chem. C* **2013**, *117*, 12337–12345.
- [176] Q. Wang, S. Jiang, B. Zhang, E.-Y. Shin, Y.-Y. Noh, Y. Xu, Y. Shi, Y. Li, 'Role of Schottky Barrier and Access Resistance in Organic Field-Effect Transistors', *J. Phys. Chem. Lett.* **2020**, *11*, 1466–1472.
- [177] C.-H. Shim, F. Maruoka, R. Hattori, 'Structural Analysis on Organic Thin-Film Transistor With Device Simulation', *IEEE Trans. Electron Devices* **2010**, *57*, 195–200.
- [178] G. G. Malliaras, J. R. Salem, P. J. Brock, C. Scott, 'Electrical characteristics and efficiency of single-layer organic light-emitting diodes', *Phys. Rev. B* **1998**, *58*, R13411–R13414.
- [179] S. A. Moiz, I. A. Khan, W. A. Younis, K. S. Karimov, in *Conducting Polymers* (Ed.: F. Yilmaz), InTech, 2016.
- [180] D. Moerman, N. Sebaihi, S. E. Kaviyil, P. Leclère, R. Lazzaroni, O. Douhéret, 'Towards a unified description of the charge transport mechanisms in conductive atomic force microscopy studies of semiconducting polymers', *Nanoscale* **2014**, *6*, 10596–10603.
- [181] W. Hourani, K. Rahimi, I. Botiz, F. P. Vinzenz Koch, G. Reiter, P. Lienerth, T. Heiser, J.-L. Bubendorff, L. Simon, 'Anisotropic charge transport in large single crystals of  $\pi$ -conjugated organic molecules', *Nanoscale* **2014**, *6*, 4774.
- [182] Y. Hu, D. X. Cao, A. T. Lill, L. Jiang, C. Di, X. Gao, H. Sirringhaus, T. Nguyen, 'Effect of Alkyl-Chain Length on Charge Transport Properties of Organic Semiconductors and Organic Field-Effect Transistors', *Adv. Electron. Mater.* **2018**, *4*, 1800175.
- [183] K. Park, R. Vijayan, T. L. Andrew, 'Large-Area Heteroepitaxial Nanostructuring of Molecular Semiconductor Films for Enhanced Optoelectronic Response in Flexible Electronics', *Adv. Funct. Materials* **2022**, *32*, 2113085.
- [184] O. G. Reid, K. Munechika, D. S. Ginger, 'Space Charge Limited Current Measurements on Conjugated Polymer Films using Conductive Atomic Force Microscopy', *Nano Lett.* **2008**, *8*, 1602–1609.

- [185] M. Zubair, Y. S. Ang, L. K. Ang, 'Thickness Dependence of Space-Charge-Limited Current in Spatially Disordered Organic Semiconductors', *IEEE Trans. Electron Devices* **2018**, *65*, 3421–3429.
- [186] S. W. Button, J. M. Mativetsky, 'High-resolution charge carrier mobility mapping of heterogeneous organic semiconductors', *Appl. Phys. Lett.* **2017**, *111*, 083302.
- [187] J. M. Mativetsky, A. Liscio, E. Treossi, E. Orgiu, A. Zanelli, P. Samorì, V. Palermo, 'Graphene Transistors via in Situ Voltage-Induced Reduction of Graphene-Oxide under Ambient Conditions', *J. Am. Chem. Soc.* **2011**, *133*, 14320–14326.
- [188] B. Blülle, A. Troisi, R. Häusermann, B. Batlogg, 'Charge transport perpendicular to the high mobility plane in organic crystals: Bandlike temperature dependence maintained despite hundredfold anisotropy', *Phys. Rev. B* **2016**, *93*, 035205.
- [189] P. K. L. Chan, 'The Motivation for and Challenges to Scaling Down Organic Field-Effect Transistors', *Adv. Electron. Mater.* **2019**, *5*, 1900029.
- [190] S. Olthof, 'The Impact of UV Photoelectron Spectroscopy on the Field of Organic Optoelectronics—A Retrospective', *Advanced Optical Materials* **2021**, *9*, 2100227.
- [191] X. Cheng, Y.-Y. Noh, J. Wang, M. Tello, J. Frisch, R.-P. Blum, A. Vollmer, J. P. Rabe, N. Koch, H. Sirringhaus, 'Controlling Electron and Hole Charge Injection in Ambipolar Organic Field-Effect Transistors by Self-Assembled Monolayers', *Adv. Funct. Mater.* **2009**, *19*, 2407–2415.
- [192] J. Wagner, M. Gruber, A. Wilke, Y. Tanaka, K. Topczak, A. Steindamm, U. Hörmann, A. Opitz, Y. Nakayama, H. Ishii, J. Pflaum, N. Koch, W. Brütting, 'Identification of different origins for s-shaped current voltage characteristics in planar heterojunction organic solar cells', *Journal of Applied Physics* **2012**, *111*, 054509.
- [193] C. Celle, C. Suspène, M. Ternisien, S. Lenfant, D. Guérin, K. Smaali, K. Lmimouni, J. P. Simonato, D. Vuillaume, 'Interface dipole: Effects on threshold voltage and mobility for both amorphous and poly-crystalline organic field effect transistors', *Organic Electronics* **2014**, *15*, 729–737.
- [194] C. Huang, X. Ding, X. Ren, X. Yu, W. Hu, 'Improving the charge injection in bottom contact organic transistors by carbon electrodes', *J. Mater. Chem. C* **2022**, *10*, 2838–2844.
- [195] U. Kraft, J. E. Anthony, E. Ripaud, M. A. Loth, E. Weber, H. Klauk, 'Low-Voltage Organic Transistors Based on Tetraceno[2,3- *b*]thiophene: Contact Resistance and Air Stability', *Chem. Mater.* **2015**, *27*, 998–1004.
- [196] A. Thomas, L. Lethuillier-Karl, K. Nagarajan, R. M. A. Vergauwe, J. George, T. Chervy, A. Shalabney, E. Devaux, C. Genet, J. Moran, T. W. Ebbesen, 'Tilting a ground-state reactivity landscape by vibrational strong coupling', *Science* **2019**, *363*, 615–619.
- [197] A. Thomas, A. Jayachandran, L. Lethuillier-Karl, R. M. A. Vergauwe, K. Nagarajan, E. Devaux, C. Genet, J. Moran, T. W. Ebbesen, 'Ground state chemistry under vibrational strong coupling: dependence of thermodynamic parameters on the Rabi splitting energy', *Nanophotonics* **2020**, *9*, 249–255.
- [198] J. Flick, M. Ruggenthaler, H. Appel, A. Rubio, 'Atoms and molecules in cavities, from weak to strong coupling in quantum-electrodynamics (QED) chemistry', *Proc. Natl. Acad. Sci. U.S.A.* **2017**, *114*, 3026–3034.
- [199] M. Botoshansky, F. H. Herstein, M. Kapon, 'Towards a Complete Description of a Polymorphic Crystal: The Example of Perylene', *HCA* **2003**, *86*, 1113–1128.

- [200] J. H. Urbelis, J. A. Swift, 'Phase-Selective Crystallization of Perylene on Monolayer Templates', *Crystal Growth & Design* **2014**, *14*, 5244–5251.
- [201] T. Yago, Y. Tamaki, A. Furube, R. Katoh, 'Growth of  $\beta$ -Perylene Crystal', *Chem. Lett.* **2007**, *36*, 370–371.
- [202] Y. Lei, Q. Liao, H. Fu, J. Yao, 'Phase- and Shape-Controlled Synthesis of Single Crystalline Perylene Nanosheets and Its Optical Properties', *J. Phys. Chem. C* **2009**, *113*, 10038–10043.
- [203] Z.-Z. Li, L.-S. Liao, X.-D. Wang, 'Controllable Synthesis of Organic Microcrystals with Tunable Emission Color and Morphology Based on Molecular Packing Mode', *Small* **2018**, *14*, 1702952.
- [204] C.-T. Hsieh, C.-Y. Chen, H.-Y. Lin, C.-J. Yang, T.-J. Chen, K.-Y. Wu, C.-L. Wang, 'Polymorphic Behavior of Perylene and Its Influences on OFET Performances', *J. Phys. Chem. C* **2018**, *122*, 16242–16248.
- [205] G. R. Desiraju, A. Gavezzotti, 'From molecular to crystal structure; polynuclear aromatic hydrocarbons', *J. Chem. Soc., Chem. Commun.* **1989**, 621.
- [206] A. Richard, Conception, Synthèse et Caractérisation de Semi-Conducteurs Moléculaires à Dimensionnalité Élevée, PhD thesis, Université libre de Bruxelles, 2017.
- [207] K. Niimi, M. J. Kang, E. Miyazaki, I. Osaka, K. Takimiya, 'General Synthesis of Dinaphtho[2,3-*b*:2',3'-*f*]thieno[3,2-*b*]thiophene (DNTT) Derivatives', *Org. Lett.* **2011**, *13*, 3430–3433.
- [208] H. A. Wegner, H. Reisch, K. Rauch, A. Demeter, K. A. Zachariasse, A. De Meijere, L. T. Scott, 'Oligoindenopyrenes: A New Class of Polycyclic Aromatics', *J. Org. Chem.* **2006**, *71*, 9080–9087.
- [209] N. G. Martinelli, J. Idé, R. S. Sánchez-Carrera, V. Coropceanu, J.-L. Brédas, L. Ducasse, F. Castet, J. Cornil, D. Beljonne, 'Influence of Structural Dynamics on Polarization Energies in Anthracene Single Crystals', *J. Phys. Chem. C* **2010**, *114*, 20678–20685.
- [210] G. te Velde, F. M. Bickelhaupt, E. J. Baerends, C. Fonseca Guerra, S. J. A. van Gisbergen, J. G. Snijders, T. Ziegler, 'Chemistry with ADF', *J. Comput. Chem.* **2001**, *22*, 931–967.
- [211] D. B. Boyd, K. B. Lipkowitz, *Reviews in Computational Chemistry. Vol. 15 Vol. 15*, Wiley-VCH, New York, New York, 2000.
- [212] A. Troisi, G. Orlandi, 'Dynamics of the Intermolecular Transfer Integral in Crystalline Organic Semiconductors', *J. Phys. Chem. A* **2006**, *110*, 4065–4070.
- [213] Y. Wang, L. Sun, C. Wang, F. Yang, X. Ren, X. Zhang, H. Dong, W. Hu, 'Organic crystalline materials in flexible electronics', *Chem. Soc. Rev.* **2019**, *48*, 1492–1530.
- [214] J. Mei, Y. Diao, A. L. Appleton, L. Fang, Z. Bao, 'Integrated Materials Design of Organic Semiconductors for Field-Effect Transistors', *J. Am. Chem. Soc.* **2013**, *135*, 6724–6746.
- [215] T. Okamoto, C. P. Yu, C. Mitsui, M. Yamagishi, H. Ishii, J. Takeya, 'Bent-Shaped *p*-Type Small-Molecule Organic Semiconductors: A Molecular Design Strategy for Next-Generation Practical Applications', *J. Am. Chem. Soc.* **2020**, *142*, 9083–9096.



# List of Publications

## Scientific papers

In relation to **Chapter 2**:

- R. Jouclas, J. Liu, M. Volpi, L. Silva de Moraes, G. Garbay, N. McIntosh, M. Bardini, V. Lemaury, A. Vercoeur, C. Gatsios, F. Modesti, N. Turetta, D. Beljonne, J. Cornil, A. R. Kennedy, N. Koch, P. Erk, P. Samorì, G. Schweicher, Y., H. Geerts  
*Dinaphthotetrathienoacenes: Synthesis, Characterization, and Applications in Organic Field-Effect Transistors*  
Advanced Science **2022**, 9, 2105674
- R. Jouclas et al., *Octyl and Decyl derivatives of DN4T: synthesis, characterization and applications in Organic Field Effect Transistors*  
Manuscript in preparation
- F. Modesti et al., *Improved charge carrier injection in organic transistors based on tert-butyl thienoacene derivatives with extended molecular core aromaticity*  
Manuscript in preparation

In relation to **Chapter 3**:

- F. Modesti et al., *The role of in-plane and out-of-plane mobility on the contact resistance of organic-field effect transistors*  
Manuscript in preparation

## Conferences

- F. Modesti, T. Musiol, R. Jouclas, M. Volpi, G. Schweicher, Y. Geerts, P. Erk; *Vacuum-deposited organic thin-film transistors based on dinaphthotetrathienoacenes*  
Poster presentation  
  
55<sup>th</sup> Course: Molecular Crystal Engineering; Online, 31 May – 04 June 2021
- F. Modesti, G. Schweicher, Y. Geerts, P. Erk, *The role of molecular structure of p-type small-molecule organic semiconductors on the contact resistance in coplanar and staggered organic field-effect transistors*

Poster presentation

Large-area, Organic and Printed Electronics Convention (LOPEC) 2022; Munich (Germany), 23-24 March 2022

- F. Modesti, K.M. Joseph, P. Erk, T.W. Ebbesen; *Exploring the effects of vibrational strong coupling on supramolecular chemistry: perylene crystallization in a Fabry-Perrot cavity*

Poster presentation

Material Research Society (MRS) Spring Meeting; Honolulu (USA), 8-13 May 2022

- F. Modesti, N. Turetta, G. Schweicher, Y. Geerts, P. Erk; *Contact resistance in field-effect transistors based on thienoacene derivatives*

Oral presentation

UHMob International Conference - Organic Semiconductors: From Principles to Applications; Mainz (Germany), 6-9 September 2022



## **Relations structures- propriétés de semi- conducteurs organiques thiénoacènes**

### **Résumé**

Le domaine de recherche des semi-conducteurs organiques a gagné en importance grâce à leur potentiel d'applications dans l'électronique imprimée. Cependant, les faibles interactions intermoléculaires provoquent un désordre statique et dynamique dans les transistors à film mince organiques, limitant leurs performances. Cette thèse étudie les relations structure-propriétés des semi-conducteurs organiques de petites molécules pour fournir des lignes directrices de conception pour des transistors à film mince organiques performants. L'étude établit l'impact de la morphologie du film mince, de l'arrangement à l'état cristallin et de l'injection de charge sur les performances électriques des thiénoacènes. Elle souligne également l'importance de maximiser la mobilité du porteur de charge dans le plan du transport de charge pour minimiser la résistance de contact dans les transistors à film mince. Enfin, ce travail explore l'effet du couplage lumière-matière sur la croissance cristalline et le polymorphisme des cristaux de perylène, en fournissant des orientations pour de futures expériences.

### **Résumé en anglais**

The research field of organic semiconductors has gained traction due to their potential applications in printed electronics. However, weak intermolecular interactions cause static and dynamic disorder in organic thin-film transistors, limiting their performance. This thesis investigates the structure-properties relations of small-molecule organic semiconductors to provide design guidelines for high-performance organic thin-film transistors. The study establishes the impact of thin film morphology, crystalline packing, and charge injection on the electrical performance of thienoacenes. It also highlights the significance of maximizing in-plane charge carrier mobility to minimize contact resistance in thin-film transistors. Finally, this work explores the effect of light-matter coupling on perylene crystal growth and polymorphism, providing guidance for future experimental setups.